Glass-ceramics in dentistry: Fundamentals, technologies, experimental techniques, applications, and open issues

Glass-ceramics in dentistry: Fundamentals, technologies, experimental techniques, applications, and open issues

Maziar Montazerian[1,*], Francesco Baino[2,*], Elisa Fiume[2], Carla Migneco[2], Amirhossein Alaghmandfard[3,#], Omid Sedighi[4,#], Anthony V. DeCeanne [5], Collin J. Wilkinson[5], John C. Mauro[5,**]

[1] Northeastern Laboratory for Evaluation and Development of Biomaterials (CERTBIO), Department of Materials Engineering, Federal University of Campina Grande, PB, Brazil

[2] Institute of Materials Physics and Engineering, Applied Science and Technology Department, Politecnico di Torino, Turin, Italy

[3] School of Engineering and Computer Science, University of Victoria, Victoria, British Columbia, Canada

[4] Department of Electrical and Biomedical Engineering, University of Vermont, Burlington, Vermont, USA

[5] Department of Materials Science and Engineering, The Pennsylvania State University, University Park, Pennsylvania, USA

** Correspondence should be addressed to **JOHN C. MAURO** via email: jcm426@psu.edu or phone: 814-865-2130.

* Co-corresponding authors: M. Montazerian (maziar_montaz@yahoo.com) and F. Baino (francesco.baino@polito.it).

# Authors contributed equally to this work

Abstract

Dental glass-ceramics (DGCs) are developed by controlled crystallization of oxide glasses and form an important group of biomaterials used in modern dentistry. They are also of great importance to scientists studying the fundamentals of crystallization. DGCs must meet strict requirements for restorative prostheses and to streamline the workflow for dentists and increase patient comfort. Considerable research has been devoted to developing new DGCs using advanced technologies, such as CAD/CAM or 3D printing, and to improve material properties. DGCs are designed to have exceptional aesthetics, translucency, high strength, chemical durability, wear resistance, biocompatibility, low thermal conductivity, and hardness similar to that of natural teeth. Some are also bioactive to stimulate a favorable response from the tooth and supporting bone. This allows treatment of hypersensitivity, regeneration of alveolar bone, and healing of periodontal tissues. In this comprehensive and critical review, we compare (inert) restorative prostheses and bioactive GCs. We elaborate on the relevant theoretical fundamentals of crystallization in oxide glasses and explain key technologies to fabricate DGCs. Advanced experimental techniques to unveil the details of crystallization in DGCs are thoroughly discussed. Finally, we propose a strategy for adopting advanced technologies, characterization tools, theoretical insights, and computer models to advance this important field.

Keywords: Biomaterials; Glass; Ceramic; Crystallization; Bioactive; Dentistry.

Graphical abstract summarizes dental glass-ceramics (DGCs) applications, which are currently extensively researched to develop restorative prostheses, treat hypersensitivity, regenerate alveolar bone, heal periodontal tissues, and coat dental implants.

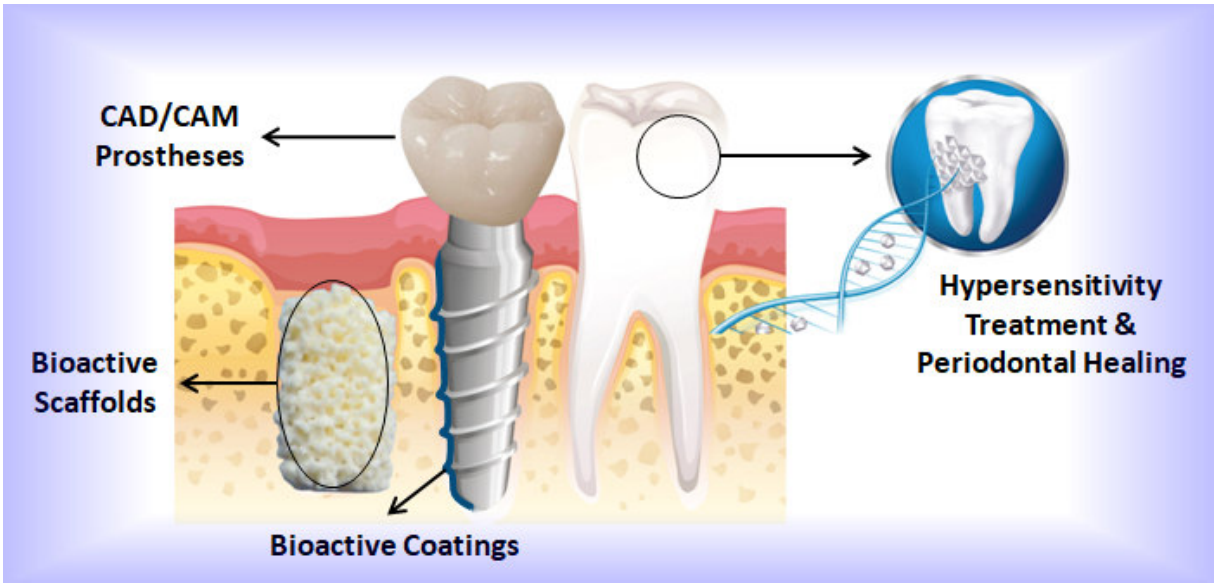

Table of Contents

1. Introduction to dental glass-ceramics (DGCs)

During the past few years, the market for bio-implant materials has grown, reaching a value of US$ 98.9 Billion in 2020 [1]. Implants are defined as a biomedical device that is made of one or more biomaterials and placed within the body. Implants can be partially or totally buried beneath epithelial surfaces. Bio-implants are mostly used as dental implants, orthopedic implants, cardiovascular implants, spinal bio-implants, ophthalmic implants, and so on. Among all these applications, one of the most ubiquitous is that of dental implants. This huge market includes a variety of segments including implants, bonding agents, impression materials, core materials, restorative materials, dental cements [2]. As an example, the dental implant market alone achieved a value of US$ 5.6 Billion in 2020 [3]. There is currently intense competition among several companies and research groups to develop a new material that is able to augment patient comfort and ease the workflow for dentists [4].

Before explaining the technical details of dental biomaterials, it is of great importance to explain the structure of a tooth briefly. Teeth are composed of cells called ameloblasts, cementoblasts, and odontoblasts [5]. Through the accumulation of ameloblast cells on the outer layer of tooth structure, a hard layer called enamel is formed. When this hard outer layer of tooth erupts, ameloblast cells cannot proliferate to repair damage to the tooth. Odontoblast cells, which are located beneath the enamel layer, form a layer called dentine. This layer is considered as the main foundation of teeth since this layer can protect the inner layer (pulp especially) and support the outer layer (enamel). Below this layer, there is another layer called pulp. This layer consists of odontoblast cells and living connective tissue. Pulp's main functions are supplying the nutrients, perceiving the pain, and forming dentin. All teeth are sealed by a marginal layer called gums and held firmly in place by bones. The outer layer

of the teeth is brittle and hard enough for chewing different kinds of foods, both soft and firm. Enamel is the hardest part of the tooth's structure; the dentine is softer and more compliant, and the bone is also more compliant to be able to withstand high pressure. There are several papers in the literature explaining more about the structure and properties of the tooth [4,6]. **Figure 1** illustrates the structure of a tooth.

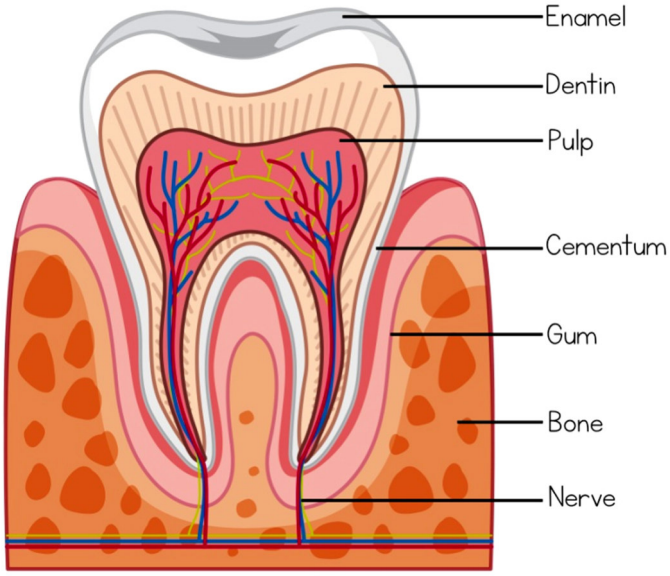

Figure 1- Structure of a tooth (credit: https://www.vecteezy.com/).

Even though metallic alloys are still used in dentistry, there is an increasing preference for metal-free solutions since metallic materials have an unnatural color and may lead to unwanted chemical-biological reactions [7]. Another group of biomaterials commercially used in the body for bio-applications like dental materials is glass-ceramics. These biomaterials can be classified into two main groups: biologically inert and bioactive dental glass-ceramics (DGCs). When reconstruction and restoration of teeth are required, restorative dental materials are used, which are inert and biocompatible [2]. Bioinert glass-ceramics can be used as inlays, onlays, partial crowns, full crowns, veneers, and bridges since they have little solubility in the oral environment. The easy process of restorative dental glass-ceramics

via advanced technology like computer-aided design & computer-aided manufacturing (CAD/CAM) turns them into one of the most significant materials in the dental industry. Moreover, restorative dental glass-ceramics have several favorable properties, including low thermal conductivity, outstanding aesthetics, chemical durability, translucency, biocompatibility, high strength, wear resistance, and hardness similar to that of natural teeth [4,8–13]. New technologies like CAD/CAM and 3D printing enable scientists to replace some conventional materials used in the dental industry like amalgam and resin-based restoratives with more effective and modern biomaterials [4,14].

Bioactive DGCs are another group of biomaterials which can bond with living bone cells and even soft tissues through a complicated procedure that includes ion leaching, controlled dissolution of material, and finally precipitation of an biological apatite-like layer on the surface of DGCs. Bioactive DGCs are mostly used where repairing and regeneration of bone tissues are required, including treatment of hypersensitivity, regenerate alveolar bone, healing periodontal diseases, coating dental implants, and repairing root canal/dentin.

The published books, chapters, and review articles in the field of DGCs are indeed relevant. However, they mostly review inert DGCs or only briefly mention bioactive DGCs currently used in dentistry. They do not provide detailed discussions of the theories, new technologies, experimental tools, recent computer simulations, or machine learning approaches obtained in the last decade [4,9–11,15–21]. We will discuss both bioactive and inert DGCs, elaborate on the theories behind their development, discuss the characterization tools in detail, and overview experimental researches, and finally combine experimental and computational findings. This paper is organized into 8 sections. In section 2, a brief history of dental materials with a particular focus on bioactive and inert DGCs is explained. The basic stages of DGC synthesis involve melting, forming, and controlled crystallization of a supercooled liquid. Therefore, relevant theories and fundamentals of glass formation during

melting and crystallization in supercooled liquids are of great relevance to this industry. These phenomena are also of particular bearing to chemists, physicists, and materials scientists dealing with the fundamentals of glass science and crystallization. In fact, "crystallization," "nucleation," and "crystal growth" are, by far, the most frequently used keywords in the past 200 years of glass science and technology [22]. Therefore, in Section 3, we will elaborate on the theories and applications of the above concepts in the synthesis of DGCs. Like other fashionable fields of materials science, emerging and advanced technologies such as additive manufacturing, 3D printing, and CAD/CAM are quickly adapted for developing DGCs. Therefore, in Section 4, these new technologies are discussed and compared with traditional methods to fabricate DGCs. In Section 5, we will focus on the key experimental tools, such as optical microscopy (OM), X-ray diffraction (XRD), differential scanning calorimetry (DSC), scanning/transmission electron microscopy (SEM/TEM), small-angle x-ray scattering (SAXS), small-angle neutron scattering (SANS), X-ray absorption spectroscopy (XAS), Raman spectroscopy (RS), nuclear magnetic resonance (NMR), etc., to unveil specific hidden details of glassy nature and crystallization behavior of DGCs, which are, one of the most important families of commercial glass-ceramics. We will show that efficient, combined use of these techniques has provided valuable insights into the complicated and rapidly changing structural environments in which crystallization happens. We also propose some strategies for adopting advanced tools and strategies to further study these exciting and crucial materials. Throughout this paper, especially in Section 6, we elaborate on the history, processing, properties, and applications of inert and bioactive DGCs. The selected papers that address promising types of DGCs are also reviewed. Future research is envisaged in which the compositional and microstructural design, synthesis, characterization, and application of biomaterials can be greatly accelerated by theoretical and computational modeling. In this review, we recognize the

publications, which accurately portray the early days, the chronology, numerous advances, and future challenges. However, as the literature has become very rich in this topic, unfortunately, very few works have addressed data/model-driven approaches to design new biomaterials or predict their properties efficiently. This task should be accelerated as a key part of the macro endeavor to decode the "glass genome." Therefore, in section 7, we first review publications that have applied molecular dynamics (MD), Monte Carlo (MC), potential energy landscapes (PEL), and machine learning for understanding DGCs. Then, we argue that the modeling approaches should be utilized to design specific properties of DGCs, such as bioactivity, chemical degradability, glass transition temperature, elastic modulus, fracture strength, fracture toughness, density, thermal expansion coefficient, porosity content, morphology, etc. We believe that theoretical and experimental research, coupled with computer simulations in this field, are crucial for understanding the nature of the glassy state and for the successful development of advanced materials, e.g., novel dental glass-ceramics. Finally, in Section 8, we point out open issues and directions for future studies that warrant further research and technology development.

2. History

2.1. Inert DGCs

Although the use of bioinert and/or bioactive glass-ceramic materials as dental materials is quite new, the desire to use an aesthetic and durable material for dentistry is ancient. Until the eighteenth century, the materials that had been used as artificial teeth were limited to human and animal teeth. The development of porcelain teeth was an end to the era of transplanting freshly extracted animal products or human teeth as artificial teeth [23]. In 1774, the first restorative ceramic-based material was developed from porcelain for use as a

tooth. Afterward, in 1837, Stockton Co. was the pioneer company to manufacture porcelain teeth [4]. In the 1950s, porcelain teeth were reinforced by metal substructures to improve their mechanical properties [24]. During the past several decades, dental bridges have been produced by metal-porcelain composite, which consists of a metallic framework for its superior mechanical properties and a coating of porcelain for improving aesthetic appearance [25]. There are also some disadvantages associated with using metals as a framework for improving the mechanical strength of porcelains, including some aesthetic disadvantages and the biological incompatibility of the metals [16,17]. This is why researchers all around the world have been motivated to search for all-ceramic restorations. The first synthetic glass-ceramic was discovered by Stanley Donald Stookey [26]. The discovery of lithium disilicate glass-ceramic was a starting point for Corning Glass Works to develop and commercialize two novel kinds of glass-ceramics based on Li–aluminosilicates (LAS) and Mg–aluminosilicates (MAS) from 1953 to 1963 [16]. The low thermal expansion coefficient of LAS glass-ceramics made it a suitable candidate to be used in many applications such as cookware or smooth cooktop surfaces. In addition to glass-ceramics, one of the materials that gained a huge amount of attention in dentistry was yttrium-stabilized tetragonal ZrO_2 (Y-TZP) since this material showed excellent mechanical properties. This material, however, showed low optical translucency. As a result, a veneering layer which is made of a compatible proclaim or glass-ceramic was still required to meet the aesthetic requirements for ZrO_2 [27]. From 1963 to 1980, most of the research was focused on developing a castable, translucent and machinable glass-ceramic [21]. Corning Glass Works was the first company to succeed in fabricating a glass-ceramic material for dental restoration [17]. Glass-ceramics containing mica crystals were the earliest type of glass-ceramic used for dental restoration, and Dicor® was the first material in this family [28]. In 1985, Vita Zahnfabrik Co. successfully developed CAD/CAM porcelain Vitablocs® Mark I, which its modified

composition is still in the market. About 5 years later, this company introduced In-Ceram® products, which were porous alumina/zirconia materials infiltered with a glass. Afterward, Nobel Biocare introduced a veneer based on pure alumina with aesthetic porcelain [24,29–32]. Different types of fillers have been used to strengthen glass-ceramic materials, such as leucite. The addition of leucite could increase the bending strength of the final porcelain to around 138 MPa [33]. Lithium disilicate glass-ceramics were introduced in 1998 for single- and multiple-unit frameworks. Then in 2006, lithium disilicate glass-ceramics were used as a partially crystallized machining block and a heat-pressable ingot to fabricate a crown or bridge framework with outstanding mechanical properties [16,18]. Currently, the majority of the toughest and strongest glass-ceramics are made using lithium disilicate. Another type of glass-ceramic containing apatite is popular for improving translucency [34]. Other classes of DGCs like fluorrichterite, fluorcanasite, and apatite-mullite have also been developed, which are known for their optical translucency and high fracture toughness (K_{IC} > 3 MPa·m$^{0.5}$) [16], [34]. The attempts to search for a glass-ceramic material with better mechanical, biological, chemical, and aesthetic properties are still continuing, and this remains a hot topic for researchers around the world.

2.2. Bioactive DGCs

One kind of material that has been widely employed for various clinical applications is bioactive glasses, which can comprise different types of material chemistries. For example, Bioglass 45S5 (the first melt-derived bioactive glass) and gel-derived bioactive glasses were invented by Hench in 1969 and 1991, respectively [14,35]. Later, bioactive glasses with ordered mesoporosity were also designed [36]. Bioactive glasses can be used in bone grafting, drug delivery, coatings, scaffolding, and soft tissue engineering. Apart from

significant bioactive properties, bioactive glasses suffer from undesirable mechanical properties like low mechanical strength and fracture toughness, K_{IC} (a bending strength of approximately 70 MPa and K_{IC} of 0.5 $MPa{\cdot}m^{0.5}$), which can restrict their applications.

Bioactive glass-ceramics embedding different crystalline phases could address their mechanical limitations. They are usually developed by controlled heat treatment of the bioactive glasses. Cerabone®, Biosilicate®, Ceravital®, and Bioverit® are the most famous and commercial bioactive GCs [37–40]. Ceravital® consists of a Na_2O–K_2O–MgO–CaO–SiO_2–P_2O_5 glassy matrix with apatite (CaO–P_2O_5) precipitates developed primarily by Brömer and colleague in 1973 [39]. In the late 1980s, the commercial AW glass-ceramic, called Cerabone®, was developed by Kokubo et al. [40]. In this kind of GC, the crystalline apatite and wollastonite are formed in the MgO–CaO–SiO_2–P_2O_5 glass system. In 1985, Höland et al. [41] prepared the other commercial bioactive GCs, the Bioverit® group, in which apatite and mica dispersed in a Na_2O–MgO–CaO–Al_2O_3–SiO_2–P_2O_5–F glass [41]. Peitl et al. [42] prepared Biosilicate® in 1996, an apatite-free glass-ceramic based on the crystallization of (a somewhat modified) Bioglass®, and showed that controlled crystallization led to excellent mechanical characteristics and a proper microstructure of a Na_2O–CaO–SiO_2–P_2O_5 glass. To be more specific, the bending strength and fracture toughness of bioactive glasses increased to ~200 MPa and ~2 $MPa.m^{0.5}$, respectively, by the development of bioactive GCs [42,43]. In recent years, extensive research has been conducted to demonstrate enhanced features of new bioactive GCs. These have often been specifically developed for orthopedics and dental applications, which will be discussed in the next sections after providing a summary of the basic theory behind GC design and production.

3. Fundamentals

3.1. Supercooled liquid and glassy states

A recent definition of glass reads [44]: *"Glass is a non-equilibrium, non-crystalline state of matter that appears solid on a short time scale but continuously relaxes towards the liquid state."* This is an intuitive description for the general public. A more detailed definition is *"Glass is a nonequilibrium, non-crystalline condensed state of matter that exhibits a glass transition. The structure of glasses is similar to that of their parent supercooled liquids (SCL), and they spontaneously relax toward the SCL state. Their ultimate fate, in the limit of infinite time, is to crystallize."*

The significance of nucleation and crystallization lies in the above definition of the glassy state. This definition points out that the ultimate fate of all glasses (and supercooled liquids) is crystallization, which occurs through the two-step process of nucleation and crystal growth. Therefore, it is useful to briefly describe the key points in the definition of the glassy state. As an aid, we start with the most well-known diagram in glass science (**Figure 2**). This figure describes the evolution of a first-order thermodynamic property, such as molar volume or enthalpy, as a function of temperature for a glass-forming liquid.

The glass-forming liquid starts in a thermodynamically stable state above the melting point (T_m) or liquidus temperature (T_L). The liquidus temperature serves as the boundary of thermodynamic equilibrium between the solid and liquid phases. Crystals become thermodynamically unstable above this temperature and will dissolve in the liquid phase. The difference between T_L and T_m is the type of compound that is melting; T_m is used for a pure system and T_L is used for a multicomponent system [44].

If a liquid is cooled quickly enough such that it does not crystallize, we reach the next state, which is called a supercooled liquid, and it occurs at temperatures between the melting

point and the glass transition temperature, T_g. A supercooled liquid is metastable, meaning a thermodynamic barrier must be overcome for crystal nucleation to take place, but a SCL will eventually crystallize if given enough time [44].

If the liquid continues to be cooled and the temperature decreases, the relaxation time of the SCL increases. This leads to the structure eventually becoming (temporarily) frozen as the relaxation time exceeds the laboratory (observation) time. In this case, the atoms do not have enough time to rearrange to the metastable equilibrium state. This leads to a deviation of the enthalpy from the SCL line in a continuous process that results in a nonequilibrium material known as a "glass."

The final enthalpy of glass depends on the cooling rate because the glass transition is a kinetic freezing process. In other words, when the SCL is cooled quickly or more slowly, the system has less or more time to relax, leading to varying amounts of enthalpy in the final glass [44]. This process is shown in **Figure 2**; specifically, that glass 2 was cooled faster than glass 1, resulting in a higher enthalpy and also a higher T_g. The value of the T_g is the temperature at the intercept between the SCL and glass lines. The continuous transition leads to a temperature range between the SCL and the glass, and this range is defined as the "glass transition" range [44].

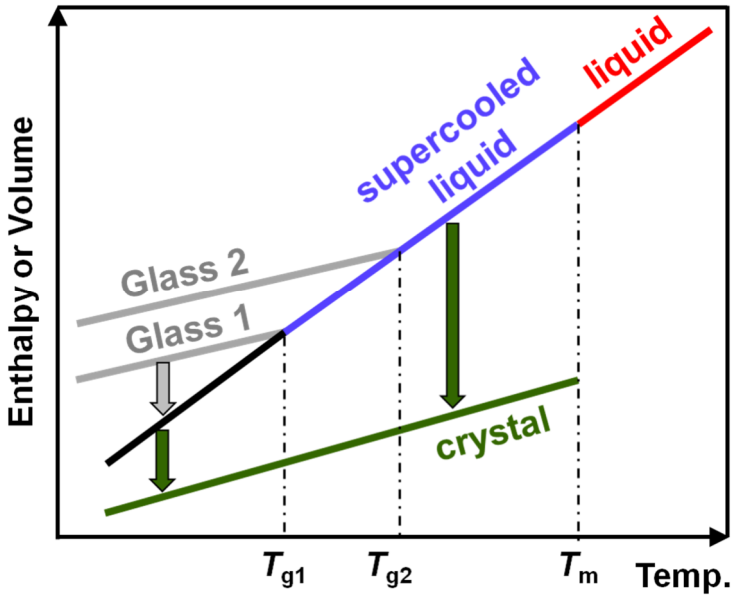

Figure 2- Schematic diagram of how a first-order thermodynamic property, such as volume or enthalpy, changes as a function of temperature for a glass-forming liquid. T_m = melting point or liquidus temperature, T_g = glass transition temperature. Glass 1 and glass 2 are distinct and vary by their cooling rates, leading to separate structures and properties, such as their respective T_g. Most glasses that relax to the crystal state must first relax to the SCL state, shown by the grey and green arrows. Reproduced from [44] with permission from Elsevier.

3.2. Crystal nucleation

Before discussing crystal nucleation, we should clarify the difference between a nucleus and a crystal. A nucleus is a precursor to a crystal and is a periodic assemblage of atoms that does not have any recognizable growth planes. On the other hand, a crystal has a periodic structure that does have recognizable growth planes [45]. Nucleation is categorized into homogeneous and heterogeneous processes. Homogeneous nucleation takes place stochastically with the same probability in any given volume. On the other hand, nucleation occurring on preferred nucleation locations, e.g., previously nucleated phases, pre-existing interfaces, and surfaces, is known as heterogeneous nucleation [45]. Depending on the location of nucleation, volume (bulk) and surface crystallization can be distinguished [44].

Inorganic glass-forming liquids are interesting models for investigations of nucleation, growth, and overall crystallization phenomena. They exhibit relatively low rates of nucleation due to their high viscosities, which may allow in-depth studies of nucleation. Also, glass-forming melts can dissolve solid impurities that then only exist as ionic species when the liquid is vitrified at deep undercoolings ($T/T_m < 0.6$), potentially giving rise to the observation of homogeneous nucleation. Additionally, different stages of the crystalline states (nucleated or growing phases) can be frozen by quenching previously heat-treated samples to room temperature due to the rapid increase of viscosity with decreasing temperature. For this reason, it has been figuratively said that glasses serve as the Drosophila of nucleation theory to test this phenomenon experimentally [45]. Glass formation and crystallization are of great scientific and technological importance, but they are competitive processes. To prepare glassy articles, one needs to avoid crystallization and control the main parameters that govern nucleation and growth. Alternatively, controlled nucleation and crystallization of glasses have led to the production of glass-ceramics [16,46], which are widely used in both domestic and high-technology applications. Moreover, inorganic glass formers such as silicate glasses are the oldest materials produced by the human, first produced roughly 6000 years ago in ancient Mesopotamia [47], but are still technologically very important. They have been important materials for the development and well-being of humankind civilization and are now ubiquitous in our everyday lives. Natural glasses, such as obsidian, are nearly as old as the universe, whereas novel glasses are being discovered daily. Glass itself is a fascinating state of matter combining aspects of the liquid and solid states [44,48]. As competently summarized in *Welcome to the Glass Age,* by D. Morse and J. Evenson [49], *Glass: the eye of science* by M. Bolt [50], and *Glass and Glass-Ceramic Technologies to Transform the World* by L.L. Hench [51], many outstanding innovations can be cited, where glass was the critical material. Some examples include optical glass fiber networks that span the globe [52], thin

and strong glass sheets for television sets and cell phones [53], high-strength and exceptionally elastic metallic glasses [54,55], semiconductive chalcogenide glasses [56], bioactive glasses for healthcare [4,13,57], and many other incredible applications of glasses and glass-ceramics comprehensively reviewed in *Prog. Mater. Sci*. [58,59]. For the abovementioned reasons, the investigation of glass crystallization kinetics is of great interest from both practical and scientific points of view because, in many cases, the nucleation stage determines the pathways of crystallization.

3.2.1. Homogeneous nucleation

Homogeneous nucleation occurs by decreasing the free energy of the system to form a new phase without the aid of external boundaries or nucleation centers [60]. The probability of homogeneous nucleation is equal throughout the volume of the material. According to classical nucleation theory, the change in free energy (ΔG) due to nucleus formation consists of two combatting contributions: a lowering of the free energy of the volume of the nucleus and an increase of the free energy due to the formation of a liquid-nucleus interface [45]. Considering these two contributions, the change in free energy due to nucleus formation is [60]:

$$\Delta G = \frac{4}{3}\pi r^3 \Delta G_x + 4\pi r^2 \gamma, \tag{3.1}$$

where r is the radius of the nucleus, ΔG_x is the change in free energy per unit volume as a result of nucleus formation, and g is the surface tension of the liquid-nucleus interface. Note that in classical nucleation theory, the nucleus is assumed to be spherical, and a sharp interface between the liquid and the nucleus is also assumed. Figure 3 shows the change of ΔG as a function of r.

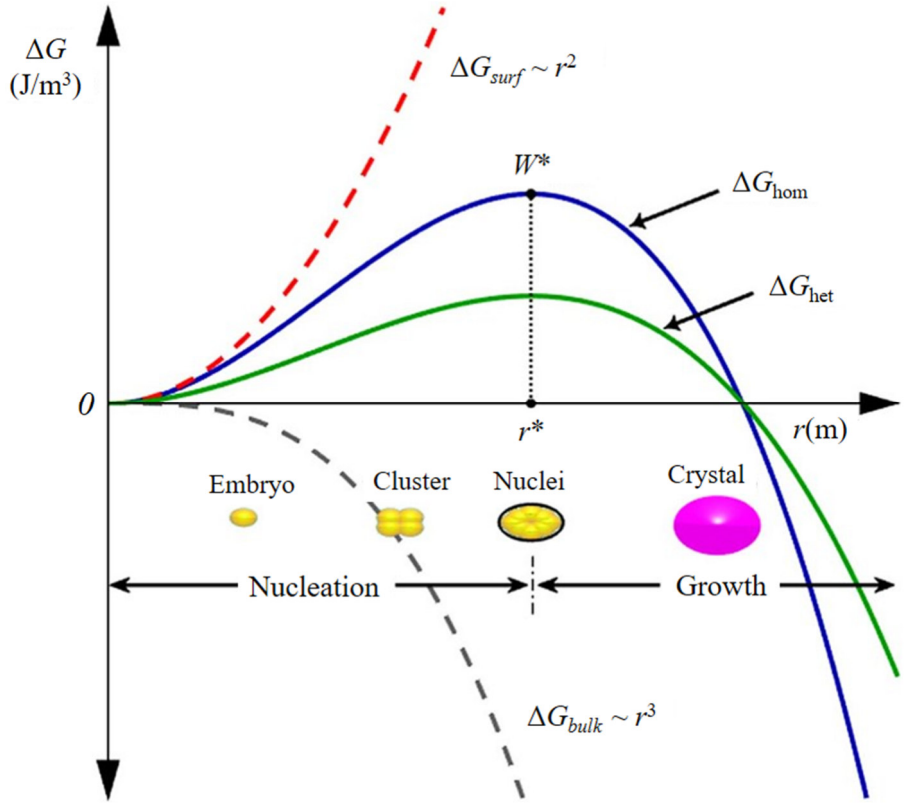

Figure 3- Gibbs free energy changes during crystal nucleation. The surface free energy (ΔG_{surf}, dashed red line), bulk free energy (ΔG_{bulk}, dashed black line), homogeneous nucleation free energy ΔG_{hom} (blue line), and the heterogeneous nucleation free energy ΔG_{het} (green line) are shown as a function of the radius *r*. The nucleation stages are also sketched. The embryo and cluster states are reversible, and the nuclei state is irreversible. Beyond the critical radius (*r**), the nucleus begins to grow (adapted with permission from [61]).

The stability of the nucleus is largely dependent on its radius. When *r* is small, the interfacial energy term is larger, resulting in a positive free energy. Therefore, the nucleus is unstable since the downward direction of the free energy leads to the nucleus shrinking until it vanishes in order to remove the undesired interface. However, when *r* is large, the volumetric term takes over and the free energy becomes negative. Here the nucleus is stable since the lowering of the free energy results in the nucleus growing [60]. The transition point from the interfacial and volumetric terms dominating is at the critical-sized nucleus, when $r = r^*$. The critical-sized nucleus occurs when [60]:

$$\frac{\partial \Delta G}{\partial r} = 4\pi r^2 \Delta G_x + 8\pi r\gamma = 0. \tag{3.2}$$

Solving for r, the critical-sized nucleus, r^*, is given by [60]

$$r^* = -\frac{2\gamma}{\Delta G_x}. \tag{3.3}$$

r^* is a positive value since ΔG_x is negative at temperatures lower than the melting point. To reiterate, when $r < r^*$, the positive interfacial term is dominant, and the nucleus prefers to shrink. When $r > r^*$, the negative volumetric term is dominant, and the nucleus prefers to grow. The work needed to form a stable nucleus is called the critical work, W^*. By inserting Eq. (3.3) into Eq. (3.1), we can calculate W^* [60]:

$$\begin{aligned} W^* &= \frac{4}{3}\pi\left(-\frac{2\gamma}{\Delta G_x}\right)^3 \Delta G_x + 4\pi\left(-\frac{2\gamma}{\Delta G_x}\right)^2 \gamma \\ &= -\frac{32\pi\gamma^3}{3\left(\Delta G_x\right)^2} + \frac{16\pi\gamma^3}{\left(\Delta G_x\right)^2} \\ &= \frac{16\pi\gamma^3}{3\left(\Delta G_x\right)^2} \end{aligned} \quad . \tag{3.4}$$

Homogenous nucleation is rarely observed in DGCs but is fundamental to understanding the basics of crystallization. DGCs are mostly derived from multicomponent glasses which undergo heterogeneous nucleation. By multicomponent systems, we imply non-stoichiometric systems in which more than one phase crystallizes upon heating.

3.2.2. Heterogeneous nucleation

Heterogeneous nucleation is defined as the random assembly of atoms on a pre-existing surface or interface [60]. The presence of these interfaces lowers the thermodynamic barrier for nucleation, therefore increasing its probability of occurrence. The surfaces or interfaces can serve as preferential sites for nuclei to form. A classic example of this situation is a crystal nucleus growing at the interface between the liquid and a solid substrate. In this situation, the total interfacial energy has three contributions [60]:

$$\gamma_{lx}A_{lx} + \gamma_{xs}A_{xs} + \gamma_{xl}A_{xl}, \tag{3.5}$$

where γ is surface tension, A is the interfacial area, and the subscripts l, x, and s refer to the liquid, nucleating crystal, and solid substrate phases, respectively. To elaborate, γ_{lx} refers to the surface tension between the liquid and nucleating crystal phases, and A_{lx} refers to its corresponding area. The contact angle (or wetting angle), θ, is given by Young's equation, $\gamma_{ls} = \gamma_{xs} + \gamma_{lx}\cos\theta$, which is used to balance the interfacial forces that are acting on the nucleus [60]. The wetting ability of the crystal nucleus on the solid substrate is described by θ. A contact angle of $\theta = 0$ results in a perfectly wetting substrate, while a contact angle of $\theta = 180°$ results in a perfectly non-wetting substrate. The foreign substrate lowers the thermodynamic barrier for nucleation when $\theta < 180°$. However, the kinetic barrier is unaffected by the presence of the substrate.

Assuming a "spherical cap" shape for the heterogeneously nucleating droplet, the critical radius for heterogeneous nucleation is the same as for homogeneous nucleation [45]:

$$r^* = -\frac{2\gamma_{lx}}{\Delta G_x}. \tag{3.6}$$

However, the work of nucleation is lowered. For a contact angle of θ, the work corresponding to the formation of a critical-sized nucleus through heterogeneous nucleation is given by [45]:

$$W^*_{\text{hetero}} = \left[\frac{16\pi\gamma_{lx}^3}{3(\Delta G_x)^2}\right] \cdot \left[\frac{1}{4}(1-\cos\theta)^2(2+\cos\theta)\right]. \tag{3.7}$$

The first factor on the right-hand side of Eq. (3.7) is identical to Eq. (3.4), which is the critical work for homogeneous nucleation. Therefore, Eq. (3.4) can be substituted into the equation for the work of heterogeneous nucleation [60]:

$$W^*_{\text{hetero}} = W^*_{\text{homo}}\left[\frac{1}{4}(1-\cos\theta)^2(2+\cos\theta)\right]. \tag{3.8}$$

From Eq. (3.8), we can see that when $\theta = 0$, a perfectly wetting substrate that has no thermodynamic barrier to nucleation exists [60],

$$\theta = 0° \quad \rightarrow \quad W^*_{\text{hetero}} = 0, \tag{3.9}$$

or in other words, nucleation is limited only by the kinetics of transporting atoms to the growing nucleus in this case. One requirement for this situation is the matching of the lattice spacing between the exposed face of the substrate and the growth habit planes of the nucleating crystal. The growth of the new crystal would be oriented to match that of the substrate. This is called epitaxial growth, where crystals are grown with a well-defined orientation with respect to the substrate [60]. In the opposite case, for a perfectly non-wetting substrate [60],

$$\theta = 180° \quad \rightarrow \quad W^*_{\text{hetero}} = W^*_{\text{homo}}. \tag{3.10}$$

In this situation, the presence of a perfectly non-wetting substrate does not lower the energy barrier and has no impact on the nucleation process, which leads to the process being identical to homogeneous nucleation.

3.2.3. Classical nucleation theory

Classical nucleation theory represents one of the first steps towards understanding crystal nucleation. One of its important results is recognizing the inevitable tradeoff between effects that are thermodynamic and kinetic in nature. During the process of a liquid being supercooled, the thermodynamic driving force for nucleation rises, but the kinetics of nucleation is also slowed down [60]. The classical theory makes several assumptions about the system, namely that the nucleus is spherical in shape and that there is a distinct interface between the matrix phase and the nucleating cluster [60]. Classical nucleation theory begins with the simplest case, one where there are no energy barriers to nucleation. In this simplified instance, thermal energy leads to the atoms in the system vibrating, and since there are no energy barriers, the nucleation rate would be:

$$I = n\nu, \tag{3.11}$$

where n is the number of atoms per unit volume and ν is the vibrational frequency. The nucleation rate is given per unit volume in this equation.

However, in reality, there are two barriers that must be overcome to achieve nucleation: the thermodynamic barrier and the kinetic barrier. As previously discussed, the thermodynamic barrier, W^*, corresponds to the critical work required to form a stable nucleus. The activation energy required for an atom to cross the liquid-nucleus interface is called the kinetic barrier, ΔE_D [60]. Structurally this often leads to atoms breaking bonds with their neighbors and repositioning themselves into the more ordered structure of the nucleus. These two barriers to nucleation mean that Boltzmann probability factors must be multiplied into Eq. (3.11) to obtain the actual nucleation rate [45]:

$$I = n\nu \exp\left(-\frac{W^*}{kT}\right) \exp\left(-\frac{\Delta E_D}{kT}\right), \tag{3.12}$$

where k is Boltzmann's constant and T is the absolute temperature.

Determining a supercooled liquid's nucleation rate experimentally is often accomplished using the Tammann method [62,63]. This method uses a series of heat treatments at varied lengths of time for a given nucleation temperature, followed by growing the clusters at a higher temperature and finally quenching the sample to room temperature [61]. The resulting microstructure of each sample is examined so that the number of crystals per unit volume, or crystal number density N, and their sizes can be measured. The crystal number density is found for multiple times, and the nucleation rate is the slope of N versus time plots [62].

Determining a fixed nucleation temperature at which the nucleation rate is maximum is of great importance for developing DGCs as it saves time and energy. This is the best nucleation temperature for the development of DGCs.

3.2.4. Diffuse interface theory

Classical nucleation theory is a great first step towards understanding nucleation. However, the assumptions within the theory often limit its accuracy. A couple of additional theories have been developed to build upon classical nucleation theory and are more mathematically intensive as they do not make the same assumptions. As previously mentioned, classical nucleation theory assumes a sharp interface between the matrix phase and the nucleus, but in reality, the actual interface is likely to be more muddled [60]. This is where diffuse interface theory jumps in, as it is an approach specifically designed to model a situation where a non-sharp interface between the matrix phase and the nucleating cluster exists [64–67]. For small groups of atoms, the width of the interface between the matrix phase and the nucleating cluster can make up a major portion of the total cluster size. The existence of a diffuse interface changes the work needed to achieve nucleus formation.

In the case of a spherical nucleating group of atoms in an isotropic liquid, the radial dependence of the free energy density is labeled $g(r)$. To successfully use this method, one must appropriately select the energy density, which is case-specific. The work of forming the nucleating cluster in this situation is [60]:

$$W(r) = 4\pi \int_0^\infty (g(r) - g_l) r^2 dr, \tag{3.13}$$

where g_l is the free energy density of the matrix phase (the liquid). Beyond the initial work differing from that found in classical nucleation theory, much of the process is similar. Just as in classical nucleation theory, the critical-sized nucleus occurs when the work is at a maximum and the derivative of the work is set equal to zero [60]:

$$\left.\frac{dW(r)}{dr}\right|_{r=r^*} = 0, \tag{3.14}$$

and then solving for r results in the critical-sized nucleus, $r = r^*$. Just like classical nucleation theory, when $r < r^*$, the nucleus is unstable and will shrink and eventually vanish. Also, a

nucleus larger than r^* is stable and will likely grow. The critical work for forming a stable nucleus is found by plugging the critical-sized nucleus into Eq. (3.13) to get $W^* = W(r^*)$ [60]. Note that one important result from this interface theory is the reproducibility of the observed positive temperature dependence of interfacial free energy during nucleation [67].

3.2.5. Density functional theory

Density functional theory, which should not be confused with the independent and unrelated theory of the same name in the field of quantum mechanics, examines local density fluctuations as an order parameter for describing the phase transition from the liquid to the crystal [60]. Note that the equations used in density functional theory are comparable to the equations used in classical nucleation theory, but they are designed for a more specific situation. Since density functional theory is based on an order parameter description, it can be extended to model nucleation in a wide range of systems, including cases that involve a coupling of more than one order parameter [60].

Density functional theory makes the assumption that the thermodynamics of nucleation can be described in terms of a spatially heterogeneous density in the system. If the liquid matrix phase and the nucleating phase have two distinct densities, then the local difference in those densities at the liquid-nucleus interface can be used as an order parameter to account for the transition area between these phases [60]. The free energy in this transition area is then expressed as a function of the density. The mathematics within the theory are rigorous and are not described in the present work but are described in detail by Mauro [60].

The main assumption made by density functional theory is that the density in the interfacial region is the most appropriate order parameter to represent the phase transition [60]. This assumption clearly falls short when the matrix and cluster phases have either similar densities, or even the same density. More universal versions of density functional

theory may be derived such that the order parameter is a function of both position and time, leading to greater accuracy for more cases.

There are several similarities between diffuse interface theory and density functional theory. The two theories qualitatively agree that there is a diffuse interface between the matrix phase and the nucleating phase. Compared to the prediction from classical nucleation theory, this leads to a more accurate prediction of the critical nucleus size [60]. Diffuse interface theory and density functional theory have both been successfully applied to metallic and organic liquids [68], as well as silicate glasses [69]. Compared to classical nucleation theory, both theories make less assumptions and therefore give better agreement to experimental data. The two advanced theories both accurately calculate the critical work needed to form a stable nucleus and agree that it is less than corresponding values predicted from classical nucleation theory.

At the center of each of these models is a simple truth: if it is possible to control nucleation, it is possible to control the glass-ceramic properties. Despite this statement being true, it is far from a trivial task to actually control the nucleation. Instead, we rely on these models to qualitatively steer our efforts. This leads to the design of a glass-ceramic being based on both qualitative information from these models as well as experimental efforts to pinpoint appropriate nucleation and growth temperatures. When a model that describes nucleation with minimal parameterization is widely available, the cost of research and development of new materials will be cut drastically.

3.3. Crystal growth

3.3.1. Normal growth

Crystal growth takes place after nucleation, as it can only begin once a critical-sized nucleus has formed. This process involves the transporting of material across the matrix-crystal interface. Therefore the crystal growth rate is a function of atoms diffusing from the liquid matrix regions across the interface to the crystal [60]. Crystal growth can be described by an activation barrier, $\Delta E'$, that must be overcome for an atom to transition from a liquid site to a crystal site [70]. Once the atom has been incorporated into the growing crystal, the change in free energy is ΔG_x. The atomic jump distance to cross the liquid-crystal interface is denoted a, and the jump frequency is v. This leads to the equation for the crystal growth rate, u [45].

$$u = av \exp\left(-\frac{\Delta E'}{kT}\right)\left[1 - \exp\left(\frac{\Delta G_x}{kT}\right)\right]. \tag{3.15}$$

From Eq. (3.15), it is clear that temperature plays a large role in the crystal growth rate. When the temperature is greater than the melting point, the change in the free energy is positive, resulting in a negative growth rate, or the dissolution of crystals. At the melting point, there is no change in free energy and therefore the crystal growth rate is 0, so crystals will neither grow or dissolve. The change in free energy is negative at a temperature below T_m, so there is a thermodynamic driving force for crystal growth. As the temperature is decreased, the thermodynamic driving force for crystal growth increases, but that increase is offset by a slowing of the kinetics at low temperatures. Similar to nucleation, thermodynamics control crystal growth at high temperatures (near the melting point), while kinetics control the process at low temperatures [60].

Another form of the crystal growth rate equation was developed in the Wilson-Frenkel theory. This theory combines Eq. (3.15) and the following equation for the diffusion coefficient of the material crossing the matrix-crystal interface [60]:

$$D = a^2 \nu \exp\left(-\frac{\Delta E'}{kT}\right). \tag{3.16}$$

From Eqs. (3.15)-(3.16), the crystal growth rate can be written in terms of the diffusion coefficient as [45]:

$$u = \frac{D}{a}\left[1 - \exp\left(\frac{\Delta G_x}{kT}\right)\right]. \tag{3.17}$$

Determining crystal growth rate experimentally is fairly straightforward. To calculate the rate, microscopy techniques are often employed, the most common being a series of heat treatments at varied lengths of time for a given temperature, followed by a quench to room temperature [62]. The resulting microstructure of each sample is examined so that crystal radii can be measured. That allows for a calculation of the growth rates from the slopes of the crystal radius versus time at various temperatures, shown below in **Figure 4** [62,71].

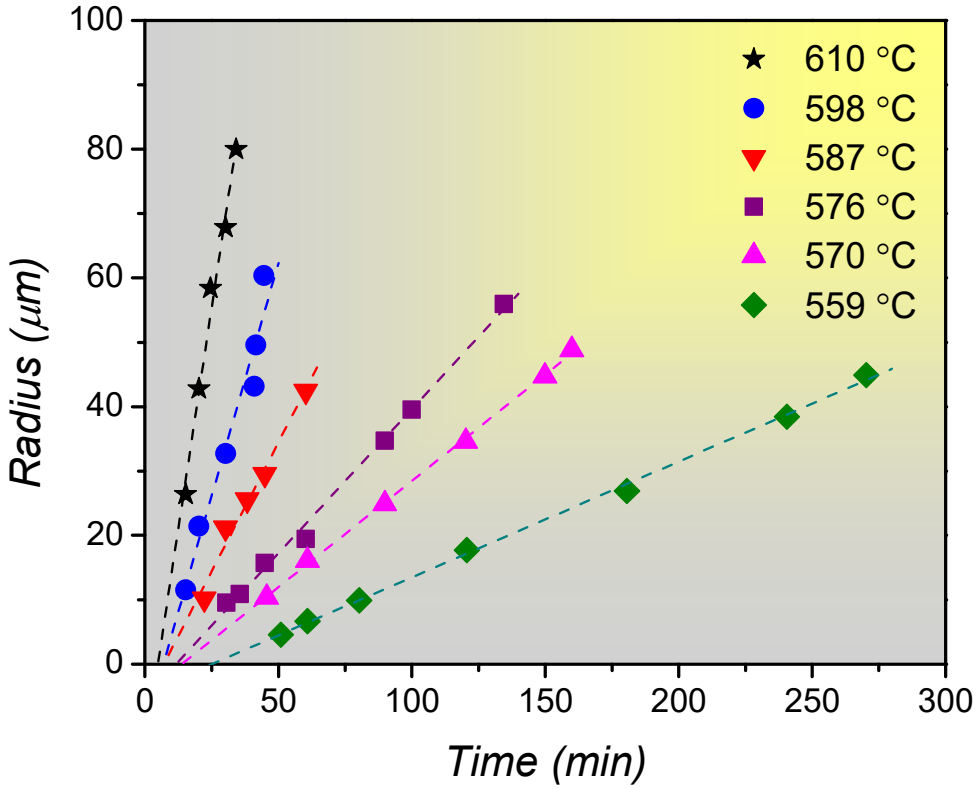

Figure 4- Crystal radius size as a function of time for lithium disilicate glass heat-treated at separate growth temperatures. Reproduced from [71] with permission from Elsevier.

3.3.2. Surface nucleation or two-dimensional growth

Surface nucleation is not as well-studied as internal volume nucleation. Work on this phenomenon has largely been limited to glass systems that cannot form glass-ceramics through an internal volume nucleation mechanism but are technologically important [16]. For example, leucite and AW glass-ceramics are two model inert and bioactive DGCs that are undergone surface nucleation and, therefore, crystallization. Nucleation rates are relatively high compared to volume nucleation, but the latter is preferred because it is easier to control, and the driving forces required for two-dimensional growth are still under investigation. One technique used is to finely grind a glass into a powder to maximize the surface area, and then perform a two-step process that first sinters the powder and initiates nucleation and second

nucleates and grows the crystals [16], as in the case of leucite and AW DGCs. The separation of these two steps aids in the control over nucleation.

3.4. Controlled crystallization

As it has been previously discussed, crystallization is a two-step process that first involves nucleation followed by crystal growth. **Figure 5** below shows overlaid curves of nucleation and crystal growth rates. This is an important plot for developing glass-ceramics, since it shows that both rates are thermodynamically limited at high temperatures. Specifically, at temperatures above T_m, the crystal growth rate becomes negative while the nucleation rate becomes 0. At low temperatures, both the nucleation and crystal growth processes are limited by kinetics [60]. Between these two boundaries, there is a temperature that results in a peak nucleation rate and a temperature that results in a peak crystal growth rate. The temperature needed to get the peak nucleation rate is often lower than the temperature required for the maximum growth rate.

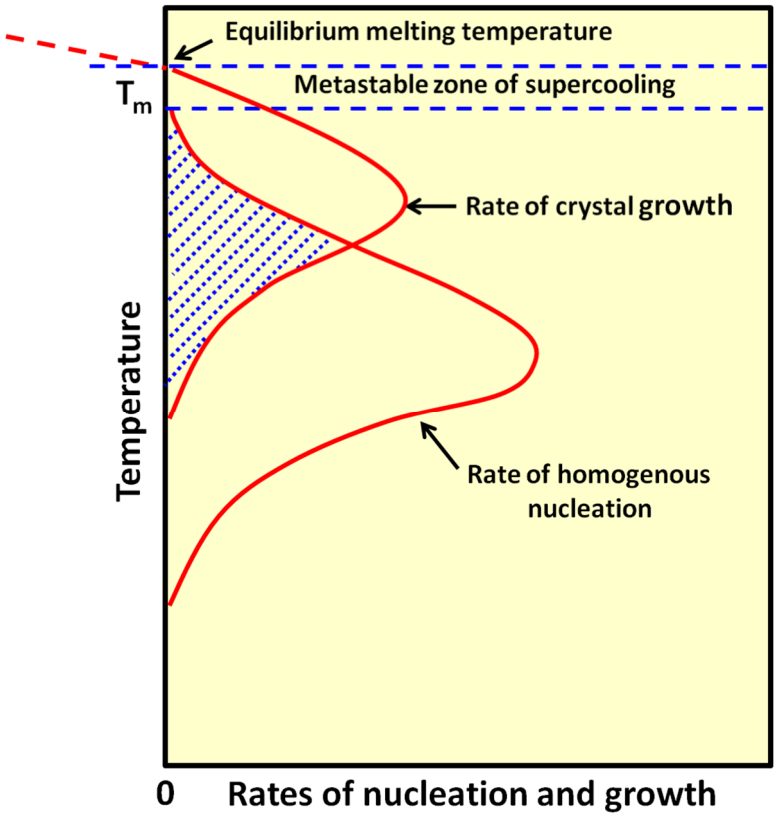

Figure 5- Overlaid nucleation and crystal growth rates vs. temperature. The peak nucleation rate occurs at a lower temperature than the peak growth rate. The two processes occur simultaneously in the shaded region. Reproduced from [45] with permission from Elsevier.

While nucleation and crystal growth are two distinct processes, the two can occur simultaneously at certain temperatures, which is shown by the shaded region in **Figure 5**. Supercooled liquids that have a small liquidus viscosity and crystallize readily, like water, for example, have a large overlapped region in their two curves. In these cases, crystallization occurs easily, and often quickly and uncontrollably [60]. Liquids that make good glass formers, like silica, are less prone to uncontrollable crystallization and have a relatively small overlapped region between the two curves.

By combining the nucleation rate and crystal growth rate, the volume fraction of crystallization can be determined. The volume fraction (α) of the crystalline phase is described as a function of time, considering simultaneous nucleation and crystal growth.

According to the Johnson & Mehl, Avrami, and Kolmogorov model (JMAK model), the volume fraction of the new phase (in this case a crystal) is given by Eq. (3.18) [72–77].

$$\alpha(t) = 1 - \exp\left\{-g \int_0^t I(T) \left[\int_{t'}^t U(T)dt'\right]^3 dt\right\} \tag{3.18}$$

where g is a shape factor that depends on the shape of crystals. If the nucleation (I) and growth (U) rates are constant throughout the transformation, and the crystals are spherical, Eq. (3.18) can be rewritten as:

$$\alpha(t) = 1 - \exp\left[-\frac{gIU^3t^4}{4}\right] \tag{3.19}$$

When the number of growing crystals, N_0, does not change with time (typical for fast heterogeneous nucleation on a finite number of active sites), Eq. (3.18) becomes:

$$\alpha(t) = 1 - \exp[-gN_0U^3t^3] \tag{3.20}$$

Avrami proposed that, in the general case, the following relation should be used:

$$\alpha(t) = 1 - \exp[-Kt^n], \tag{3.21}$$

where K represents the so-called rate constant, and n is the Avrami coefficient. Eq. (3.21) can be used in the form of

$$\ln(-\ln(1-\alpha)) = ln\,K + n\,ln\,t \tag{3.22}$$

The values of K and n is estimated by fitting the experimental data of $\alpha(t)$ (crystal volume fraction of isothermally heat-treated glass) to Eq. (3.22). Therefore, the coefficient K includes I and U, or N_0 and U [78–81].

In Eq. (3.22), n is called the Avrami coefficient, which depends on both nucleation and growth mechanisms, as shown in Table 1. Knowledge of that coefficient is very helpful to understand the mechanism of phase transformation and growth dimensionality at any given temperature [82].

Table 1. Values of the Avrami exponent (*n*) for several mechanisms of crystallization [82].

Polymorphic change, interface-controlled growth	***n***	**Diffusion-controlled growth**	***n***
Increasing nucleation rate, 3D	> 4	Increasing nucleation rate, 3D	> 2.5
Constant nucleation rate, 3D	4	Constant nucleation rate, 3D	2.5
Decreasing nucleation rate, 3D	3-4	Decreasing nucleation rate, 3D	1.5-2.5
Zero nucleation rate (nucleation site saturation) 3D	3	Constant nucleation rate, 2D	2
Constant nucleation rate, 2D (plate)	3	Zero nucleation rate, 3D	1.5
Zero nucleation rate, 2D (plate)	2	Constant nucleation rate, 1D	1.5
Constant nucleation rate (nucleation site saturation), 1D	2	Zero nucleation rate, 2D	1
Zero nucleation rate, 1D (needle)	1	Zero nucleation rate, 1D	0.5

D: growth dimensionality

The JMAK theory is frequently employed to analyze experimental data and determine the degree of crystallinity in both isothermal and non-isothermal heat-treated glass systems. Researchers determine the so-called Avrami coefficient (*n*) from the slopes of experimental $\ln[\ln(1-\alpha)^{-1}]$ *versus* $\ln(t)$ plots. However, there is some uncertainty in such analyses because different combinations of nucleation and growth laws may lead to the same Avrami coefficient. For this reason, a separate investigation of the growth kinetics may be required to reach definite conclusions. For example, in non-isothermal cases, the general relationships, Eq. (3.18), must be used to describe overall crystallization [78–81].

As stated previously, supercooled liquids may have a large or small overlap in their nucleation and crystal growth curves, which affects crystallization behavior. When a supercooled liquid has separation between the nucleation and crystal growth curves, it is possible to control the nucleation and crystal growth steps independently. This allows for greater control over the crystallization process and the resulting microstructure [16,60].

When crystallization is successfully controlled on a supercooled liquid, it then becomes a glass-ceramic. Glass-ceramics are a class of materials that contain a parent glassy phase and at least one crystalline phase formed through controlled crystallization [8,16,83–85]. The number of crystals is governed by the nucleation step, while the size of the crystals is

determined by the crystal growth step. After a controlled crystallization, glass-ceramics include a residual glassy phase with one or more crystalline phases. The amount of crystalline phase can be diverse from 0.5 to 99.5%, although mostly it is in the range of 30 to 40% [62]. A comprehensive review of the design and history of glass-ceramics may be found in the textbook by Höland and Beall [16].

4. Technologies (melt-quenching and sol-gel)

Glass-ceramic materials are traditionally used in different industrial and technological fields owing to their attractive properties for optical, construction, and electronic applications. Furthermore, they are highly appealing in the biomedical field for a wide range of clinical applications, which are mainly related to orthopedics and dentistry [21]. Because of the multiplicity of their applications, different processing techniques have been proposed and applied to produce glass-ceramic materials; however, the basic preparation methods are the traditional melt-quenching route and the more recent sol-gel synthesis [86].

Melting procedures begin from raw precursors, which should be pure to avoid contaminations. Sometimes the precursors (solid powders), after being mixed, are ball-milled with acetone to further provide homogeneity to the blend and, hence, to the glass-ceramic structure. The resulting mixed powders are dried in air. Once raw materials are dry, they are typically melted in alumina or platinum crucibles in a furnace at high temperatures, ranging between 1200 and 1500 °C. However, the platinum crucible is recommended to prepare glass-ceramics for biomedical applications as contamination by other types of crucibles is avoided. The melt can be cast either into a mold, thus obtaining a monolithic glass, or into water, thereby producing a “frit” – which is the name of the product achieved by sudden solidification of the melt once in contact with water. Both these melt-derived products can be reprocessed to obtain desired shapes, geometries, etc. [4].

Sol-gel synthesis is a chemically based method for producing glass-ceramic materials at a much lower temperature than the traditional melt-quenching route [4]. This processing method comprises seven main steps. All reagents are initially mixed at room temperature, creating strong covalent bonds between elements, then poly-condensation and hydrolysis reactions occur simultaneously. Afterward, the obtained sol is cast in a mold. The third step involves gelation, when the three-dimensional glassy network is formed, and viscosity progressively increases. The aging step allows the matrix to densify, and it is fundamental to limit crack formation in the subsequent drying step. Chemical stabilization of the final product is completely achieved in the sixth step. The last step requires a high-temperature thermal treatment in the range of 600 to 800 °C [87–90].

Further details on both the melt-quenching and sol-gel process will be provided in section 4.2.1, “Powders and monoliths”.

Because of their attractive properties, glass-ceramics are considered highly promising materials for dental applications. Specifically, dental glass-ceramics can be divided into main groups: the restorative (inert) prostheses and the bioactive materials [4].

4.1. Inert DGCs

Restorative dental glass-ceramics are bioinert and biocompatible, which are key requirements needed in restoration and reconstruction applications of dental tissues. Their appealing properties match the physico-chemical features of natural tooth structure [91]. In fact, considering the aesthetics, inert glass-ceramics are characterized by color and translucency which make them perfectly suitable for several dental applications [21]. These materials also possess low thermal conductivity, good wear resistance and chemical durability, and high strength and hardness values which are fundamental properties for dental prostheses [21].

For all these reasons, restorative glass-ceramics are largely employed as dental onlays, inlays, crowns, veneers, and bridges (**Figure 6**).

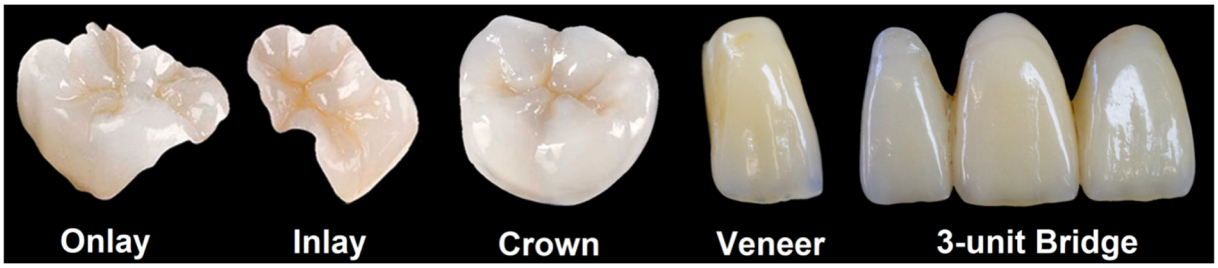

Figure 6- Images of restorative dental glass-ceramics [16,62].

Inert glass-ceramic materials are widely employed in dentistry due to their relatively easy processability. In the following paragraphs, the principal processing methods of inert dental prostheses will be illustrated.

4.1.1. Lost-wax technique

The lost-wax technique is traditionally employed in dentistry to produce inert prostheses, such as inlays, overlays, crowns and components of removable dentures [92]. This method allows dentists and dental technicians to fabricate custom-made restorations for missing or damaged teeth. In fact, wax is chosen for this procedure because it is inexpensive, very easy to manipulate and adapt to custom-made restoration. In the first step of the lost-wax procedure, the dentist obtains an accurate impression of the damaged tooth of the patient (**Figure 7a**) and a cast is then realized from the impression (**Figure 7b**) [4]. A wax pattern of the final dental restoration is shaped on a working die of the tooth which is realized to describe the damaged tooth and the oral structure around it (**Figure 7c**). Both a sprue and the wax model are covered by an investment composed of a binder and a refractory material which allows them to resist at high temperatures. The sprue creates a channel in the investment through which the molten glass/glass-ceramic material comes to form the

restoration (**Figure 7d**). Wax burnout occurs at 900 °C, when the ceramic mold is partially sintered. The glass-ceramic material comes in the form of molten liquid during the heat treatment at 1300-1500 °C, when it is moved to the ceramic mold (**Figure 7e**). The so-obtained glass restoration is then polished, cleaned and removed from the mold at room temperature. This product is converted to a glass-ceramic material through controlled crystallization process in oven. As the last step, the surface of the restoration is colored to match the aesthetics of the patient's natural teeth [4].

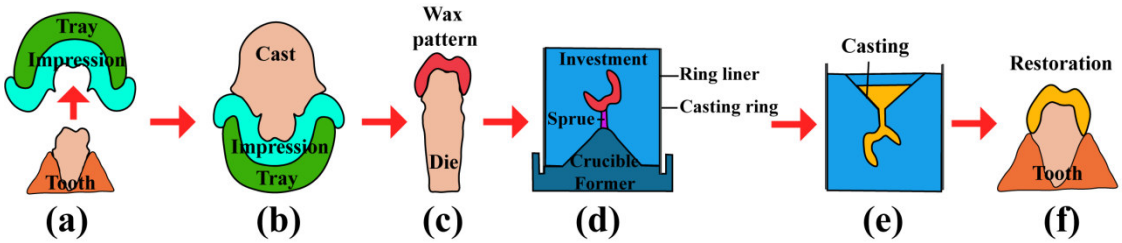

Figure 7- Schematic representation of a lost-wax procedure for dental applications. Reproduced from [4] with permission from Wiley.

If this procedure is followed precisely in each step, the product of the lost-wax technique can be very accurate and characterized by a tolerance of less than 20 μm, but an error in any step could result in a product unsuitable for clinical applications. For example, a serious risk is represented by the distortion of wax pattern and the short time that should elapse between the removal of the wax pattern from the die and its investment.

4.1.2. Heat-pressing

The heat-pressing method was developed in Zurich in 1983 to fabricate ceramic restorations. The initial steps follow the lost-wax route previously described and the mold of dental defects is fabricated [93]. The glass-ceramic ingot and the mold are placed in a special porcelain furnace which has a pneumatic ram, which is properly designed for this specific processing method (**Figure 8**).

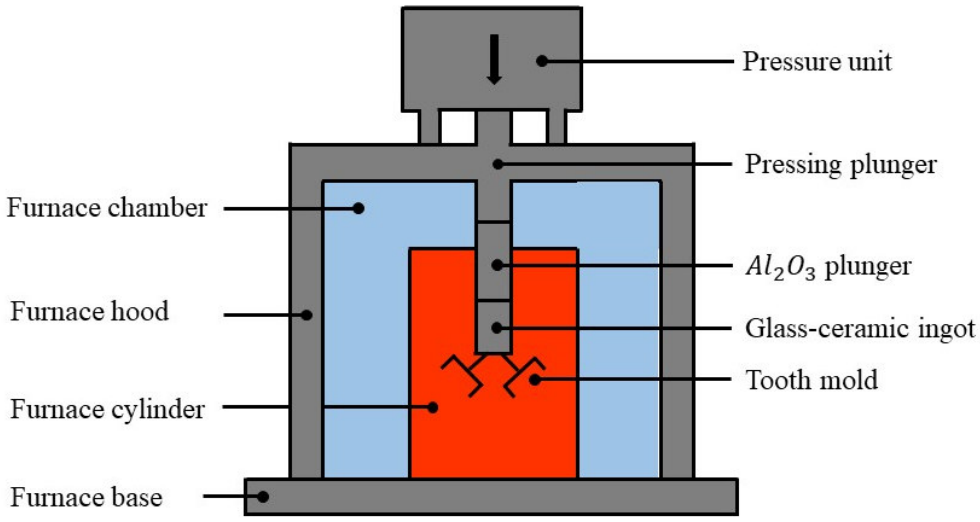

Figure 8- Schematic of the furnace designed for heat-pressing treatment. Reproduced from [4] with permission from Wiley.

The device presses the ingot into the mold at high temperatures under vacuum conditions. As temperature increases, the glass-ceramic ingot becomes a viscous fluid. Approximately at 1000-1200 °C, the glass/glass-ceramic fluid is forced by an alumina plunger, which applies forces in the range of 200-300 N, into the mold. Once the material is cooled, the investment is removed from the realized glass-ceramic restoration by blasting it with silica sand or SiC grit paper [4]. The benefits of heat-pressing method for producing dental glass-ceramics over castable products include net shaped processing, increased flexural strength and excellent marginal fit [94,95]. Furthermore, heat-pressing products are characterized by the absence of shrinkage during the crystallization process [4]. Azar et al. have even reported that lithium disilicate crowns fabricated with the pressing technique have measurably smaller marginal gaps compared with those fabricated with CAD/CAM techniques within in vitro environments [96].

4.1.3. CAD/CAM

The first dental restoration fabricated through computer-aided design and computer-aided manufacturing (CAD/CAM) process was realized in 1985 [97]. Over the last 30 years, impressive technological improvements have been achieved in each step of the CAD/CAM method allowing the achievement of high-resolution scanning devices and very simple, fast and accurate software [98].

CAD/CAM technology can be potentially applied to all dental applications which need the use of custom-made devices, such as in restorative dentistry, prosthetic dentistry or orthodontics [98]. In this process, different devices co-operate to realize the final dental product (**Figure 9**).

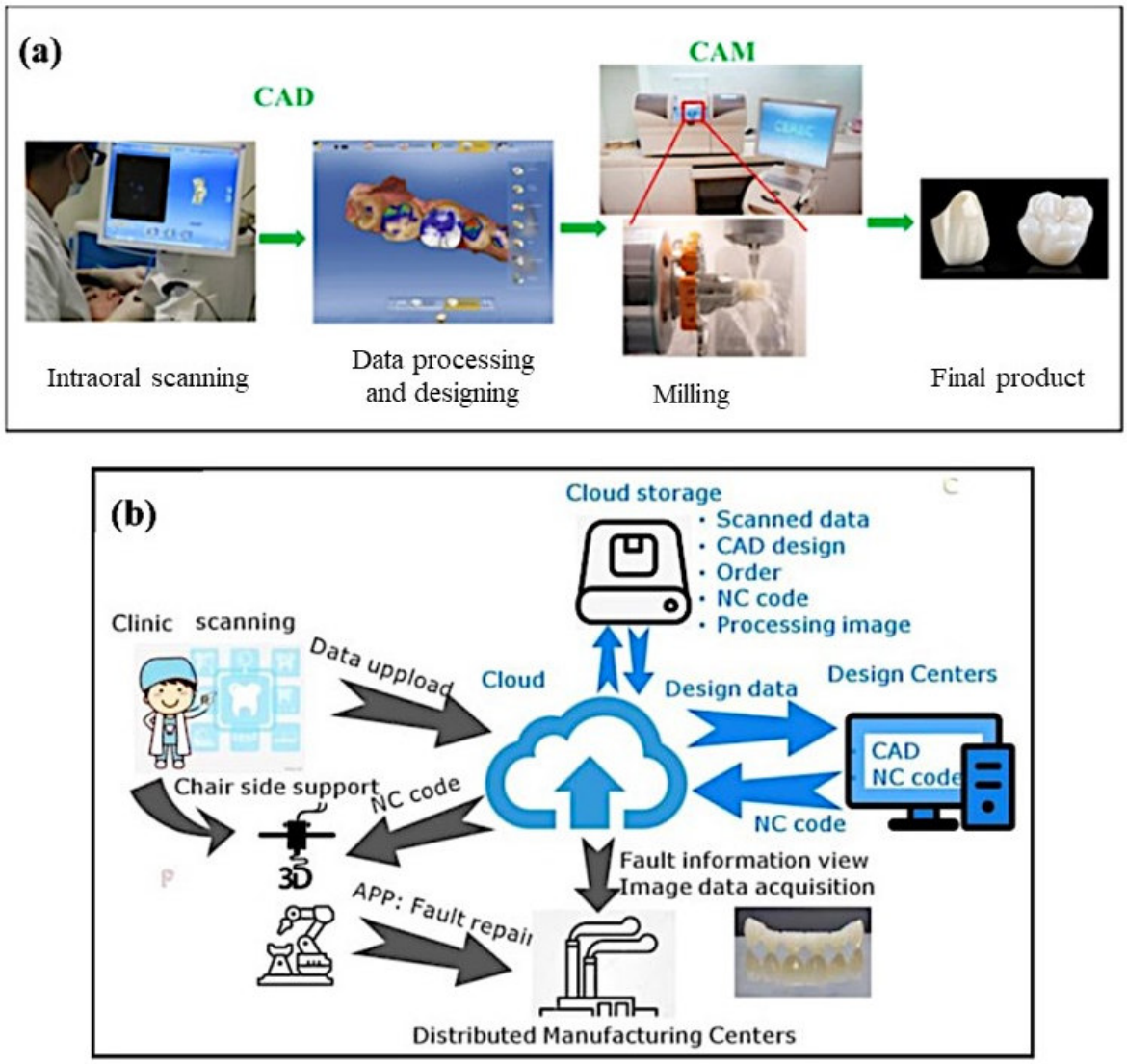

Figure 9- Schematic representation of computer-aided design and computer-aided manufacturing process for dental applications [21].

The first step of this processing method involves the realization of a digital impression, an intraoral image of the defected area of the patient and surrounding teeth, obtained through a scanning device [4,21]. The image constitutes the input data of the process and it is sent to a software, which is able to design the virtual complementary restoration. At this point, the file of the restoration is sent to a CAD/CAM device, which caves a solid block of glass-ceramic material to obtain the dental product. This step could be known as “hard milling”, if a block of sintered material is machined to obtain the prosthetic restoration, or as “soft milling”, if the device machines a partially-sintered block and a further final sintering step in a furnace is

required to achieve the final product [21]. Hard milling allows the realization of very accurate restorations but suffers from heavy abrasion of milling tools. Soft milling is largely used to manufacture dental prostheses made of lithium disilicate glass-ceramic [21]. Stains and glazed can be fired on restoration surface to achieve proper color and aesthetics which match natural tooth appearance [4]. In the last step, the dental prosthesis is implanted in the patient's mouth through the use of cement [32,99]. Products of CAD/CAM technology are extremely accurate thanks to the high resolution of the defect scanning and software.

Although CAD/CAM techniques have already been largely employed for dental applications, their major drawback is the high amount of material wasted during the machining step (in some cases up to 90% of the material). For this reason, additive manufacturing techniques (AMTs) have recently been used to realize dental restoration. In fact, all these processes fabricate the final product by depositing material layer by layer avoiding any waste [21].

Another innovative route is represented by Completely Digital Design and Completely Digital Manufacture (CDD/CDM) which represent the new trend in digital dentistry. These techniques separate the designing step from manufacturing one, both achieving a complete digitalization. Strong collaboration between clinicians, technicians, design and productive centers would also reflect on improved efficiency, accuracy, and reliability of the whole manufacturing process [100].

4.2. Bioactive DGCs

4.2.1. Powders and monoliths

In 1969, the invention of bioactive glasses (BGs) by Prof. Larry L. Hench represented a true revolution in materials science, marking the beginning of a new era, i.e., the birth of third-generation biomaterials [101]. Unlike inert implants, which were widely used at that

time, these innovative materials are characterized by the extraordinary capability to chemically bond to the native tissue while stimulating the synthesis of new bone [102], thanks to a complex chemical mechanism based on ion-exchange phenomena at the material/tissue interface. This process shortly yields the complete osteointegration of the material, which is progressively converted to hydroxyapatite (HA), a calcium phosphate with chemical and crystallographic features very similar to those of natural bone bio-apatite [103].

Nowadays, the extreme versatility of BGs, both in terms of compositional features and processing strategies, makes them clinically effective in a wide variety of medical fields, ranging from hard to soft tissue regeneration [104–109]. In particular, due to their well-known osteoconductive and osteoinductive properties, BGs have been widely and successfully employed in dentistry and orthopedics for the regeneration of bone tissue [110,111]. Nevertheless, their use in clinical practice has not yet reached its maximum potential due to their intrinsic brittleness, which discourages their use in load-bearing applications [112].

One of the most common and easiest strategies to improve the mechanical performances of BG-based products relies on the use of high temperature treatments that favor the nucleation of crystalline phases within the material [16]. In this way, glass-ceramic materials with improved mechanical properties can be obtained [113].

In general, glass-ceramics are polycrystalline materials obtained from the controlled heating at high temperature (above T_g) of a base glass with the aim of inducing the nucleation and growth of specific crystalline phases within the material [114]. Thus, a glass-ceramic material is characterized by the presence of one or more crystalline phases embedded into a residual amorphous matrix, where the level of crystallinity can vary between 0.5 and 99.5 %, but most frequently ranges between 30 and 70% [46].

There is experimental evidence that glass devitrification improves not only the mechanical properties of the material, but also its chemical stability; concerning bioactive materials, this aspect has to be carefully considered, as it can hinder the interaction between the material and the physiological environment, thus compromising the performances of the device [40,42].

As a result, several research groups have already investigated the effect of devitrification phenomena on the bioactive potential of BGs, reporting the decrease in HA deposition rate resulting from the nucleation of crystalline phases in the parent BG: ion-release phenomena involved in the mechanism of formation of HA layers at the interface between the material and the physiological environment are, indeed, mainly related to the residual amorphous phase, characterized by a lower chemical stability (i.e., higher reactivity) [42]. Despite that, it is possible to obtain glass-ceramics showing bioactive properties comparable to those of BGs currently used in dentistry and orthopedics (e.g., Biosilicate®).

Indeed, manufacturing technologies for obtaining glass-ceramic materials offer the possibility to opportunely control and tailor the nucleation and growth of crystalline phases by properly setting the heating conditions, thus allowing an additional control on the overall physical and chemical properties of the final material [16].

Provided that the composition of the base glass is intimately related to the feature of the crystalline phases which nucleate upon heating, there are two methods used for controlling the nucleation of crystalline phases:

(i) Controlled internal (or *bulk*) crystallization within the base glass, performed into two different subsequent phases: a) nucleation of crystallites at low temperature (slightly above the T_g) and b) crystals growth and join at grain boundaries, performed at higher temperatures [114].

(ii) Controlled crystallization on the surface of the base glass, in which the nucleation of crystals can be induced directly on the surface of the material. In this case, glass is crushed into fine particles and the surface of glass powders is activated to produce crystals, which proceed to grow inwards from the surface of the glass particles [114].

Just like BGs, the melt-quenching route and sol-gel process are both suitable synthesis methods for the production of bioactive glass-ceramics, offering the possibility to adapt the shape of the final product according to the specific application. The main steps of the melt-quenching and sol-gel route for obtaining glass-ceramic monoliths and powders are depicted in **Figure 10**.

Melt-quenching route is the most common and traditional way to obtain glass materials by the melting at high temperatures of specific reactants, acting as oxides precursors [86].

Typically, powdered rough reagents are mixed in proper amounts, according to the specific composition, and further reground to increment the homogeneity of the batch. Afterward, the powders are transferred into a platinum or alumina crucible and melted in a high-temperature furnace. The melting temperature must be selected according to the compositional features of the material, where higher temperatures (up to 1500 °C) are required for highly stable aluminosilicate compositions, while borate and phosphate materials are usually melted between 1200-1300°C. The use of alumina crucible is usually restricted to those glasses with low melting point, to avoid diffusion phenomena inside the glass composition and preserve the purity of the final product.

Before casting, it is advisable to keep the temperature constant in order to improve the homogeneity of the melt.

According to the final application, different forming routes are available:

(i) Direct forming via casting into molds, which allows the production of glass monoliths, which are then thermally treated to obtain a bulk glass-ceramic material.

(ii) Quenching into water, leading to the production of a glass frit, which can be easily ground and sieved, thus facilitating the manufacturing of glass powders with the desired grain size. Powders can be subsequently pressed to form compact pellets, and then sintered to achieve higher densification. By this approach sintering and crystallization are concurrent phenomena, but the nucleation of crystals is usually limited to the surface, with poor internal crystallization [86,89].

Recently, much attention has been addressed to sol-gel synthesis due to the possibility to obtain highly homogeneous and chemically pure glass and glass-ceramic products exhibiting very interesting properties in medical applications [115].

Unlike melting, sol-gel chemistry allows silica nanoparticles to form and assembly at room temperature leading to the formation of a gel network which is then thermally treated to produce a glassy matrix.

The main difference between melt quenching and sol-gel chemistry concerns the texture of the final product. Sol-gel glasses indeed are intrinsically nanoporous, while melt-derived BGs are highly dense materials.

The resulting nanotopography confers to sol-gel materials very attractive features for biomedical applications: as an example, the very high surface reactivity leads to enhanced cellular response, as well as faster HA deposition rates in body fluids [90].

As a result, sol-gel glasses are bioactive in a wider compositional range (up to 90 mol.% of SiO_2) compared to melt-derived ones and their composition could be extremely simplified as modifiers (e.g., Na_2O) are not required to decrease the melting temperature and facilitate the casting procedure [116],

In a typical sol-gel synthesis 3 main phases can be identified:

(i) preparation of sol

(ii) gelation of the sol

(iii) removal of the solvent.

By maintaining a very slow heating rate, gel monoliths can be obtained, even if the formation of cracks is very recurrent upon drying due to the elimination of the residual liquid phase.

If cracks are formed, it is still possible to manually grind the dried gel before the heating treatment and press gel particulates in order to produce gel pellets, which can be subsequently thermally treated, as previously described for melt-derived glasses.

Thus, in order to produce a glass-ceramic, it is sufficient to perform controlled heat treatments on the dried gels by selecting the most suitable temperature on the basis of the thermal behavior of the material, which needs to be previously assessed by proper thermal analyses. A similar approach has been recently described by Fiume et al. in a study comparing the physical properties of sol-gel and melt-derived materials for bone tissue engineering applications characterized by the same nominal composition [117].

It is also possible to obtain sol-gel glass-ceramic products by performing controlled heating treatment on the already calcined gels, in the form of both monoliths and powders. This approach, however, requires an additional step to obtain sol-gel glassy products first.

One of the major issues related to the synthesis of bioactive sol-gel glass-ceramic products with improved reaction kinetics is the strong relationship existing between the thermal treatment, required for inducing the controlled nucleation of crystalline phases, and the nanotextural properties of the final material. In this regard, Jones et al. observed a decrease in the specific surface area (SSA) of sol-gel bioactive foams from 122.7 to 42.5 m^2/g as the temperature increased from 700 to 800 °C and up to 12.8 m^2/g as the temperature increased to 1000°C [118]. Likewise, Fiume and coworkers reported a halving of the SSA by

increasing the calcination temperature of highly bioactive silica-based sol-gel products from 625 °C to 800 °C [117].

When considering sol-gel route it is thus fundamental to opportunely tune the calcination conditions in order to preserve the intrinsic nanotexture given by the process itself, forecasting a certain decrease of the SSA and, consequently, a further slowing down of the HA deposition rates.

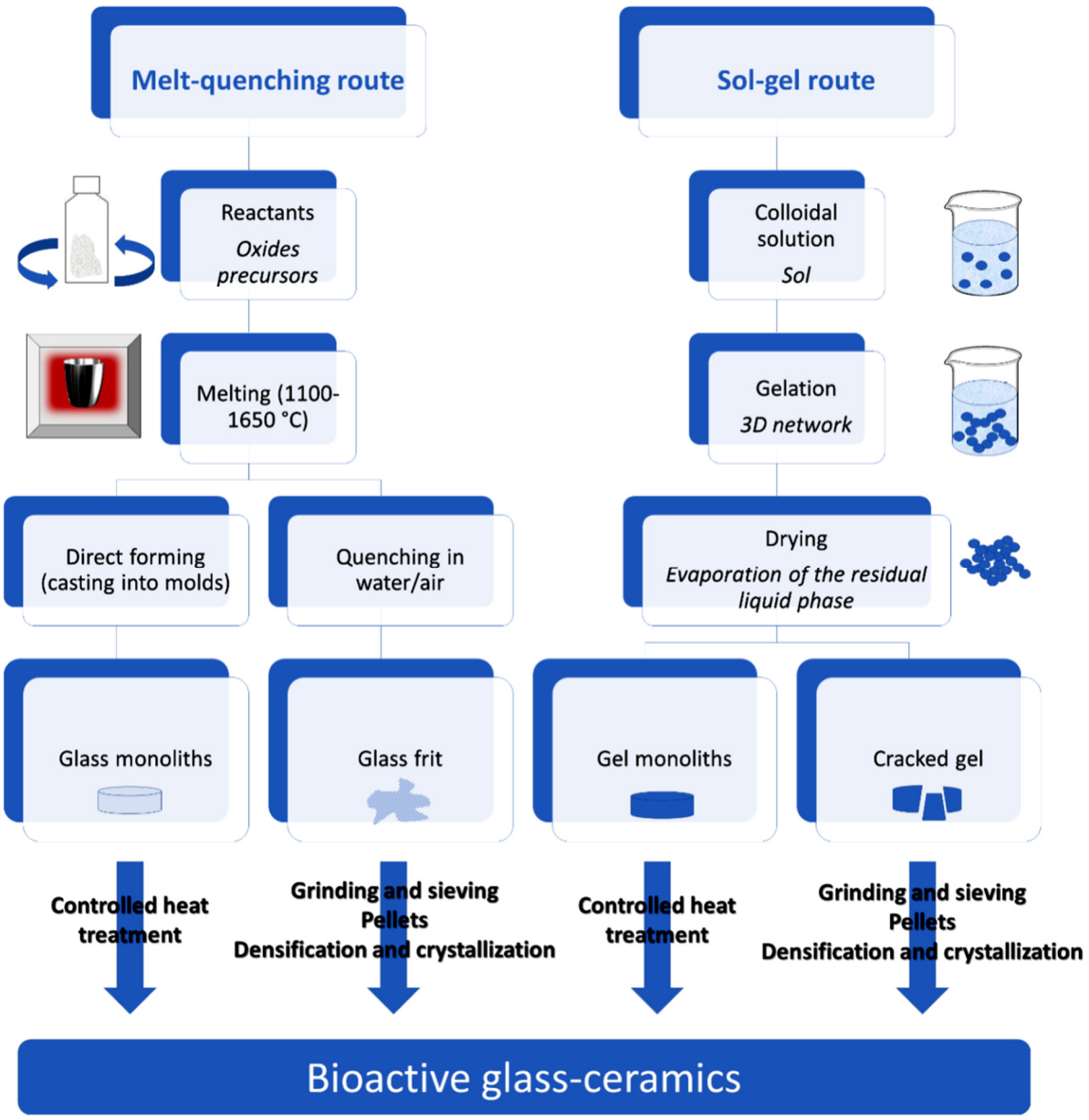

Figure 10- Manufacturing methods for obtaining bioactive glass-ceramic products.

4.2.2. Scaffolds

The term *scaffold* literally means "supporting framework" and can be used in different fields. In tissue engineering and regenerative medicine applications, scaffolds are *"materials that have been engineered to cause desirable cell interactions contributing to the formation of new functional tissue for medical purposes"* [119]. In bone and dental regenerative applications, scaffolds typically are 3D porous structures that provide support to cells allowing them to adhere, migrate, proliferate and differentiate [89,120,121].

Nowadays, BGs are considered the gold standard materials to fabricate 3D scaffolds for clinical applications. BG-based scaffolds should mimic as much as possible the structure of the healthy bone and its architecture in order to optimize the integration with the host tissue [112].

In general, the goal of scaffolds is to deliver bio-factors such as cells, genes and proteins to the defected sited aiming at inducing regeneration process into the surrounding tissue. Therefore, an ideal scaffold should:

1) Provide the correct anatomic geometry
2) Support mechanical load typical of the interested site
3) Have high regeneration capability

In order to achieve the abovementioned high-level results, the design and development of a scaffold should consider different requirements (**Figure 11**), including:

1) Biocompatibility and bioactivity
2) Capability to bond the host tissue without scar formation
3) Porous and interconnected structure
4) Moldability in different shapes and sizes
5) Suitable degradation rate

6) Maintenance of mechanical properties

7) Easy fabrication

8) Sterilization [89,122].

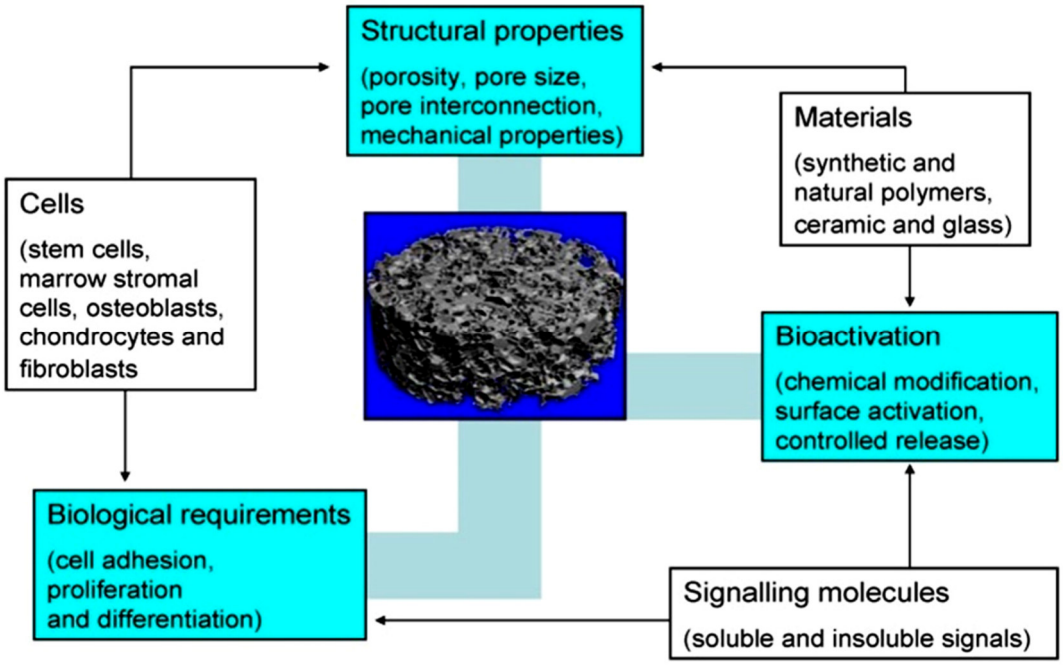

Figure 11- Schematic diagram of the key factors involved in the design of an optimal scaffold for bone tissue engineering [123].

Table 2 gives a brief overview of the required properties that a BG-based 3D scaffold for bone or dental regeneration applications should possess.

Table 2. Overview of key properties for a scaffold aimed at regenerating bone or dental tissue [120].

Property	**Effect/explanation**
Ability to deliver cells	The materials should not only be biocompatible but also foster cell attachment, differentiation and proliferation
Osteoconductivity	Osteoconductivity does not only inhibit the formation of fibrous tissue around the implant (encapsulation) but it also brings a strong bone between the scaffold and the host tissue
Biodegradability	The material composition, combined with the porous structure of the scaffold, should lead biodegradation *in vivo* at rates appropriate to tissue regeneration
Osteoinductivity	The ion dissolution products released from the scaffold stimulate

	bone cells towards paths of regeneration and self-repair
Mechanical properties	The mechanical strength of the scaffold, which is determined by both material properties and structure porosity, should be sufficient to provide mechanical stability in loading-bearing sites
Porous structure	The scaffold should have an interconnected porous structure, characterized by diameters between 300 and 500 μm for cell penetration, tissue ingrowth and vascularization
Fabrication	The material should possess desired fabrication capability, e.g. being readily produced into irregular shapes of scaffolds that match defects of individual patients
Commercialization potential	Material synthesis and scaffold fabrication should be reproducibly suitable for commercialization. The scaffold should also be sterilizable and accessible at a reasonable cost

Since the realization of the first BG scaffold in 2002 by sol-gel foaming, a lot of scientists have focused their studies on the optimization of manufacturing processes to realize the "perfect" scaffold [120] The ideal manufacturing process should be easily repeatable and should provide the same outputs, thus guaranteeing constant characteristics of scaffolds and potentially allowing mass production. Therefore, processing route should also be economically sustainable and safe for the health of all workers who participate in the fabrication process [120].

The following paragraphs provides a picture of the main manufacturing methods for the production of glass and glass-ceramic scaffolds having special relevance to dentistry. As summarized in **Table 3**, several strategies have been experimented over the years to fabricate BG-derived scaffolds, but only a subset of these techniques has been specifically used or has somehow shown promise for dental applications. Most of conventional methods – except for foam replication – are partly unsuitable or have been overcome by additive manufacturing approaches that allow a better degree of accuracy and versatility. The interested reader is addressed to previous literature for more details on all these techniques [124].

An important issue also deserves to be taken into account: most of the methods listed in **Table 3** yield "rigid" scaffolds which are difficult to adapt to the restricted and complex

geometries of dental spaces. Hence, injectable pastes or moldable materials are usually preferred by dentists.

Table 3. Overview of the methods used to fabricate glass and glass-ceramic scaffolds.

Manufacturing Methods	Technological Class	Specific Methods
Conventional	Foaming techniques	Gel-casting foaming, sol-gel foaming, H_2O_2 foaming
	Thermal consolidation of particles	Organic phase burning-out; polymeric porogens, starch consolidation, rice husk method
	Porous polymer replication	Coating methods, foam replica method
	Freeze-drying	Freeze-casting of suspensions, ice-segregation-induced self assembly
	Thermally induced phase separation	
	Solvent casting and particulate leaching	
Additive manufacturing	Selective laser sintering	
	Stereolithography	
	Direct ink writing	3D printing, ink-jet printing, robocasting

4.2.2.1. Foam replica method and foaming strategies

A high level of porosity and well interconnected bone-like structure are fundamental features exhibited by BG scaffolds. Polymeric foams have ordered 3D pore/structure architecture which can be replicated to obtain 3D scaffolds with up to 90 vol.% of porosity [125].

Foam replica method involves the use of a polymeric (e.g., polyurethane) sponge (**Figure 12**), exhibiting the desired pore structure, as a sacrificial template for the realization of BG made scaffolds (**Figure 13**) [126].

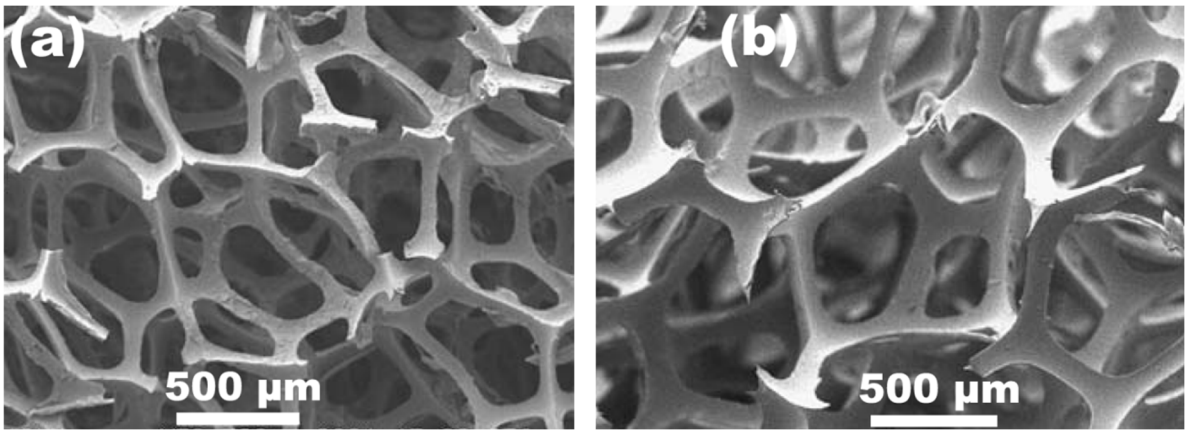

Figure 12- SEM images of 60 ppi (a) and 45 ppi (b) sponges, before performing the impregnation with glass slurry. Reproduced from [127] with permission from Springer.

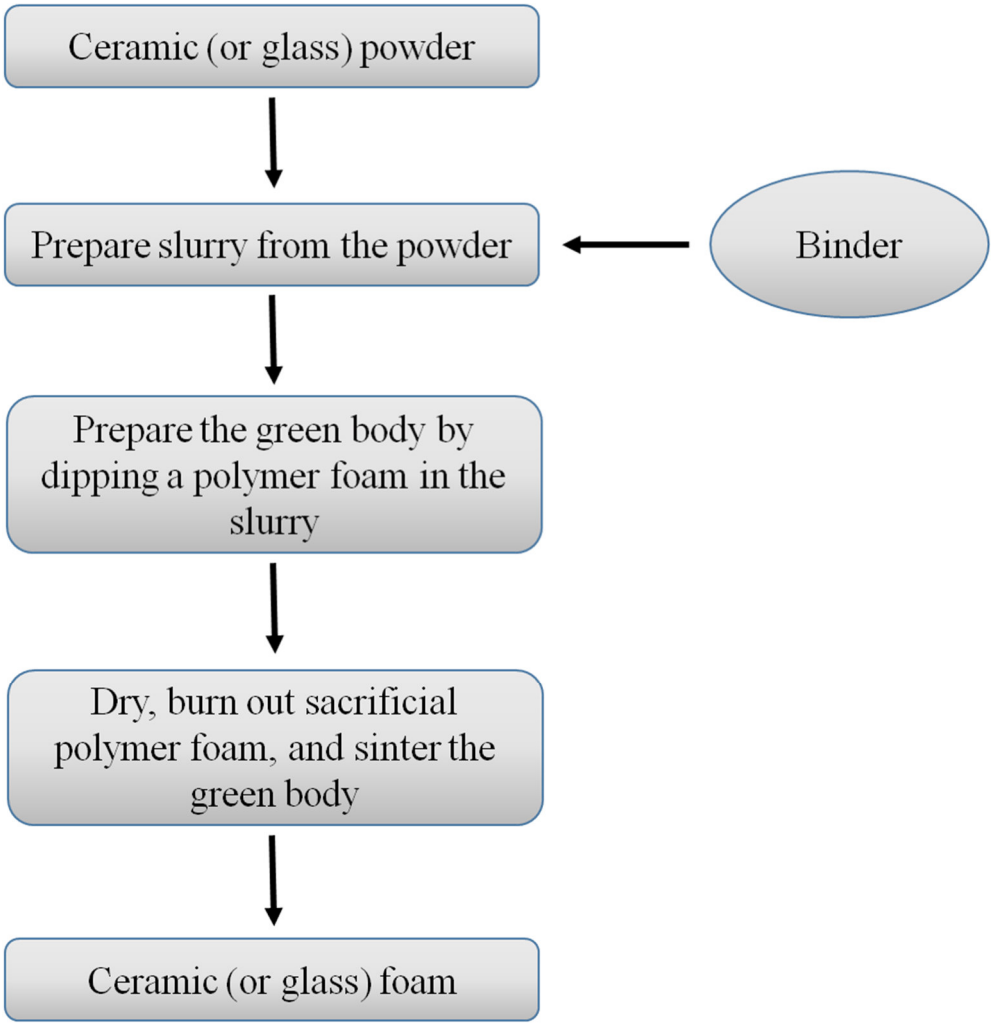

Figure 13- Flowchart of the foam replica method for the fabrication of glass-ceramic scaffolds [126].

The polymeric template (foam) is soaked into the slurry, a suspension obtained by the mixing of distilled water, polyvinylalcohol (PVA) and BG powder, which subsequently penetrates the sponge structure permitting BG particles to adhere onto the polymer surface. After the immersion, the polymeric sponge is compressed to eliminate the excess slurry. The coating thickness could be modulated by multiple immersion cycles. The obtained sample, known as green body, is dried on a smooth surface at room temperature. Green bodies are often rotated during the drying process in order to achieve a homogenous distribution of the slurry throughout the volume of the template. After the drying process, the samples are thermally treated in order to remove the polymeric porous template (burning-off) and sinter BG particles [120,126,128]. The parameters of the sintering process are properly set up to achieve the desired density of glass-ceramic network [126]. In this way, a level of porosity comparable with that of cancellous bones can be achieved (>50 vol.%). On the other hand, scaffolds produced by this method may often suffer from poor mechanical features [112].

Foam-like structures mimicking the trabecular architecture of cancellous bone have also been produced by applying different foaming strategies to both melt-derived (e.g., gel cast foaming [129], dolomite foaming [130]. and sol-gel BGs (foaming of the sol until gelation is achieved) [131,132]. Although being potentially interesting and deserving further investigation, these scaffolds have not been proposed for dental applications due to some drawbacks (poor mechanical strength, poor interconnectivity of pores left behind by the bubbles).

4.2.2.2. Freeze casting

Although not specifically used to process dental glasses and glass-ceramics, freeze casting deserves to be mentioned here due to its potential as it is a relatively simple technique to produce obtain anisotropic porous scaffolds [133] In this approach, a ceramic (glass) slurry

is poured into a mold and then frozen (-20 °C) [134]. Subsequently, the sample is subjected to freeze drying, often in vacuum conditions in order to inhibit crack formation that usually occur during normal drying process. Solvent removal has a big impact on final product because the porous structure may be destroyed through its uncontrolled removed. After these steps, dried samples are sintered and porous glass, ceramic or glass-ceramic scaffolds are obtained. Scaffolds realized by freeze casting method are characterized by an anisotropic structure, exhibiting the formation of oriented and elongated crystals (**Figure 14**).

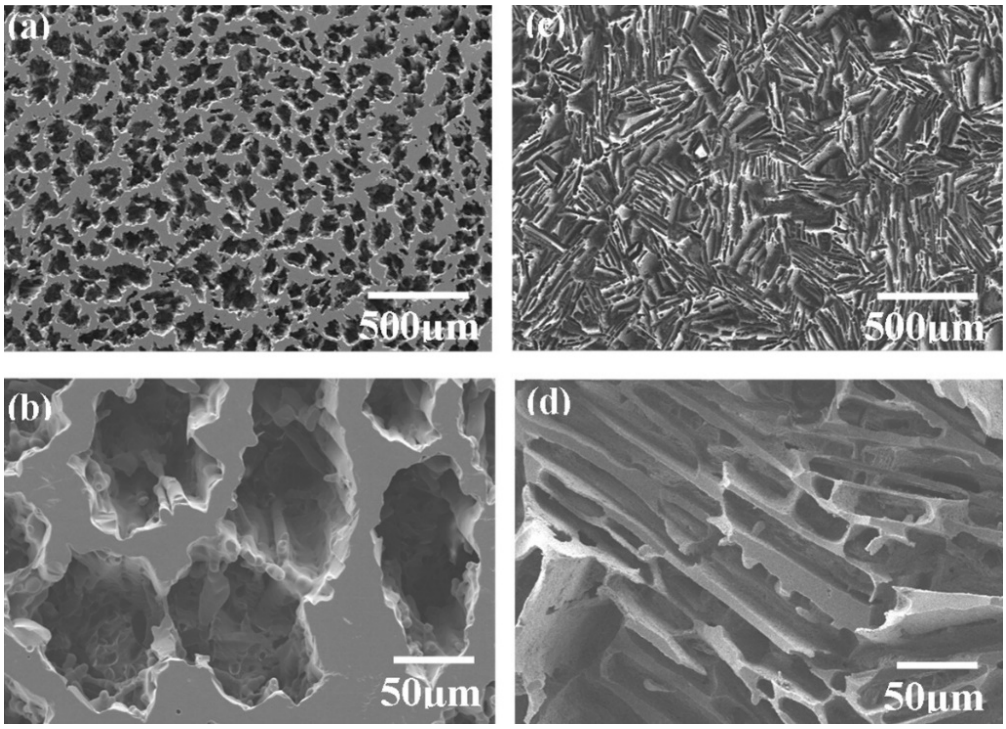

Figure 14- SEM images of BG scaffolds prepared with different microstructures from suspensions containing 15 vol.% particles: (a), (b) columnar microstructure (solvents: water + 60 wt.% dioxane); (c), (d) lamellar microstructure (aqueous solvent). The cross sections are perpendicular to the freezing direction [135].

The presence of oriented microcrystals is one of main advantages of freeze casting technique, conferring to scaffolds much higher compressive strength. When only water is used as solvent, pore size typically ranges from 10 to 40 μm. For this reason, in bone tissue applications, other organic solvents are added in the solution to achieve larger pore size, comparable to the pore size in cancellous bone (>100 μm) [112].

4.2.2.3. 3D printing

Additive manufacturing technologies (AMTs) refer to those bottom-up approaches where 3D structures are fabricated by progressively adding materials in the form of ultrathin layers to obtain the desired morphology, thus achieving the possibility to fabricate more detailed objects than conventional methods characterized by a top-down approach [136]. Therefore, AMTs include all the manufacturing processes which rely on using a CAD model or a computed tomography (CT) scan of the final product as input data [120,137].

Considering the AMTs which process glass-ceramic materials, two groups can also be distinguished, i.e., direct and indirect fabrication techniques depending on the need for a post-process heat treatment. In direct fabrication techniques, such as selective laser sintering (SLS), melting and consolidation of glass/glass-ceramic particles occur during the shaping of the product related to the use of a laser or electron beam [120,138]. Four categories of indirect AMTs which need post-treatments, such as de-binding and sintering, are individuated (**Table 4**).

Table 4. Overview of main categories of AMT indirect techniques.

Categories	**Basic principle**	**Techniques**
Laminated object manufacturing	Binders are included in feedstock and sheets of materials are glued together and then cut into desired shapes	
Extrusion-based techniques	A filament of material is extruded by a robot-controlled nozzle	Robocasting, fused modelling deposition, dispense plotting
Methods based on stereolithography apparatus (SLA)	These methods are based on the use of a light beam	Digital light processing (DLP), laser-based systems
Fusing of bed powders	Particles are kept together by a binder deposed on the working plan	3D printing

Likewise, the other direct AMTs, only one step is needed for the realization of the final object by SLS. In this method, a YAG laser guided by CAD model is employed to scan glass/glass-ceramic powders deposited on the working plan. **Figure 15** schematically shows a SLS device where two different chambers, the laser and a scanning system are identifiable [139]. The powder feedstock is prepared in the first chamber and then moved by a roller to the other chamber, where powder bed is built through a layer-wise approach. Once the layer is prepared, surface laser scanning fixes the powders consolidating them. After that, another layer is deposited, and the process continues through the repetition of these steps [128,139].

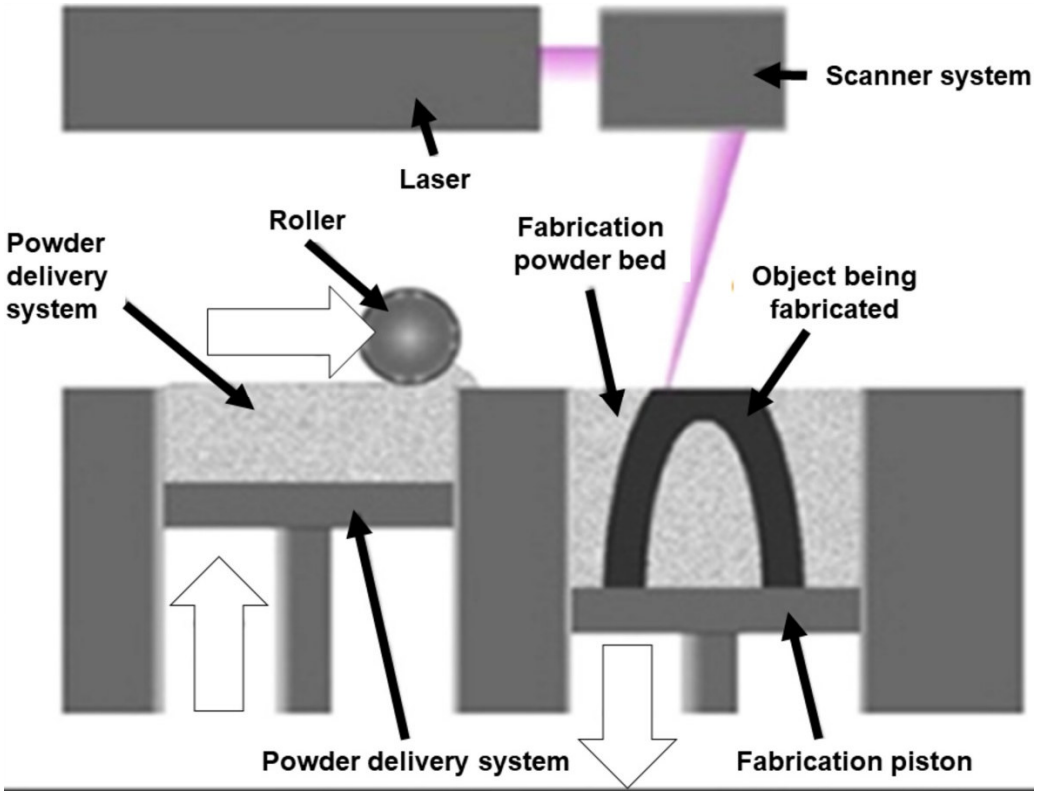

Figure 15- Schematic representation of a selective laser sintering device [140].

The first BG-based scaffold produced via SLS method was developed by Liu *et al.* [141] in 2012. Since then, several research groups have developed scaffolds based on BGs by SLS technique trying to optimize process parameters in order to achieve the best sintering and

densification, improved mechanical properties and excellent bioactive performances [142,143].

Stereolithography (SLA) represents probably the most precise AMT, reaching high resolution values up to 20 μm. In this process, a liquid UV-sensible resin, a UV-laser and a movable platform are used to realize layer by layer the 3D object [137]. The laser beam scans the surface following the path described by the CAD model and curing the resin to build the first layer of the object. Then, the platform is moved vertically allowing the surface covering by a more viscous layer of polymer. The laser beam scans again the surface, and this mechanism is repeated to progressively build layer by layer the final product [120,144].

More recently, a novel processing method belonging to SLA techniques has been developed in order to reduce the processing time, known as digital light projection (DLP) system (**Figure 16**). These systems are characterized by the presence of a digital mirror device used to illuminate and reproduce every single layer at once, eliminating the need for laser beam scanning. In this way, the processing time is only related to exposure time of material, gaining the time needed for scanning process. DLP systems allow the use of inks containing ceramic/glass particles (40-60%) [120]. Even if some viscosity problems are associated to ceramic/glass-filled inks, DLP systems have been used by different researchers to fabricate BG scaffolds with promising results [144–147].

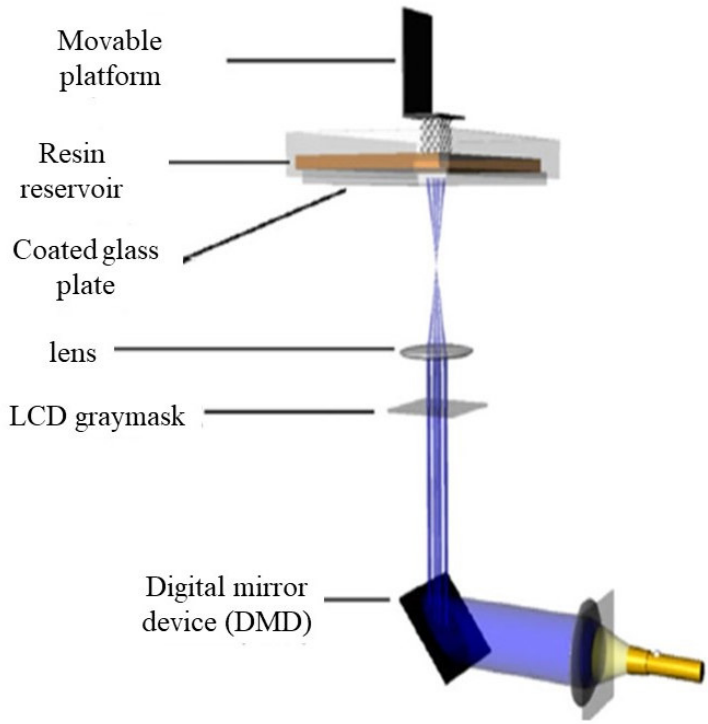

Figure 16- Schematic illustration of a digital light projection system. Image adapted from [137].

Direct ink writing methods include many different AMTs, such as 3D printing, ink-jet printing and robocasting. In all these techniques a print head or nozzle builds up a 3D object by following computer instructions which translate a pattern-generating device [120]. Ink-jet printing is a technique based on dispensing ink droplets to fabricate a 3D product layer by layer. In this method, all the components required by the process are contained in the ink. On the contrary, in 3D printing technique the ink is formed by the binder while glass particles are in the building bed [120].

Commonly speaking, the expression “3D printing” is often used to indicate all the direct ink writing methods – including robotic deposition or robocasting: although being acceptable, this is not formally correct. As all AMTs, 3D printing is based on the use of a computer-controlled device which follows the pattern designed by a CAD model. 3DP setup is similar to that of SLS machine: typically, 3D printing device is composed by a print head, in which a

syringe containing BG paste is inserted, and a working platform, on which the material is deposited (**Figure 17**) [148]. The printing head can work in two different modes: continuous inkjet printing (CIJ), in which ink flows continuously through a nozzle and can be deviated by an electric field, or drop-on demand mode (DOD), where the drop is generated by a piezoelectric or thermal system only when needed [121].

In robocasting, the ink is typically extruded through a nozzle by mean of pressurized air under controlled pressure and velocity [148].

In all direct ink writing methods, 3D complex structures can be obtained by controlling through a dedicated software the movements of both printing head and building bed. The 3D object is realized layer by layer thanks to a cyclical mechanism of material deposition.

Robocasting is probably the most common technique between AMTs. Its main advantage is the possibility to change ink viscosity through chemical and physical processing achieving strong 3D structure [120]. Robocasting is currently considered as one of the most versatile and relatively easy methods to produce BG-based structures with complex hierarchical structures [148]. In fact, robocast BG scaffolds characterized by pore size from tens of micrometers to half a millimeter can be fabricated using extrusion nozzles ranging between 100- 580 μm and particles below 30 μm [120,128].

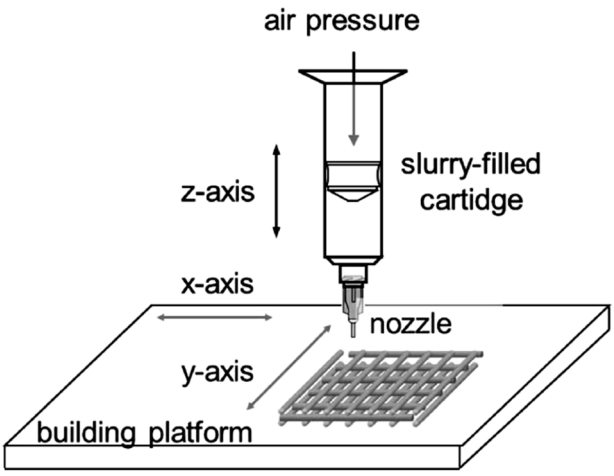

Figure 17- Schematic representation of a robocasting system [128].

The ink used for bone repair applications is usually prepared by stirring BG powders in an aqueous solution containing a polymeric binder, such as Pluronic®. Ink rheological properties are fundamental parameters for the manufacturing of BG scaffolds [149]. Recent experiments have shown that, after being opportunely set, 3D printing/robocasting devices also allow the production of MBG scaffolds (**Figure 18**).

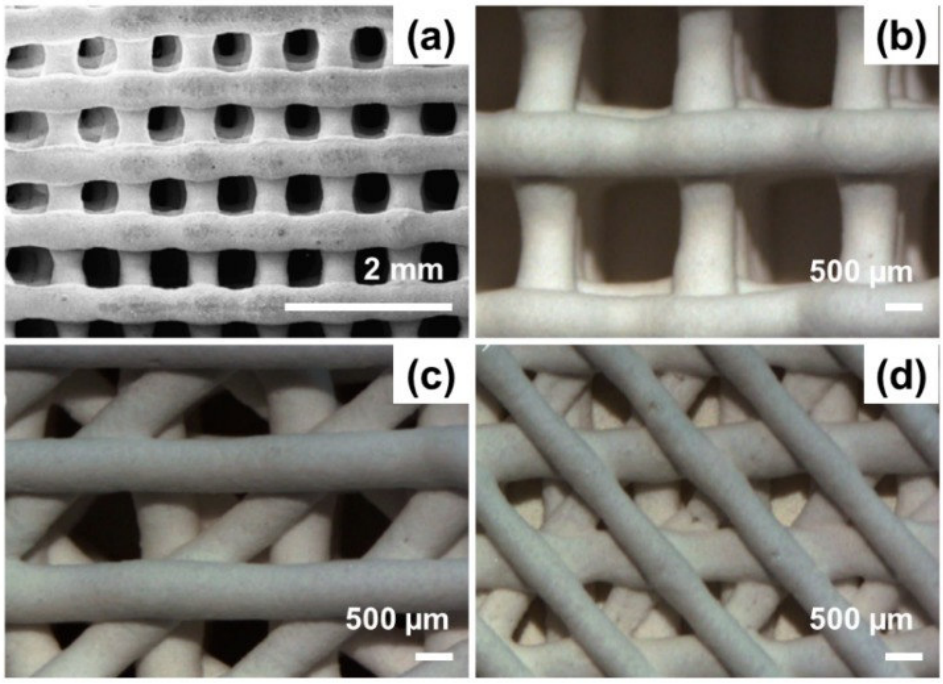

Figure 18- SEM images show different macropore architectures that can be obtained by robocasting of MBGs: (a) squared, (b) rectangular and (c) ,(d) irregular macropores [150,151].

4.2.3. Bioactive glass-ceramics coatings

Osteointegration is a complex remodelling process based on the direct structural connection between the living bone tissue and the surface of the implant material [152].

Due to their exceptional biocompatibility, high wear resistance, high fracture toughness and mechanical properties matching the physiological loading conditions, zirconia (ZrO_2) and

titanium/titanium alloys are currently the most common materials for the production of dental implants. However, these materials are chemically inert, i.e. they are only able to establish a mechanical interaction with the native tissue thanks to the micro-roughness of their surface (morphological fixation) [153].

Despite chemical inertness has to be preferred when dealing with long-term implants, interfacial displacements determined by inadequate interfacial adhesion is one of the main causes of early failure of the implant and the lack in osteointegration may additionally result in the development of a non-adherent fibrous capsule around the implant, also known as *foreign body reaction* [154].

In this regard, the application of a bioactive coating exhibiting osteo-integrative properties may represents an effective strategy to improve the overall performance of the medical device while bringing valuable benefits to the patient [155–157].

The main advantages deriving from the application of bioactive coatings on the surface of inert metallic implants include [158]:

1. Protection against corrosion and degradation;
2. Hindered interaction between the native tissue and the degradation by-products of the substrate.
3. Improved bioactive fixation of the implant to the living bone by osteointegration mechanism
4. Possibility to confer additional properties to the coating by including biologically active ions able to provide multiple therapeutic actions.

As an example, the application of bioactive coatings with antibacterial properties has recently attracted the scientific attention of many research groups operating in the dental field for the treatment of antibiotic-resistant infections associated to periodontitis and periimplantitis, which are the two most common diseases associated to the implantation of

dental prostheses. Both of them, in fact, are associated to the accumulation of periodontal pathogens within the preimplant pocket and, if not properly treated, they can lead to severe bone resorption and subsequent tooth loss [159].

The most critical aspect related to coating strategies is related to the need for obtaining good adhesion between the two materials at the interface. The most common analyses used to investigate the interface characteristics are scratch tests, usually followed by morphological evaluation by SEM or optical microscopy, tensile (pull-out) tests, performed according to ASTM D4541 or ASTM C633-13 standards, and nanoindentation tests on the cross-section to assess the interfacial adhesion strength between the coating and the metallic substrate [160]. Other relevant properties include abrasion resistance, chemical corrosion and thermal shock resistance that can be determined according to IS/ASTM/DIN [161].

Over the years, several deposition strategies for the application of BG and glass-ceramic coatings have been developed, as comprehensively reviewed by Joy-anne et al. [156], Baino et al. [157], Brunello et al. [160] and Sergi et al. [162].

In the present section, just a brief overview of the main deposition strategies reported in literature for the production of bioactive glass-ceramic coatings on metallic implant will be provided.

4.2.3.1. Enameling

Enameling is a traditional surface treatment based on the melting of a glass layer on the surface of a metallic implant. Glass powders, most frequently obtained by traditional melt-quenching in water or air, are dispersed into a liquid medium (i.e., ethanol or water) to obtain a glass slurry, which is then applied onto the metallic surface by dipping, spraying, or painting. After drying, a controlled thermal treatment (firing) is required to fuse the coating on the metallic surface [156]. During this step it is fundamental to:

1. Set the temperature in order to favor the formation of sintering necks between adjacent particles, while inducing the controlled nucleation of specific crystalline phases;
2. Keep the firing time as short as possible to prevent undesired reactions between the coating material and the substrate, which can lead to the detachment of the coating from the substrate;
3. Preserve the bioactivity of the coating upon heating.

Time and temperature selected for the firing as well as the cooling stage are crucial aspects to be controlled in order to guarantee a good quality of the coating. Moreover, thermal stresses during cooling stage must be avoided to prevent the formation of cracks. In this regard, it is suggested to wisely design the coating composition in order to have a lower coefficient of thermal expansion as compared to that of the metallic surface [158].

In silica-based glasses and glass-ceramics, the coefficient of thermal expansion can be reduced by increasing the silica content; however, dealing with melt-derived glasses and glass-ceramic, it is necessary to keep the silica amount lower than 50-60 mol.% to preserve the HA-forming ability of the material in contact with body fluids, thus favoring the osteointegrative process of the implant [89]. However, substituting CaO with MgO and Na_2O with K_2O are also effective strategies to lower the thermal expansion coefficient of silica-based glasses and glass-ceramics [163].

Advantages of enameling include low cost of processing, ease of operation, and the possibility of optimization by changing the parameters. The enameling method along with tailoring the composition of the glass is known to be a possible option to fabricate BG coatings onto bioinert metal substrates with adequate thermal expansion coefficient, good adherence, and bioactivity [156].

4.2.3.2. Thermal spraying

Thermal spraying is a well-established technique used for coatings deposition in a wide variety of applications, from automotive industry to medical applications.

More precisely, the expression thermal spraying refers to a large family of coating deposition processes, classified according to the energy source used into 3 main groups: a) kinetic energy, b) chemical energy and c) electric energy [162]. Within these categories, further subclasses can be identified, as summarized in **Table 5**.

Table 5. Summary of available thermal spraying technologies classified according to the energy source employed.

Energy source	Technique	Acronym
Kinetic energy	Cold spraying, low/high pressure	CS (L/H)
Chemical energy	Flame spraying	FS
	High velocity oxygen fuel	HVOF
	High velocity air fuel	HVAF
	Detonation gun	D-gun
Electric energy	Atmospheric plasma spraying	APS
	Suspension plasma spraying	SPS
	Solution precursor plasma spraying	SPPS
	Vacuum plasma spraying	VPS
	Wire arc spraying	WAS
	Plasma radio frequency	PRF
	Shroud plasma spraying	Sh-PS

In a general thermal spraying approach, molten, semi-molten or solid particles are deposited onto a substrate, followed by controlled solidification and sintering processes, which will define the microstructural properties of the coating layer [164].

The operating principle relies on a continuous melting-spraying process in which the particles of the coating material are melted and accelerated to a high velocity through use of combustion or cold flame. As soon as the molten and semi-molten particles hit the surface of the substrate, they rapidly solidify, forming flat particles (“splats”). In this way, the coating is

built up by the subsequent deposition of adjacent layer up to the desired thickness, usually of few dozen of micrometers [158].

The major factors affecting the final properties of a thermal-sprayed coating are: a) the type of thermal and kinetic energies used during the process, b) the cohesive strength between adjacent flat particles, c) the size and the morphology of interstitial pores and d) the presence of cracks and imperfection in the coating layer [158,162].

Dealing with biomedical applications, thermal spraying is the only coating deposition strategy commercially approved by US Food and Drug Administration (FDA) according to the minimum requirements for ASTM F1854-15 [165].

Among the technologies listed in **Table 5** undoubtedly plasma spraying (PS) deserves special attention in the production of BG and glass-ceramic coatings on metal implants. Briefly, a gas flow, typically Ar, H_2, N_2, or He, is injected into a chamber, where a high temperature plasma flame is produced by means of an electric arc. In this way, the temperature of the gas is increased up to 10000-30000 K and the powders (grain size: ~80 μm) are injected into the chamber, rapidly heated and accelerated through a nozzle toward the substrate, reaching a mean velocity of about 100-350 m/s. The hot material hits on the surface of substrate and rapidly cools, forming a coating [158,162]. A schematic representation of a plasma spraying process in depicted in **Figure 19**.

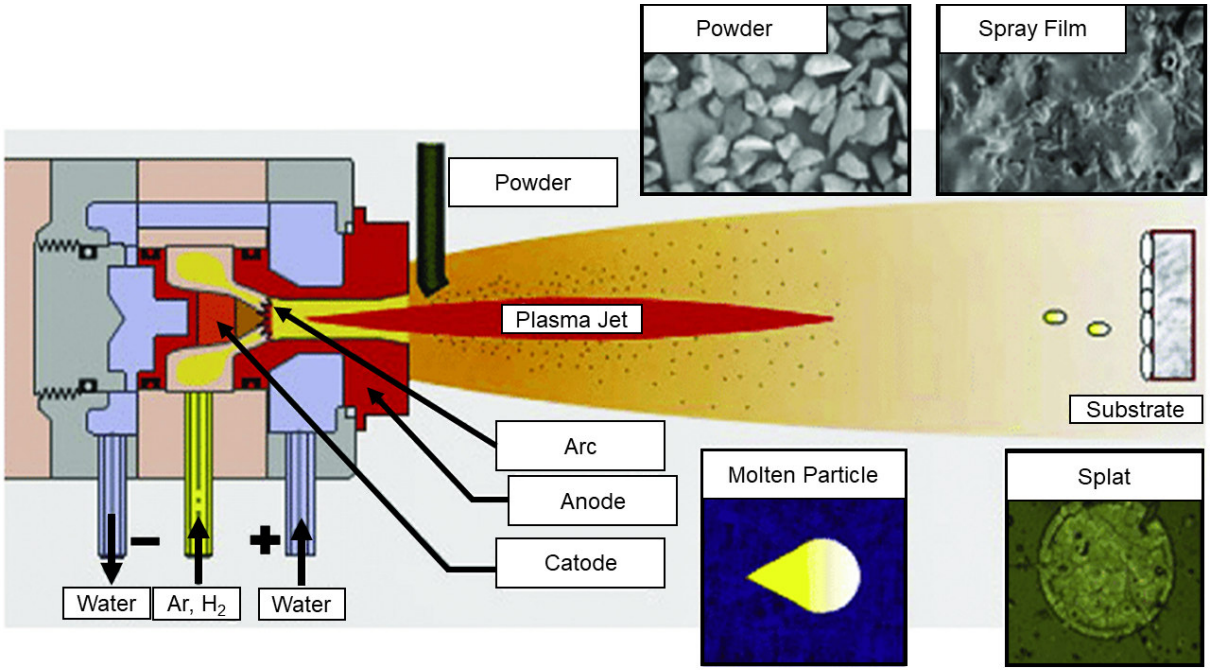

Figure 19- Schematic representation of a plasma spraying process. Adapted from Zhang et al. [166].

By operating a proper control on deposition parameters, this expensive technology offers several advantages, including a high control on the chemical and structural properties of the coating, high deposition speed, minimum size tolerance as well as the possibility to obtain highly homogeneous coatings even on irregularly-shaped substrates, thus guaranteeing high protection against substrate corrosion.

Nevertheless, some studies reported poor durability of the coating over time, associated to low mechanical strength and chemical stability of the layer in contact with body fluids, as well as the risk to induce undesired changes in thermodynamically unstable materials, used for the realization of the coating, such as, for example, glasses [167].

4.2.3.3. Radiofrequency magnetron sputtering (RF-MS) deposition

RF-MS technique is a low-pressure method that allows the deposition of uniform coatings with controlled thickness and superior adhesion strength as compared to the other methods.

Unlike traditional sputtering, radiofrequency (RF) magnetron sputtering deposition uses a radio-frequency power force: a magnet behind the target enhances ionization and directs the sputtered atoms towards the substrate where the coating is deposited atom by atom [158], as depicted in **Figure 20**.

During the process, there is a strong interaction between the substrate and a dense plasma, which determines an intense ion bombardment of the growing coating.

According to the discharge RF excitation frequency, the positive ions are accelerated and impacted on the substrate with high energies. Then, the bombardment of the surface by high energetic oxygen species (O^-) happens under target erosion zone. These ions are generated at the target surface, accelerated in the cathode dark space and move perpendicular from the target towards the substrate surface with a high energy [168].

By this technique, large areas can be covered uniformly and without moving the substrate. Dense uniform and adherent films with similar properties to the bulk material can be easily obtained and the properties of the film can be modified by acting on the deposition parameters, such as gas pressure, substrate bias, and deposition temperature [168].

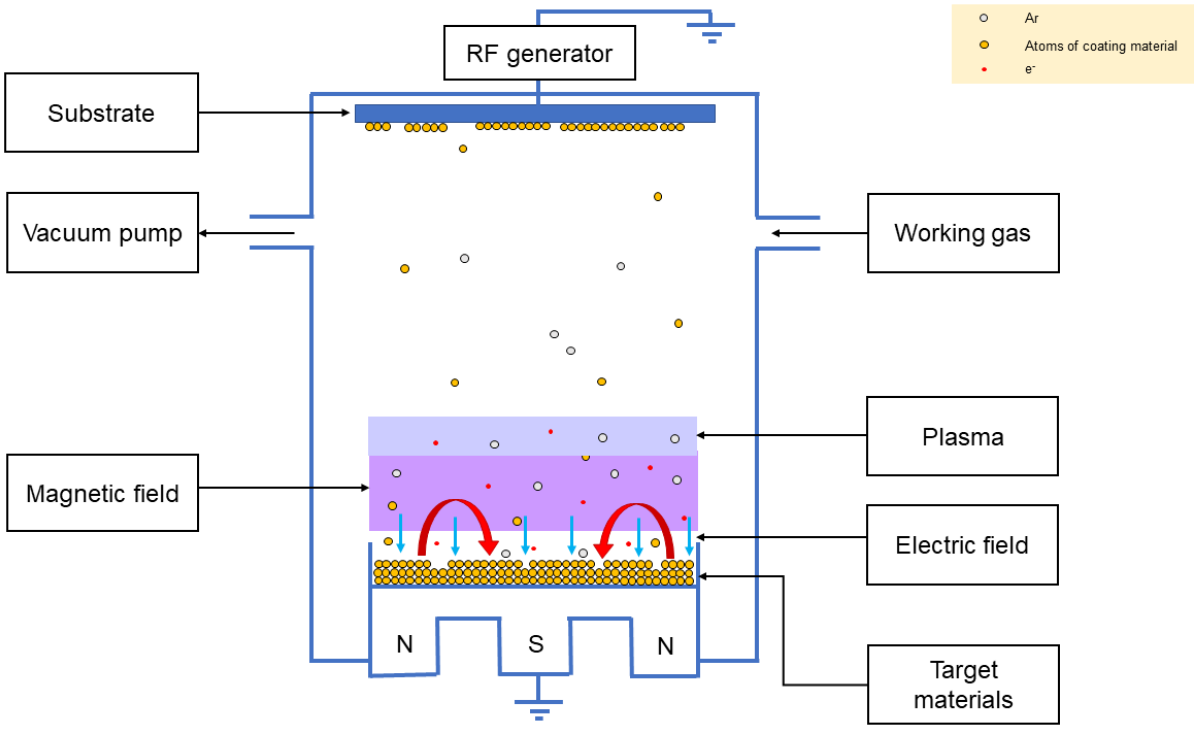

Figure 20- Schematic representation of a RF magnetron sputtering. Adapted from Bosco et al. [169].

4.2.3.4. Pulsed laser deposition (PLD)

Pulsed laser ablation (PLD) is a versatile deposition strategy which can be implemented with a wide variety of coating materials. The schematic diagram of a pulsed laser deposition set up is depicted in **Figure 21**.

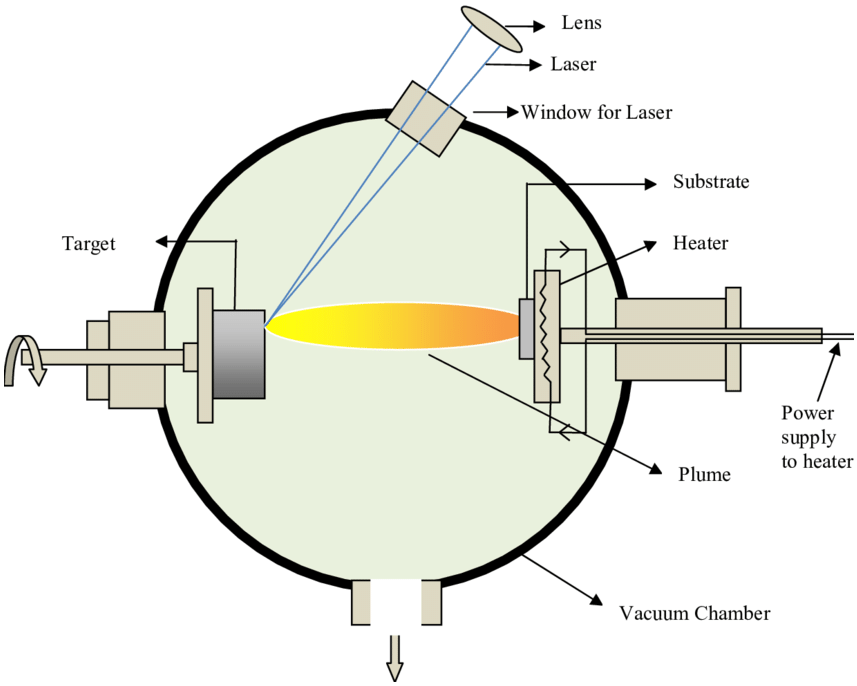

Figure 21- Schematic diagram of a pulsed laser deposition set up. Reproduced from [170] with permission from Trans Tech Publications Ltd.

The process can be divided into 5 subsequent steps: a) Interaction of a laser radiation with a solid target; b) Absorption of energy; c) Localized heating of the surface; d) Material evaporation (ablation plume) with consequent plume-laser interactions and particles collisions within the plume; e) Plume impact on the substrate surface.

By properly combining atmospheric pressure, wavelength, energy density and target-substrate distance, PLD technology allows an easy control on the surface properties (coating thickness, morphology, roughness, chemical composition and crystallinity), while the temperature of the substrate is the main factor affecting the adhesion strength between the coating material and the substrate.

Compared to traditional enameling and plasma spraying technology, PLD shows several advantages, including the production of films from high-temperature materials, stoichiometric transfer of the target composition, lack of contaminations and fine control on

the film properties. However, compared to RF-MS, coatings deposited by PLD technique are characterized by lower density [158,162].

4.2.3.5. Sol-gel coatings

As already seen in section 4.2.1, sol-gel method allows the formation of solid materials through the gelation process of a sol, which can be used to produce a wide variety of products with different shapes and morphologies.

Sol-gel coatings can be easily produced by 3 different strategies, as represented in **Figure 22**:

1. Dip-coating process, for large samples with a complex shape
2. Spin coating deposition, for small and flat samples.
3. Electrodeposition, allowing a good control on the thickness and morphology of the sol gel film by acting on potential, time, concentration of the sol and surfactants.

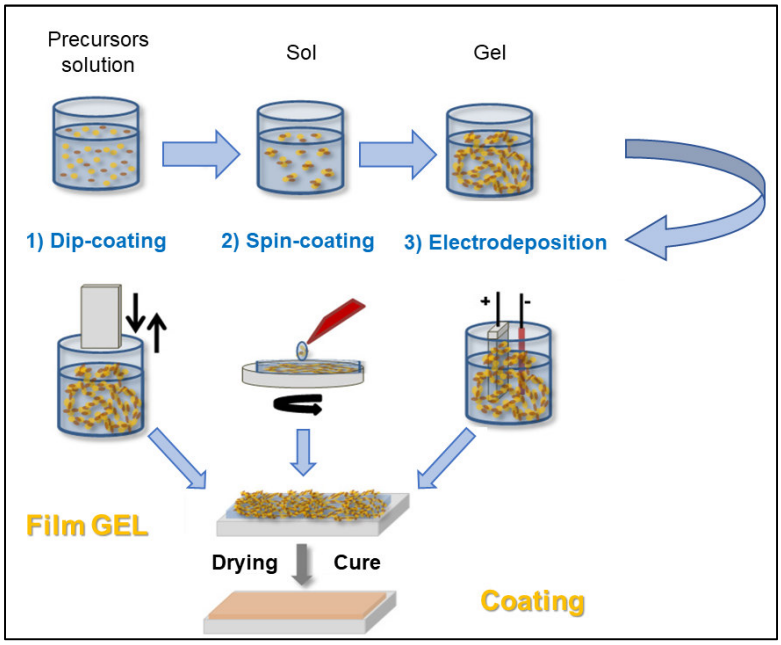

Figure 22- Processing route to obtain sol-gel coatings. Adapted from Figueira et al. [171].

Sol-gel technology for coatings deposition offers several advantages that directly derive from the synthesis process: sol-gel coatings are, in fact, characterized by high purity and chemical homogeneity, as well as superior textural properties which make them particularly suitable for being functionalized with therapeutically active particles and organic molecules, while favoring cellular interaction with the implant [115].

4.2.3.6. Electrophoretic deposition

Electrophoretic deposition (EPD) is based on the electrophoresis mechanism, which induces the movement of charged particles suspended into a solution under the action of an electric field, leading to the deposition of such particles on the substrate [162].

In a typical EPD process, an electric field is applied between two electrodes. The charged particles suspended in a suitable liquid media move towards the electrode with opposite charge (electrophoresis), accumulate on the surface of the deposition electrode and create a compact and homogeneous coating (**Figure 23**).

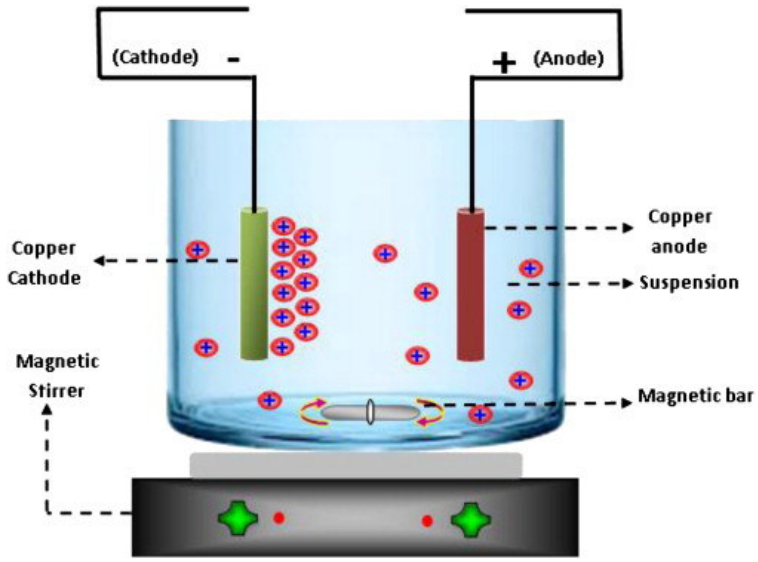

Figure 23- Schematic representation of an experimental set up for electrophoretic deposition. Reproduced from [172] with permission from Elsevier.

The EPD process is a very versatile technology which allows the deposition of both ceramic and glass materials on the surface of a metal substrates of any shape in a very short time and by means of a simple experimental set-up [173].

Generally, BGs are dispersed into organic solvents or water to avoid the problem of electrolysis and gas evolution, but distilled water is usually preferred to minimize the environmental impact of organic solvents.

The thickness and the morphological features of the coating, as well as the deposition time, the pH and the stability of the suspension are highly affected by the applied voltage and the initial concentration of the suspension.

Despite all these advantages, realizing coatings from more than one material still remains an interesting challenge, which can potentially open up new possibilities in several medcial and non-medical fields [162].

4.2.4. Composites

As well as bone tissue, tooth is a natural composite material characterized by a complex structure in which different levels of organization can be distinguished and different phases can be identified [174].

This situation is quite common in biological system and is the reason why, since ‘80s, a huge variety of bioactive composites – inspired by Nature – have been investigated as substitute materials for clinical applications in tissue engineering and regenerative medicine [175].

A material may be defined as a “composite” when is constituted by two or more distinct phases (metallic, ceramic, or polymeric) characterized by different physical or chemical properties, which are constructed into an architecture at micro-, meso- or macro-scale levels [176].

The aim of advanced composites is to provide improved performance compared to their constituent materials through the combination of the latest developments of different individual materials, thanks to compositing, interface or dimensional effects at different levels [176].

Engineered composite materials can be classified according to the matrix materials (metal-, ceramic- and polymer-matrix composites) or the reinforcement dimensions or shapes (particulates, short fibers or continuous fibers) [177–183].

Biomedical composites can be classified by the matrix materials into:

- Polymer-matrix composites, e.g., carbon/PEEK, HA/HDPE.
- Metal-matrix composites, e.g., HA/Ti, HA/Ti-6Al-4V.
- Ceramic-matrix composites, e.g., stainless steel/HA, glass/HA [175]. In biomedical applications, although excellent mechanical performances are desirable and often the target of improvement, the key feature to fulfil is biocompatibility. Even if the coexistence of two or more types of materials may enhance the possibility of causing an adverse reaction into the host tissue, the design of bioactive, tough materials must overcome the brittleness of bulk bioactive glass-ceramics ensuring a bioactive response in vivo [175]. For this reason, another classification of biomedical composite materials may be identified based on the bioactivity of composites. Of course, this classification method can be applied only if at least one of the constituent materials of the composite is bioactive (in some cases, two or all constituent materials are bioactive).

Three types of biomedical composites have been individuated, using bioactivity as basis for classification:

- Bioinert composites, e.g., carbon /carbon, carbon/PEEK.

- Bioactive composites, e.g., stainless steel/Bioglass®, HA/HDPE, HA/Ti-6 Al-4V.
- Bioresorbable composites, e.g., TCP/PLA, TCP/PHB [175].

In order to realize bioactive composites for tissue repair applications, the bioactive constituent should exceed a certain volume fraction, below which the bioactive behavior is not exhibited by the composite. It has been demonstrated that the critical volume percentage of bioactive glass-ceramic phase is around 20%, above which bioactivity of composite material is assured [184].

Correct design of a composite is achieved by a deep understanding of the relationships among properties, structure and processing of the constituent material.

Properties of biomedical composites are directly influenced by different factors, such as:

1) Reinforcement shape, size and distribution;
2) Reinforcement properties, and volume percentage;
3) Bioactivity of the reinforcement (or the matrix);
4) Matrix properties (molecular weight, grain size, etc.);
5) Distribution of the reinforcement in the matrix;
6) Reinforcement- matrix interfacial state [175].

Properties of constituents are major influencing factors, but also composite architecture and reinforcement/matrix bonding condition play an important role. The mechanical and biological performances of bioactive composite materials can be finely tailored by controlling these factors.

Reinforcement shape, size and distribution directly impact on mechanical properties of composites. Considering bioactive composites, reinforcing particles may have different shapes, from irregular forms, typical of commercially available HA particles, to plate-like or acicular shapes.

Interphase between reinforcement and matrix in another important factor to be considered in determining the bioactive composite features. Mechanical properties can be finely tuned through the control of the interfacial state. In fact, a strong interfacial bond can assure the effective load transfer from the matrix to the reinforcement, while a weak interfacial bond may lead to enhancing facture toughness [185]. In most bioactive composites, the interface bond is totally dependent on mechanical interlock by phases while chemical bonding between constituents usually does not exist [186]. For this reason, when the stress concentration exceeds the low interfacial strength provided by locking mechanisms, debonding phenomenon between different phases takes place.

Conventional processing methods for engineering composite materials can be used to realize composites for biomedical applications. However, biomedical composites need extreme attention during their production to avoid contamination and to precisely achieve clinical demands [175].

The first step needed before effectively producing bioactive composites is the characterization of all raw materials involved in the final composite both for assessing the chemical and physical properties of materials and for using these data as quality control to medical devices [187]. These characterizations are carried out by using various techniques, such as Fourier transform infrared spectroscopy, X-ray diffraction, X-ray fluorescence, BET specific surface, area analysis, particle size analysis, scanning electron microscopy, differential thermal calorimetry, etc.

BG/polymer composites are a relatively new class of bioactive materials that combine the peculiar features of BGs, such as bioactivity, with polymer properties, as flexibility, thus overcoming some BG limits such as low fracture toughness [39].

Regarding polymer/ceramic composite, there are different production techniques to realize non-porous, bioactive composites, as showed in **Table 6**.

Table 6. Production techniques for non-porous bioactive ceramic/polymer composites [175].

	Route I: Physico-chemical methods	Route II: Thermo-mechanical methods
Method 1	Precipitating mineral crystals in situ in the polymer matrix	Impregnating a porous bioceramic matrix with a polymer
Method 2	Dispersing bioceramic particles in the polymer solution with subsequent consolidation	Incorporating bioceramic particles into the polymer matrix using conventional plastics processing technologies

Figure 24 shows a typical flowchart describing the production process of bioceramic particles dispersion in polymer solution and their consolidation. In this method, a solvent must be selected to achieve the desired distribution of particles. The ceramic powder and polymer granules are dissolved forming the solution. The gelling step occurs while solvent is progressively eliminated. It is important that there are no solvent residues in final composite products.

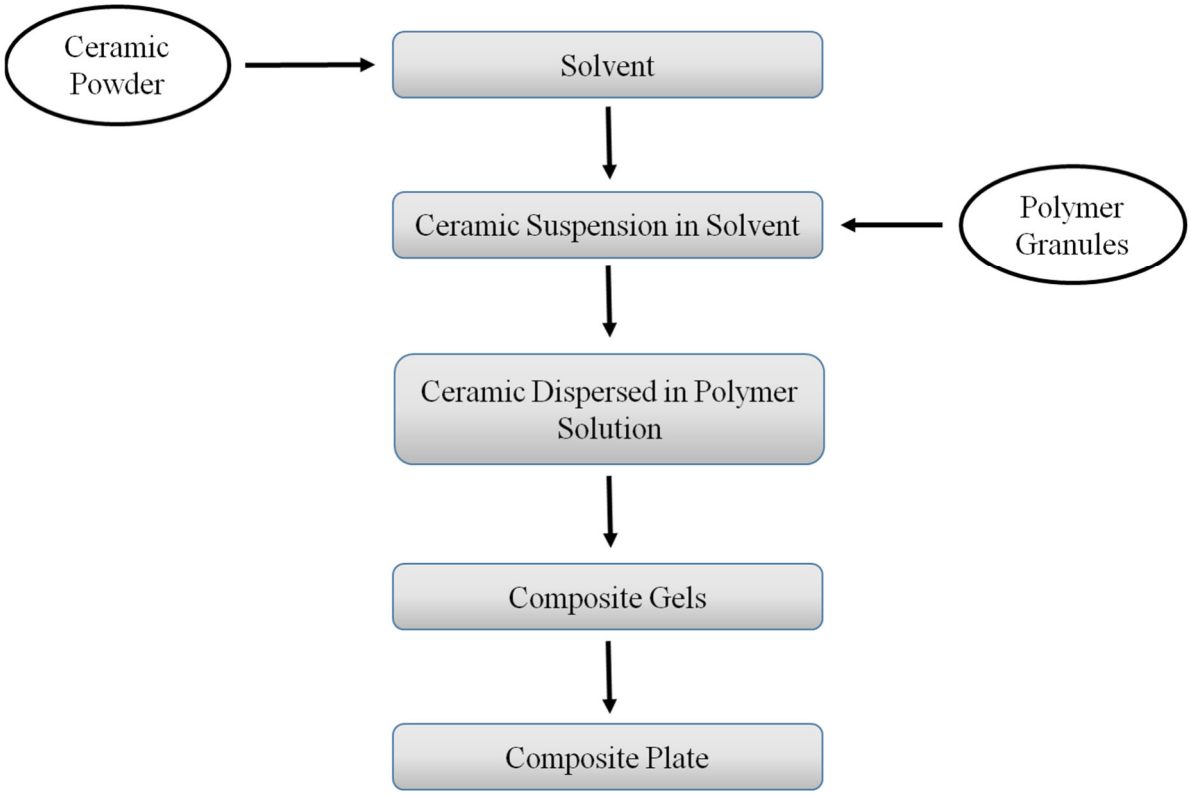

Figure 24- Manufacturing process of bioactive composites by polymer solution-casting technique [175].

Considering physico-chemical methods, the first method had been used in '90s [188] for the precipitation of calcium phosphate into collagen matrix, while poorly crystalized HA particles were dispersed in chitin solution and then consolidated [189]. Both experiments had shown excellent bioactive performances in vitro. Collagen-based composites containing bone-like apatite were produced by a combination of these two methods [190].

Using a thermo-mechanical method, biodegradable composites are produced by impregnating a porous bioceramic matrix with a polymer [191]. However, the incorporation of bioceramic particles into a polymer matrix through conventional polymer processing technologies (**Figure 25**) still represents the most common method to realize bioactive composites [184,192–198].

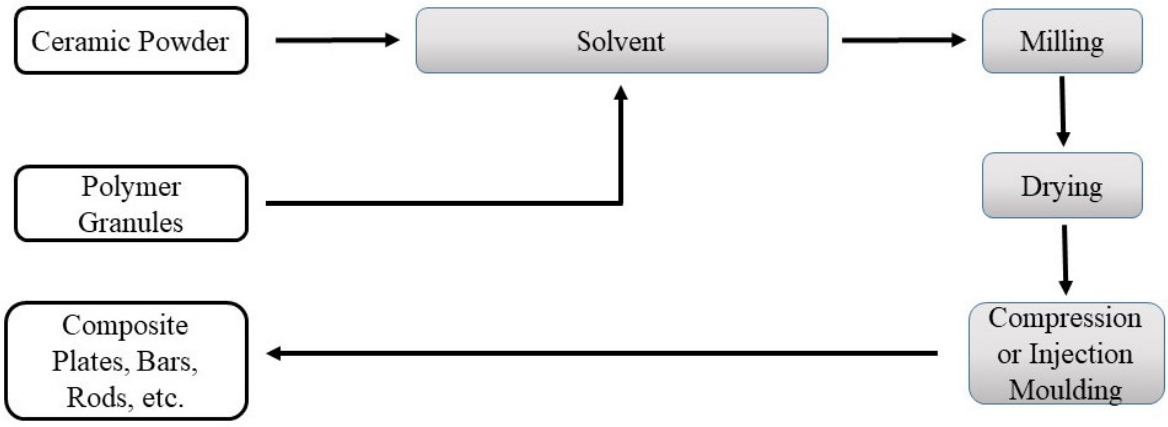

Figure 25- Manufacturing of bioactive composites using polymer processing technologies [175].

As shown in **Figure 25**, this manufacturing process generally consists of compounding, milling and compression or injection molding. The first step of compounding produces a homogenous distribution of bioceramic particles in the matrix, playing a key role in the composite final features. Afterward, the compound is milled to obtain small pieces which can be used for compression or injection molding. This last step is characterized by two parameters, i.e., molding temperature and pressure, which are dependent on molding behavior and viscosity of composites. Molding temperature should be carefully selected for composites having heat-sensitive polymers (e.g., PHB) to avoid thermal degradation.

The quality of the manufacturing process can be determined by scanning electron microscopy and image analysis techniques which provide particle dispersion and distribution in the composite material [199]. More recently, the development of mesoporous bioactive glasses (MBG) has allowed the realization of composite materials characterized by superior bone regenerative performances as compared to traditional melt-derived glasses [200].

MBG particles and a polymeric or inorganic matrix can be processed by direct mixing or surface coating techniques to realize composite materials characterized by appealing features for medical application, as the production of hierarchical 3D porous scaffolds [200]. The addition of silica-based mesoporous particles confers bioactivity to the otherwise inert polymeric matrix. Different research groups have recently developed MBG composite systems by different processing methods, as summarized in **Table 7**.

Finally, looking at the existing literature, it can be observed that relatively few examples of bioactive glass-ceramic/polymer composites can be found compared to glass/polymer composites; on the other hand, the same methods/approaches used to produce glass/polymer composites can be potentially extended to glass-ceramic/polymer composites.

Table 7. Hierarchical composites containing a mesoporous glass phase [200]. (MBG: mesoporous bioactive glasses; PCL: poly(caprolactone); PLGA: poly(lactic-co-glycolic acid); PLLA: poly(L-lactic acid).

Mesoporous Phase	**Matrix**	**Processing**	**Effect**	**Refs.**
MBG	Collagen	Mixing	Improved bioactivity in vitro and mechanical properties	[201]
Sol-gel glass	PLLA	Solid- liquid phase separation + solvent extraction	Improved bioactivity in vitro	[202]
MBG	PLGA	Mixing	Improved bioactivity in vitro, drug release	[203,204]
MBG	Polyamide	Solvent casting/ particulate leaching	Improved bioactivity in vitro and bone regeneration in vitro	[205]
MBG	PCL	Solvent casting/ particulate leaching Robocasting + salt leaching	Improved bioactivity in vitro, drug release Improved bioactivity in vitro and mechanical properties, pliability	[206] [207]
MBG	Alginate	Mixing 3D plotting	Improved bioactivity in vitro, drug release Improved bioactivity in vitro, drug release	[208,209]
MBG	Silk	Freeze- drying	Improved bioactivity in	[210,211]

	fibroin		vitro and mechanical properties	
MBG	Calcium phosphate	Mixing+ freeze drying	Adequate mechanical properties and bone regeneration in vivo	[212]
MBG	Chitosan	Freeze-drying	Hemostasis to promote wound healing	[213]

5. Analytical tools to study DGCs

The study of dental GCs has relied heavily on the development of new and improved experimental techniques. The non-crystalline nature of the glasses has always presented a particular challenge to researchers, and insights had to wait until the technology can provide a clearer picture of its structure and behavior. Although our understanding of the application of these materials is already established, the essential role of state-of-the-art experimental techniques remains true.

This section provides a snapshot of the state of several techniques to study DGCs. Several techniques, briefly introduced here, count on a plethora of advanced technology measurements that were nonexistent back then. Some methods, neutron or small-angle X-ray scattering, represent completely new advances. This section has been designed to serve a pictural purpose, presenting some examples for the students and researchers who want to explore the capabilities of each technique and study DGCs. To enhance this purpose, the section includes case studies, and the discussion has been kept, where possible, short. Other common techniques such as optical spectroscopy, electron microscopies, X-ray diffraction, Raman, infrared and optical spectroscopies are also provided.

5.1. Optical spectroscopy

In order to provide excellent aesthetic restoration of dental glass-ceramics, researchers should provide information about fundamental principles and optical properties of restorative materials. The major aim in aesthetic restorative is to fabricate restorations that match the optical characteristics of the natural tooth. Different factors have been investigated for the impact of process parameters on the color of restorations, such as firing, glazing, the crystal/glass ratio, and surface texture [214–217]. In dental materials, one of the most significant advantages of glass-ceramics is the semi-translucency that improves the aesthetics [218,219]. They are highly recommended, compared to metal-ceramic restoratives, since these prostheses facilitate light to pass through. Fluorescence and opalescence are the optical properties to measure the materials' appearance characteristics. It is vital to mention that the natural tooth emits blue fluorescence under ultraviolet (UV) light, which makes the tooth whiter and brighter under daylight [220,221]. The opalescence or opal effect utilizes light scattering in translucent materials that make an orange effect in transmission and a blue effect in reflected light due to the scattering of short-wavelength light [222].

Recently, glass-ceramics are widely used as dental materials, and this is due to the promising optical properties, ideal water resistivity, promising culpability, and no toxicity. As a case in point, due to the small size of the crystals (~1-5 μm), these materials, which are named translucent materials, demonstrate reduced visible light scattering or absorption. Different types of research have been done on the synthesized glass-ceramics via two-step controlled nucleation and crystallization, which are mainly leading to the precipitation of small crystals in a glassy matrix [223–226]. Additionally, the use of luting cement is significantly important in providing optimal aesthetics when using glass-ceramics. For example, Chang et al. demonstrated that the zirconia crown (Katana®) could have a significant impact on the color difference of composite cement in the cervical area. In

contrast, composite cement with the glass-ceramic made of a lithium disilicate crown (Empress®) slightly affects a perceptible color difference in both the cervical and body area [218].

Controlled crystal nucleation and growth discussed in Section 3 also involve a functional relationship between heat treatment and the properties of the glass-ceramic, such as the linear thermal expansion coefficient and optical properties. By using fundamental theories of optical spectroscopy in glass-ceramic science, it is possible to establish the best transparency/translucency of glass-ceramics which could be achieved when the crystallite size is compared to the wavelength of visible light [16,45]. It is also noteworthy to mention that thermocycling, surface modification, aging, ultrasonic scaling, staining techniques, and repeated firings have an influence on the surface properties, color, and translucency of computer-aided design/computer-aided manufacturing CAD/CAM lithium disilicate [215,227–232].

5.2. X-ray diffraction

One method to characterize the formation and structure refinements of the crystalline phases in glasses is X-ray diffraction analysis. As a case in point, Kleebuscha *et al*. [233] investigated the formation of phases during the crystallization of Li_2O-Al_2O_3-SiO_2 glass containing ZrO_2 as a nucleating agent. This study shows different steps in isothermal/isochronal phase evolution in glass-ceramics, from the pre-nucleation stage (ZrO_2 formation) to the crystallization of β-quartz. Initially, the impact of different crystallization temperatures was measured by XRD shown in

Figure 26a. These patterns showed that the formation of different phases was significantly temperature-dependent during crystallization at 24 h. The peaks at 2θ = 30.1°,

34°, and 52° demonstrated either tetragonal or cubic phase of the ZrO_2 at 720 °C. At the higher temperature (730 °C), in addition to the former peaks, the peak at 2θ=25.6°, which corresponds to the (101), indicating the high-temperature phase of quartz (β-quartz). At the higher temperature, different structures can be observed due to the incorporation of the Al^{3+} at Si^{4+} and Li^{+} sites at interstices for charge compensation. Besides, at 740 °C, more quartz concentration and less intense glass hump were detected. Finally, no changes were observed for thermal treatment at a higher temperature than 740 °C for 24 h [233]. This research also investigated the time-dependent crystallization at the fixed temperature (750 °C) in order to provide a higher crystallization degree (

Figure 26b). After the 1 hour of thermal treatment of the as-cast glass, the amorphous structure was obtained, while after the three to eight-hour thermal treatment, broadened peaks (2θ≈30°), which is contributed to ZrO_2 were detected. After crystallization for 12 h, a peak at 2θ=25.8° appeared with the low-intensity, corresponded to the high quartz solid solution. As the time of thermal treatment increase to 18 h and 24 h, the intensified, sharp peaks were appeared [233].

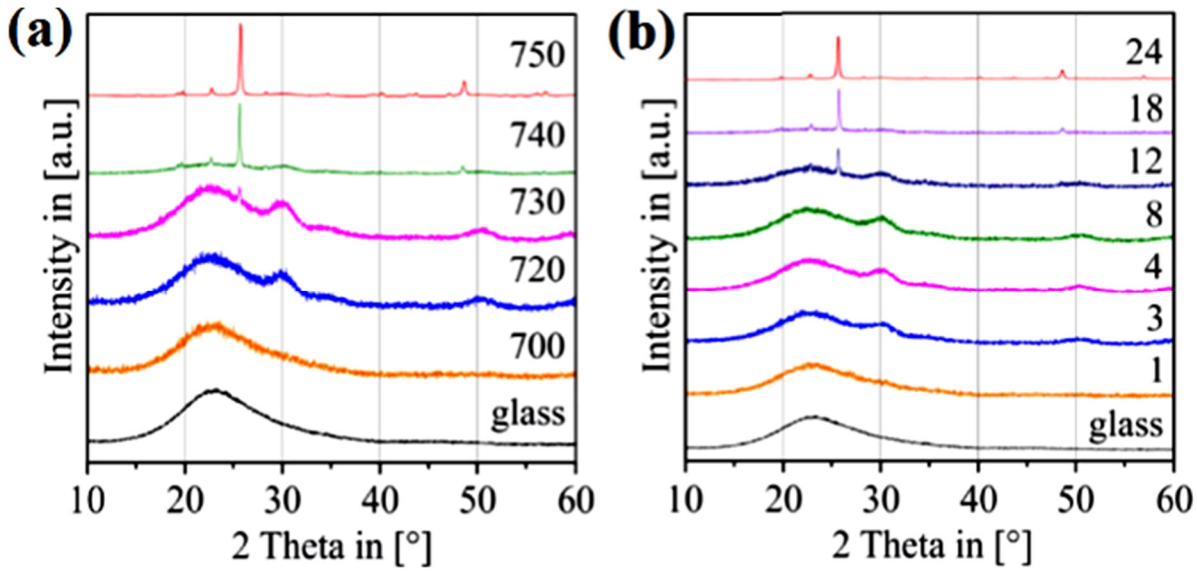

Figure 26- (a) XRD patterns of powdered samples of glasses thermally treated for 24 h at various temperatures, (b) XRD patterns recorded from Li_2O-Al_2O_3-SiO_2 glass heat-treated at 740 °C for 1–24 h and subsequently powdered [233].

Besides time and temperature, other parameters also affect the crystallization of materials [234,235]. In 1995, Alizade and Marghussian showed that the nucleating agents like Fe_2O_3 and WO_3 mixture delayed the cristobalite formation in the SiO_2-CaO-MgO-Na_2O glass-ceramics, while V_2O_5 and MoO_3 accelerate the formation of this phase [236]. In another research, the XRD pattern of the CaO-MgO-SiO_2 glass-ceramics system indicated that the diopside phase ($MgCa(SiO_3)_2$) was more thermodynamically favorable than others [237]. This research also demonstrated that apart from P_2O_5 and ZrO_2, other nucleation agents like TiO_2 reduce the crystallization activation energy, and regarding the higher crystalline seeds, TiO_2 provided smaller crystals. It is crucial to add TiO_2 and ZrO_2 as nucleation agents to the parent glasses, which lead to the formation of $ZrTiO_4$ nuclei during heating for enhanced crystallization of a β-quartz phase and transformation to β-spodumene at a higher temperature. Effects of different elements' contents on the crystallization of glass-ceramics have been widely investigated by researchers using an XRD to reveal the phase evolution [238–240]. Denry and Holloway investigated the niobium and sodium contents ratio on the crystallization behavior of the SiO_2-MgO-CaO-Na_2O-K_2O-F glass-ceramic, one of the promising mica-based DGCs [241,242]. The results showed that after heat treatment for 1 h, two main crystalline phases, including mica taeniolite ($KLiMg_2Si_4O_{10}F_2$) and diopside, were formed. For the highest Na content, fluorrichterite ($K_xNa_{(1-x)}CaMg_5Si_8O_{22}F_2$) and diopside were the main phases. Effect of different additional components like Al_2O_3, Cr_2O_3, iron oxide, etc. on the nucleation and crystallization of different glasses have drawn enormous worldwide attention [243–246]. For example, by sintering CaO–MgO–SiO_2–P_2O_5 system, β-$CaSiO_3$–$Ca_2MgSi_2O_7$ were prepared. The higher MgO concentration leads to a higher glass crystallization temperature, and the crystallization of glass-ceramics changed from bulk to

surface crystallization. Besides, the more MgO content resulted in the gradual decline in the degradability and delay in apatite formation. Researchers also fabricated the cordierite-based glass-ceramic glaze by using B_2O_3 as a flux, and TiO_2, as a nucleus agent to form cordierite glass in the CaO–MgO–Al_2O_3–SiO_2 system and is widely characterized by XRD diffraction pattern [247].

5.3. Differential scanning calorimetry

The result of the thermal analysis, such as thermogravimetry (TGA), differential thermal analysis (DTA), dynamic mechanical analysis (DMA), and calorimetry like differential scanning calorimetry (DSC), depend on some of the intrinsic (e.g., mass, shape, internal structure) and the environmental parameters (e.g., atmosphere, heating rate, pressure) [248].

TGA is a method to calculate the mass loss of a specimen by temperature or time increase and can be used in both dynamic modes (constant heating rate) and under isothermal conditions (constant temperature) with the inert, reactive or oxidizing atmosphere. In order to accurately investigate the rate of the mass change, the first derivation of TGA (DTA) is carried out. Simultaneous TG-DTA and TG-DSC give us valuable information about the specimen behavior. The most probable mass change in the TGA curve is water or volatile evaporation, thermal decomposition in an inert atmosphere, oxidative decomposition in oxygen or air, gas desorption or absorption, and oxidization [249].

Apart from TGA, DSC, developed in 1966, is widely used for ceramics and glasses characterization [250]. DSC analysis depicts the energy differences vs. temperature change and also measures heat flow signal, which corresponds to the energy flow inside or outside the specimen plotted as a function of temperature or time. Some features like melting temperature (T_m), the crystallization temperature (T_c), the glass transition temperature (T_g),

enthalpy changes etc. can be measured by the DSC techniques. As mentioned above, nucleation is mainly comprising of nuclei formation, which is followed by their growth into well-defined crystals. For glass formers, homogeneous nucleation occurs below the temperature of maximum crystal growth rates (T_G); however, heterogeneous nucleation rate happens close and even overlap with those of crystal growth [251]. DSC technique can specially measure an exothermic process of the glass crystallization, whose peak generally appears after the glass transition, T_g, as depicted in **Figure 27**. For stoichiometric glass compositions, the onset crystallization temperature is called T_x, and the crystallization temperature (T_c) is attributed to the peak temperature in a DSC trace. At the higher temperature, an endothermic peak is assigned to the melting for a pure system or liquidus temperature (T_L) for a multicomponent system, as in the case of DGCs. More than one crystallization and melting temperature are related to the off-stoichiometric compositions [252].

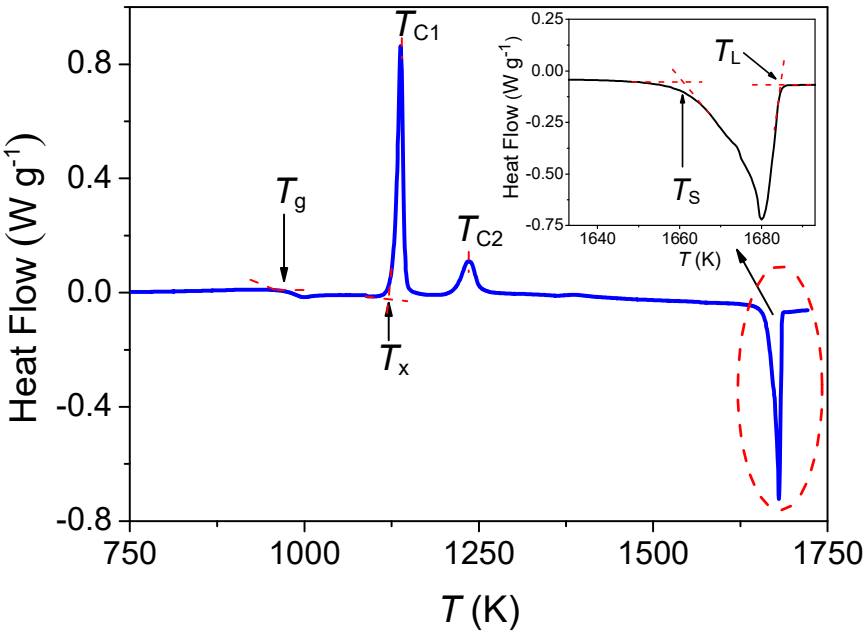

Figure 27-Typical DSC upscan trace for barium disilicate ($BaO{\cdot}2SiO_2$) glass showing the glass transition temperature (T_g), the crystallization onset (T_x), the crystallization peaks (T_{c1}, T_{c2}), and the solidus (T_S) and the liquidus temperatures (T_L) [253]

In order to have control over the crystallization or prevent devitrification during cooling, enough knowledge about the thermodynamics and kinetics of crystal nucleation and growth like nucleation time, crystal growth rate, glass stability, and forming ability are vitally necessary [8,83,254,255]. T_L is also very important since it is the highest temperature of thermodynamic equilibrium between the solid and liquid phases. To be more specific, above which crystals are unstable and dissolves in the liquid. Accurately manage the temperatures (T_L) is challenging and time-consuming, especially for glass compositions that are difficult to crystallize.

In order to prepare the best composition for dental applications, some properties like the coefficient of thermal expansion (CTE), glass transition temperature, melting point, etc. should be precisely determined. As a result, determining T_g, T_c, and CTE is the critical factor for the selection of materials. It is proven that dental glass-ceramics have a high viscosity above T_g and solidify after cooling. The change from these forms provides shrinkage and stresses at the interface, depending on the heating and cooling rates. Consequently, adjusting the cooling rate is significantly important to prevent internal stresses to make a promising interface between the ceramics veneer and the substructure of dental prosthetic restoration [248].

The simultaneous DTA/TG analysis results are crucial in the successful development of sol-gel-derived glass and glass-ceramics. Montazerian et al. [256] have shown (**Figure 28**) that the DTA/TG curve for a gel-derived $68SiO_2$–$27CaO$–$5P_2O_5$ (mol%) should be thoroughly investigated for the successful development of this glass which is supposed to have application in bone tissue regeneration and periodontal therapy. These gels experience three different mass loss steps and become stable at approximately 700 °C. The first mass loss step happens at ~25-160 °C and is related to the endothermic process of desorption of physically adsorbed water and alcohol used in the sol-gel process. The second mass loss step

occurs near 250 °C and is associated with water volatilization, a known endothermic chemical desorption process. The third mass loss stage, between 375-702 °C, was more pronounced and important. This stage is ascribed to the evolution of the resulting sub-products from partial condensation of the precursors, mostly eliminating the nitrate. The exothermic peaks near 935 °C and 1020 °C are shown the onset of crystallization. The gel-glass is obtained if the sample is sufficiently heat-treated at ~700 °C for stabilization, above which the chance of crystallization increases leading to glass-ceramic formation [256].

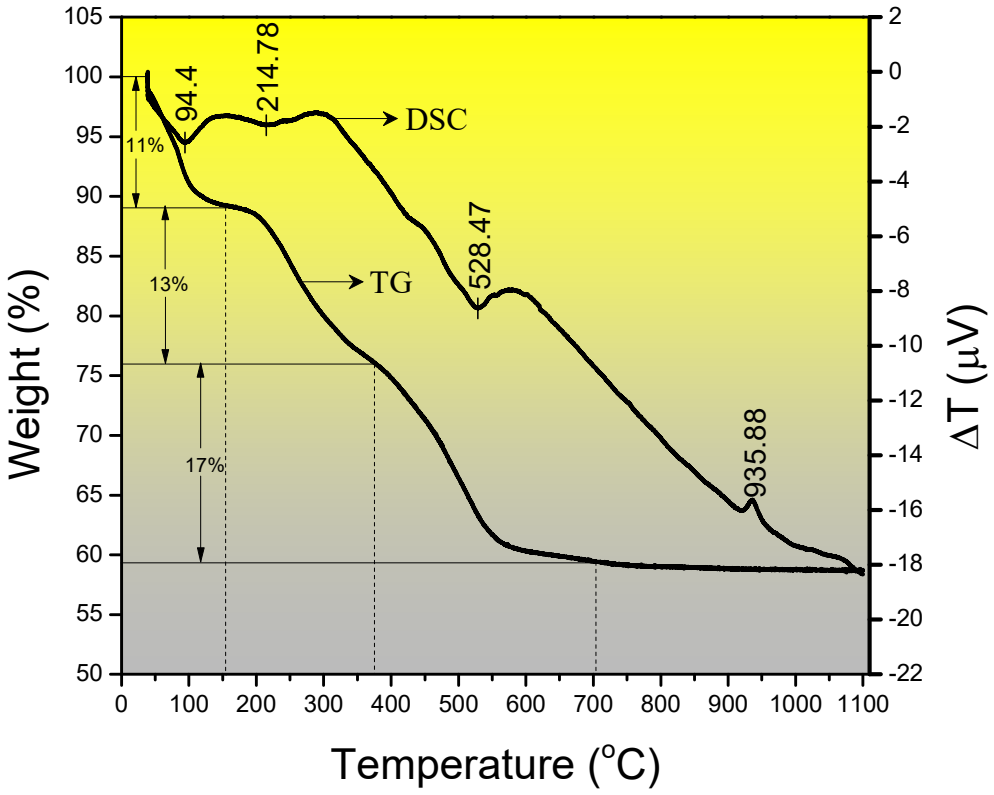

Figure 28-DTA/TG curve for a gel-derived $68SiO_2$–$27CaO$–$5P_2O_5$ (mol%) glass. Reproduced from [256] with permission from Elsevier.

5.4. Scanning electron microscopy

Microstructure plays a vital role in determining the glass-ceramics' properties. One method to analyze the microstructure is the scanning electron microscopy (SEM) technique

which is a useful method in many disciplines in nanometer and micrometer organic and inorganic materials with high magnification of about 300,000× and even 1,000,000× (in some modern models) in producing images. In this technique, the electron beam is focused on the sample and scanned in a raster. In some cases, SEM has been worked with Energy Dispersive X-ray Spectroscopy (EDS) for presenting qualitative and semi-quantitative results and provide fundamental information about the composition of the specimen [257,258].

SEM can investigate the nucleation and crystallization of glass-ceramics to obtain suitable morphology and distribution of crystals. Pioneering researchers at Corning, Linda Pinckney and George Beall showed in Ref. [259] and **Figure 29a** that nucleation, crystallization, and growth of spherulitic fluormica crystals begin at 550 ^{o}C, comprising the single-crystal nature of the mica crystals. At the higher temperature, the spherulitic fluormica crystals have grown and then recrystallized to lens-shaped books, and mica cleavage is pronounced with planar growth. Subsequently, rather than the usual tabular form of mica, the morphology of the subspherical and the enclosed glass change to the lenticular morphology (**Figure 29b, c**). In 900 ^{o}C, completed recrystallization of interlocking diopside, K-richterite and mica are occurred, with the diopside phase obtained by the top crystallization temperature (**Figure 29d, e**) [259].

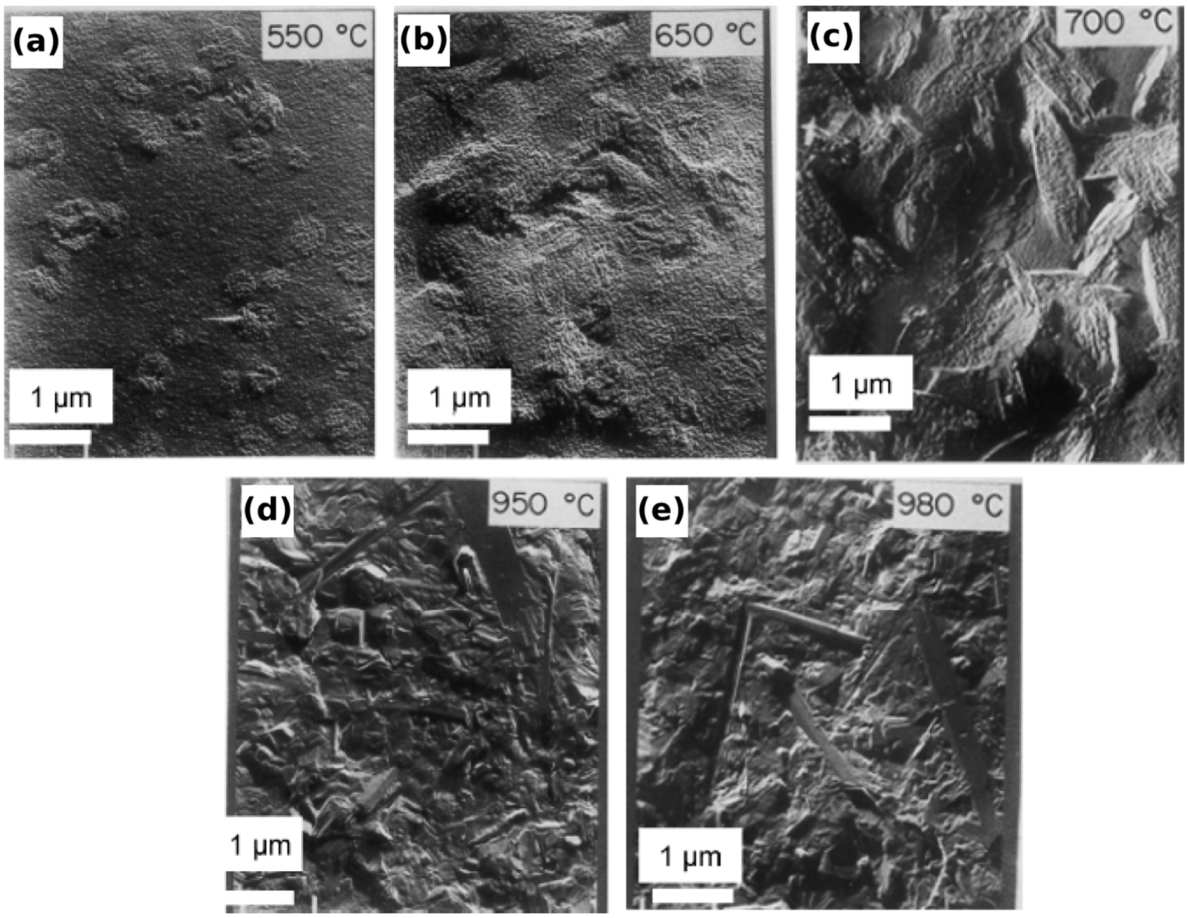

Figure 29- (a)-(e) Crystallization sequence and microstructural evolution in F-K-richterite glass-ceramics. Scale bars = 1 µm. Reproduced from [259] with permission from Wiley.

Abo-Mosallam and Mahdy [260] investigated the crystallization of glasses with different proportions of fluorocanasite and lithium disilicate. These materials were the main crystalline phases prepared by the controlled crystallization of the prepared glasses. They demonstrated that by substituting lithium disilicate with fluorocanasite for glasses, the crystallization tendency got improved, which corresponds to the reduction of the levels of crosslinking in the glasses. As a result, the effect of changing the glass composition on the properties, morphology, and microstructure of glass-ceramic materials for potential use in dental applications was presented (**Figure 30**). After thermal treatment at T_g and T_p for 2 h, the microstructure of the prepared glass-ceramic sample with 100 wt.% fluorocanasite (GC1), comprising the dense and highly crystalline interlocked blade-like fluorocanasite phase,

which is homogeneously distributed in the glassy matrix (**Figure 30a**) [260]. Additionally, the SEM micrograph of the fluorocanasite (wt.%) to lithium disilicate (wt.%) equal to 1 (GC3) depicted the fine fibrous-like growths of lithium disilicate and fluorocanasite phases in a nearly holocrystalline material and amorphous matrix (**Figure 30b**). Finally, in a sample with 100 wt.% of lithium disilicate (GC5), nearly holocrystalline needle-like crystals of lithium disilicate in a glassy matrix were detected by SEM (**Figure 30c**) [260].

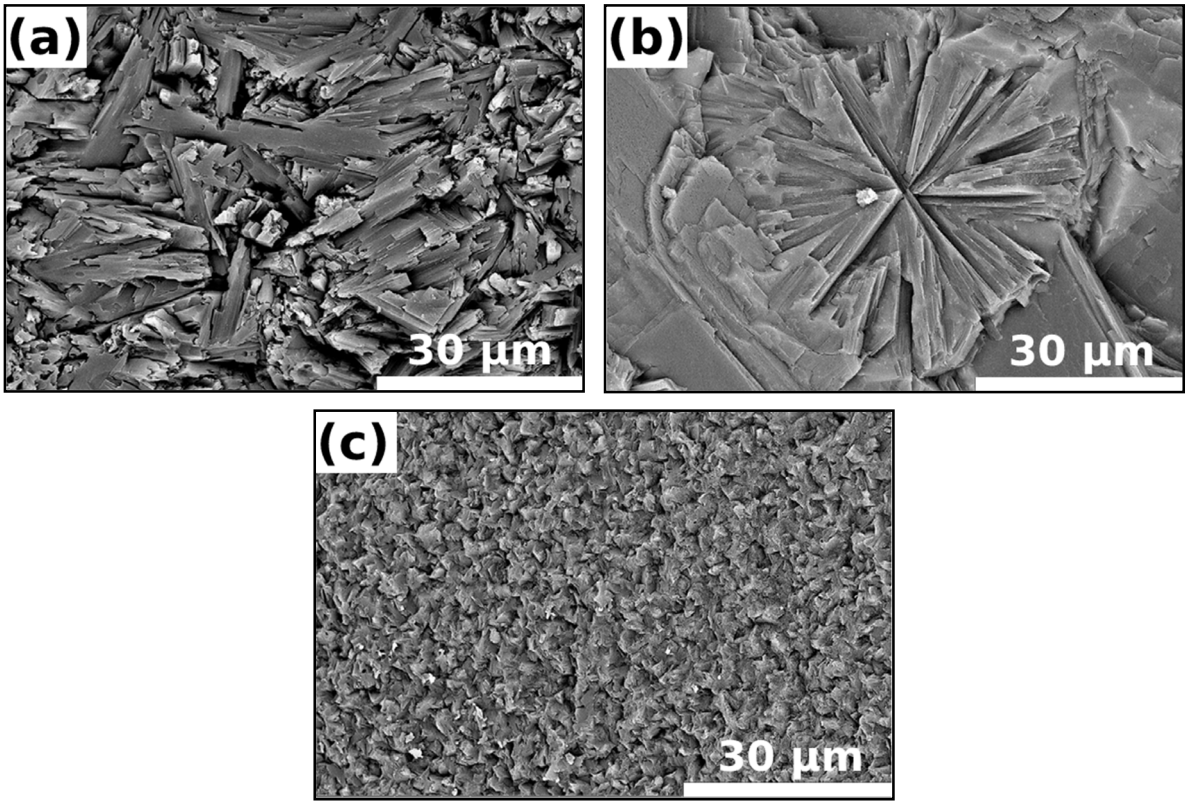

Figure 30- SEM micrographs of fluorocanasite and lithium disilicate joint glass-ceramic composition. Reproduced from [256] with permission from Elsevier.

SEM can also display the change in the surface morphology and structures when it is supposed to corrosion [261]. While high surface roughness is obtained for leucite DGCs after contact with the corrosive solution, in other porcelains containing nano-crystals and micro-crystals, a smoother surface is provided. However, to have an in-depth investigation of the

surface structural changes, it is necessary to know about the pre-, post-corrosion elemental surface composition of the ceramic materials and of the corrosive medium [261].

5.5. Transmission electron microscopy

Compare to optical microscopy and SEM, a transmission electron microscope (TEM) provides the image as small as a single column of atoms with high resolutions, and this is mainly due to the smaller de Broglie wavelength of the electron, which helps us in localizing the electron beam. Besides, to make atomic structure pictures, high-resolution transmission electron microscopy (HR-TEM) is commonly employed. The microstructure of glass-ceramics affects their properties, which are directly correlated to the application. TEM micrographs are helpful to investigate the nucleation and crystallization phenomena. In dental applications, TEM images mostly illustrated metastable phases for heterogeneous nucleation, and detect intrinsic heterogeneities used for nucleation and atomic ordering in a non-crystalline structure, and observe phase separation before nucleation.

Some researchers have used high resolution HR-TEM for different reasons, such as determining size, shape, distribution of the fabricated materials [262–264].

One critical issue that influences the application of bioactive DGCs is their crystallization behavior, which helps in improving the mechanical strength of 3D porous scaffolds and monolithic pieces. Despite numerous studies, crystallization of DGCs is not fully understood yet, concerning the mechanisms of crystalline phase formation. Jaimes et al. [265] have recently shown how cutting-edge imaging techniques, such as high-tech transmission electron microscopy (TEM) coupled with energy-dispersive X-ray spectroscopy and X-ray nano-computed tomography (nano-CT), permit visualizing modifications in microstructure from nucleation to full crystallization in bioactive Bioglass 45S5. They could detect the formation of phase-separated nano-droplets in the glassy matrix by light microscopy (LM) at the early

stages of heat treatment at 660 °C (**Figure 31a**, top left). Later, the crystallization of combeite ($Na_2Ca_2Si_3O_9$) spherical crystals in the volume was predominant and identified by XRD. The 3D morphology of these spheres was investigated by nano-CT (**Figure 31a**, right), while TEM-EDX confirmed the homogeneous composition of the microstructure. TEM also revealed that the combeite structure was composed of sub-micron grains (**Figure 31a**, bottom left). The surface crystallization, coarsening, and merging at near-complete crystallization of combeite were recorded by optical microscopy (**Figure 31b**). These results preset the significance of using complementary methods for gaining insight into the crystallization process in glass-ceramics. TEM and nano-CT are also appropriate and emerging characterization techniques to picture the crystallization in fast crystallizing systems, such as bioactive glasses [265].

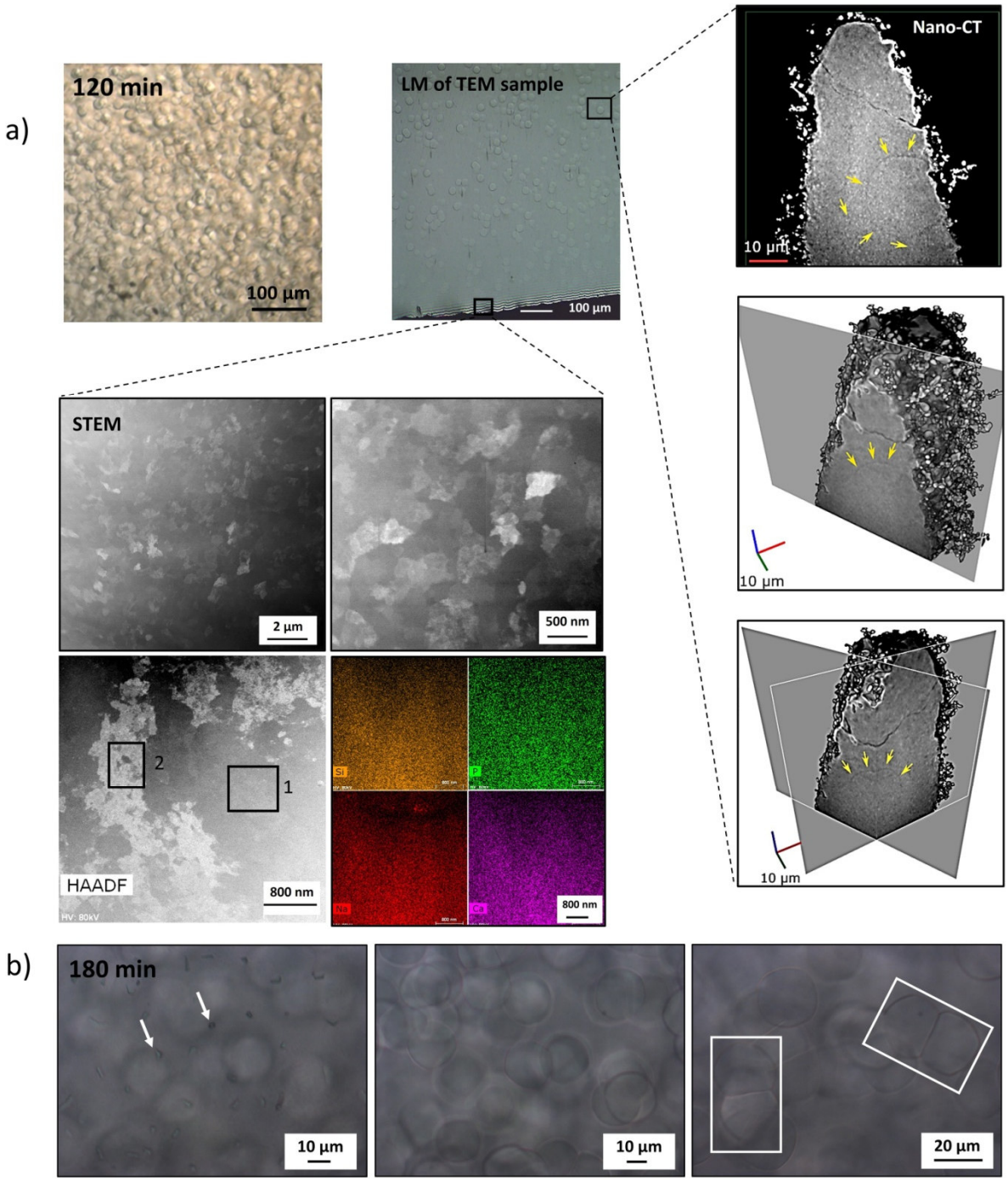

Figure 31- (a) **Top left:** high-temperature optical microscopy image showing the interior volume of Bioglass 45S5 heat-treated at 660 °C for 120 min. **Top center:** Image of the sample used for TEM. **Top right:** Nano-CT micrographs highlight single projection and volumetric reconstruction with one (center) and two (right) virtual cuts. Yellow arrows point out the border of the round-shaped crystal. **Bottom:** scanning TEM images at different magnifications and HAADF image and related EDX elemental distribution mapping (Si, P, Na, and Ca) demonstrating the homogeneous microstructure. Rectangles 1 and 2 show the areas where EDX was performed. **(b)** Optical microscopy images of the surface (left) and internal volume (center, right) of the cross-section of a polished sample heated at 660 °C for 180 min. White arrows illustrate features at the surface, while the spheres are observed below the surface. Coarsening of particles is captured inside white frames [265].

Montazerian and Zanotto [266] have employed a SEM and HR-TEM to investigate the crystallization pathway in an enstatite-zirconia glass-ceramic. Crystallization of glass in SiO_2–MgO–Na_2O–ZrO_2–TiO_2 glass was first stimulated by holding a sample at 700 °C for 12 h (near T_g) and then at 800 °C for 120 min (near T_c). **Figure 32** shows the SEM microstructure of the glass after such heat-treatment. Internal crystallization of spherical crystals with an average size of 2-5 µm is observed. The SEM images in the back-scattered mode show very fine, bright particles (~100 nm in size) inside the spherulitic enstatite crystals [266]. The brighter particles confirm the presence of a heavy element, such as zirconium or titanium, which backscatters electrons stronger than the lighter elements Si, Mg, and Na. Therefore, these particles could be considered as zirconia (ZrO_2), titania (TiO_2), or spinel (Mg_2TiO_4), which seem to be acting as the nucleating agent for heterogeneous nucleation of the main crystal phase, enstatite [266].

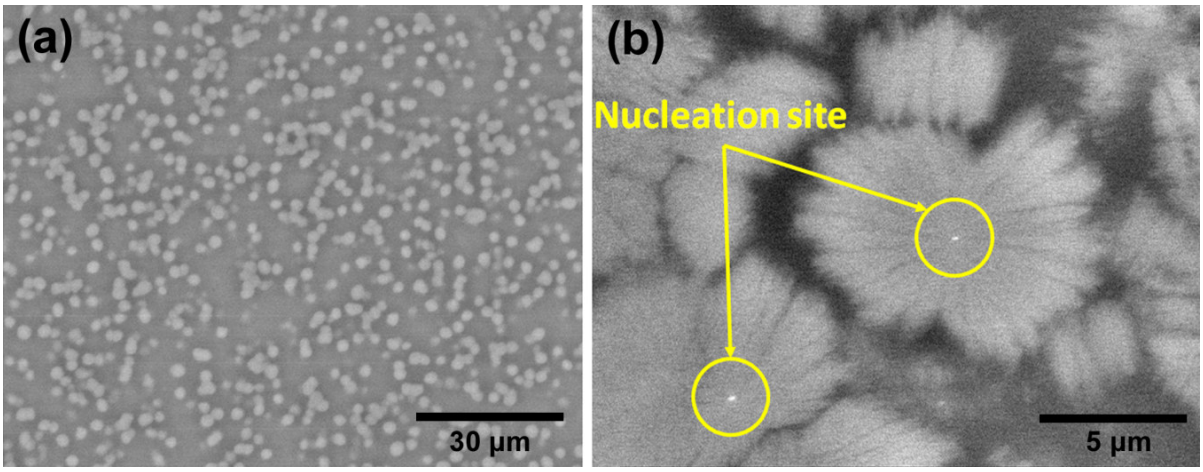

Figure 32- SEM images showing internal crystallization of spherulitic enstatite crystals, with an average size of ~2-5 µm, after treatment at 700 °C for 12 h and 800 °C for 120 min. Figure (b) shows a nucleation site in the crystals that were cut in the center [266].

They could attribute the bright particles to tetragonal ZrO_2 for, at least, some of the very first detectable crystallites during the nucleation process. **Figure 33** shows both the

TEM-HAADF image (right image) and selected area (electron) diffraction pattern (SAED) (left image) performed on a glass sample treated at 700 °C for 12 h and then 775 °C for 30 min. TEM-HAADF, which is used to reveal chemical contrast, disclosed that the sample is not homogeneous at this scale, showing some degree of chemical dissimilarity. The SAED presents an axis zone compatible with the [100] direction of t-ZrO_2. The diffraction pattern shows spots corresponding to the (012), (002) and (020) planes of t-ZrO_2. Therefore, the crystallization pathway in this glass-ceramic, similar to many other DGCs, depends largely on the self-nucleating ability of oxide phases like ZrO_2. It is possible that phase separation of ZrO_2-rich amorphous regions occurs, upon which main crystals form. In some cases, ZrO_2 crystals could also precipitate directly from the homogenous supercooled liquid.

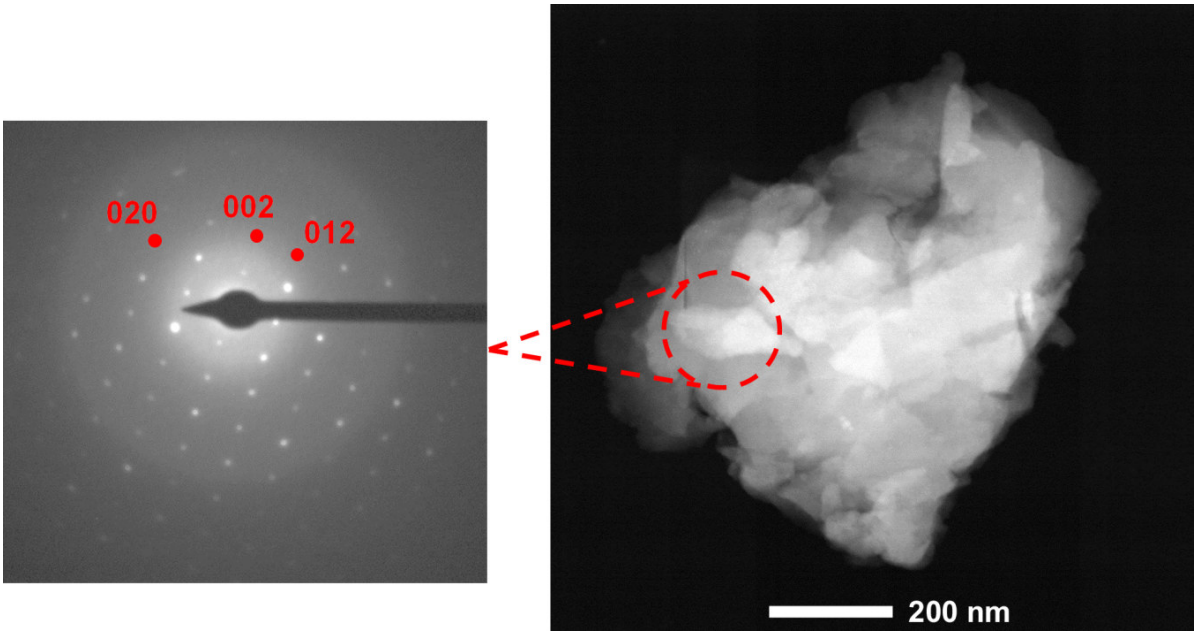

Figure 33- High-resolution TEM-HAADF micrograph of an estatite-zirconia glass-ceramic heat treated at 700 °C for 12 h and then at 775 °C for 30 min (right), and a selected area electron diffraction pattern of the bright region corresponding to the [100] direction (left) of t-ZrO_2.

5.6. Fourier-transform infrared spectroscopy

FTIR spectroscopy is a vibrational spectroscopic technique that is fairly simple, nondestructive and reproducible. Moreover, in this technique, only a small amount of sample with minor sample preparation is required. This technique enables scientists to investigate the functional groups, bonding types, the bonding's formation or breakage, and molecular conformations. The chemical reactions taking place in the in vitro tests of bioactive DGCs can be revealed by this technique, usually coupled with SEM images, which help us to learn about phase transition in these dental biomaterials. Vibrational spectra include spectral bands which are molecule specific and provide direct information about biochemical composition. Therefore, this technique has a variety of applications to study the nature of different kinds of materials from biological to mineral phases [267,268]. When it comes to FTIR, the change in the dipole moment of the molecule can be detected. Among FTIR results, there are some characteristic bonds that can be used as a fingerprint to identify the material's type. The vibrational spectroscopy can also be used to study the bonding in the interface area between dentin/enamel and the dental material [269].

The FTIR spectra from the surfaces of a gel-derived SiO_2–CaO–P_2O_5–(ZrO_2) GCs, developed by Montazerian et al. [256], before exposure to SBF and after 3 h and 12 h (**Figure 34a-b**) demonstrate three broad bands at approximately 1260 cm^{-1}, 1120 cm^{-1} and 470 cm^{-1}, which can be attributed to the vibration of the chemical bonds in the crystalline phases and Si–O–Si bond vibration. Additionally, two identified peaks at wavenumbers 605 cm^{-1} and 560 cm^{-1} can be ascribed to the deformation modes of the P–O bond in such phosphate-like phases as hydroxyapatite [256]. Because the HA formation on the glass-ceramic surfaces was not observed by SEM after 3 h and 12 h, these two vibration bands could be attributed to crystalline hydroxyapatite in the polycrystal matrix, which was confirmed by the XRD results. This observation suggests that the presence of P-O vibration

band in the FTIR spectra is, sometimes, due to the HA crystals in the material and not HA formation on the surface [256].

After increasing the testing time to 24 h and 144 h, HA covered the surface of the Zr-free glass-ceramic (GC-24 and GC-144), and a new spectrum was detected by FTIR that displayed the typical HA bands located near 1130 cm^{-1}, 1060 cm^{-1}, 605 cm^{-1} and 560 cm^{-1}. However, in the glass-ceramic containing zirconia (**Figure 34b**), HA vibration bands appear only after 14 days of exposure to SBF. HA formation was previously confirmed via SEM (**Figure 35**) [12,256].

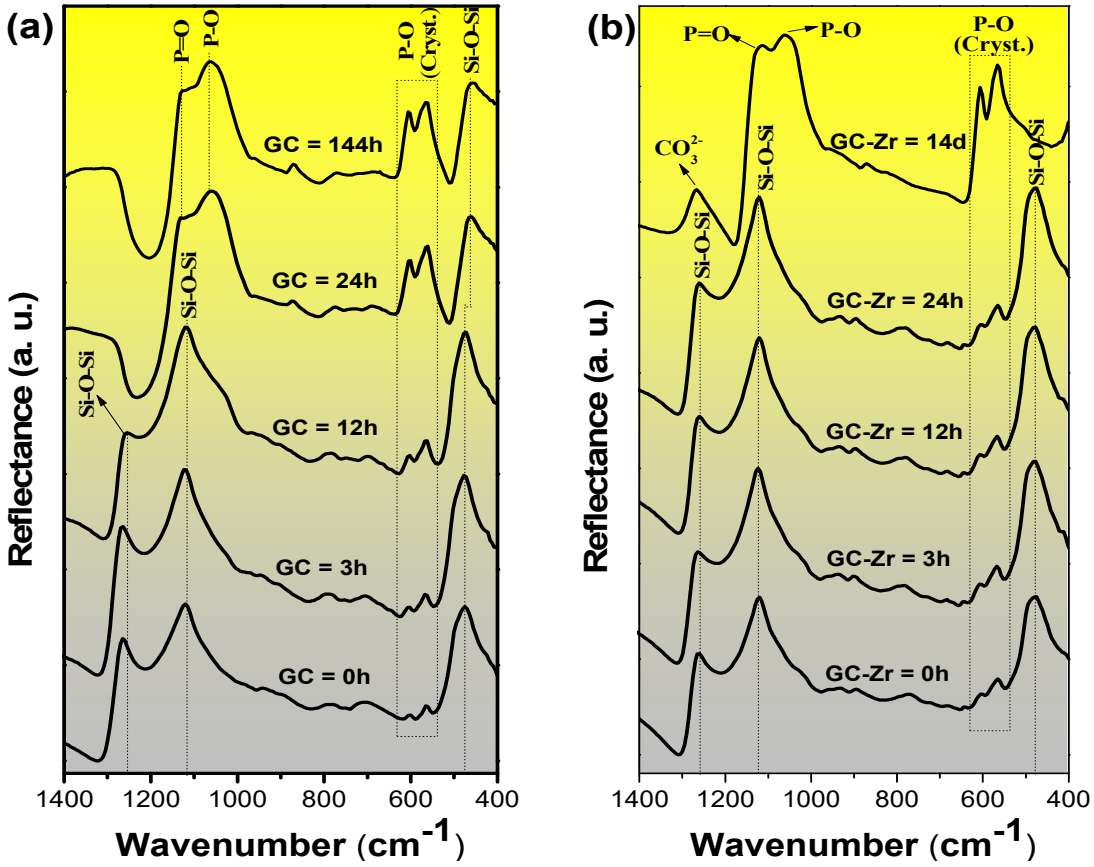

Figure 34- FTIR spectra of samples GC (a) and GC-Zr (b) before and after soaking in SBF at different testing times [256].

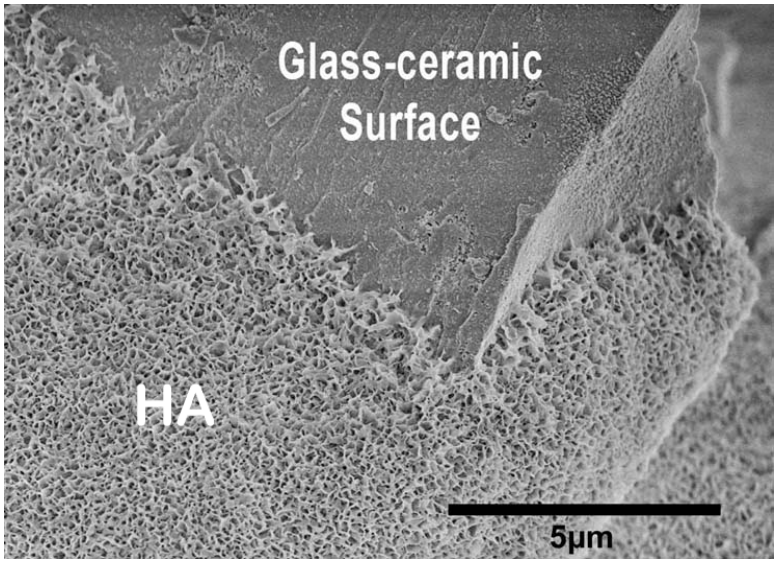

Figure 35- HA formation on the SiO_2–CaO–P_2O_5–ZrO_2 GCs surface (partially sintered powder) after 24 h exposure to simulated body fluid (SBF) (personal image).

5.7. Raman spectroscopy

Another vibrational spectroscopic technique is Raman spectroscopy. The most noteworthy difference of this technique with FTIR spectroscopy is that in Raman spectroscopy, a change in the polarization of molecules is observed [269]. Raman spectroscopy can also be applied for the measurement and identification of chemical composition and molecular structure. Although Raman spectroscopy is a strong tool, in the majority of the studies, most of its application has been mostly limited to find the degree of conversion (DC) of dental materials, adhesive, and setting reaction of cement [270–272]. When it comes to comparing FTIR to Raman spectroscopy, the poorer sensitivity of Raman and the presence of broadband fluorescence which interferes with the Raman signal of interest, has been limited the application of Raman spectroscopy. While FTIR can detect the species present in the concentration of 0.1%, Raman can only be used when the concentration is about 1%. Esmati et al. [273] used Raman spectroscopy to characterize as-synthesized dental materials and study the bioactivity of the final products. The main aim of this research was to investigate the structure, biodegradation, bioactivity, and biocompatibility of SiO_2–

MgO–CaO glasses doped with different amounts of fluoride for a biomedical application like dental material. To study the bioactivity of the specimens, samples were immersed in SBF then their Raman spectroscopy was compared with the samples previous to immersion in SBF. Results showed that the intensity of the peak, related to Ca-O band, was increased after immersion which was proof of the existence of Ca-containing species (apatite). There was also a peak at 1081 cm^{-1} for the F-containing samples, which was assigned to the incorporation of fluoride into apatite. Recently, Ghahsareh et al. [274] have utilized Raman spectroscopy to investigate the role of CeO_2 on crystallization behavior and microstructural features of canasite glass-ceramics for dental applications. Their results show that the addition of cerium oxide to the glass composition leads to a slight increase in crystallization temperatures and a significant decrease in thermal expansion coefficients of the parent glasses. According to the Raman spectroscopy results, cerium ions increase the network connectivity of the parent glasses by increasing the number of bridging oxygens.

Deshpande and Satyanarayana [275] developed lithium disilicate-based glasses containing P_2O_5. The replacement of ($Li_2O + SiO_2$) with P_2O_5 and the resulting structure was studied using FTIR and Raman spectroscopy. Although glasses containing $P_2O_5 \leq 0.5$ mol % mainly possess Q^3 units, the lithium disilicate phase has not been developed; instead, the lithium silicate phase has been developed in their corresponding glass-ceramics. The glasses with $P_2O_5 \geq 1$ mol % showed an increase in Q^2 and Q^4 units and the desired LS2 phase could be developed in the g1ass-ceramics, which could be due to the nucleation effect of P_2O_5.

There has been an increasing need for non-invasive methods to monitor living cells *in vitro*, the growth of engineered artificial tissues, and the development of cell-based biosensors. On all of these matters, Hench and collaborators successfully integrated Raman spectroscopy into their studies on tissue regeneration, in most cases triggered by bioactive glasses and glass-ceramics. Raman spectroscopy is an optical technique based on inelastic

scattering of laser photons by molecular vibrations, which provides a chemical fingerprint of biomaterials and cells/organelles without fixation, lysis or the use of labels and other contrast-enhancing chemicals. Hench *et al.* have employed this technique in situ and in real-time to follow-up HA formation on biomaterials and characterize different living and dead cells (e.g., osteoblasts, lung cells and stem cells) attached on them. They elicited Raman signals from living cells, e.g., for detecting changes in cell phenotype, involving irradiating the cell with laser light at selected wavelengths [57]. They also managed to show that this spectroscopic method could be used to study the most important cellular functions involved in cell-biomaterial interactions, such as cell death, differentiation, de-differentiation and mineralization. The method offers the potential for studying cell-bioceramic interactions and reduces the need for animal testing until the final steps of proving usefulness prior to clinical trials [57]. Currently, bio-photonics is central to cancer studies. Interested readers can refer [270] and [276], which cover the applications of this technique and emphasize its potential impact on modern scientific endeavors, such as tissue engineering, cancer identification and drug discovery.

5.8. Anomalous small-angle X-ray scattering

Anomalous small-angle X-ray scattering (ASAXS) is a powerful technique to analyze the spatial distribution of a target element. This technique records the intensity of the elastic scattering of X-ray (wavelength ~0.1-0.2 nm) by the sample at very low angles (typically 0.1-10°). This method has been used to investigate nucleation and phase separation phenomena in a wide range of glasses [277–280]. SAXS can provide beneficial information on the average number, diameter, and surface area of the amorphous phase-separated droplets, meta-stable phases, clusters, and nano-scaled inhomogeneity of glasses. There is another similar but more

advanced method which is called anomalous small-angle X-ray scattering (ASAXS), which is able to analyze the integral averaged composition of the structures by using the anomalous dispersions of the atomic scattering amplitude near the absorption edge of the sample element. Hass et al. [281] synthesized oxyfluoride glass-ceramic with the composition of $21.1SiO_2$–$6.5B_2O_3$–$7.0Al_2O_3$–$21.0PbF_2$–$14.3CdF_2$–$11.0YbF_3$–$0.5\%ErF_3$–$11.0PbO$–$7.6CdO$ (mol%). They investigated the structure and chemical composition of the prepared materials, using a variety of techniques, including ASAXS. They reported that the final products contained two main phases: fluoride nanocrystals and an oxide glass matrix. They also stated that nanocrystals initiate growth at a temperature above transformation temperature at 678 K. ASAXS operated at energies of X-ray absorption edges of Cd, Er, Pb, and Yb. It was reported that the nanocrystals could be described as polydisperse spheroids and the length of larger and smaller axes were about 17.7 ±3 .9 and 6.4 ± 1.4 nm, respectively.

There was also another research investigating the formation and structure of nanosized $ZrTiO_4$ crystals in the matrix of lithium aluminosilicate (LAS) glass - one of the basic mother composition which is used in developing restorative DGCs - during heat treatment at 750 °C for different periods of time with anomalous small-angle X-ray scattering (ASAXS) [282]. For the sample annealed for 30 minutes, results of the ASAXS close to the X-ray absorption edge of Ti and Zr proved the formation of particles ($ZrTiO_4$) which were surrounded by a shell-like region. When the samples were annealed for 240 minutes, ASAXS results revealed the two different kinds of particles formed after heat treatment (spherical core-shell: $ZrTiO_4$ and large spherical particles: $LiAlSi_2O_6$). In this study, they could also obtain the average composition and volume fraction of the nanocrystals, the shell region, and the remaining glass matrix from ASAXS results. Another research conducted by Hoell et al. [283] synthesized the glasses with the composition of $1.88Na_2O$–$15.04K_2O$–$7.52Al_2O_3$–$69.56SiO_2$–$6.00BaF_2$ and $1.88Na_2O$–$15.03K_2O$–$7.52Al_2O_3$–$69.52SiO_2$–$6.00BaF_2$–

0.05SmF_3 (mol%). After annealing, the samples at 580 °C or 600 °C, cubic BaF_2 were crystallized in the matrix. SAXS and ASAXS were both performed and confirmed the core-shell structure, and in both samples, the shell composition is enriched with SiO_2. The size of the BaF_2 cores for both samples is around 11 nm, and the shell had a thickness of 2.6 nm. During the last few years, a number of studies have been conducted to analyze the quantitative structural parameters such as size and size distribution of nanoparticles and averaged chemical composition of different glass-ceramic materials with ASAXS technique [282,284,285]. Such techniques should be further utilized to shed more light on the mechanism of nucleation in parent oxide glasses of DGCs.

5.9. Small-angle neutron scattering

Small-angle neutron scattering (SANS) is a powerful technique for investigating the structure of various substances of the order 1 nm to over 100 nm. This technique can also be used to investigate the nucleation and crystallization process in glassy materials. SANS is similar to SAXS, although SANS has some advantages over SAXS, like its sensitivity to light elements, having larger penetration depth, the strong scattering by magnetic moments, and the possibility of isotope labeling. It should be noted that there are some weaknesses attached to SANS, which have limited its application as the limited sources of the low flux of neutron compare to similar methods like X-ray sources and complexity of data analysis [286]. Wright et al. [287] added TiO_2 to a glass-ceramic material ($MgO–Al_2O_3–SiO_2$) as a nucleating agent and used SANS to study the early stage of nucleation and crystallization. Their study showed that there was a good scattering contrast between the host phase and precipitation. Another noteworthy result was that it was possible to study regions around Q = 0.005 $Å^{-1}$, where Q stands for scattering vector. The region with a scattering vector of Q = 0.005 $Å^{-1}$ is a region between the scope of light scattering measurements in SAXS. Nucleation and crystallization

of basalt glass material had been investigated using the SANS technique [288,289]. They could prove that during the growth process, smaller particles tend to dissolve as larger ones. They also discussed the details of the procedure of the particles' redissolution during the growth of the stable nuclei. In a recent study, the structure of an of up-conversion luminescent nanoparticles in oxyfluoride glass-ceramics doped with rare-earth ions with the composition of $29.5SiO_2$–$21PbO$–$30PbF_2$–$10CdF_2$–$7.5GeO_2$–$1Eu_2O_3$–$1YbF_3$–$0.1Tm_2O_3$ (mol%) and $40SiO_2$–$18PbO$–$30PbF_2$–$10CdF_2$–$1Eu_2O_3$–$1YbF_3$–$0.1Tm_2O_3$ (mol%) have been studied [290]. The final results showed a two-stage process of luminescence nanoparticles' formation in the glass composites: formation of relatively large nanoparticles of lead fluoride and the gradual change in the size and morphology of the initial particles after reaching 380 °C during the heat treatment. Small-angle neutron scattering results indicated that the number of small crystalline nanoparticles augmented with two factors: increasing the temperature of heat treatment and increasing the time of thermal processing. There was another study on oxyfluoride lead-silicate glass matrixes doped with rare-earth oxides [291]. In this study, crystallization, and formation of the predominantly amorphous nanoparticles and clusters of PbF_2 in the initial glass matrix were detected using the SANS technique. Kilcoyne et al. [292] developed machinable mica-based glass-ceramics as restorative dental material. They used SANS as a technique to study nano–crystalline-amorphous phase mica-type glass-ceramic's interface which exhibited Q^{-4} dependence (Porod scattering), indicating that, on a 100 Å scale, the surface of the crystals is smooth. Fernandez-Martin et al. [293] researched nucleation and growth of nano-sized crystals in two glass-ceramics: a lithium-aluminosilicate (LAS) and a (Mg, Zn) spinel. They also used SANS as one of the characterization techniques and the results proved that by raising the temperature, the phenomena of transient happened between the regions of nucleation and growth in the LAS and did not follow standard kinetic theories. On the other hand, it was observed that the spinel material had a smooth transition

during the temperature ramp between the nucleation and the growth stages and followed a more conventional growth pattern. These results were also confirmed by DSC.

5.10. X-ray absorption spectroscopy

In addition to several methods mentioned to investigate the nucleation, crystallization, and growth in glass-ceramics, X-ray absorption spectroscopy (XAS) like X-ray absorption near-edge structure (XANES) and extended X-ray absorption fine structure (EXAFS) are other techniques to show different phenomena. This method determines the local atomic structure and electronic state of matter and has been widely studied for nucleation and crystalization phenomena in different glasses [294]. Generally, an X-ray can excite the electrons inside the atom to the unoccupied level (a transition studied by XAS) or an unbound situation, creating a core hole. If the electron is ejected, the produced excited ion and photoelectron are studied by X-ray Photoelectron Spectroscopy (XPS). XAS needs high-energy X-ray excitation occurring at synchrotron facilities. In this analysis, samples can be in the gas phase, solutions, or solids. From the incident photons energy and the spectrum from the environment of the atomic species, the K-threshold of a particular element is investigated.

Cormier *et al.* also revealed the nucleation and crystalization process using (XAS) on the environment around Zr [295,296], Ti [297], and Ni [298] in glasses and glass-ceramics [299]. They showed the effect of ZrO_2 as a nucleating agent for the nucleation and crystallization of Li-, Mg-, Ca- and Zn-bearing aluminosilicate glasses compared to the Na-bearing glasses [295]. While ZrO_2 facilitates the nucleation in Li-, Mg-, Ca- and Zn-bearing glasses, and had no effects on the Na-bearing glasses crystallization. To be more specific, coupling XAS at both Zr K- and $L_{2,3}$-edges demonstrated the Zr environment, corresponding to six-fold coordinated sites (Li/Na-bearing glasses) and seven-fold coordinated locations in Mg, Ca, Zn glasses. The results elucidated that the coordination number has an insignificant impact on

crystallization. Apart from Na-bearing glasses, direct Zr–Zr polyhedral linkages could be detected for all glasses. No correlation between the local Zr sites and their ability to encourage nucleation could be observed. Besides, regarding the lack of direct linkages of Zr atoms, the Na-bearing glasses had a low ability to crystallize [295]. Cormier and coworkers also demonstrated the nucleation ability of nanocrystals of tetragonal (ZrO_2) in $MgO–Al_2O_3–SiO_2$ parent glass explained by XANES and EXAFS [296]. At 4 mol% ZrO_2, a statistically random distribution of Zr^{4+} would give an average Zr–Zr distance in the random distribution of Zr^{4+} was more than the experimental value (3.4 Å), with about 11 Å, suggesting the Zr inhomogeneous distribution attributes the formation of locally ordered domains. Patzig *et al.* [300] reported the Zr $L_{2,3}$ edge XANES of $51.9SiO_2–21.2MgO–21.2Al_2O_3–5.7ZrO_2$ (in mol%) glass-ceramics. They showed that the coordination number of Zr increase from 6 in the primary glass to 8 in the crystallized glass-ceramic, and this is due to the homogeneously distributed Zr and formation of nanocrystalline ZrO_2 after nucleation and crystallization, and was determined to be t-ZrO_2 by Zr $L_{2,3}$ edge fingerprinting, as well as by the theoretical Zr $L_{2,3}$ edge fingerprints obtained by ab initio multiplet calculations (**Figure 36**) [300].

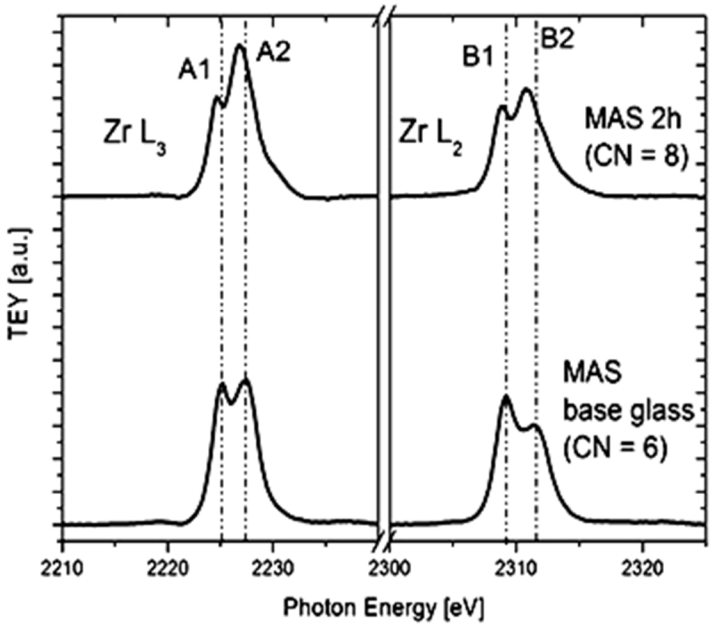

Figure 36- (a) the Zr L_2 and L_3 edge XANES spectra of the amorphous MAS base glass-sample (bottom) and the fully crystallized glass-ceramic sample (top) [300].

Mastelaro *et al.* [299] employed EXAFS to investigate the correlation between the modifier cations' local structure and the ability of the nucleation in glasses. They analyzed EXAFS results on the local system around Ca and Pb atoms in both vitreous and crystalline samples. In this research, three different silicate glasses, including wollastonite ($CaSiO_3$) and soda-lime-silica ($Na_2Ca_2Si_3O_9$), and lead metasilicate ($PbSiO_3$), which studied for volume nucleation and the nucleation occurred only on the sample surfaces in laboratory conditions. In $Na_2Ca_2Si_3O_9$ and $CaSiO_3$, in which a high nucleation tendency was observed, the local structures of these modifier cations were similar to their short-range order in the isochemical crystalline phases, whereas the local structure in the $PbSiO_3$ glass that presented a low nucleation tendency was entirely different from that of its isochemical crystal phase [301].

Recently, Cicconi *et al.* [302] used Ca K-edge XAS to study the Ca structural role in silicate glasses. The result sill shows that the Ca pre-edge peak provides information about the different Ca surroundings and their structural role. They analyzed their approach to the SiO_2 content of 50 and 76 mol% on Ca-aluminosilicate glasses. In these glasses, calcium

should act either as a network modifier and charge compensator. Cicconi *et al.* [302] observed that variations in the pre-edge peak centroid energies depended on the changes in the role of Ca as a network modifier (Al = 0 mol%), on the charge compensator (aluminosilicate join), and on a more involved role in the peraluminous domain, based on the fraction of Al coordination numbers (4, 5 and 6). This approach was further used to study Fe-bearing and diopside glasses at different temperatures [302]. Besides, the Ca K-edge XAS signals obtained from in situ studies at high temperature (HT) in an Al/Fe free system in which Ca has a more restricted number of sites were investigated by Neuville *et al.* [303,304].

5.11. Nuclear magnetic resonance

Nuclear magnetic resonance (NMR) is a phenomenon that nuclei in the strong constant magnetic field with a weak magnetic oscillator field can perturb, producing an electromagnetic signal, which occurs near resonance. Real-time (*in situ)* NMR spectroscopy can be a useful method for investigating chemical exchanges structural and dynamic changes in glass-forming liquids to track the reversible phenomena (dynamical exchange or structural relaxation mechanism). However, nucleation and crystallization (irreversible phenomena) can be more easily followed by an *ex situ* technique [305].

It should be mentioned that researchers describe the local structures of glasses by different structural units. As a case in point, the "n" in the Q^n, which is the symbol of the silicate tetrahedra in silica glasses, is denoted the number of bridging oxygen atoms (–Si–O–Si– linkages) per tetrahedron, and Q^n distribution can be measured by NMR. It is important to link the NMR result to the crystal nucleation kinetics. NMR can also demonstrate the effect of internal nucleation and different structural parameters like short-range order (network modifier cation-oxygen distances, coordination numbers, and network former Q^n

distributions), intermediate-range order (network former connectivity, network modifier distance distributions, network modifier distance distributions), and medium-range order (silicate tetrahedral ring-size statistics) [306]. Zanotto *et al.* concluded that although there is a relation between homogeneous nucleation capability and structural similarity in the short- and intermediate-range order of the network modifier cations, no correlation could be detected between structural parameters [306].

Hill *et al.* [307,308] showed the crystallization of a $29.7SiO_2$–$16.1Al_2O_3$–$11P_2O_5$–$29.7CaO$–$2CaF_2$–$5.6MgO$ (wt.%) parent glasses, which were annealed for 8 h at 850 °C with the quick colling to the room temperature. They demonstrated that ^{31}P MAS-NMR spectra could detect the amorphous phase separation (APS). ^{19}F MAS-NMR spectra also showed that after the heat treatment at 850 °C and 950 °C, F was below the detectable limits in the amorphous environment incorporated into the fluorapatite (FAP) crystal phase. They revealed that the formation of nano-sized crystals in oxyfluoride glass-ceramics needs a rapid nucleation rate with a low crystal growth rate.

Montazerian *et al.* [256,309] prepared nano-apatite-zirconia glass-ceramics. Their structure and crystallization behavior were studied by using NMR and HR-TEM to detect the conversion of the gel-derived glasses into nano–glass-ceramics. In this research, Zr and K acted as a glass former and a modifier, respectively. They also mentioned that some of these glasses could be used in bioactive glasses for dental applications. In a comprehensive review by Eckert [310], he concludes that NMR spectroscopy offers an element-selective, inherently quantitative and experimentally very flexible approach for the structural elucidation of non-crystalline materials. He introduces the basic concepts of this technique, highlighting the use of advanced NMR methodology for characterizing short- and intermediate range order in bioactive glass systems. NMR can give clear and quantitative answers to the extent of network polymerization and the spatial distribution of the network former and network

modifier species. NMR results support our understanding of the influence of DGCs composition upon the dissolution kinetics and bioactivities. Eckert provides knowledge on more advanced experimentation, in the hope of their increased usage and circulation in future applications [310].

6. Applications of DGCs

6.1. Restorative inert DGCs

Regarding the increasing demand for aesthetic dental treatment with desirable mechanical and physical properties, searching for suitable materials and development techniques has become crucial for dentists and patients. Appeal dental appearance with an aesthetic smile can help improve self-confidence in many areas of life. For example, glass-ceramic veneers/crowns/bridges have become a conservative teeth restorative method due to the relative long-term predictability and high aesthetics results. As a result of previous kinds of research on these materials and based on their properties like strength, longevity, conservative nature, biocompatibility, aesthetics, and ability to form the “contact lens effect,” glass-ceramic have been proven as a conventional group of materials for treating teeth from 1985 [311]. One method to promote the physical and properties of the GCs is the controlled crystallization of crystals within a glassy matrix. This method helps scientists to enhance strength, fracture, thermal shock, and corrosion resistance. Although these crystals improve the mentioned characteristics of GCs, other aesthetic properties like translucency have to be justified.

Various types of restorative dental glass-ceramics have already reached the market. These materials and their typical characteristics are listed in **Table 8**. Additionally, the main mechanical properties, commercial names and recommended applications for these materials

are summarized in **Table 9**. Hereafter, we review the current status and recent developments regarding restorative dental glass-ceramics [13,16].

Table 8. Typical dental glass-ceramics and their representative compositions and main characteristics [62].

Commercial Dental Glass-Ceramics	**Typical Glass composition (wt. %)**												**Fabrication Procedures**	**Typical Crystalline Phase(s)**
	SiO_2	**Al_2O_3**	**MgO**	**CaO**	**Li_2O**	**Na_2O**	**K_2O**	**ZnO**	**ZrO_2**	**P_2O_5**	**CeO_2**	**Others**		
Mica-based GCs	56-64	0-2	15-20	-	-	-	12-18	-	0-5	-	0.05	(4-9)**F**	Lost-wax casting and CAD/CAM	Mica ($KMg_3AlSi_3O_{10}F_2$)
Leucite-based GCs	59-63	19-23.5	-	0.5-3	-	3.5-6.5	10-14	-	-	-	0-1	(0-1)**B_2O_3** (0-1.5)**BaO** (0-0.5)**TiO_2**	Heat-pressing and CAD/CAM	Leucite ($KAlSi_2O_6$)
Lithium disilicate GCs	57-80	0-5	0-5	-	11-19	-	0-13	0-8	0-8	0-11	-	-	Heat-pressing and CAD/CAM	Lithium disilicate (Li_2O–$2SiO_2$)
Apatite-based GCs	60-65	8-12	-	0-1	-	6-9	6-8	2-3	-	0-1	-	(0-1)**F**	Pressureless sintering	Fluorapatite ($Ca_5(PO_4)_3F$)
Lithium zirconium silicate GCs	42-59	3-5	-	-	7-15	2-3	4-5	-	15-28	4-15	-	-	Heat-pressing	Lithium phosphate (Li_3PO_4) and Zirconia (ZrO_2)

Table 9. Typical/approximate mechanical properties and recommended applications for commercial dental glass-ceramics [62].

Dental glass-ceramics	Bending strength (MPa)	Fracture toughness ($MPa.m^{0.5}$)	Young's modulus (GPa)	Vickers Hardness (HV)	Thermal expansion coefficient ($\times 10^{-6}\ K^{-1}$)	Recommended applications	Typical commercial products (COMPANY NAME)
Mica-based GCs	150	1.4-1.5	70	3.5	7.2	Veneers / Inlays / Onlays / crowns	Dicor/Dicor MGC (DENTSPLY)
Leucite-based GCs	160	1.3	65	6.2	15-18.25	Veneers / Inlays / Onlays / crowns	Paradigm (3M), Lumineers (DEN-MAT), Ceramco/Cergo Kiss (DENTSPLY), IPS Empress (IVOCLAR), IPS InLine (IVOCLAR), EX-3 Press (NORITAKE), Optec OPC (PENTRON), Vitablocs (VITA)
Lithium disilicate GCs	350-450	2.3-2.8	70	6-6.5	10.5-11.5	Crown / Bridge	Cameo (AIDITE), Celtra Duo (DENTSPLY), Obsidian (GLIDEWELL), IPS Empress II/Press/CAD (IVOCLAR), 3G (PENTRON), UpSil Press/CAD (UPCERA), Suprinity (VITA)
Apatite-based GCs	90	-	-	5.4	9.5	Veneered over restorative materials	IPS d.SIGN (IVOCLAR), IPS Eris (IVOCLAR), IPS e.max Ceram (IVOCLAR), IPS e.max ZirPress (IVOCLAR), Vitapm (VITA)
Lithium zirconium silicate GCs	160-260	1.1-1.9	55-59	5.3-6.3	9.4-9.7	Placed on ZrO_2 post and abutment	IPS Empress Cosmo (IVOCLAR)

6.1.1. Mica-based glass-ceramics

Mica-based GCs are traditional materials that are commonly used as dental GCs. Mica GCs have some disadvantages like a high risk of fracture, low mechanical strength, and difficult processing conditions [4,16]. In order to overcome the weakness of these GCs, the pioneering works by Denry's group at Ohio State University were done on improving the properties of the Dicor®, the first mica-based DGCs. A tough structure based on the crystallization of mica ($KNaMg_2Si_4O_{10}F_2$), and K-fluorrichterite ($KNaCaMg_5Si_8O_{22}F_2$) crystals was obtained by modifying the composition [34,241,312]. Denry et al. could enhance thermal and mechanical properties by substituting of potassium with lithium and preparing taeniolite ($KLiMg_2Si_4O_{10}F_2$) [313]. In addition, by replacing K^+ or Na^+ with Ba^{2+} or Ca^{2+} as the interlayer ions of mica crystals, high strength and toughened mica GCs were developed by Uno et al. and Qin et al. after using hot-pressing or extrusion processes [314–320]. The properties of the GCs can also be tuned by ZrO_2 [321–324]. Uno et al. showed that tetragonal-ZrO_2 increased flexural strength and fracture toughness to 500 MP and 3.2 $MPa.m^{0.5}$ which is related to the crack deflection by mica plates and ZrO_2 particles [321]. CeO_2 and zircon-based ceramic pigments are kinds of materials to enhanced the mica-based GCs properties without any significant effect on their microstructure [325]. It is also demonstrated that crack-bowing and trapping cause the toughening mechanisms, higher elastic modulus, and fracture toughness of the crystal precipitates [326].

6.1.2. Leucite-based glass-ceramics

One kind of dental GCs is leucite with a mechanical strength of 164 MPa and high thermal expansion. Considering the low strength, these kinds of GCs are rarely used for fixed posterior

restorations. To be more specific about the usage of these GCs in crowns/bridges, this type of GC is veneered onto a flexible, tough metallic framework [16]. The leucite-based GCs contain high amounts of leucite crystals. One of the leucite crystal advantages is its higher thermal expansion than the residual glassy matrix. By combining leucite crystals and aluminum oxide, the enhanced performance is obtained [327,328]. To avoid GCs pulling away probability from the metal surface, sintering is commonly used at a temperature range of 550-900 °C, and shrinkage must be controlled to prevent tearing [329,330]. Researchers demonstrated that providing nano-coatings on leucite-fluorapatite GC powder before sintering could also enhance the sinterability [331]. An exclusive polymer and inorganic chemicals like $ZnCl_2$, $AlCl_3$, or BCl_3 combined with polyethylene glycol (PEG) are chosen for the coatings to promote the properties of the GCs for sintering and diminish extensive tearing [331].

In 2013, for surface crystallization of the high number of the leucite nanocrystals with an average size of the ~0.05μm^2, and higher bending strength than that of other commercial material, sintered commercial glass particles at the nanoscale (Ceramco® and IPS Empress®) was used by Theocharopoulos *et al.* [332]. The results showed that the mean bending strengths of the prepared leucite glass-ceramic is 255 ± 35 MP, which is much higher than that of for Ceramco® (restorative porcelain) and IPS Empress® (Leucite GC) with 76 ± 7 MPa, and 166 ± 31 MPa, respectively [332]. Ivoclar Vivadent AG significantly worked on the leucite-based GCs for the CAD/CAM process (**Figure 37**) [333]. This product is available in multi-colored CAD/CAM blocks. The block allows the optical properties of natural teeth to be closely imitated. This glass-ceramic consists of a total of four to eight main and intermediate layers [334].

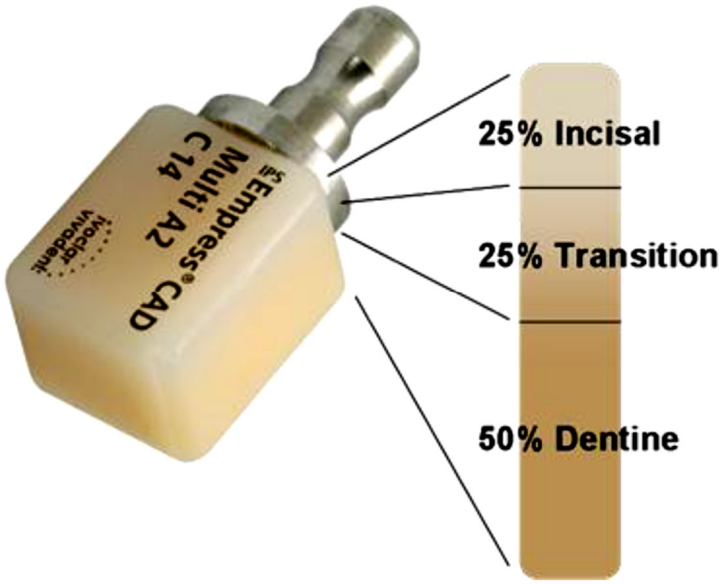

Figure 37- Multicolor block of leucite-based glass-ceramic for a CAD/CAM process [334].

In 2000-2011, Cattell and coworkers worked on the novel low-wear/high-strength leucite-based GCs to enhance the dental ceramic restorations properties. They fabricated leucite-based glass-ceramics by heat-extrusion to overcome the brittle fracture of ceramic restorations and their low survival rate for dental application. The benefits of this novel method are its high crystal distribution and reliability with controlling the leucite crystal size to 0.15 ± 0.09 μm^2 (Weibull modulus, m = 9.4 and σ = 159 MPa) compared to the Empress® as commercial materials (m = 6.1 and σ = 120 MPa) [334–336]. Besides, they studied the nucleation and growth of leucite GCs and controlled surface crystallization by investigating the powder processing and producing fine and then nanoscale leucite GCs, which will help reduce enamel wear, enhance aesthetics and improve strength [337–339]. Finally, this material could be commercialized after heat-extrusion, CAD-CAM, and 3D printing procedure by Den-Mat Holdings as an aesthetic restorative material with the name of Lumineers®.

6.1.3. Lithium disilicate glass-ceramics

The third generation of dental GCs with high flexural strength (above 300 MPa) and fracture toughness (more than 2 MPa) which are roughly two-fold higher than leucite GCs, is dental lithium disilicate (LS2) GCs [4,16]. Great mechanical properties are one of the most notable features of this class of glass-ceramics and when Zhang et al. [340] compared this glass-ceramic with leucite reinforced glass-ceramic, feldspathic glass-ceramic, and fluorapatite glass-ceramic, they reported that lithium disilicate displayed the highest fracture toughness, flexural strength, elastic modulus and crystallinity. These materials, which are used in crown and bridge systems, are available as a crystallized, heat-pressable ingot. This glass-ceramic is a promising candidate for aesthetics or full-contour restorations since this material possesses excellent optical properties like translucency. Lithium disilicate ceramic mainly consists of ~70% of lithium disilicate ($Li_2Si_2O_5$) crystals with a few microns having a needle-like structure in the glassy matrix [341,342].

Lithium disilicate glass-ceramic is usually shaped by CAD/CAM. To meet the challenging requirements of the CAD/CAM process, a particular heat treatment is followed, as shown in **Figure 38**, e.g. for IPS e.max® CAD [343]. First, a monolithic piece of glass is prepared by casting the melt in a mold (**Figure 38a**). Second, a glass-ceramic containing lithium metasilicate ($Li_2O–SiO_2$) is developed by intermediate heat treatment of the glass at 690-710 °C for 10-30 min (**Figure 38b**). This intermediate material (which is supplied in blue color) has been specially designed to facilitate the machining process in the CAD/CAM technique (**Figure 38b**). After the machining process (**Figure 38c**), the material is heated at 850 °C for 20-31 min to form the lithium disilicate glass-ceramic that displays a characteristic tooth color (**Figure 38d**). The resulting dental restorations can be polished and completed with glazing to match the color of the

patient's teeth. The glass-ceramic ingot containing lithium metasilicate crystals, as provided by the material suppliers, has a flexural strength of 130 MPa, but the strength and fracture toughness increases to 360 MPa and 2.3 MPa.m$^{0.5}$, respectively, after conversion of the machined glass-ceramic to the final product. The reduced strength and toughness of CAD/CAM materials compared with the heat-pressed material is due to the fact that the latter glass-ceramic contains needle-like and elongated crystals with a higher aspect ratio than its CAD/CAM counterpart [31], [35], [86].

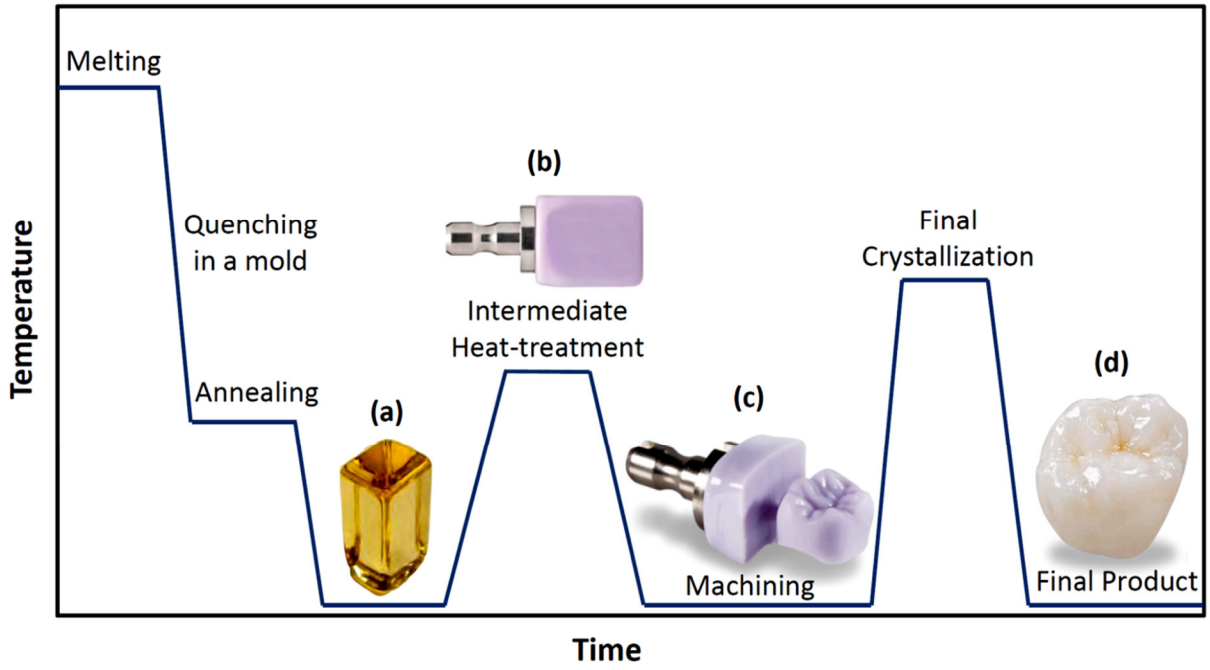

Figure 38- Various stages for the CAD/CAM fabrication of lithium disilicate glass-ceramics. Modified from [4] with permission from Wiley.

Lien et al. [344] showed the GCs formation through controlled crystallization and investigated the effect of intermediate heat treatment at the different temperatures on the final microstructure and lithium disilicate glass-ceramic properties (IPS e.max® CAD). In the higher

than 780 °C, irregularly oblate crystals of $Li_2O–2SiO_2$ were obtained, while at the temperature between 590 °C and 780 °C, spherical-like phases of $Li_2O–SiO_2$, $Li_2O–2SiO_2$, and Li_3PO_4 predominated. At lower temperatures, the finely knitted mesh of $Li_2O–SiO_2$ emerged. Lien et al. demonstrated that the $Li_2O–2SiO_2$ crystals growth was related to the minimum temperature threshold (780 °C) and independent of the overall heating time. At high temperatures, up to 840 °C, the improved properties, high flexural strength, fracture toughness, and elastic modulus were obtained [344]. To support this report, Simba et al. revealed that by heat-treating lithium metasilicate (Li_2SiO_3) at 820 °C, 830 °C and 840 °C for 7 min, the lithium disilicate ($Li_2Si_2O_5$) phases formed and reduced amorphous phase is detected at higher temperature [345,346]. Besides, the result of this research showed that the onset of crystallization temperature of lithium disilicate is 814 °C. They also indicated that the higher crystallization phase and amount of the $Li_2Si_2O_5$ phase can provide improved mechanical properties like the reduction of the hardness (preferred for CAD/CAM), enhanced fracture toughness, and improvement of the bending strength [346]. In addition, the size of the crystalline lithium metasilicate increase by passing the time and temperature [325]. In other research, Chung *et al.* [347] have reported the flexural strength of lithium disilicate glass-ceramic (IPS Empress® II) will be decreased by repeated heat-pressing. As a result, dental lithium disilicate ceramics with high flexural strength (350 MPa) and fracture toughness (2.9 MPa) [348–355]. It was also revealed that the densification by spark plasma sintering (SPS) was feasible for processing LS2 GCs (IPS e.max® CAD). The outcome was a textured and fine-grained microstructure of LS2 GC, which could be useful in the dental CAD/CAM materials [356]. Lithium disilicate GCs with different translucencies depicted different biaxial flexural strength and translucent parameters values [357].

Baumgartner et al. indicted for the first time that stereolithographic ceramic manufacturing (LCM) can be used to the reliable lithium disilicate GCs samples with promising mechanical properties and aesthetics and meets the requirement for dental restorations [358].

In the case of compositional development, it is proven that ZrO_2 has a more benefit on the strength and crystallization of lithium disilicate GCs by using crystal growth, hampering and adjusting the translucency [353,359]. 10 wt.% ZrO_2 dissolved in the residual glass provides a desirable toughness for new commercial lithium disilicate glass-ceramics for CAD/CAM. The higher amount of the ZrO_2 content results in lower crystallization, and the higher crystallization temperature leads to crystal growth [384]. Finally, it is important to consider that the monolithic lithium disilicate ceramics' survival rates are high enough (97.4%) to survive up to 5 years post-treatment and survive up to 8 years post-treatment (94.8%) [19].

The current DGCs still show a lower load-bearing capacity than polycrystalline ceramics (e.g., Al_2O_3 and ZrO_2). Therefore, long-span restorative and high-stress areas (e.g., 3-unit bridges, implant abutments, etc.) are restricted to ZrO_2, Al_2O_3, or metals. Belli *et al.* [360] designed a new method for strengthening these materials to discover reinforcing sites by the microstructural preparation of lithium disilicate (LS2) GCs. This method revealed needle-like $Li_2Si_2O_5$ crystals in the LS2 GCs that deflect propagating cracks. In order to provide high mechanical anisotropy, crystals should align in patterns by heat-pressing of the glass melt through specifically oriented injection channels (**Figure 39**) [360]. A strong anisotropic of LS2 GCs, resulting in higher fracture energies than that found for the isotropic 3Y-TZP ceramic, was discovered [360].

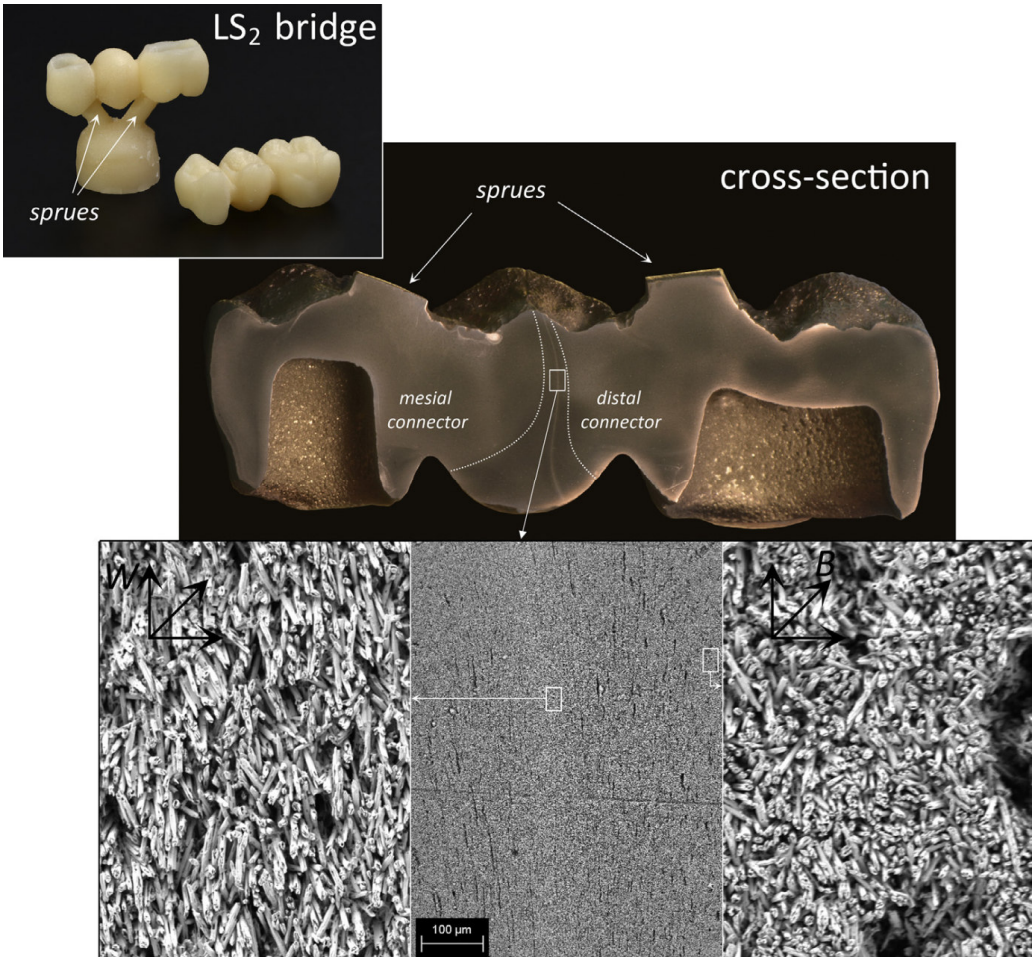

Figure 39- Cross-section of a LS2 dental bridge showing the crystal alignment pattern. Different crystal orientations can be distinguished on the gold-sputtered cross-section from the different "shadows" on the surface. An S-shaped bundle of parallel crystals formed orthogonal to the long-axis of the bridge to the left of the distal connector, right at the midspan. Around it, in the area defined by the dotted lines, crystals follow a distinct orientation due to the convex geometry of the artificial tooth pontic. Mixed orientation patterns formed above the distal connector, leading to negative crack deflection angles and wavy fracture surfaces, all caused improved mechanical properties [360].

6.1.4. Apatite-based glass-ceramics

Apatite glass-ceramic is another type of materials used for dental restorative material as a veneer containing fluorine, with the formation of fluorapatite ($Ca_5(PO_4)_3F$) and enhanced chemical properties[9]. Also, in order to adjust the wear behavior to that of the natural tooth, and

promote optical properties like the translucency, different kinds of GCs are veneered with an appropriate apatite-containing GC by a pressureless sintering process, which is commonly available in all classical tooth shades [4,16]. Researchers fabricated restorations containing needle-like apatite building blocks, similar to those of natural teeth. The needle-like apatite crystals positively have an influence on the aesthetic properties and various mechanical properties. Regarding the acid erosion induced by saliva, fluorapatite GCs and antagonistic tooth have a larger wear rate and friction coefficient in the saliva environment than in a dry environment because of the increase of acid erosion induced by saliva and adhesion between the two contact surfaces [361]. However, surface roughness has an insignificant impact on the tribological performance in wet conditions. Lower friction coefficient and wear in dry friction can be obtained by the smooth surface of the fluorapatite GC. Regarding the crystallinity of the fluorapatite phase, it was a research proving that different content of CaO and heat treatment temperature could change the crystallinity of the main fluorapatite crystal [362]. Larger crystallinity can increase the mechanical properties, significantly affecting friction and wear behaviors of the glass-ceramic material. Hsu et al. [363] investigated the dental fluoroapatite GCs performance in the oral environment. They demonstrated that 95% of the fluorapatite GC veneer is the amorphous glassy phase, while $Ca_5(PO_4)_3(OH)/F$ is known as the crystalline phase. In another work done by Hsu and coworker, the protective effect of novel silicon carbide (SiC) coating on the chemical resistance of a fluorapatite GC veneer under different pH conditions as evidenced by decreased weight loss and ion release in solution was investigated [364]. Besides, the fabricated GCs can tolerate the severe pH conditions and improve the restoration longevity by an increase in the chemical resistance and minimizing fracture. In addition, SiC coating not

only minimizes plaque accumulation by providing a smoother surface after corrosion but also reduces secondary caries and periodontal inflammation probability.

6.1.5. Lithium zirconium silicate glass-ceramic

In 1999, Schweiger *et al.* [365] developed the lithium zirconium silicate GCs for a restorative material on ZrO_2 root canal post and implant abutment to modify the ZrO2 linear thermal expansion coefficient (Figure 40). Regarding the enhanced mechanical features and low importance of the aesthetics and the opacity of materials in the posterior region, the GC with 20 wt.% ZrO_2 was shown as the proper material for this region of the mouth. Finally, the linear thermal expansion coefficients for the ZrO_2 are higher than that of GCs. Consequently, a crack-free bond between the GC and the ZrO_2 abutment is formed [16,365]. Souza et al. demonstrated that the presence of some phases like $ZrSiO_4$ for lithium-zirconium and β-spodumene for lithium-zirconium-alumina silicate glass-ceramics resulted in materials with appropriate thermal expansion behavior, which can be modified by adding zirconia or alumina [366].

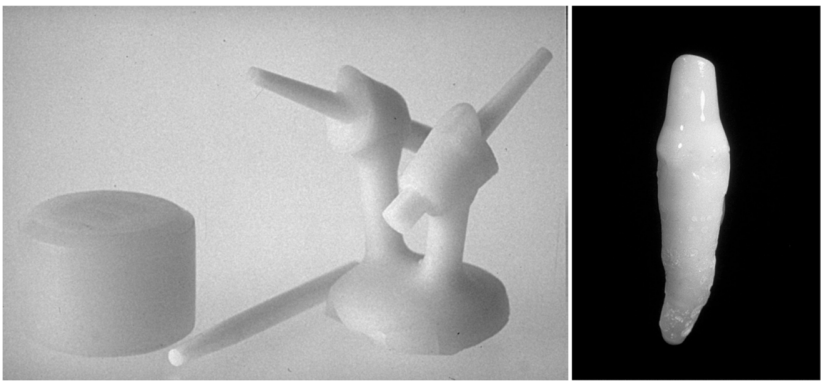

Figure 40- (a) Ingot, cylindrical ZrO_2 post with a conical tip, and an all-ceramic core buildup produced in a hot-pressing procedure using a lithium zirconium silicate glass-ceramic. (b) All-ceramic core buildup on a treated root canal (made by H.P. Foser, Ivoclar Ltd, Schaan, Liechtenstein) [365].

6.1.6. Miscellaneous dental glass-ceramics

Although dental glass-ceramic materials have been attracted a considerable amount of attention for dental applications, compared to metal and ceramics materials, they showed some weaknesses that constrained their application. Glass-ceramics displayed low mechanical strength and fracture toughness which are a negative point for their application as long-term high load-bearing dental implants. Hence, there are still several ongoing attempts and studies to improve their mechanical properties to be able to reach good clinical performance. During this section, the materials that have been designed to overcome this obstacle will be reviewed.

6.1.6.1. Fluorrichterite glass-ceramics

Fluorrichterite-based ($Na_2CaMg_5Si_8O_{22}F_2$) glass-ceramics are known for their high fracture toughness (K_{IC} > 3 MPa.$m^{0.5}$), optical translucency, high resistance to thermal shock, and excellent acid and alkali chemical durability [16]. The obtained mechanical properties are related to the crystalline phase, which is developed during crystallization. In a study conducted by Denry et al. [34], a fluorrichterite glass-ceramic was developed as a dental material. They investigated the role of magnesium content in the system of 67.5SiO_2–2Al_2O_3–12MgO–9CaF_2–4Na_2O–3.5K_2O–1Li_2O–1BaO (wt.%). Results showed that in the sample containing 18 wt.% MgO, both mica and fluorrichterite phase have been crystallized, and the microstructure includes interlocked acicular crystals of fluorrichterite (5-10 micrometers) and mica which leads to promoting crack deflection. Casasola et al. showed that when fluorine content increases in the glass-ceramic material, a modification in the location of the first developed crystals will take place [367]. In another study, they added a variety amounts of sodium to the system of 57.7SiO_2–23.9MgO–6CaF_2–0Na_2O–8.5K_2O–3Li_2O–1BaO (wt.%) [241], which leads to decreasing all transformation

temperatures. It was observed that the viscosity of the glass-ceramics was declined for the samples composed of mica and fluorrichterite and retained after heat treatment at 1000 °C for 4 h. It was also reported that the glass-ceramic sample containing 1.9 wt.% sodium showed the highest mean fracture toughness (2.26 ± 0.15 $MPa.m^{0.5}$), which was not substantially different from the control sample [312]. As illustrated in **Figure 41**, the interlocked sheet-like mica crystals and prismatic fluorrichterite can be seen in the glass-ceramic sample's microstructure. When this glass-ceramic is compared to the mica-based glass-ceramics, the reason behind the substantial increase in fracture toughness might be fluorrichterite's crystallization. The same research group also conducted another study to evaluate the impact of crystallization on the biaxial strength of fluorrichterite glass-ceramics and its microstructure. They concluded two main factors were affecting the flexural strength of fluorrichterite glass-ceramics: duration and temperature of the crystallization heat treatment. It was suggested that this phenomenon happened due to the formation of a low-expansion surface layer composed of roedderite ($K_2Mg_5Si_{12}O_{30}$). The increase of the flexural strength of the glass-ceramic is due to the development of surface compressive stresses, which was promoted by expansion mismatch. Longer duration of heat treatment or higher temperature makes the layer thicker and decreases the surface compressive stresses' intensity and causing a decrease in strength. In order to obtain better mechanical properties and tougher glass-ceramics, other attempts have been made to crystallize different chain silicate minerals, such as diopside or wollastonite, in the vicinity of mica crystals [368–370]. Moreover, other studies synthesized diopside and leucite-diopside glass-ceramics to create mechanically strong and thermally compatible veneers for zirconia restoration to overcome brittle fracture [371,372].

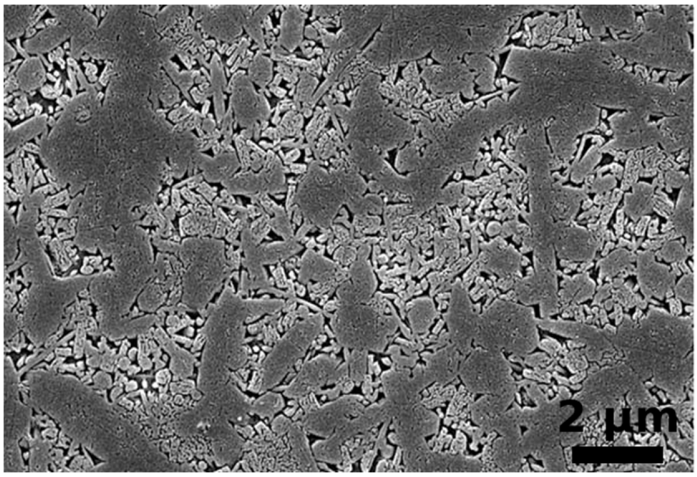

Figure 41- Scanning electron micrograph of mica-fluorrichterite glass-ceramic. The darker area represents prismatic fluorrichterite crystals dispersed in the brighter area of mica crystals. Reproduced from [312] with permission from Elsevier.

6.1.6.2. Fluorcanasite glass-ceramics

Fluorcanasite ($Ca_5Na_4K_2Si_{12}O_{30}F_4$) is another type of double-chain silicate mineral that has been used to increase the strength and fracture toughness of the glass-ceramics [4]. A number of studies have been tried to synthesize fluorcanasite glass-ceramics with appropriate properties to be used as dental material. It was reported that fluorcanasite glass-ceramics which was derived from a system of $60SiO_2–10Na_2O–5K_2O–15CaO–10CaF_2$ (wt.%) can show promising features as a dental material [373,374]. Moreover, in another study, it was reported that fluorcanasite glass-ceramics does not show enough chemical durability to be used as a dental material [349,375]. Therefore, they had tried to address this hurdle by addition of different amounts of Al_2O_3 up to 15 wt.% which was not a successful attempt. While the addition of Al_2O_3 could improve neither chemical durability nor mechanical strength, alumina addition significantly affects the crystal shape, crystal size, aspect ratio, and crystal aggregation characteristics of the fluorcanasite glass-ceramics. In another research, SiO_2 and $AlPO_4$ were systematically added to fluorcanasite glass-ceramic to control its solubility [376]. They managed to reduce solubility

from 2359 to 624 μg/cm^2 (according to ISO 6872). Furthermore, small additions led to an increase in biaxial flexural strength (123-222 MPa). Results displayed that further additions declined the strength to 147 MPa. The authors claimed that their findings are attributed to the increase in volume fraction of residual glassy matrix. In another study, researchers tried to decrease the chemical solubility of these glass-ceramics by changing the contents of K and Na in these glass-ceramics and reported that the solubility of the final product is a function of the alkali species present in the matrix [377]. By changing the glass's alkali ratio (the above composition) from K/(K+Na) = 0.33 to 0.47, it was possible to noticeably decrease the chemical solubility of the glass-ceramic. At the composition of K/Na=7/8, they have reached the minimum chemical solubility. This amount of solubility could be enough for dental core ceramics (standard solubility for dental core ceramics: less than 2000 μg/cm^2). However, this is not enough for direct contact with the mouth environment which needs solubility of less than 100 μg/cm^2 [377,378]. Subsequently, researchers added ZrO_2 to the fluorcanasite glass-ceramic structure and obtained the composition of $61SiO_2$–$6Na_2O$–$8K_2O$–$11CaO$–$12CaF_2$–$2ZrO_2$ (wt.%) [379]. After the heat treatment schedule of 2 h nucleation and 2 h crystallization, they reached the most prominent crystal structure of fluorcanasite phase. The obtained material showed high biaxial flexural strength (250 ± 26 MPa), acceptable chemical solubility (722 ± 177 μg/cm2) and fracture toughness (4.2 ± 0.3 MPa.m$^{0.5}$) and hardness (5.2 ± 0.2 GPa). All these features made this glass-ceramic system a possible candidate to be used as a core material for veneered resin-bonded ceramic restorations. Further studies investigated the strength of the bonding that forms between this glass-ceramic and a composite resin and they proved that this bonding is durable enough without the need for acid etching with HF solution [380]. In another research, fluorcanasite glass-ceramic has been sintered pressurelessly at 1000 °C and they reached an

appropriate relative density of 91.3 ± 0.1 % and desirable mechanical properties (σ = 137 ± 7 MPa and K_{IC} = 2.6 ± 0.1 MPa.$m^{0.5}$) [381]. Takav et al. [382] added different amounts of TiO_2 to the structure of fluorcanasite glass-ceramic (57.1SiO_2–7.4K_2O–9.8Na_2O–13.3CaO and 12.4 CaF_2 (wt %)). They found out that addition of TiO_2 in the glass-ceramic system, declined crystallinity via enhancement of the glass viscosity. They have seen the precipitation of goetzenite ($NaCa_6Ti(Si_2O_7)_2OF_3$) beside calcium fluoride and fluorcanasite phase when more than 6 weight ratios of TiO_2 was added to the glass-ceramic and the final product showed higher chemical resistance. By increasing the amount of TiO_2 content, flexural strength and fracture toughness were decreased because of the simultaneous decrease of crystallinity and interlocking arrangement between the precipitated crystals.

6.1.6.3. Apatite-mullite glass-ceramics

It was in 1995 that Hill et al. [383] introduced apatite-mullite glass-ceramics as a potential candidate to be used as dental material and they reported 33.33SiO_2–11.11P_2O_5–22.22Al_2O_3–22.22CaO–11.11CaF_2 in mol% as the optimum glass-ceramic system. They also performed a heat treatment on the glass-ceramic material and the final product consisted of elongated fluorapatite ($Ca_{10}(PO_4)6F_2$) and mullite ($3Al_2O_3.2SiO_2$) crystals. They also reported that the amount of fracture toughness could be more than 3 MPa.$m^{0.5}$ [383,384]. This glass-ceramic later was synthesized via a heat-pressing technique by reducing the content of Al_2O_3 to develop a dental restoration material [385,386]. It was observed that this reduction adjusted the viscosity for heat pressing. They also concluded that the glasses with various Al_2O_3 contents are easily formed and crystallized to fluorapatite. They also reported the formation of mullite and/or anorthite as the second crystal phase [386]. In another study, it was reported that the addition of

CaF_2 reduces the T_g and T_c of the glass composition [387]. Regarding mechanical properties, it was reported that the sample of $32.6SiO_2$–$10.9P_2O_5$–$20.3Al_2O_3$–$32.6CaO$–$3.6CaF_2$ (mol%) heat-treated for 8 h at 1150 °C could reach the fracture toughness of 2.7 ± 0.4 $MPa.m^{0.5}$. After heat pressing of the same sample for 1 h at 1150 °C, the highest flexural strength of 194 ± 75 MPa was obtained. Longer holding time led to increasing the crystal size and the extent of microcracking in the structure of the glass-ceramic which can negatively affect the flexural strength. Although, it was mentioned that the presence of microcracks can increase the fracture toughness of the final product by the mechanism of crack termination [385]. It should be noted that the main obstacle on the way of using apatite-mullite glass-ceramics as dental ceramics is their relatively high solubility which was then tried to be addressed by varying the CaF_2 content ($4.5SiO_2$–$3Al_2O_3$–$1.5P_2O_5$–$3CaO$–$XCaF_2$ (x = 0.5-3)) [388]. All compositions formed glasses and after heat treatment the crystallization of apatite and apatite-mullite were observed. Increasing the amount of CaF_2, increased bending strength (reached maximum bending strength of 157 ± 15 MPa) as well as the solubility [389]. It was reported that the chemical solubility was 150-380 $\mu g/cm^2$ which was higher than the control glass-ceramic (IPS Empress® II, 78 $\mu g/cm^2$). This amount of solubility can be acceptable for a dental core ceramic [388]. The addition of TiO_2 and ZrO_2 were another attempt to adjust the mechanical properties and solubility of this class of glass-ceramic materials [390,391]. After the addition of different amounts of TiO_2 and ZrO_2 they could achieve the highest bending strength of 174 ± 38 MPa and the lowest solubility of 204 ± 29 $\mu g/cm^2$. They also reported that when the concentration of TiO_2 in the glass-ceramic materials exceeded 2.5 wt.%, a significant increase in solubility and a decrease in bending strength have been observed. Mollazadeh et al. [392] showed that the addition of 3 wt.% TiO_2 and BaO to apatite-mullite glass-ceramics could improve its bending strength and fracture toughness. Still,

the addition of the same concentration of ZrO_2 and an extra amount of SiO_2 had no noteworthy influence. Moreover, they reported that the addition of TiO_2 and BaO could effectively reduce the crystallization temperature of the fluorapatite and mullite crystalline phases, although the addition of ZrO_2 and the extra amounts of SiO_2 increased the crystallization temperature. Regarding the mechanical properties, the sample containing BaO showed the highest strengthening and toughening in comparison to other glasses since this sample was crystallized more extensively rather than the others. The same research group studied the solubility of this glass-ceramic and they reported that after immersion in hot water, the concentration of the released ions of Ca^{2+} and F^- from samples with BaO or with extra amounts of SiO_2 were higher than glass-ceramic samples with TiO_2 and ZrO_2 [393]. The promising features of the apatite-mullite glass-ceramics have been discussed and their high solubility raises concerns about using them in mouth environment. Hence, these materials must be first considered for core build-up.

6.1.7. Survival rates of restorative DGCs

A recent systematic review and meta-analysis reported that survival rates for ceramic inlays, onlays, and overlays including glass-ceramics were from 92% to 95% at 5 years (n = 5,811 restorations) and were 91% at 10 years (n = 2,154 restorations) [394]. Failures were linked to fractures/chipping (4%), followed by endodontic complications (3%), secondary caries (1%), debonding (1%), and severe marginal staining (0%). Odds ratios (95% confidence intervals) were 0.19 (0.04 to 0.96) and 0.54 (0.17 to 1.69) for pulp vitality and type of tooth involved (premolars vs. molars), respectively. Ceramic inlays, onlays, and overlays displayed high survival rates at both 5 and 10 years, and it was reported that the most frequent cause of failure were fractures [394]. Moreover, Fradeani *et al.* [395] studied the survival rate of leucite glass-

ceramic crowns. The period of studied crowns was varied, ranging from 4 to 11 years. The possibility of survival of 125 crowns was 95.2% at 11 years (98.9% in the anterior segment and 84.4% in the posterior segment) and only six crowns had to be replaced. Most of the 119 successful crowns were evaluated as excellent. According to Kaplan-Meier method, the cumulative survival rate of lithium disilicate crowns is 94.8% after 9 years [396]; however, just 71.4% of three-unit bridges survive after 10 years [397]. As a result, it can be noted that crowns which are made of a lithium-disilicate framework can be safely applied in the anterior and posterior regions [396], but a higher risk of fracture is associated with bridges in comparison to metal-porcelain prostheses or other more recently developed ceramic materials, including zirconia and alumina [397,398]. When it comes to the machinable dental glass-ceramics material, LS2 has displayed significant superior clinical survival rates. This has been shown from a recent database retrospective cohort study operated by Belli *et al.* [399]. They aimed to connect the clinical reality and structural investigations on reasons to fracture. To reach this aim, they had gathered the clinical lifetime of approximately 35.000 all-ceramic restorations placed over 3.5 years (**Figure 42**); among them 491 fractures were reported. The study also showed a trend of clinicians replacing the use of leucite-based glass-ceramics towards the LS2 glass-ceramics for inlays, onlays, crowns and ZrO_2-supported bridges. They concluded that LS2 glass-ceramics increasingly gain more attention and acceptability and use within clinical indications [399].

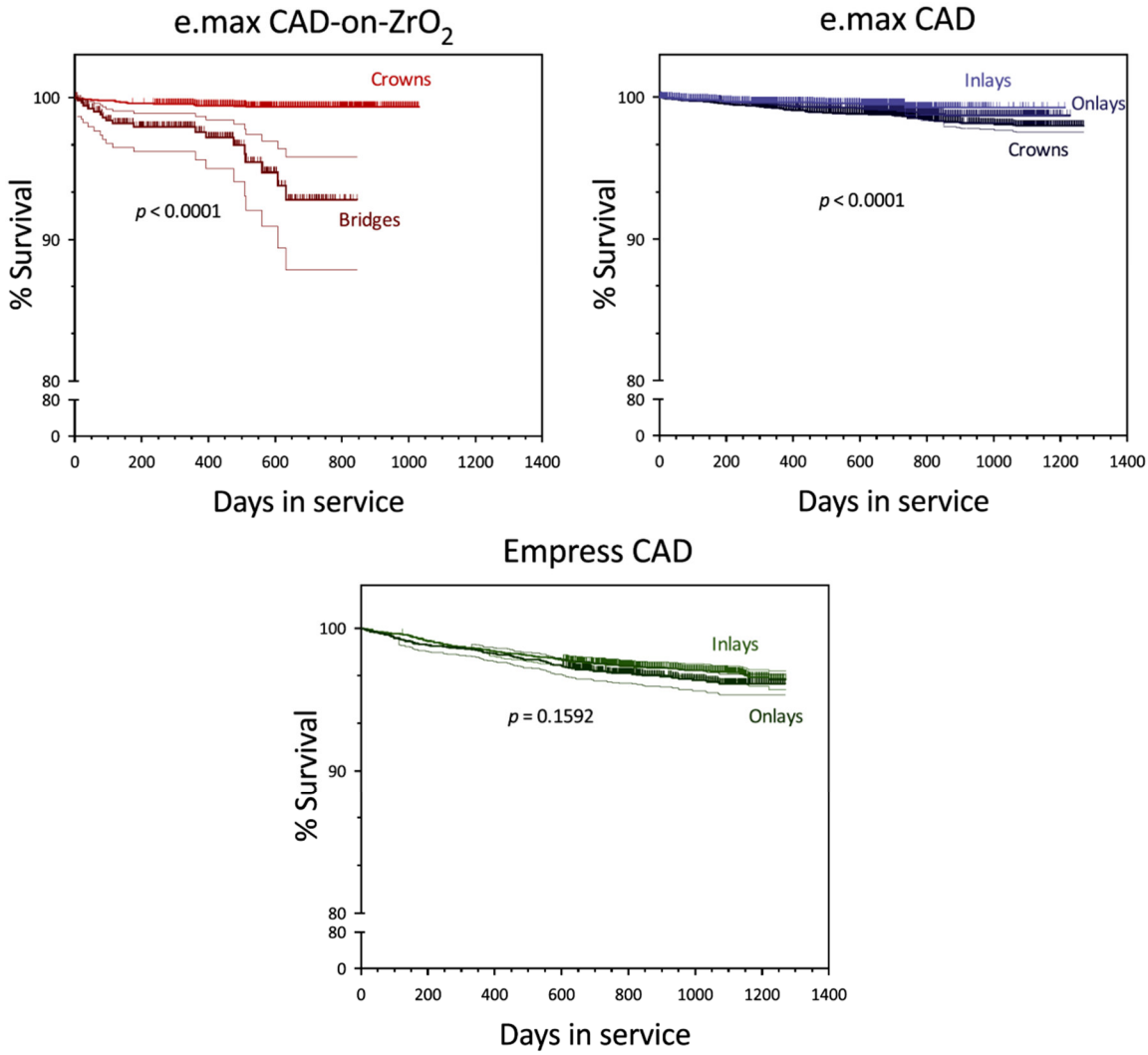

Figure 42- Kaplan-Meier survival curves comparing the restoration type for the same restorative system. IPS e.max CAD and IPS Empress CAD are lithium disilicate and leucite-based glass-ceramics, respectively [399].

6.2. Bioactive DGCs

6.2.1. Hypersensitivity treatment

Dentinal, cervical and root sensitivity/hypersensitivity (DS/DH, CS/CH and RS/RH, respectively) are all medical expressions indiscriminately used to indicate a very common

clinical condition characterized by the exposure of dentinal tubules, commonly caused by gingival recession or enamel wear [400,401].

Clinically, DH can be defined as a short and sharp pain arising from the exposed dentine in response to thermal, evaporative, tactile, osmotic or chemical stimuli, which cannot be attributed to any other dental defect [402].

Nowadays, the high incidence of DH on the world population makes it one of the most relevant problems in dental health, affecting patients of any age group and sex. The most common risk factors for developing a DH disorder can be related both to the presence of specific pathological conditions, i.e., bulimia, xerostomia, ageing-derived gingival recession and periodontal diseases, and to bad dental care and eating habits, including overbrushing, consumption of acid food/drinks, smoking and tobacco chewing [403].

For a successful management of DH, the cooperation between dentists and patients is a key point for an early and accurate diagnosis, usually carried out by the assessment of the severity of the disorder. To date, several methods have been proposed and clinically used for the treatment of DH; however, despite all the efforts, most of them are still considered almost unsatisfactory, with minimal effects on improving the quality of patients' lives [404,405].

Understanding the origin of the DH disorder is fundamental for developing effective therapeutic strategies.

In literature, three different mechanisms of DH have been described: i) the odontoblastic transduction theory, ii) the neural theory, and iii) the hydrodynamic theory [406], but, actually, only the third theory, based on the movements of fluids inside the dentinal tubules, seems to be supported by scientific evidence.

The first theory, in fact, assumes that odontoblasts act as receptors, despite they are commonly recognized to be matrix-forming, not-excitable cells and the existence of synapses between odontoblasts and nerve terminals has not yet been proven [407,408].

The neural theory is an extension of the previous one and associates the exaggerate response to stimuli to the mechanical stimulation of nerve endings, responsible for the generation of action potentials; however, there is lack of experimental evidence of the innervation of outer dentine, despite its very high sensitivity [406].

The last theory was proposed for the first time by Brannstrom and coworkers, who attributed the sharp dentinal pain to hydrodynamic phenomena, i.e., the movement of fluids within dentinal tubules which stimulates pressure-sensitive nerve receptors, thus leading to the transmission of the stimuli. Unlike the previous two theories, which are considered too weak due to the lack of supporting evidence, the widely open tubules observed by scanning electron microscopy (SEM) on the dentinal surface in people suffering from DH significantly corroborate this hypothesis [409,410].

Current treatment strategies for DH include both at-home and in-office procedures and are mainly based on nerve desensitization, anti-inflammatory agents, covering or plugging dentinal tubules, periodontal soft tissue grafting, crown placement/restorative materials and lasers [406].

In particular, consistently with the hydrodynamic theory, several efforts have been made in the development of dental materials able to stop the sensitive mechanism by the closure of open dentinal tubules, such as fluorides, oxalates, varnishes, cements and even BGs [405].

The first use of BGs in the treatment of hypersensitivity dates back to 2004, when 45S5 Bioglass® was added to Sensodyne toothpaste in the form of a very fine particulate (NovaMin,

grain size: 18 μm) in order to be used as abrasive agent instead of conventional alumina particles (NovaMin Technology, FL; now owned by GlaxoSmithKline, UK) [116].

Clinical studies showed that the mechanism of bioactivity of 45S5 Bioglass® with the consequent deposition of HA on the surface of the dentin was truly effective in creating a bonding surface compositionally similar to tooth enamel, thus closing the widely open dentinal tubules and alleviating the painful symptomatology, along with other beneficial effects such as reduction in gingival bleeding and delay in plaque growth [411].

Based on the same operating mechanism, bioactive glass-ceramics could exhibit a potential added value in DH treatment compared to BGs, which is directly related to the partial devitrification of the material upon heating: the presence of crystalline phases, indeed, yields the absence of sharp cutting surfaces that are typical of mechanically-ground glassy materials and can determine nasty side effects, such as gum irritation, bleeding and enamel damage during daily brushing routine [4]. Thus, bioactive glass-ceramics deserve to be considered as a promising and valuable alternative in this specific application field: the mechanism of action of bioactive glass-ceramics is, in fact, comparable to that of BGs and thus suitable for an efficient occlusion of open dentinal tubules.

In this regard, Biosilicate® represents the most significant example among bioactive glass-ceramics used so far for the management of DH disorder (and not only), with enthusiastic results both *in vitro* and *in vivo*. In the past Biosilicate® was defined as a multipurpose material due to its many remarkable qualities, including osteoconductivity, osteoinductivity, non-cytotoxicity, non-genotoxicity, antibacterial effect, exceptional *in vitro* bioactive potential (very close to that of 45S5 Bioglass®) as well as fair machinability, thus being potentially suitable for the fabrication of implants with different shapes for multiple specific applications [412]. Biosilicate®

is a highly bioactive glass-ceramic ($23.75Na_2O–23.75CaO–48.5SiO_2–2.4P_2O_5$, wt.%), which, under controlled double-stage heat treatments, can be engineered to compose one or two crystalline phases: a sodium–calcium silicate ($Na_2CaSi_2O_6$) or both $Na_2CaSi_2O_6$ and a sodium–calcium phosphate ($NaCaPO_4$) phase [412].

Preliminary clinical tests demonstrated the capability Biosilicate® powders to efficiently occlude dentinal tubules due to a rapid reaction with the surrounding physiological environment and, in 2007, a new patent (WO 2004074199A1) with title: "Process and compositions for preparing particulate, bioactive or resorbable biosilicates for use in the treatment of oral ailments" was granted [413].

Subsequent studies, carried out by Tirapelli and coworkers, confirmed the efficacy of Biosilicate® in the treatment of DH disorder [414]. The glass-ceramic used in the study was in the form of micrometric particles comprising the single $Na_2CaSi_2O_6$ crystalline phase. A dentin disc model was employed to compare dentinal tubule occlusion determined by the use of different products, as well as the deposition of HA on dentin surface following the use of Biosilicate®, after a single application. SEM micrographs after 1, 12 and 24 h of immersion in artificial saliva are shown in **Figure 43** [409].

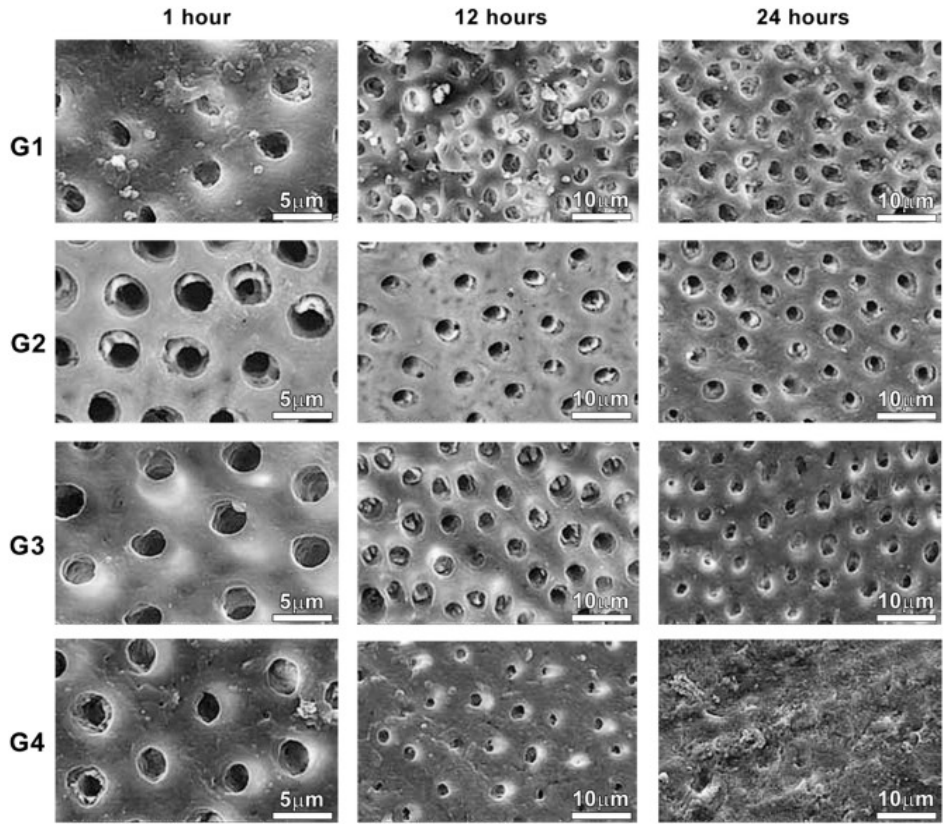

Figure 43- SEM analysis of dentin discoidal samples soaked into artificial saliva at different time points. G1- Dentifrice with potassium nitrate and fluoride; G2- Two-step calcium phosphate precipitation treatment; G3- Water-free gel containing Biosilicate® particles (1%); G4- Biosilicate® particles mixed with distilled water in a 1:10 ratio. Reproduced from [414].

Biosilicate® mixed with distilled water in a 1:10 ratio was able to induce the precipitation of a thick HA layer after just 24 h of immersion, leading to the complete occlusion of dentinal tubules [414].

One year later, a clinical study was performed on 120 volunteers (230 teeth) in order to compare the effect of Biosilicate® particles (1-20 μm) with other commercially available products for the treatment of DH disorder [415]. The patients were divided into 4 groups, according to the treatment received:

1. G1-Sensodyne®: applied at home daily for 30 days;
2. G2-SensiKill®: applied once a week by a dentist;

3. G3-Biosilicate® incorporated in a 1% water-free-gel: applied at home daily for 30 days;

4. G4-Biosilicate® mixed with distilled water in a 1:10 ratio: applied once a week by a dentist.

Pain level was evaluated by means of a visual analogue scale (VAS) weekly during the treatment and during a 6-month follow-up period. Although all the products were efficient in the management of DH disorder, Biosilicate® mixed with distilled water (G4 group) had the greatest effect in reducing pain during the first period of the experiment, providing an immediate, effective and long-lasting benefit as compared to the other desensitizing agents [415].

In 2015, another clinical study investigated the *in-situ* influence of Biosilicate® particles on whitened enamel and dentin surfaces after tooth bleaching procedure, which may induce transient tooth sensitivity (TS) [416]. 140 participants without TS received 16% carbamide peroxide (14 days-04 h each) (T1) or 35% hydrogen peroxide (single session-45 min) (T2). Participants used concomitantly (10 per group):

1. desensitizing dentifrices (D1-experimental bioactive glass-ceramic; D2-commercial potassium nitrate; D3-commercial calcium and sodium phosphosilicate) in-home, daily

2. desensitizing pastes (D4-experimental bioactive glass-ceramic; D5-experimental 45S5 Bioglass®; D6-commercial calcium phosphate), in-office, immediately after the treatment and more 4 times.

3. No desensitizing agent (control group).

This study showed that Biosilicate® was also able to improve hardness of the tooth, thus preventing demineralization [416].

Another research group in China investigated the efficacy in reducing dentin permeability of a novel bioactive glass-ceramic, named HX-BGC, based on the system SiO_2-P_2O_5-CaO-Na_2O-SrO and developed by the Materials Laboratory at the State Key Laboratory of Oral Diseases, West China Hospital of Stomatology, Sichuan University [417].

The study analyzed dentin discs from human third molars, randomly associated to 5 groups:

1. Group 1: distilled water
2. Group 2: Sensodyne repair toothpaste (Novamin technology)
3. Group 3: HX-BGC toothpaste (with 7.5% HX-BGC)
4. Group 4: control toothpaste without HX-BGC
5. Group 5: HX-BGC powders

Samples of Group 2 and Group 3 (Sensodyne Repair and bioactive glass-ceramic toothpaste, respectively) exhibited a significant and immediate reduction in dentin permeability and the HX-BGC powder group (Group 5) revealed the highest reduction in dentine permeability after only 7 days of treatment, thus indicating the enormous potential of HX-BGC in the treatment of dentine hypersensitivity [417].

One of the latest studies evaluated the potential of a new BG based on the system CaO–P_2O_5–SiO_2–MgO and its glass-ceramic derivative containing whitlockite for the treatment of DH disorder. SEM and AFM analyses confirmed the formation of HA on the surface of the analyzed materials, resulting in the complete occlusion of most of the exposed dentinal tubules [418].

The most relevant studies describing the use of glass-ceramic materials for the treatment of DH disorder are summarized in **Table 10**.

Table 10. Glass-ceramic materials for DH treatment compared to 45S5 Bioglass® (Novamin®).

Material name	Oxide composition	Crystalline phases	Grain size	Clinical application	In vitro studies	In vivo studies	Ref.
Novamin® (45S5 Bioglass)	46.1 SiO_2, 24.4 Na_2O, 26.9 CaO and 2.6 P_2O (mol.%)	None, amorphous	18 µm	DH treatment	Good adhesion to dentine Improved mineralization (calcium phosphate deposition over the dentine tubules)	Good adhesion to dentine and formation of an HA layer compositionally similar to tooth enamel; Occlusion of the dentine tubule; Pain relieve for longer periods; 58.8% reduction in gingival bleeding; 16.4% reduction in plaque growth.	[411,419–421]
Biosilicate®	23.75Na_2O-23.75CaO-48.5SiO_2-2.4P_2O_5, wt.%	$Na_2CaSi_2O_6$	1-20 µm	*DH treatment*	*Environment:* Artificial saliva *Analyzed materials:* G1- Dentifrice with potassium nitrate and fluoride, G2- Two-step calcium-phosphate precipitation treatment, G3- Water-free gel containing Biosilicate® particles (1%), G4- Biosilicate® particles mixed with distilled water in a 1:10 ratio. *Main results:* *G4: Complete occlusion of the tubules after 24 h*	*Clinical trial:* 120 volunteers, 230 teeth *Analyzed materials:* G1-Sensodyne®: applied at home daily for 30 days; G2-SensiKill®: applied once a week by a dentist; G3-Biosilicate® incorporated in a 1% water-free-gel: applied at home daily for 30 days; G4-Biosilicate® mixed with distilled water in a 1:10 ratio: applied once a week by a dentist. *Main results:* *G4: Immediate, effective and long-lasting treatment for patients affected by DH*	[414,415]
Biosilicate®	23.75Na_2O-23.75CaO-48.5SiO_2-2.4P_2O_5, wt.%	$Na_2CaSi_2O_6$	1-20 µm	*Treatment of post-bleaching TS*		*Clinical trial:* 140 partecipants without TS *Analyzed materials:* Desensitizing dentifrices (D1-experimental bioactive glass-ceramic; D2-commercial potassium nitrate; D3-commercial calcium and sodium phosphosilicate) in-home, daily; Desensitizing pastes (D4-experimental bioactive glass-ceramic; D5-experimental Bioglass type 45S5; D6-commercial calcium phosphate), in-office, immediately after the treatment and more 4 times; No desensitizing agent	[416]

						(control group). *Main results:* *Improved tooth hardness and hindered demineralization*	
HX-BGC	SiO_2-P_2O_5-CaO-Na_2O-SrO	$NaCaPO_4$ Hydroxylapatite	N.A.	*DH treatment*	*Environment:* Artificial saliva *Analyzed materials:* Distilled water, Sensodyne Repair toothpaste (NovaMin technology), Control toothpaste, Pure HX-BGC *Results:* Dentine permeability data expressed as per cent of maximum values: Immediately after treatment: 49.0±8.8; After 24h: 41.0±16.1; After 1 week: 21.3±10.1 *Overall performances comparable to commercial Sensodyne Repair toothpaste*	N.A.	[417]
Whitlockite glass-ceramic	3CaO-P_2O_5- SiO_2-MgO	Whitlokite	N.A.	*DH treatment*	*Environment:* Artificial saliva *Analyzed materials:* *G1 - Negative Control (no treatment); G2 - Positive Control (treated by Bioglass® 45S5); G3 – BG (treated by bioactive glass based on 3CaO.P2O5-SiO2-MgO-system); G4 – BGC (treated by bioactive whitlockite glass-ceramics).* *Results:* *The material promoted the formation of HA on the demineralized dentine, similarly to Bioglass® 45S5.*	N.A.	[419]

6.2.2. Scaffolds for engineering/healing supporting bone or restoring dental tissues

Most common approaches in replacement of dental tissues are based on non-biological substitutes, but they comprise several disadvantages, such as uncomfortable sensation, low biocompatibility, and damage to surrounding tissue. Although different scaffold-based procedures have been employed in tooth regeneration (e.g., long-lasting ceramic, polymeric, collagen, chitosan scaffolds [422–426]), the use of scaffolds that are really able to regenerate dental tissues involves several complications depending on constituent materials. For example, polymeric scaffolds could trigger a nonspecific inflammatory response and the by-products derived from their degradation may stimulate adverse effects on dental tissue formation [427,428].

Bioactive BG/glass-ceramic scaffolds potentially exhibit important advantages compared to polymeric ones, such as tailored porous structure and chemical composition that stimulates mineralization of the extracellular matrix, as well as the absence of toxic degradation products [429]. On the other hand, structure complexity and porosity sometimes confer to BG/glass-ceramic scaffolds an intrinsic brittleness which make them awkward to handle and fit in small defects. For this reason, as mentioned in the section 4.2.1, dental surgeons often still prefer to employ powders or injectable cements to restore dental defects thanks to their mouldability and possibility to easily and perfectly fit the injured zone.

Therefore, clinical application of 3D BG and glass-ceramic scaffolds in dentistry still is an open challenge. Recently, several research groups have focused their attention on the possibility to employ properly-doped BG scaffolds for specific dental disease, such as periodontitis (**Figure 44**).

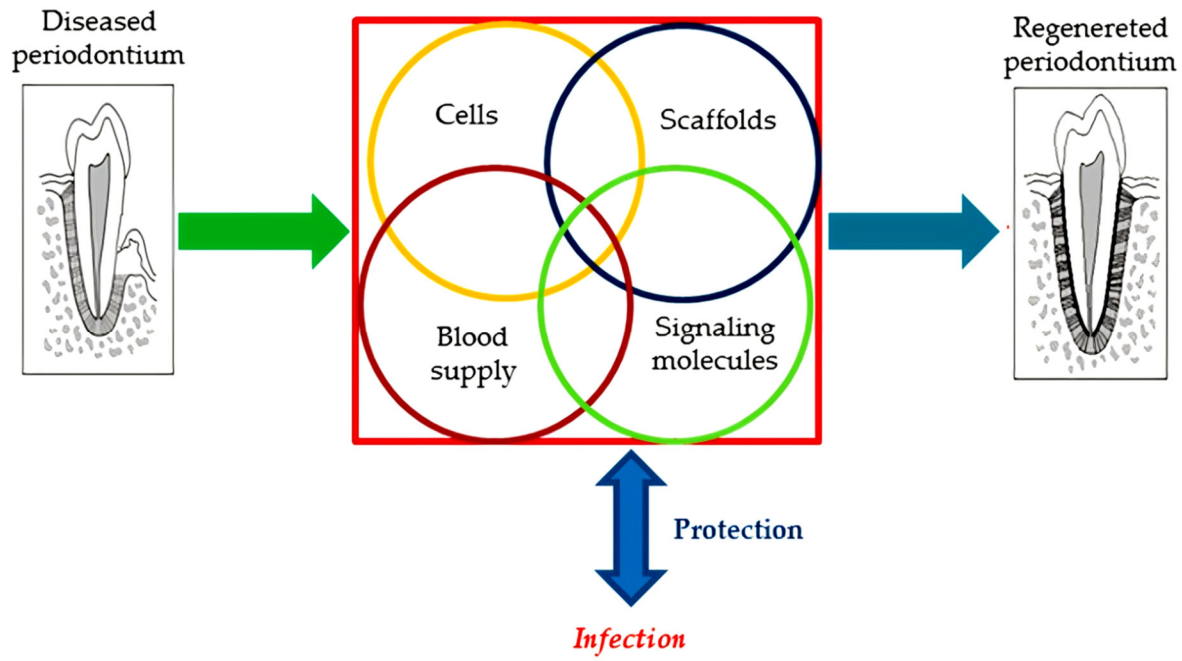

Figure 44- Schematic representation of scaffolds involvement in periodontal regeneration [430].

A study conducted by Han *et al.* [431] has investigated the influence of lithium (Li) in MBG scaffolds. Results have shown biological effects of Li ions released from bioactive scaffolds on cementogenesis in periodontal tissue applications, particularly on cementogenic differentiation of human periodontal ligament-derived cells (hPDLCs). In this study, Li-doped MBG scaffolds were fabricated by using a co-templating approach (Pluronic P123 and foam replication to generate mesopores and macropores, respectively) [431]. These hierarchical scaffolds exhibited a well-ordered structure and uniform mesoporous channels with pore size of 5 nm. Attachment and proliferation of hPDLCs were examined by SEM analysis for three different Li concentrations (0%Li, 2%Li, 5%Li) (**Figure 45**). Alkaline phosphatase (ALP) activity and calcium concentration of hPDLCs were also assessed in vitro to provide a complete biological evaluation. It was found that the incorporation of 5% Li into MBG scaffolds significantly improved cell proliferation and cementogenic differentiation in hPDLCs, and lithium incorporation generally

enhanced cell growth and ALP activity. This study suggests that Li-doped MBG scaffolds can have a promising potential for applications in periodontal tissue engineering (**Figure 46**) [431].

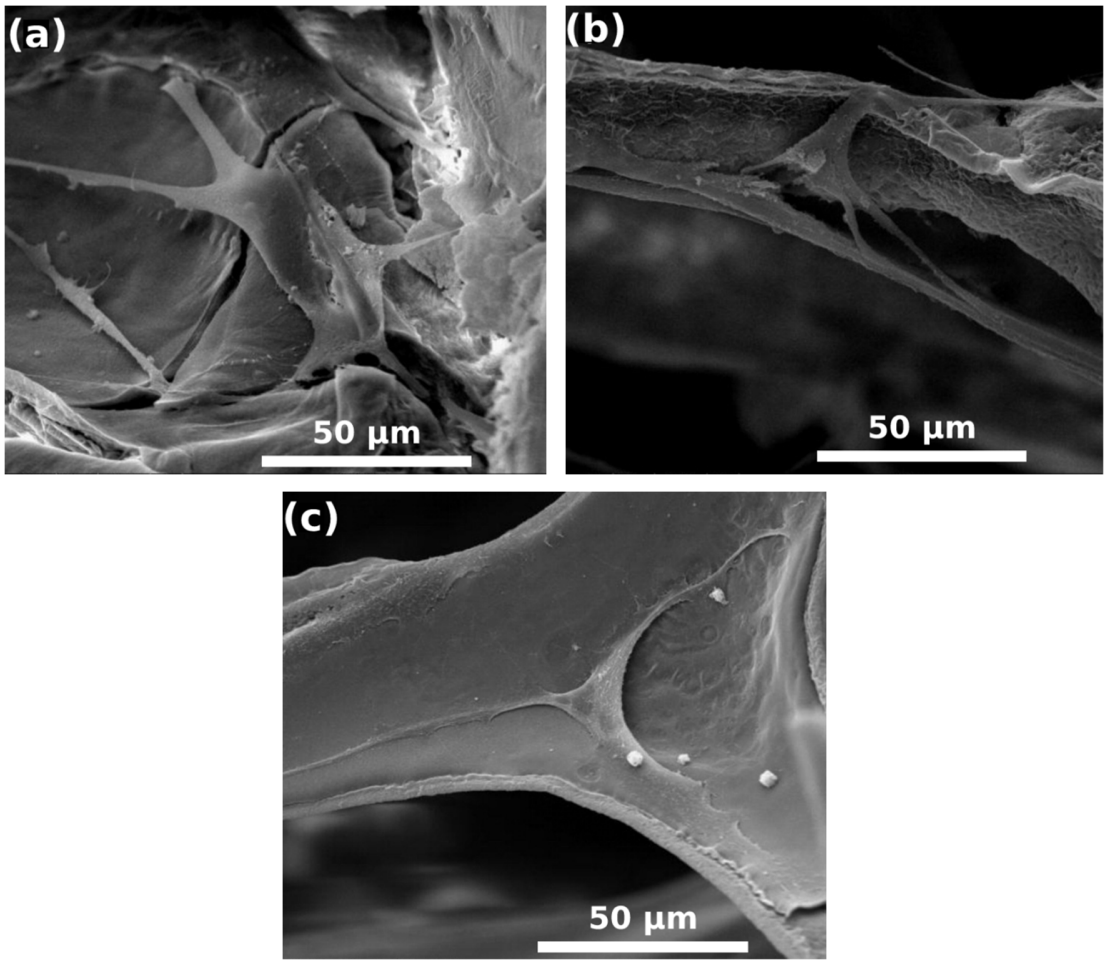

Figure 45- hPLDCs attachment on 0Li-MBG (a), 2Li-MBG (b), and 5Li-MBG scaffolds after culturing for 7 days. Reproduced from [431] with permission from Elsevier.

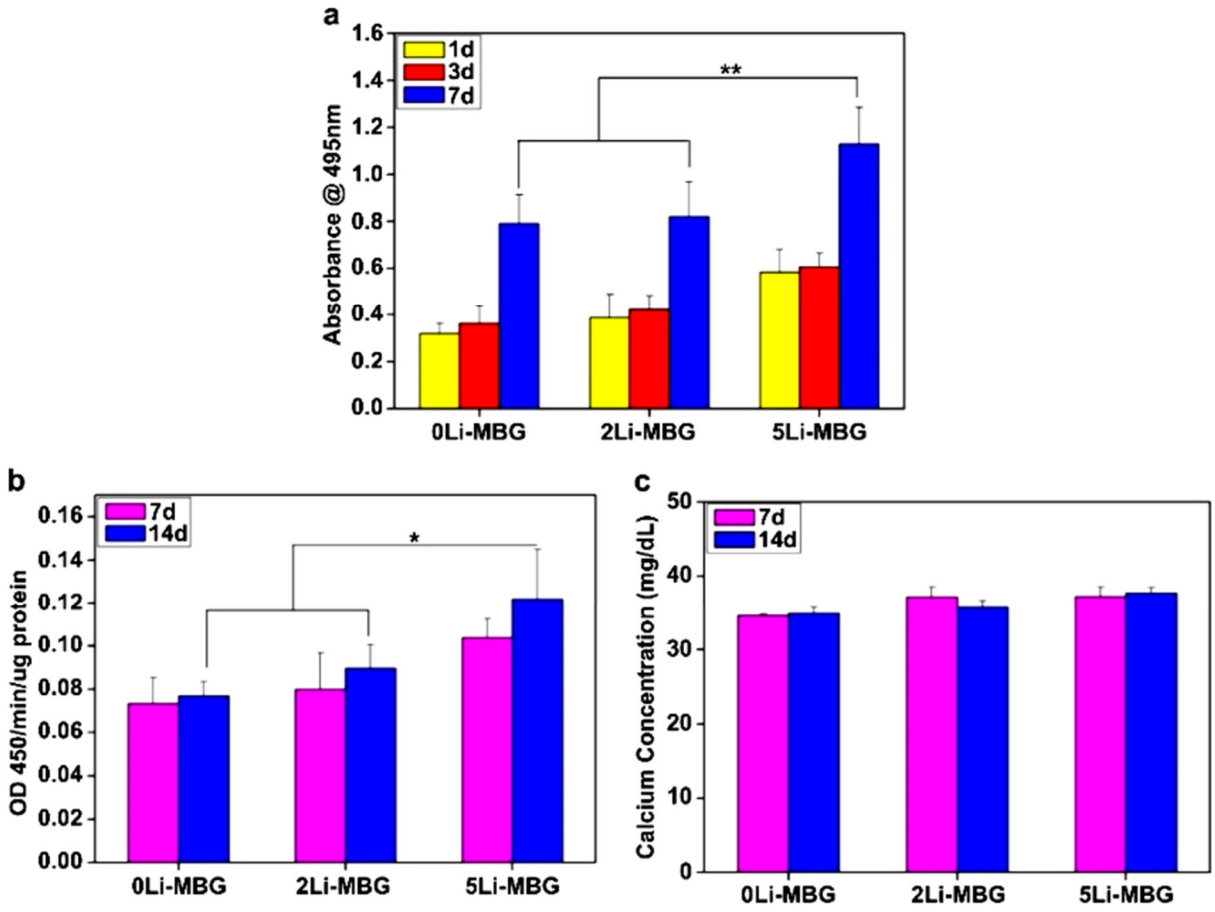

Figure 46- The cell proliferation (a), relative ALP activity (b), and calcium mineralization of hPDLCs (c) at three different Li concentration [431].

Another attractive study in the context of periodontal regeneration was conducted by Zhang et al. [432], who developed strontium-incorporated MBG scaffolds and tested them *in vivo* (rat model). The aim of this work was to determine if strontium introduction could have some beneficial effects on bone regeneration, and in particular if Sr-doped MBG scaffolds could be employed in the treatment of alveolar bone defects typical of periodontal disease. These scaffolds were implanted in acute-type periodontal defects in rats demonstrating, for the first time, that incorporation of Sr in MBG scaffolds enhanced alveolar bone formation as compared to Sr-free MBG scaffolds [432].

The MBG scaffolds described above, being rigid, suffer from difficult intraoperative shapability; in the attempt to overcome this apparently unavoidable drawback, a very interesting example of "moldable" BG scaffold was reported by Poologasundarampillai et al. [433], who prepared hierarchical sol-gel BG fibrous scaffolds ($70SiO_2$–30CaO mol%) by electrospinning. This "wool-like" bioactive material (fiber diameter 0.5-2.0 μm) has significant advantages over a rigid scaffold or granular filler used as a dental bone graft substitute (**Figure 47**).

As a matter of fact, the studies described above deal with fully amorphous BG scaffolds rather than partially crystalline structures; in these cases, crystallization was deliberately avoided as it would reduce or even destroy the mesoporous texture, thus inhibiting the peculiar properties of these materials (high specific surface area, high bioactivity, sustained ion delivery etc.).

Pointing to the future, a study deserves to be mentioned where the feasibility of a bilayered dental implant, formed by two different glass-ceramic materials, was explored [434]. The idea was to develop a single-piece implant comprising a bioactive "bottom layer", which can promote osteointegration with the alveolar bone (root substitution), and an aesthetic bioinert "top layer". This ambitious approach aims at the substitution of the whole tooth that was lost. Although a simple, non-porous prototype was prepared in this early work by differential compaction of glass powders followed by one-step sintering, more sophisticated evolutions can be figured out, for example comprising a bioactive porous glass-ceramic (i.e. a scaffold) implanted at the root extraction site.

In summary, BG and glass-ceramic scaffolds show great promise for dental applications: this field has very interesting perspectives in biomaterials science as well as challenging technological and functional aspects to be investigated.

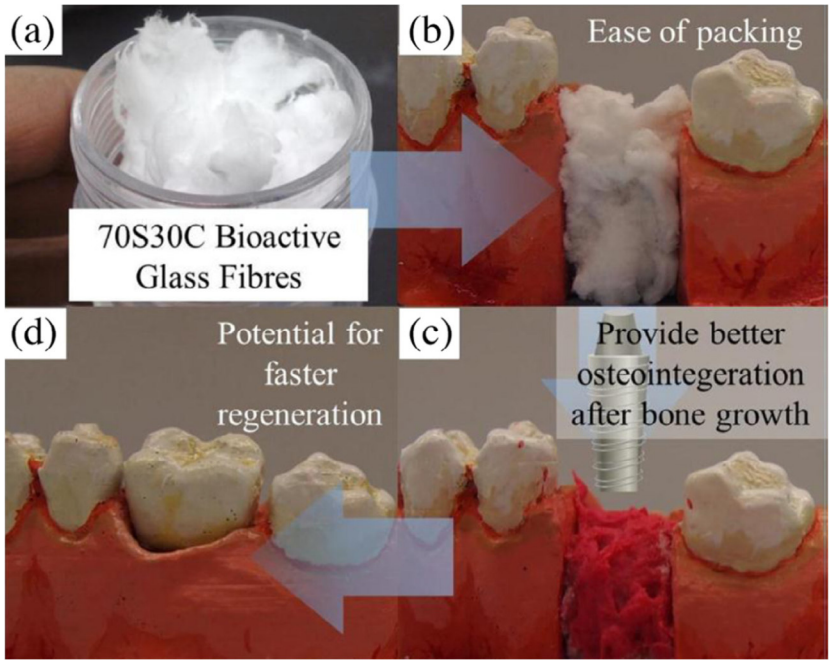

Figure 47- Demonstration of ease of packing of (a) "wool-like" BG in a (b) tooth extraction socket, (c) insertion of implant following bone regeneration and (d) crown placement [433].

6.2.3. Demand for tough bioactive dental implants

As previously illustrated, the advent of a new generation of biomaterials, to which BGs belong, has carried different appealing properties, such as osteoconduction, osteoinduction, ability to bond both hard and soft tissues, which can be used in a variety of applications in dentistry, for example as bone grafts (e.g., restoration of alveolar bone lost in periodontal disease, implantation in tooth extraction sites) or bioactive toothpaste for DH [4].

However, the use of BGs for clinical applications in dentistry is mainly limited by their low mechanical strength and fracture toughness, which compromise their employment in those practices where the implant is subjected to significant loads and stresses, as often occurs in dental request [4]. This drawback can be compensated by the use of partially crystallized glasses. After 1973, when the first commercial glass-ceramic (Ceravital®) was developed, the demand for tougher bioactive materials impressively rose up all around the world [4].

Glass-ceramic biomaterials are realized by controlled nucleation and crystallization processes of glasses, which confer to them new final properties. These physical, mechanical and biological properties can be properly tailored through the variation of the glass composition or heat treatment conditions [16]. For example, considering aluminosilicate glasses and glass-ceramics, oxygen can be replaced by nitrogen so that elastic modulus and hardness linearly increase with nitrogen content in the composition [111].

Another strategy has been developed from Saadaldin et al. [435] who deeply studied crystallization mechanisms and kinetics with the aim to produce tougher bioactive materials. In 2012, their first study [435] concerned the development of a machinable miserite glass-ceramic for dental implant applications. Miserite is a bioactive and biocompatible crystalline phase which has never previously been employed as biomaterials for dental applications. Following a deep thermal analysis, glass-ceramic samples were processed by different heat treatments and their mechanical properties were evaluated (Table 11). A significative improvement was reported in fracture toughness considering the experimental result obtained from bioactive miserite glass-ceramic.

Table 11. Comparison of stiffness and fracture toughness properties between dental tissue, principal inert materials and experimental bioactive miserite glass-ceramic (GC) [435].

Mechanical Properties	**Dental Tissue**	**Zirconia**	**Titanium**	**45S5 Bioglass**	**Experimental GC**
Young modulus	4-20 GPa	200 GPa	105-116 GPa	70-76 GPa	80-96 GPa
Fracture toughness	4.8 $MPa.m^{0.5}$ (root dentin) 2.1 $MPa.m^{0.5}$ (crown tissue)	6-10 $MPa.m^{0.5}$	28-108 $MPa.m^{0.5}$	0.7-1.1 $MPa.m^{0.5}$	4.77 $MPa.m^{0.5}$

Similar results were reported in the synthesis and characterization of wollastonite glass-ceramics produced by the same scientists [435]. In this experiment, glass-ceramic samples exhibited Young's modulus of 89-100 GPa and fracture toughness about 4.62-5.58 MPa.$m^{0.5}$ [435].

These authors demonstrated that, by properly varying heat treatment conditions, tougher bioactive dental materials can be successfully obtained where bioactive performances are not compromised. This is indeed considered a hot topic in biomaterials science and an intense research is still underway for new approaches to design bioactive implants with improved toughness for dental applications.

6.2.4. Coatings on dental implants

To the best of our knowledge, the use of apatite-wollastonite glass-ceramic is clinically working very well as a coating on the acetabular cup or stem of the implant in total hip arthroplasty [436]. Moreover, over the last two decades, many efforts have been made by several research groups for developing other suitable glass-ceramic coatings on dental implants, too [437].

In the past, the use of PLD technology for the production of BG-based coatings deriving from melt-quenching route has been extensively described by many authors [438–440].

In 2012, Rau and coworkers [441] described for the first time the use of sol-gel derived glass-ceramic targets for the production of innovative glass-ceramic coating (RKKP) to be deposited on Ti substrates. Targets prepared by conventional melt-quenching route were used as controls. In particular, this pioneering study investigated the effect of two different PLD parameters on the quality of the final coatings, i.e., the laser fluence and the temperature of the

deposition substrate. PLD deposition performed at 12 J/cm^2 and 500 °C allowed the deposition of crystalline films guaranteeing an efficient and congruent transfer of the target composition to the coating. The use of sol-gel process for the production of the target material was found to favor the growth of a finer granulated surface, resulting in a more compact and uniform microstructure: the average surface roughness, in fact, was found to be higher in the coating deposited from the melt-derived target compared to the sol-gel one, with values of 17.5 ± 0.5 nm vs. 8.1 ± 0.5 nm, respectively. However, better mechanical properties were observed in the melt-derived RKKP film (thickness 0.6 mm, hardness of 12 GPa) as compared to the sol-gel coating (thickness 4.3 mm, hardness of 17 GPa [441].

In 2014, a novel glass-ceramic, called M2 with nominal composition 43.19CaO–7.68MgO–49.13SiO_2 (wt.%), was applied to a Ti–6Al–4V substrate by using APS technology. Commercial plasma-sprayed HA coatings were used as positive control for the study. The microstructural and morphological properties of the coatings were investigated before and after thermal treatment and bioactivity and cytocompatibility were preliminarily evaluated by soaking tests in simulated body fluids (SBF) and *in vitro* cellular tests to assess the HA-forming ability as well as osteoblast proliferation, differentiation and adhesion. Recrystallization of the coating was observed upon heating and optimal features were identified by sintering at higher temperature: in fact, compared to the positive control, the experimental coating treated at 800 °C exhibited less micro-cracks and the bonding strength of M2 coating to Ti–6Al–4V substrate was 35.43 MPa, nearly twice as much as that of HA coating. *In vitro* bioactivity test revealed a good apatite-forming ability, following a similar mechanism to that of the original M2 glass-ceramic. The mechanism of dissolution of the material, associated to the release of Ca, Mg and silicate ions, led to enhanced osteoblastic activity and promoted cell adhesion, proliferation and differentiation [442].

In the light of the promising results obtained by Chen and coworkers [442], M2 glass-ceramic coatings were recently tested *in vivo* by Zhang et al. [443]. M2-coated Ti-6Al-4V cylinders were prepared by APS and successfully implanted into New Zealand rabbits up to 3 months; the result was compared to HA coating/Ti6Al4V used as positive controls. Both groups showed good bonding with the surrounding tissue and X-ray imaging confirmed that newly-formed bone grew around and towards the implants, while neither foreign body reaction nor tissue necrosis were observed. From the histological sections, it is obvious that the experimental device (**Figure 48b**) was more favorable in inducing osteogenesis and neo-vascularization in the whole process and, compared to the control (**Figure 48a**), demonstrated a better osseointegration with the host bone.

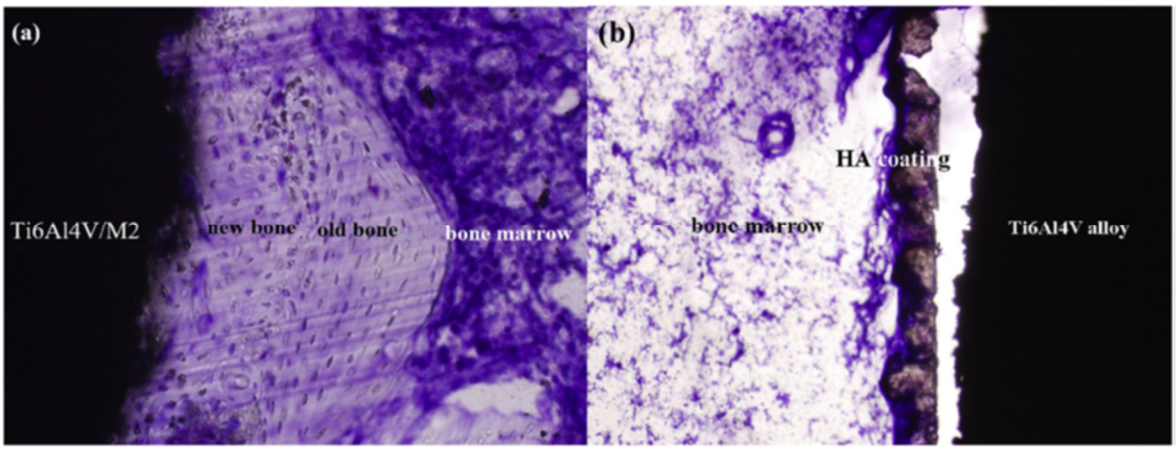

Figure 48- The ability to induce osteogenesis of M2 and HA coatings on Ti6Al4V alloy in bone marrow after 3 months in rabbit. (a) M2 coating; (b) HA coating. Reproduced from [443] with permission from Elsevier.

In summary, these promising results not only confirmed the suitability of M2 glass-ceramic to be used *in vivo* as coating for metallic implant, but also revealed the superior performances of the experimental device compared to the commercial control, indicating the concreate possibility

to substitute conventional HA coatings with the osteogenetic M2 ones in dental and orthopedic load-bearing applications [443].

In the last two decades, liquid precursor plasma spraying (LPPS) has been employed in the synthesis of nanostructured powders and coatings in several application fields. Briefly, the process uses a suspension or a solution as feedstock material, which is then atomized into liquid drops through an atomization nozzle or directly injected into the plasma plume. By LPPS, coatings with nanostructure (nanopores around 20-30 nm) and splat size (less than 5 μm) smaller than those from the conventional APS process can be produced [444,445]. Xiao et al. [446] used LPPS process to manufacture P_2O_5–Na_2O–CaO–SiO_2 bioactive glass-ceramic coatings on Ti substrates. Liquid suspension was used as feedstock, thus avoiding the step required for powders preparation used in conventional APS process. The as-deposited coatings comprised a predominant amorphous phase and a crystalline phase ($Na_2Ca_2Si_3O_9$). From a morphological point of view, the coating was characterized by the presence of various structures, such as pancake-like splats and nanoscale spherical particles (**Figure 49**).

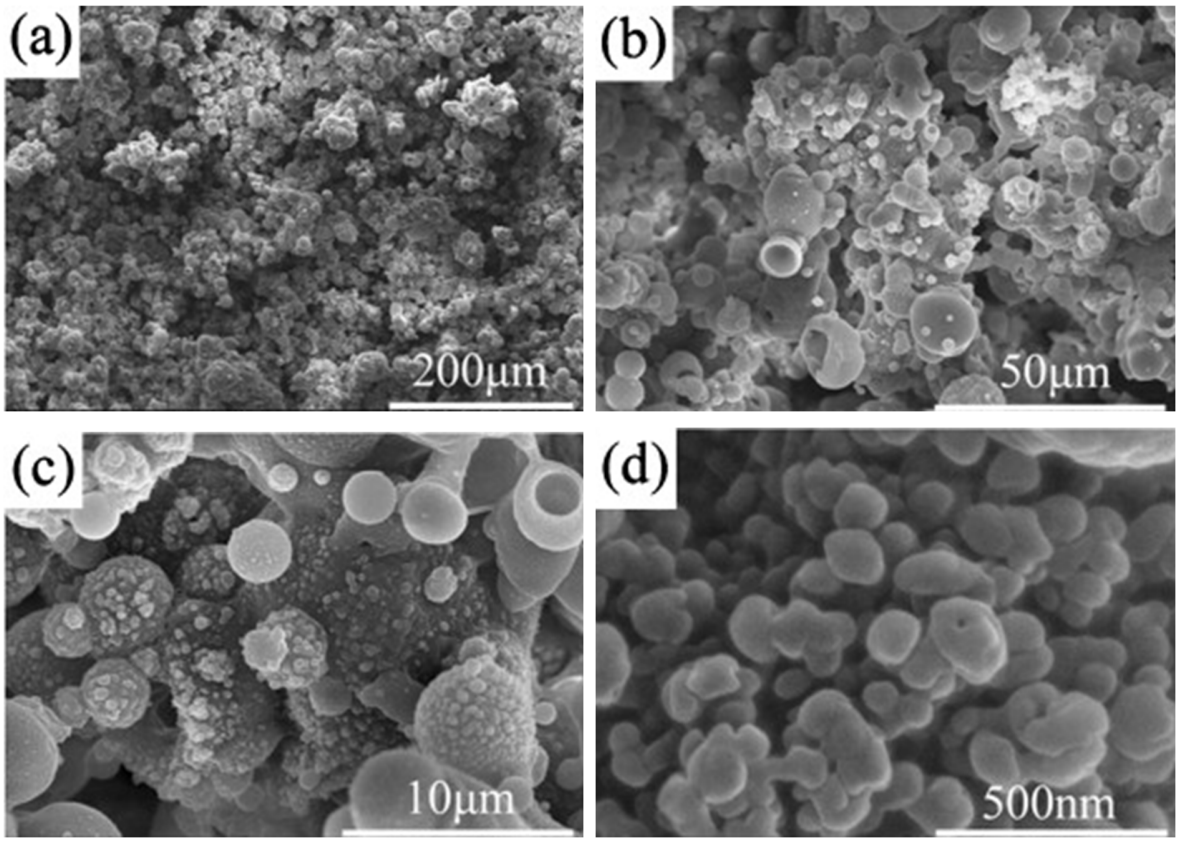

Figure 49- rayed bioactive glass–ceramic coating top surface at different magnifications. Reproduced from [447] with permission from Elsevier.

Soaking tests in SBF revealed a very fast bioactivity mechanism, as HA phase was observed after just 4 h from the beginning of the test, as indicated by XRD and FTIR analyses [446].

In another study, Xiao and coworkers compared P_2O_5–Na_2O–CaO–SiO_2 bioactive glass-ceramic coatings produced using sol and suspension precursor as feedstocks, respectively [447]. Coatings with higher crystallinity were obtained using the sol precursor, while predominantly amorphous nanostructured coatings were synthesized using the suspension precursor. For the latter, the fraction of the amorphous phase increased with the increase in plasma power and the decrease in liquid precursor feed rate. Preliminary bioactivity tests in SBF revealed a good apatite-forming ability: after being immersed for 7 days, the coating materials were completely

covered by plate-like precipitates with length scale of 100-300 nm, corresponding to crystalline hydroxyl carbonate apatite; it was suggested that the presence of a nanostructured surface, resulting from the combination of thermal spraying and sol-gel chemistry, could maximize the interactions between the material and the surrounding environment [447].

Faster HA deposition rates have been proved to favor the osteointegration of the implant, providing mechanical stability in a shorter time. However, it is usually advisable to design biomaterials matching the physiological biomineralization mechanism, thus minimizing the risk of implant failure.

Araújo et al. [448] developed a new BG to be used as coating on ZrO_2-3%Y_2O_3 substrates. The final composition of the glass was obtained by the original formulation of the SiO_2–P_2O_5–CaO–Na_2O–K_2O–MgO–CaF_2 glass, in order to obtain a low Ca/P ratio. A 345 μm-thick, crack-free coating was successfully obtained, thus indicating a good matching between the thermal expansion coefficient of the substrate and the coating (**Figure 50**).

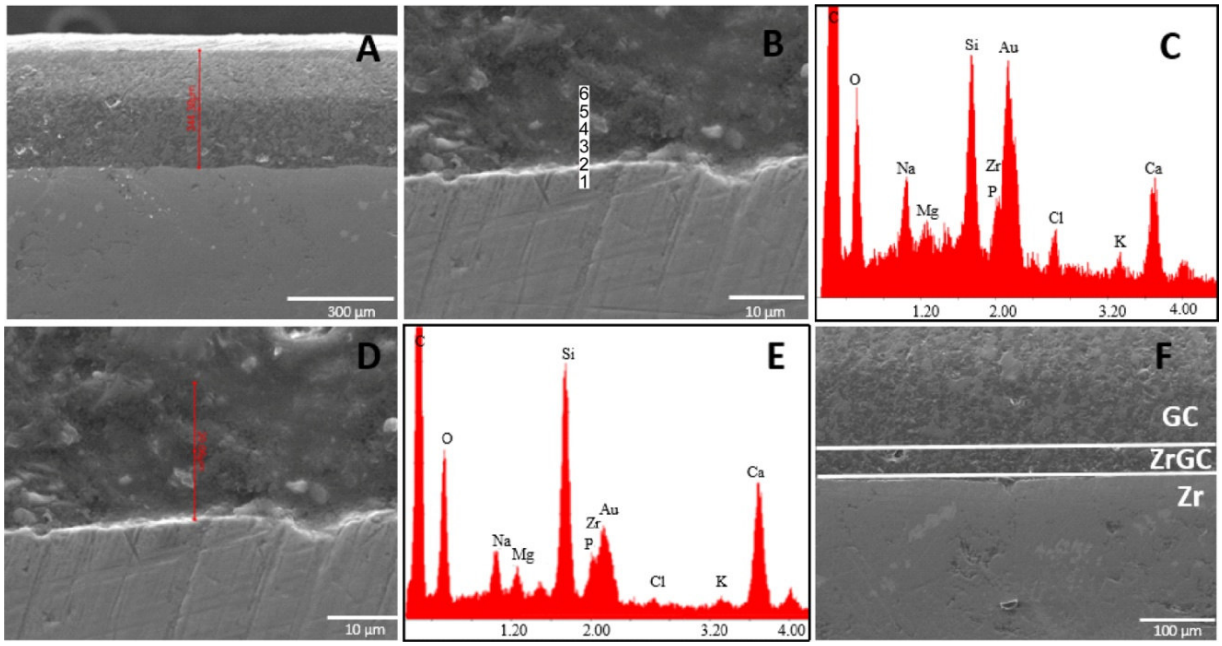

Figure 50- SEM-EDS of the B4 glass-ceramic coating. Magnifications: 200× (A), 5000× (B; D), 1000× (E). EDS analysis performed at distances of 20 µm (C) and 100 µm (F) from the interface towards the coating on images B and D, respectively. Image D: Zr—Zirconia, ZrGC—Zirconia-glass-ceramic, GC—glass-ceramic. Reproduced from [448] with permission from Elsevier.

HA was observed after just 3 days in SBF and the rate of HA formation was comparable to that of the parent glass, constituting a promising material for application as dental prosthetic devices [448].

In another study, Braem et al. [449] described the synthesis of a bioactive glass–ceramic coating on Ti alloy substrates using cathodic EPD followed by vacuum sintering. Undesired oxidation of the Ti at the substrate/coating interface was avoided by using isopropanol-based suspensions and vacuum sintering atmosphere. In this way, it was possible to apply higher voltages and reduce the deposition time. After 60 s of deposition at 60 V, uniform coatings with an average thickness of 8 µm were obtained. Post-deposition sintering treatment at 800 °C allowed improving the mechanical integrity of the coating, achieving a tensile bond strength of 41.0 ± 11.1 MPa. As shown in **Figure 51**, the EPD process allowed the deposition of a uniform

layer on the outer surface of complex components (a-b), characterized by a good sintering level (c) and regular thickness (d-e) [449].

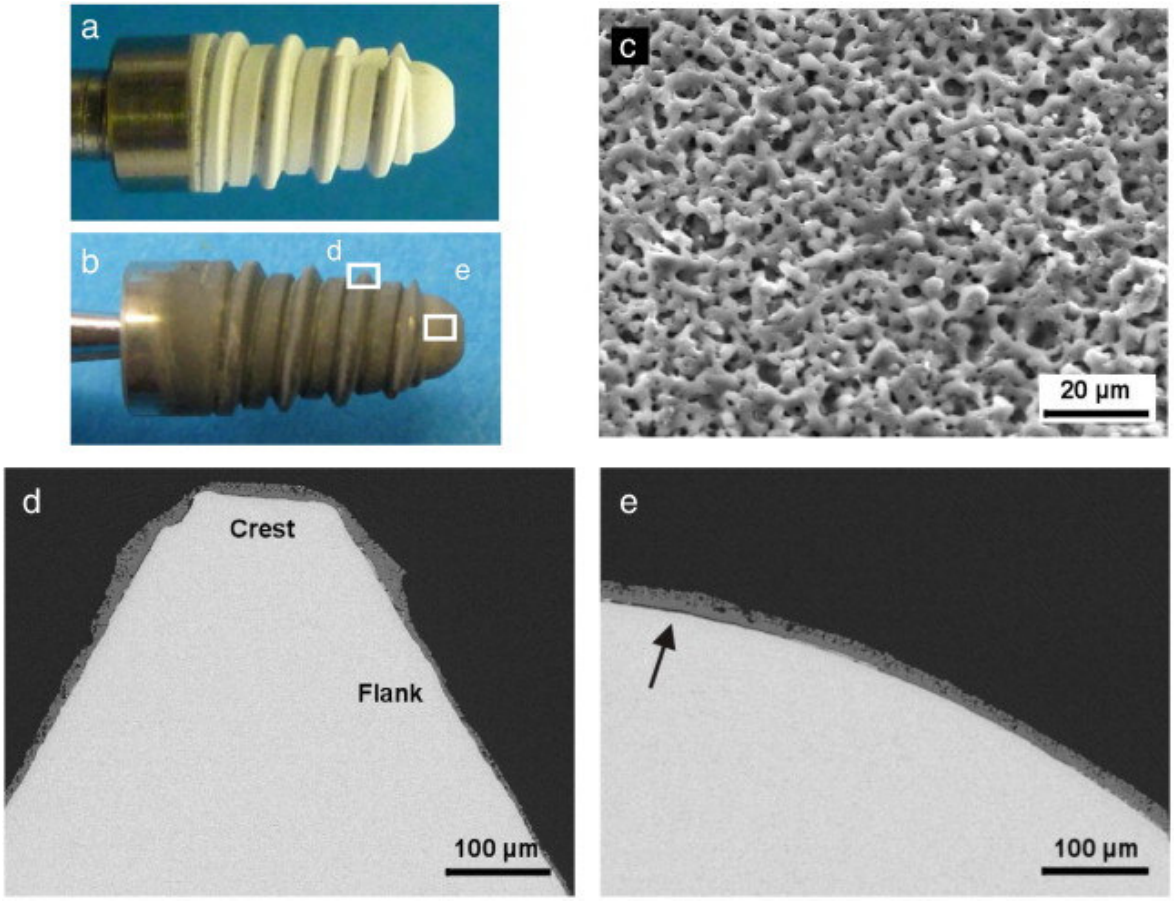

Figure 51- Cp Ti dental implant with bioactive glass coating obtained by EPD (a) followed by vacuum sintering (b). Detailed SEM pictures of a sintered coating demonstrate complete covering of the Ti surface (c–e). The arrow indicates delamination of the coating due to the cutting or grinding during preparation of the cross-section [449].

Recently, much attention has been addressed to the development of antimicrobial glass-based coatings for the treatment of antibiotic-resistant pathogens typical of periodontal diseases [159,450]. Antimicrobial glass-based coatings have been applied to Al_2O_3/Ce-TZP nanocomposite sandblasted substrates by novel screen-printing technology, using a mixture of epoxy and glass powders as polymeric ink [451]. In vitro biofilm formation on different ceramic

biomaterial surfaces: Coating with two batches. The study compared the performances of two different glasses:

1. an antimicrobial soda–lime-glass powder, named G3-GC, with chemical composition (wt.%): 41.6 SiO_2, 20.0 Na_2O, 19.5 CaO, 10.1 Al_2O_3, 6.4 B_2O_3, 0.21 MgO and 0.61 K_2O
2. a zinc-containing glass, named 35ZnO-G, with chemical composition (wt.%): 19.39 SiO_2; 34.24 B_2O_3; 5.55 Na_2O; 5.13 Al_2O_3 and 34.73 ZnO.

The bactericidal effect was tested against selected bacterial species, which are representative of the bacteria associated with periodontal health and disease, including initial colonizers as *S. Oralis*, intermediate colonizers, belonging to the genus *Actinomyces* or *Veillonella*, and late colonizers, as *A. Actinomycetemcomitans* and *P. Gingivalis*, strongly associated to both periodontitis and periimplantitis. In spite of the various limitations of in vitro models, the results of this study confirmed that the addition of bactericidal glasses to the tested biomaterials exerted a clear antimicrobial effect on the development of a complex biofilm when compared with HA control surface, and such an effect was indeed dependent on the material used. Specifically, the 35ZnO-G glass had a significant impact on bacterial growth for *A. acti-nomycetemcomitans* at 48 and 72 h and for *P. gingivalis* at 72 h of incubation, thus representing a good candidate for further testing in dental implant applications [451]. **Table 12** provides a summary of the studies analyzed in the present section.

Table 12. Glass-ceramic coatings for future use in dental applications.

Deposition technique	Substrate	Coating	Deposition and Post-depositon thermal conditions	Crystalline phases	Mechanical properties	Bioactivity	Notes	Ref
PLD	Ti	a) RKKP sol-gel (SG-RKKP) b) RKKP melt derived (MD-RKKP) *Composition (RKKP):* 43.68 SiO_2 – 24.00 β-$Ca_3(PO_4)_2$ – 18.40 CaO – 4.92 CaF_2 – 4.53 Na_2O – 2.78 MgO – 0.19 K_2O – 1.00 Ta_2O_5 – 0.50 La_2O_3 (wt.%)	a) N_2 flux-1000°C b) No post deposition treatment	a) fluorinated hydroxyapatite (FHAp; b) β-tricalcium phosphate (β-TCP); wollastonite ($Na_2CaSi_2O_6$) (deposited at 500 °C)	Hardness: a) 17 GPa b) 25 GPa	n.a.	Compact and uniform microstructure	[441]
Enameling	ZrO2-3%Y2O3	40% SiO_2, 7% Na_2O, 0,3%K_2O, 30% CaO, 17% P_2O_5, 4% MgO, 1,3% CaF_2 (wt.%)	Post deposition: 670 and 725°C for 40 min to obtain glass and glass-cearmic coatings, respectively	Apatite	n.a.	High amount of crystals with low Ca/P ratio (Ca/P = 1.1) covering the glass surface, detected after 3 days soaking in SBF solution	Elongated crystals The rate of formation of the apatite layer(PCPDF 98-007-7967) was not affected by the slight diffusion of theglass into the ZrO_2-3%Y_2O_3support	[448]
EPD	Ti-6Al-4V	53SiO_2, 20CaO, 23Na_2O and 4 P2O5	Post deposition: 700-800 °C	Sodium calcium silicate	Adhesion strength: 41.0±11.1 MPa	n.a.	Ti-silicide interlayer at the coating/substrate interface.	[449]
SPPS	Ti-6Al-4V	SiO_2 45%, Na_2O 24.5%, CaO 24.5%, and P_2O_5 6% (wt.%)	Substrate temperature: 350-400 °C	$Na_2Ca_2Si_3O_9$	n.a.	Apatite phase observed after 7 days in SBF	Successful synthesis of nanostructured bioactive glass-ceramic coatings with good in vitro bioactivity	[447]
APS	Ti-6Al-4V	M2: 3.19% CaO–7.68% MgO–49.13% SiO_2 (wt.%)	Post deposition: 650, 700, 750, 800 °C/ 6h	Akermanite Wollastonite Dicalcium silicate	n.a.	After 14 days soaking in SBF, the surface appeared to be completely covered by an HA layer with Ca/P ratio of 1.58, very close to the stoichiometric one.	Ca, Si and Mg improved cell proliferation and differentiation; good adhesion of osteoblasts to the coating, indicating good cytocompatibility.	[442]
	Ti-6Al-4V	M2: 3.19% CaO–7.68% MgO–49.13% SiO_2 (wt.%)	Post-deposition: 800 °C/6h	Akermanite Wollastonite Dicalcium silicate	n.a.	n.a.	In vivo studies revealed a faster and more effective osteogenesis in the experimental group compared to the control one (HA coating) Higher osteconductive and osteinductive properties compared to HA	[443]
Screen-printing	Al2O3/Ce-TZP nanocomposite	35Zn-O: 19.39 SiO_2; 34.24 B_2O_3; 5.55 Na_2O; 5.13 Al_2O_3	Post deposition: 750 °C/1h	35Zn-O: Willemite	n.a.	n.a.	Differences in biofilm formation were detected among the different	[451]

		and 34.73 ZnO (wt.%) G3-GC: Na_2O, 19.5 CaO, 10.1 Al_2O_3, 6.4 B_2O_3, 0.21 MgO and 0.61 K_2O (wy.%)		G3-GC: nepheline and combeite			tested mate-rials. The 35Zn-O coating has an effect on the vitality of A. actinomycetemcomitansgrowing in an in vitro biofilm model.	

6.2.5. Glass-ionomer composites

Over the last decade, several research groups have focused their attention on the development of new bioactive composite materials for dental applications. Composites containing a glass-ceramics phase exhibit bioactive surfaces able to create a strong implant-tissue bond by the formation of a HA layer which stimulates tissue regeneration [452].

Periodontitis is one of the most common dental diseases and consists in the degradation of the connective tissue provoked by the accumulation of calculi and microorganisms [453]. The conventional approach requires the employment of barrier membranes to induce the guided tissue regeneration (GTR) of periodontal tissue by physically blocking the migration of epithelial cells which prevent bone formation [454]. This blocking mechanism allows the necessary time for osteoblast proliferation and consecutive tissue regeneration of the damaged area [455,456]

Chitosan (CHT) has been largely employed for biomedical applications thanks to its excellent biodegradability, biocompatibility, immunogenicity properties. Therefore, products derived from its degradation are non-toxic, non-antigenic, non-carcinogenic and non-immunogenic. Considering the body reaction to a foreign material, chitosan induces minimal response once implanted in a tissue [457–462]. For all these reasons, CHT is considered an attractive material for applications in GTR membranes. However, chitosan does not show osteoconduction and osteoinduction abilities. Once soaked in simulated body fluid (SBF), no apatite formation is observed on the surface of pure chitosan scaffolds [463]. In the attempt to overcome this limitation, Mota *et al.* [464] have developed new composite materials for periodontal regeneration based on CHT biodegradable matrix combined with BGs which promote guided bone regeneration (GBR), thus conferring a dual GTR/GBR function to medical devices [465]. In this study, BG nanoparticles (BG-NPs) were prepared by sol-gel route with the

aim to confer them a high surface area. Chitosan/BG-NPs composite membranes were obtained by solvent casting method, through the dissolution of purified CHT and BG-NPs in an acetic acid solution. After complete solvent evaporation, resulted homogenous membranes were neutralized with NaOH solution and left to dry at room temperature [464]. The physical, biological, and bioactive properties of these composite membranes were assessed. In vitro bioactivity tests (**Figure 52**) confirmed no apatite formation in pure chitosan membranes, while apatite formation is observed in composite membranes after immersion in SBF [464].

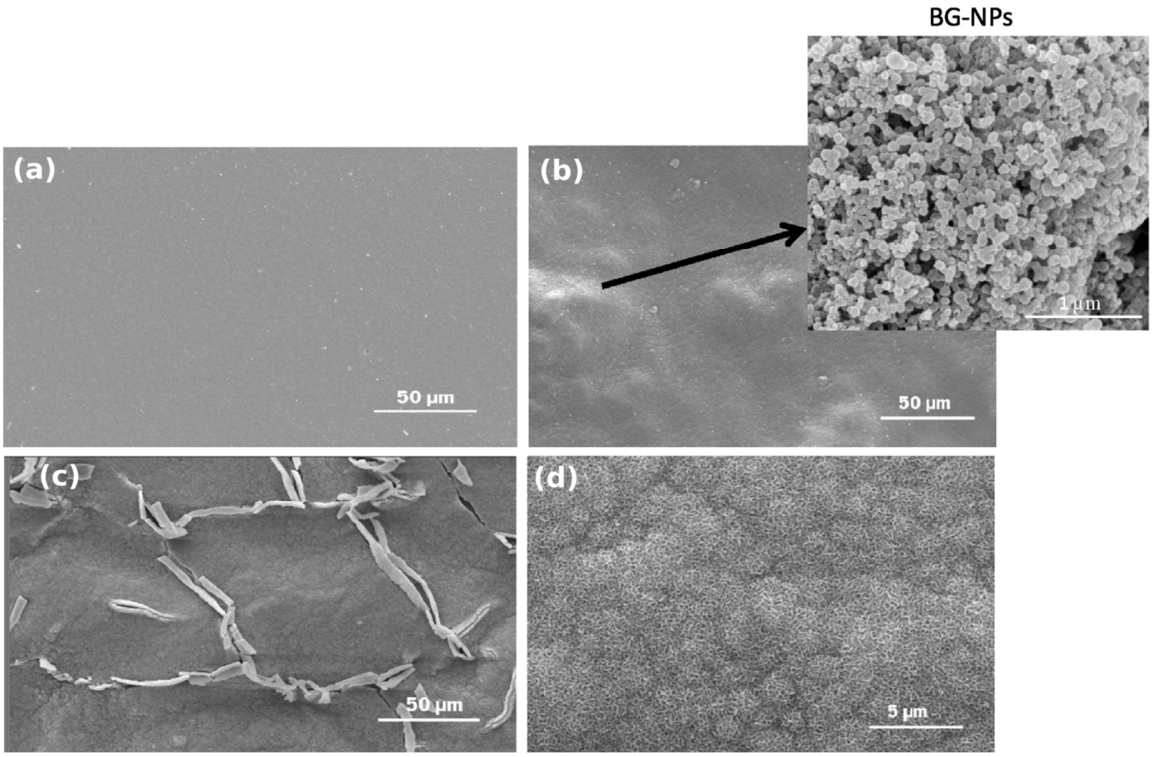

Figure 52- (a) Pure chitosan membranes immersed in SBF, (b) 70% CHT- 30% BG-NPs membranes before soaking in SBF showed some agglomerates of BG-NPs, (c,d) composite CHT-BG-NPs membranes after immersion in SBF for 5 days, respectively low and high magnification. Reproduced from [464] with permission from Elsevier.

The production of these composite membranes confirmed the expected bioactivity results, promoting the possibility of periodontal regeneration. Therefore, hPDLCs and human bone

marrow stromal cells (hBMSC) were used in biological tests to evaluate the performance of the membranes. The metabolic activity of hPDLCs and hBMSCs was significantly enhanced by the addition of BG nanoparticles to chitosan membranes and the bioactive composite membranes stimulated greater cell matrix mineralization as compared to CHT alone [464].

Another common problem in dentistry is related to recurrent decay of traditional dental materials and subsequent loss of restoration [466]. In order to overcome this problem, several attempts have been tried to introduce antimicrobial elements such as fluoride and chlorohexidine, but these methods have shown different limitations, including diminished fluoride release and uptake with time [467]. Other experiments have been made using quaternary ammonium or metal particles as additives but it has been demonstrated that their incorporation has a negative impact on the physical properties and bond strength of the final material [468].

Silver (Ag) ions are known for their antibacterial action thanks to their ability of inactivating bacterial proteins inhibiting replication and interaction of DNA groups [469]. For this reason, Ag-doped BGs have been extensively studied and developed by several scientists, confirming the Ag-BG ability to support cell proliferation in a bacteria-free environment, improve bond strength and, subsequently, restoration lifetime [470]. Hence, an important result in the field of composite materials for dental applications is certainly represented by the fabrication and characterization of bioactive and antibacterial composites [470]. In 2014, a new composite material was developed by the incorporation of Ag-BG in natural extracellular matrix (ECM) hydrogel with the aim of realizing a new dental material combining regenerative and antibacterial properties [470]. The processing method for this composite involved the realization of ECM hydrogels from decellularized porcine urinary bladder matrix (UBM), which was frozen and lyophilized; then, gelation was induced in UBM samples [471]. Ag-free BG and Ag-doped BG were

produced by sol-gel synthesis. Composite materials were obtained by mixing technique (Ag-doped BG powder was pipetted in ECM pre-gel) [470]. Different ratios of composite samples had demonstrated homogenous incorporation of BG particles and no changes in gelation process of hydrogel [470]. ECM/Ag-doped BG composites combined the advantages derived both from ECM use, such as injectability, ability to fill irregular space and provide a support to cell proliferation, and from Ag-BGs introduction, including bioactive behaviour and bactericidal actions. For all these reasons, these composite materials have shown a great potential in dental application for healing and regeneration of injured dental pulp [470].

Other studies were conducted by Chatzisravrou, Boccaccini et al. [452,472] about new composite materials obtained by combining dental glass-ceramics (such as commercial high-fusing leucite-based feldspathic porcelain powder) with BG. The first experiment yielded a bioactive composite combining a sol-gel derived glass-ceramic based on the system $60SiO_2$–$3P_2O_5$–$14Al_2O_3$–$6CaO$–$7Na_2O$–$10K_2O$ (wt.%) with 58S glass [472]. The composite material was produced by mixing and stirring both components. The batch was aged and dried, then gelation process occurred at 180°C and finally the material was treated at 700°C. Final composite product was used to fabricate coatings by mixing the solid material with a liquid to create a slurry [472].

Unlike glass-ceramic-coated pellets, which did not reveal any apatite deposition on the surface even after 20 days of immersion in SBF, composite coatings were able to promote the growth of an uniform layer of HA uniform even after only 3 days of immersion (**Figure 53**) [472].

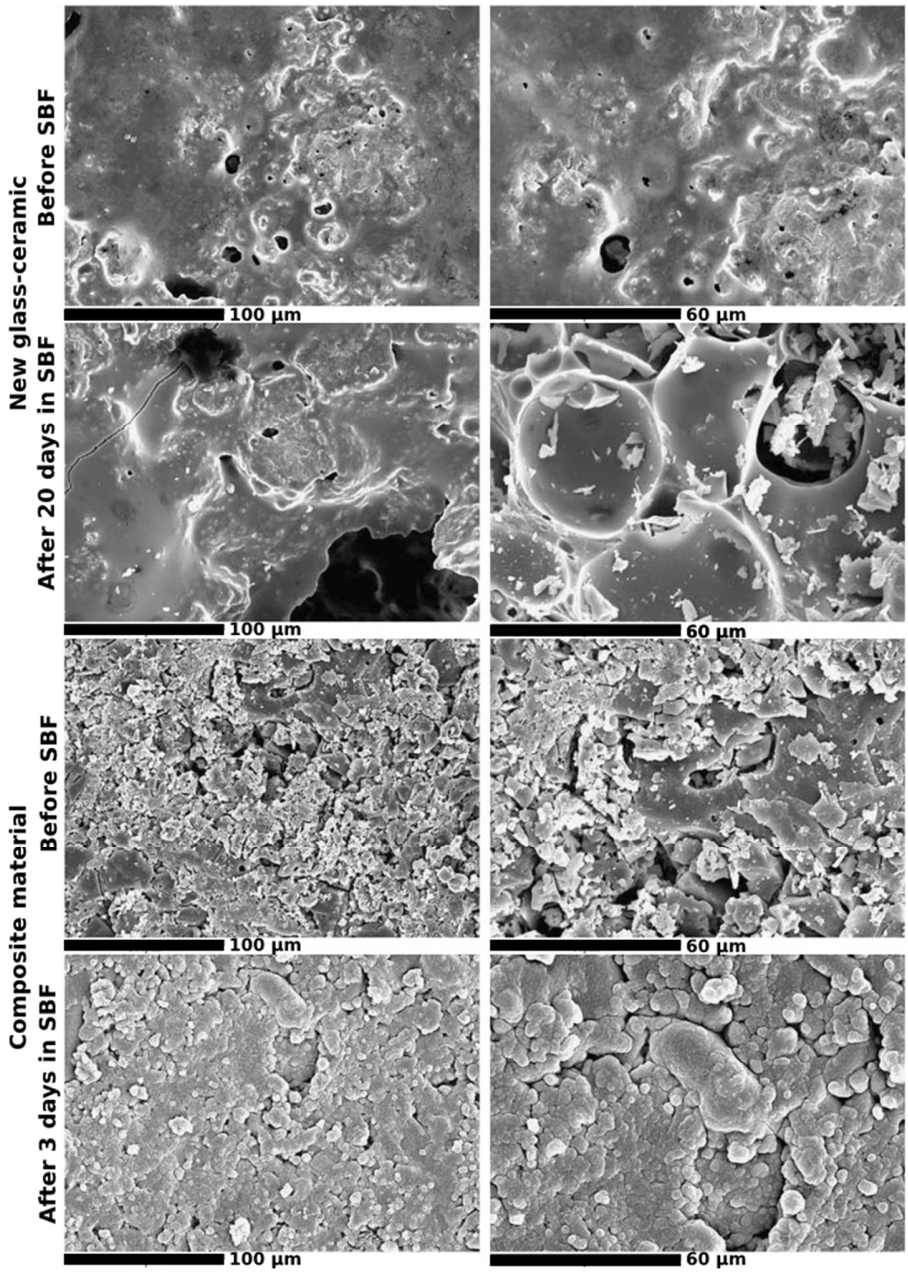

Figure 53- SEM image of glass-ceramic and composite samples before and after immersion in SBF. Reproduced from [472] with permission from Elsevier.

The same processing method was applied to another composite material used as coating, composed by commercial high-fusing leucite and 58S glass [452]. Even in this experiment, the composite coating promoted HA formation after only 3 days immersion in SBF (**Figure 54**).

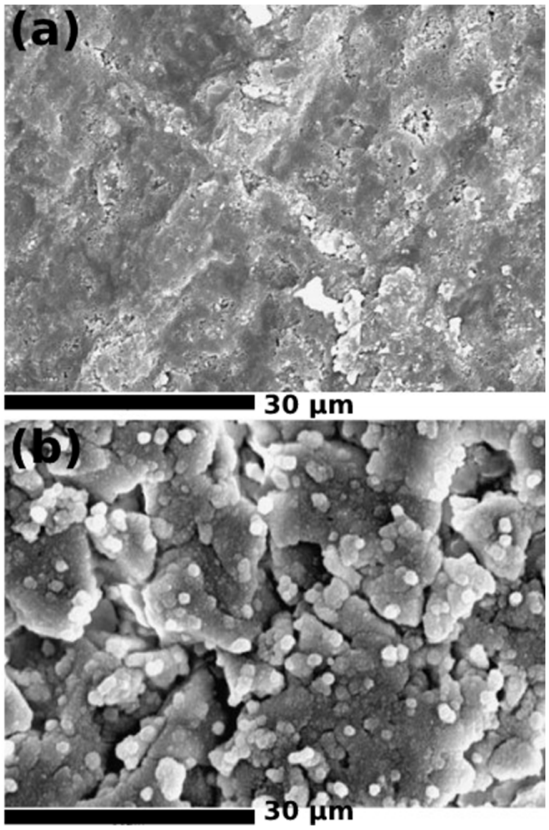

Figure 54- SEM images of the composite-coated samples (a) before and (b) after immersion for 3 days in SBF. Reproduced from [452] with permission from Elsevier.

Perhaps the most commonly used dental composites containing glasses/glass-ceramics are glass-ionomer cements, chemically known as glass polyalkenoate. They are obtained by the reaction between fluoro-alumino-silicate glass powder (size range within 15-50 μm) and polyacrylic acid. The addition of lanthanum, strontium or barium oxides provides radio-opacity. Favorable properties of glass ionomer cements include setting within a few minutes – which leaves enough time for manipulation – and eventual formation of a bone-like hard substance that is water-resistant after setting [473].

Glass ionomer cements are used on restorative dentistry to prevent caries through a steady fluoride release over a prolonged period and exhibit hydrophilic properties, allowing them to be

an alternative to hydrophobic resins in the generally wet oral cavity. In fact, resin-based sealants are prone to be destroyed by saliva contamination.

The main disadvantages of glass ionomer cements include inadequate retention, lack of strength and toughness over time, and limited wear resistance. Hence, periodic recalls are necessary, even after 6 months from the first application, to replace the lost sealant. Different methods have been used to address the physical shortcomings of glass ionomer cements, including the addition of mica-fluoroapatite-containing [474] and fluoroapatite-mullite-containing glass-ceramics [475] as reinforcing fillers. Although glass ionomer cements have not been specifically designed to be bioactive, incorporation of bioactive glass-ceramics would impart new extra-functionalities to these materials.

7. Modeling techniques: Physics-based models and machine learning

Despite the growing demand and applications for glass-ceramics, the design process for these materials has largely remain unchanged since the development of the first commercial products. This is due to overwhelming magnitude of possible glass compositions that can be studied and fabricated. Thus, the design space that must be optimized over is infinitely variable [476,477]. The number of components in a glass can scale from one compound up to 11 or more. If there are a number of compounds, *c,* there is a chemical space of *c*-1 that must be searched for a glass that reaches the desired properties (since at least one dimension is redundant). There is at least one additional dimension that corresponds to the thermal history [476] resulting in *c* dimensions that must be optimized over. However, when a degree of crystallinity is added there are two

additional dimensions added for each phase (p) possible (the nucleation and the growth) giving a total of $c+2p$ total degrees of freedom for the design of a glass-ceramic. There exist some tools to help design the c dimensions of the glass [477–483], however, designing in the $2p$ dimensions remains largely a mystery. To enable a new generation of glass-ceramics, new models must be easily parameterizable and must consider the additional space provided by the nucleation and growth phases.

It must be admitted that there is no perfect modeling technique and instead, for a holistic picture, there must be a range of techniques from mathematical to computational modeling that will be explored here. Computational techniques range from empirically driven methods such as machine learning to more fundamental techniques such as ab initio modeling [484]. Though there is a wide range of techniques available only a few have been applied to the study of glass-ceramics. These techniques include molecular dynamics (MD) [485–487], Monte Carlo (MC) [488,489], potential energy landscapes (PEL) [490], and machine learning (ML) [491,492]. In this section, we will review the physics, strengths, and weaknesses of each of these techniques. It is also important to reemphasize that each of the methods and techniques discussed are related to the glass-ceramic community. Crystallization modeling is prevalent in other fields such as thin film growth [493] and is not discussed here in detail because it does not reflect the reality of nucleating a crystal in a bulk liquid.

7.1. Simulation of glass structure and crystallization

Recently, nucleation computational studies have been largely focused on one of two categories: validating CNT or alternatively calculating the critical work (W) for nucleation. The most common form of nucleation is given by,

$$I = Z_e D(T) \exp\left[-\frac{W^*}{kT} \right] \tag{7.1}$$

In which Z_e is the Zeldovich factor, k is Boltzmann's constant, T is temperature, and D is the kinetic function related to nucleation. CNT explicitly relates the work function to the Gibb's free energy difference and the interfacial energy as discussed in Section 3. We will discuss MD methods used to test CNT in this section and in the next, we will discuss a method to parameterize the work function. Unfortunately, the diffusion coefficient does not receive as much attention when relating the values to more macroscopically available values. Often it is simply treated as an inverse viscosity value despite limited evidence for this relationship.

MD, MC, and PEL work by using an empirical inter-atomic potential (also known simply as potentials) that can be fit using either experimental data and a series of molecular dynamics simulations or using ab initio calculated energies as a function of distance of two ions [494,495]. One common potential is the Lennard-Jones (LJ),

$$V_{LJ} = 4\text{ò}\left[\left(\frac{\sigma}{r} \right)^{12} - \left(\frac{\sigma}{r} \right)^{6} \right] \tag{7.2}$$

in which ò and σ are fitting parameters for every pair-wise set of ions in a system, V is the potential energy contributed by the two-atom interactions, and r is the distance between the two ions in question. The LJ form is simple and easy to parameterize; however, it is unable to recreate complicated material behaviors for a non-modeled glass. Thus, a more complicated potential is often used such as a Buckingham, Coulombic, or Morse potential. The Morse potential includes an additional columbic and repulsive term and was parameterized by Pedone et al. [494] for silicate glasses such that

$$V_{pedone} = \frac{Z_i Z_j e^2}{r} + Y\left[\left(1-\exp\left[-a\{r-r_0\}^2\right]\right)-1\right] + \frac{C}{r^{12}} \tag{7.3}$$

Here, Z is the charge of a given ion, e is the charge of an electron, and Y, C, a, and r_0 are fitting parameters. It is also worth noting that in the Pedone potentials, accurate predictions can be made while only considering the interactions between each individual ion species with oxygen and letting all other interactions have a value of *0* for C and D [494]. For instance, Si-O, Na-O, and O-O are all explicitly parameterized while Si-Na only interacts coulombically (the first term). This is a very brief discussion of inter-atomic potentials there are extensive resources available for those readers who wish to learn more [496–499].

MD is the most common computational technique used in the glass/glass-ceramics community as it has been commonly found since the 1970s for predictions of properties and gain insights into the nature of complex phenomena in glasses and liquids. Its popularity has only grown due to convenient MD packages that can be downloaded and ran without much programming knowledge such as LAMMPS [500].

MD is fundamentally a classical method which uses potentials to approximate quantum interactions and as a result, the trajectory of an ion is calculable. In MD the potential energy of an ion, i, is given by

$$V_i = \sum_{i \neq j}^{N} V_{ij} \tag{7.4}$$

where V_{ij} is given by a potential form and N is the number of atoms. Once the potential energy is obtained, the acceleration is given as,

$$a_i = -\frac{1}{m}\nabla V \quad . \tag{7.5}$$

The change in position and velocity is then modified according to an integrator such as the velocity Verlet integration algorithm,

$$\begin{aligned}\mathbf{r_i}(t+\Delta t) &= \mathbf{r_i}(t) + \Delta\mathbf{v_i}(t) + \frac{\Delta t^2}{m_i}\mathbf{f_i} \\ \mathbf{v_i}(t+\Delta t) &= \mathbf{v_i}(t) + \frac{\Delta t}{2m_i}\left(\mathbf{f_i}(t) + \mathbf{f_i}(t+\Delta t)\right)\end{aligned} \quad . \tag{7.6}$$

Here, ***r*** is the position vector, ***v*** is the velocity vector, and ***f*** is the force vector. For a single ion, the length of each vector is equal to the number of dimensions (*d*) in which the experiment is held if all atoms in the system is considered the length of the vector, *dN.* Many such integration algorithms are available and each have their own strengths [501].

The description of the molecular dynamics method above, results in a simulation where volume, energy and the number of atoms (NVE ensemble) is held constant. This, however, is not necessarily correct when trying to recreate experimental conditions because it requires fabricating the glass under a constant volume. In contrast, experiments are generally conducted in constant pressure environments. In order to maintain a constant temperature and pressure in MD, we must independently vary the amount of kinetic energy in the system and the size of the system. To do this, a set of methods called thermostats and barostats are available that rescale the property fractionally to reach the target value of the corresponding property (temperature and pressure). For thermostats and barostats, the most common method is called the Nosé-Hoover which uses a damping factor to rescale the volume every step to reach a target value by the end of the simulation. The addition of barostats and thermostats allow for different ensembles and the most common are NVT (constant number of atoms, constant volume, and controlled temperature), and NPT (constant number of atoms, controlled pressure, and controlled temperature) Between the conditions of the thermostat, barostat, and the numerical integration of

the atomic location, a small step size must be used. A typical value for a step size is around 1 fs. Due to this small step size, molecular dynamic simulations are limited to times much shorter than one second.

Despite these short times, there are still many useful applications for MD. One common application of MD is in glass synthesis to achieve a realistic glass structure. One way in which this is achieved is placing atoms (a couple thousand atoms typically) that match the desired compositions in a box matching the room-temperature density. The velocities are then randomly assigning velocities such that the sum of the kinetic energies matches the temperature desired. The liquid is then quenched as a constant cooling rate (often 1 K/ps) to room temperature where the structure is then quantified [502–506]. This is particularly useful when the glasses of interest are not simple and the structure cannot be quantified easily. Despite MD's ability to address glass structure, fundamentally it cannot directly capture crystallization due to its temporal constraint.

The studies trying to understand the validity of CNT date back to the proposal of the theory, however, only recently has MD been able to weigh in on this statement. It should be noted that each of these simulations are highly dependent not only on the methods but also on the potentials and systems used. One of the earliest MD comparisons come from Aga et al. [507] in which a model system of aluminum was used to compare the predicted lag times from experiment and a model parameterized using MD simulations. Due to the limitation in MD sizes, the method worked by simulating 4 different system sizes (6 912, 16 384, 108 000, and 1 000 188 atoms) as well as running smaller systems repeatedly. There was an excellent agreement found between the nucleation lag times as parameterized through experiments and as parameterized using CNT and MD. However, it was assumed that the interfacial energy could be represented as

$$\gamma(T) = a\rho^{2/3}\Delta H(T) \quad . \tag{7.7}$$

where a is a constant, ρ is density, and ΔH is the enthalpy of fusion as a function of temperature. a is a constant that does not change greatly with composition; however, it does vary greatly with crystal structure. A typically value is ~0.45 for metals and ~0.32 for non-metals. The same form has been used omitting the density factor as well. Mahata et al. [508] followed closely to try to validate CNT when comparing the classical nucleation critical nucleus size and the MD nucleation radius. At low temperatures, the critical nucleus size varies widely; however, as the temperature passed the temperature of the maximum rate, the size of the nucleus converged.

In 2019, Prado et al. [485] did simulations of BaS (36 000 atoms) where calculations of the enthalpy of melting, the melting temperature, the diffusivity, and the density are made directly from MD. The free energy difference was calculated with the Turnbull and Hoffman [509] approximations. The only unknown parameter was the interfacial surface energy which was calculated using the nucleation rate found in MD. The interfacial energies, the size of the nucleated phases, and the temperature range all qualitatively compared with the insights from CNT. Though this is a step in the direction of validating CNT, it falls short quantitively. It is possible to use MD to get diffusion rates as a function of temperature, the melting temperature, the enthalpy of fusion, and the interfacial energy, however, the Gibbs free energy is not directly accessible and thus the free energy difference must be estimated using some approximation such as the Turnbull or Hoffman expression. The resulting crystal structure must also be known at the start of the simulation process. The same method was also applied to a simulation of Ni50Ti50 [486] and found equally valid agreement.

More recently there has been an attempt to calculate the validity of CNT using supercooled Ge [510]. In this work they used quantitative knowledge of the number of nucleation sites to

back calculate the surface energy. They then calculated the nucleation rate using all parameters calculated with the techniques from Prado et al. [485] This resulted in an accurate prediction of the nucleation (within a few orders of magnitude) without any fitting parameters though some parameters came from experiments. This was a major step in the process of validating CNT; however, it only worked on an extremely fast nucleating material. Though it is now possible to obtain all parameters from MD, as far as the authors can tell, there is no work directly testing the applicability of MD to achieve accurate predictions of oxide glass nucleation (including relevant approximations such as the Turnbull approximation, the diffusivity, and the surface energy).

To achieve reasonable predictions of nucleation, MD methods still require some form of approximation since the nucleation rate for commercial glass-ceramics is not directly accessible from the simulation technique. To circumvent this issue other methods can be deployed such as energy landscapes or Monte Carlo to achieve accurate predictions of key parameters with fewer approximations.

7.2. Energy landscape modeling

MD iterates through time with a small timestep with each atom evolving according to the energy and forces in the system. Though this is the classical deterministic process of what occurs, this is not the only way to view the evolution of the system. Alternate methods rely on statistical mechanical insights which come from the energetics that naturally arise due to the interactions of atoms in their unique positions. This can be understood by not thinking of N sets of atom location in a shared d-dimensional space but instead thinking of a singular position in a high dimensional space (dN) that uniquely defines the energy of the system. The concept of a high dimensional space defining the energy uniquely is the energy landscape (PEL) [511–513].

What we then have is a hierarchy of dimensions when determining the properties of a sample. As discussed earlier, we have $c+2p$ dimensions, the unique location in that chemical space then define the probability of our occupation in dN dimensions that in turn determine the energetics and dynamics of the system. Though this is a headache-inducing exercise it is the most descriptive way we have to understand the dynamics of these complicated systems.

Understanding the landscape leads to quantifiable insights. To model nucleation rates, we can use information from the landscape that describes the difference of free energy between the liquid states in equilibrium and the solid states in equilibrium. It is also possible to obtain the key transition point energies. To put it more plainly, we need to know the kinetics and thermodynamics of the system. This can be achieved explicitly by physically mapping the energy as a function of each of the $3N$ coordinates in three-dimensional space [478,490]. Mapping every possible coordinate is not feasible given a finite amount of time, instead, we focus on the energy minima also called inherent structures (where it is most likely to find the structure) and the first order saddle point between these minima, called transition points. This information, along with the curvature at each inherent structure, results in enough information to input into transition point theory to make novel predictions of nucleation.

To *physically* achieve this prediction, some inputs are needed. The first input needed is the initial structure. In the case of the method presented here, this must be the structure *after* nucleation because this technique goes from low entropy states to high entropy ones. This is perhaps the biggest downside of this technique since it requires the ending crystal structure to be known *before* the process is started. As a result, this limits the technique to only well-known crystalline structures. The next thing we need is a calculator that allows us to find the energy for a given organization of atoms. This tool typically uses inter-atomic potentials discussed earlier

(here we will use the Pedone potentials) [514]. Once this calculation is implemented, then the only problem left to solve is how to vary the atoms intelligently such that the inherent structures and transition points are found efficiently. There are many methods to explore the landscape but in the work of Wilkinson et al., a technique called Eigen-Trieban was used (ET) [478,490]. ET allows for an efficient exploration of the landscape by diagonalizing the Hessian where the hessian is defined as,

$$H = \begin{bmatrix} \frac{\partial U}{\partial x_1 \partial x_1} & \frac{\partial U}{\partial x_1 \partial y_1} & \cdots & \frac{\partial U}{\partial x_1 \partial z_N} \\ \frac{\partial U}{\partial y_1 \partial x_1} & \frac{\partial U}{\partial y_1 \partial y_1} & \cdots & \frac{\partial U}{\partial y_1 \partial z_N} \\ \vdots & \vdots & \ddots & \vdots \\ \frac{\partial U}{\partial z_N \partial x_1} & \frac{\partial U}{\partial z_N \partial y_1} & \cdots & \frac{\partial U}{\partial z_N \partial z_N} \end{bmatrix} . \tag{7.8}$$

U is the energy, xyz are the coordinates for an atom (denoted as a subscript). When the Hessian is diagonalized, the eigen-vectors refer to unique directions in which we can explore to find new inherent structures. In ET we push along a chosen eigen-vector with a specified distance and then use a minimization technique to see if we have ended up in a new basin (determined by the high dimensional Pythagorean distance from the previous basin). This gives a route to efficiently discover new inherent structures. This method, however, does not find the transition points and an alternate method must be used to find these barriers. In ExplorerPy [478] (an open source software made by the authors to do this calculation), this is achieved using what is called a nudged-elastic band calculation [515–517]. An in-depth discussion of nudged-elastic band methods is beyond the scope of this work, however, there exist a plethora of resources available elsewhere [501,516,517]. The last required parameter needed for predictions is the degeneracy of each state. This is a difficult parameter to obtain and is classically calculated by using complex

Monte Carlo methods. However, more recently it has been approximated using a hyper-sphere volume as a value proportional to the degeneracy. A landscape for $BaSi_2O_5$ (colored by the average distance to a lattice point) is shown in **Figure 55**.

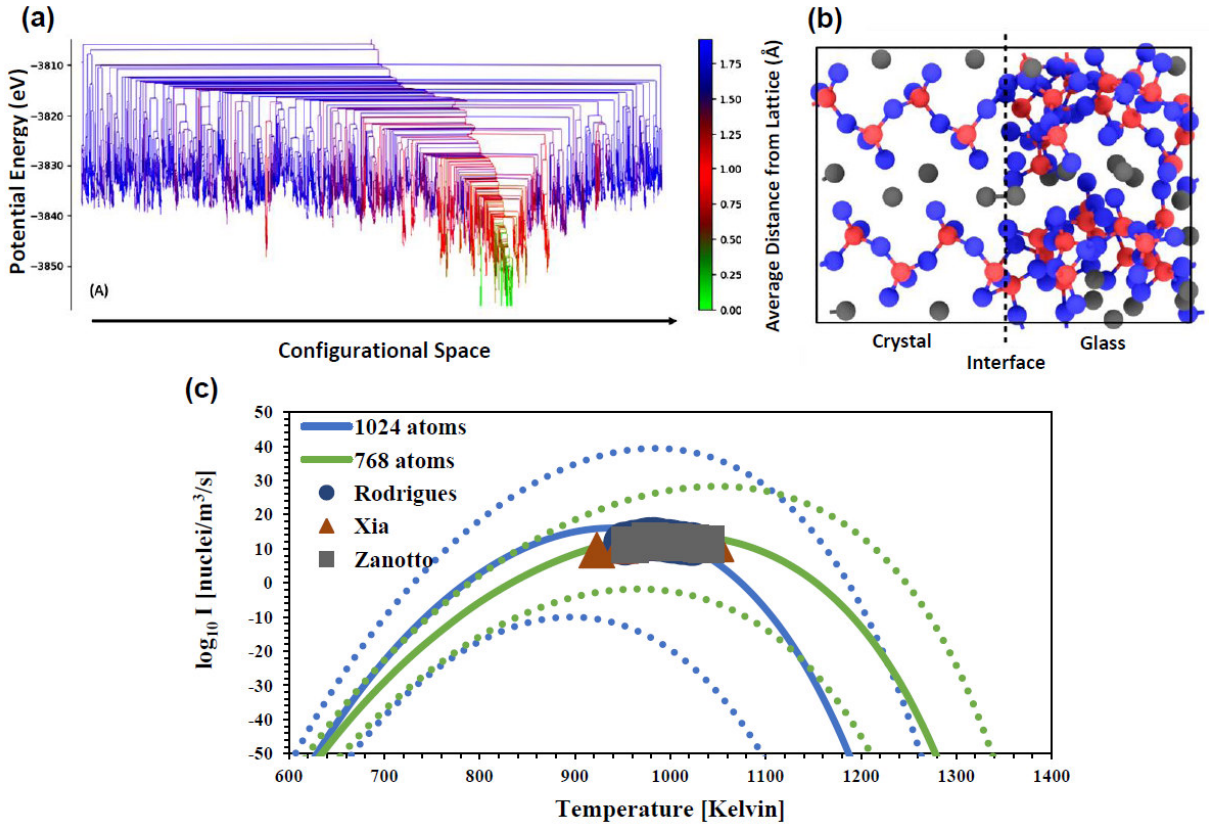

Figure 55- (a) The energy landscape of a barium disilicate system. The colors tell the average distance of an ion from the crystalline lattice location for that ion. (b) An example interfacial structure between the crystalline phase on the left and the last SCL/glass phase on the right for a barium disilicate system. The gray atoms are barium, silicon is shown in red, and blue represents oxygen. (c) Prediction of energy landscape compared to values found in literature. The lines represent the error in the prediction calculated from the interfacial energy [490].

In the method used by Wilkinson et al., they used the landscape to directly calculate the parameters for CNT. It is worth noting that calculating thermodynamic/kinetic properties using energy landscapes in this way is common practice when considering protein folding problems [518]. The parameters calculated using this method were the surface energy, the free energy

difference between the crystal and liquid, and the interfacial free energy. Helmholtz free energy was used to explore these systems which requires a constant volume. The free energy was calculated by first partitioning all basins into either crystal or liquid basins based on the mean distance from the nearest lattice point. The equilibrium value for each state was calculated using a restricted set of basins (corresponding to either liquid, crystal, or all states), *x*. To write the free energy, we must know the probability of each state as given by,

$$p_i = \frac{g_i}{Q}\exp\left[-\frac{U_i}{kT}\right] \quad . \tag{7.9}$$

T is the absolute temperature, *k* is Boltzmann's constant, g_i is the degeneracy of the state and *Q* is the partition function given by,

$$Q = \sum_{j=0}^{x} g_j \exp\left[-\frac{U_j}{kT}\right] \quad . \tag{7.10}$$

The free energy at equilibrium of the entire system is given by,

$$\langle G \rangle = \sum_{i=0}^{All} p_i U_i - kT\left[p_i \ln g_i - p_i \ln p_i\right] \quad , \tag{7.11}$$

and the liquid state enthalpy is restricted over liquid/glass basins. The free energy is then given by,

$$\Delta G = \langle G_{liq} \rangle - \langle G_{all} \rangle \quad . \tag{7.12}$$

This gives access to the thermodynamic driving force for nucleation.

The next parameter that needs to be calculated is the kinetics of the system. Many experimental studies of nucleation substitute the diffusion value with the Stokes-Einstein (see

[Ch. 3]) expression, this is contentious since it is not guaranteed that the self-diffusion of ions in the melt is the same as the rate of ions attempting to form a nucleus. It is done experimentally despite its contentious nature because there is no other option experimentally; however, since explicit information is known here about the barriers and the curvature, we can write an exact rate of transition that is free of viscous assumptions. To do so we must first start with the vibrational frequency based on the curvature of each basin, ω, and the mass, *m*,

$$\nu = \frac{1}{2\pi}\sqrt{\frac{\omega}{\langle m \rangle}} \quad . \tag{7.13}$$

Using this vibrational frequency and the barrier from *i* to *j*, ΔU_{ij} we can write a one-directional transition rate,

$$K_{ij} = g_j \exp\left[-\frac{\Delta U_{ij}}{kT}\right] \quad . \tag{7.14}$$

This leads to a total kinetic transition rate from the liquid set of basins (*liq*) to the crystalline set of basins (*cry*) of,

$$D(T) = \frac{1}{\sum_{i}^{liq} p_i \sum_{j}^{cry} p_{ij}\left(\frac{1}{K_{ji}+K_{ij}}\right)} \quad . \tag{7.15}$$

In Eq. (7.15) the only unknown parameter is p_{ij} which is given by,

$$p_{ij} = \frac{g_j}{Z}\exp\left[-\frac{\Delta U_{ij}}{kT}\right] \quad . \tag{7.16}$$

Z is given by,

$$Z = \sum_{i \neq j} g_j \exp\left[-\frac{\Delta U_{ij}}{kT} \right] \quad . \tag{7.17}$$

The last unknown is the interfacial energy. This is difficult parameter to obtain from both computational and theoretical viewpoints. There has been no experimental method proposed to actually quantify this value. Most tests of CNT fit the parameter. When the value is fit as a constant, it can lead to many orders of magnitude in error; however, when it is fit as linear function with respect to temperature, the fit to experimental data can be reasonable. However, this introduces multiple free parameters into the prediction.

The simplest method proposed was deployed in the study by Wilkinson et al. where they took the first and last basin and found the energy of them independently, then placed them together to form an interface (as shown in Fig. 1.B) to then calculate the energy difference. This was then normalized to the area of the interface and fit with a straight line as a function of temperature. An alternative method was proposed by Bording and Tafto when working on Ge [519] in which they related a liquid and inserted various nuclei of different sizes and found if the size of the nucleus grew or shrunk to find the critical nucleus size (r^*). This nucleus size could be used to back calculate the interfacial free energy (similar to work previously discussed by Prado et al. [485]) to find the interfacial free energy with additional information from the landscape,

$$\gamma = \frac{-r^* \Delta G}{2} \quad . \tag{7.18}$$

When these values are calculated and used in the expression for CNT, a very accurate prediction of the nucleation is made; however, this whole process is computationally expensive and has limitations. An alternative is the insights gained by McKenzie and co-workers [488,489] through Monte Carlo.

All of the work from the perspective of energy landscapes requires two conditions: i) that the ending crystal structure is known and ii) that a theoretical form for the work of nucleation is chosen. These both limit the wider applicability of energy landscapes. However, there is an alternate method. By slowly building a nucleus in atomic simulations, we can achieve reasonable approximations for the work of nucleation and also what the nucleus looks like. Monte Carlo is a general class of stochastic algorithm in which actions are chosen at random and information is gained based on each action. The specific form of Monte-Carlo (grand canonical Monte Carlo) used by McKenzie et al. [488] slowly builds the nucleus from a simulated infinite surrounding liquid. Details of how to simulate the liquid as it grows into a nucleus is discussed elsewhere [488,489]. Once the initial system is obtained, a series of trial additions and subtractions from the cluster are chosen using advanced techniques to improve the sampling (Aggregation-Volume-Bias Monte Carlo, Histogram-Reweighting, and self-adaptative umbrellas sampling). Whether a move is a cluster addition or subtraction is equally likelihood, the probability of acceptance is given by,

$$acc\left(A \to B\right) = \min\left[1, \frac{V_{in} N \exp\left[\frac{\mu}{kT}\right] \exp\left[-\frac{\Delta E}{kT}\right]}{\left(N_{in}+1\right)\left(N+1\right)}\right] \tag{7.19}$$

Conversely, the move of cluster subtraction is,

$$acc\left(A \to B\right) = \min\left[1, \frac{N_{in} N \exp\left[-\frac{\mu}{kT}\right] \exp\left[-\frac{\Delta E}{kT}\right]}{V_{in}\left(N-1\right)}\right] \tag{7.20}$$

In these expressions, N is the total number of atoms, N_{in} is the number of particles in a growth volume (V_{in}), μ is the chemical potential is the liquid, and ΔE is the energy difference before and after the trial move. This allows for a complete calculation of the dynamics of the evolving system. This can be thought of as constructing an inherent structure one atom at a time in such a way to minimize the work needed to form the nucleus. Since the growth mechanism that requires least work is the most likely one to be actualized, it describes the most likely nucleation method. The power of this method is shown in **Figure 56** where a constructed nucleus is compared to SEM images of the same lithium metasilicate system.

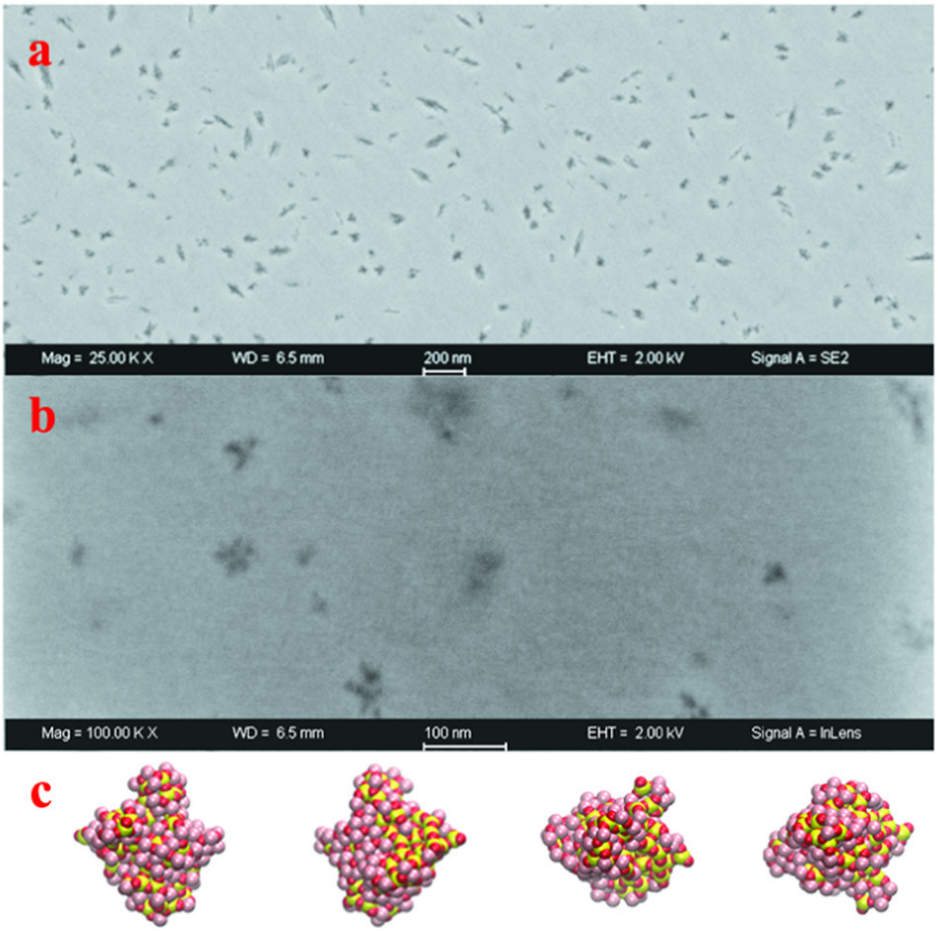

Figure 56- Parts a and b show SEM images of lithium metasilicate clusters. The SEM scale bar is 200 nm and 100 nm. Panel c shows a 80 formula units of lithium metasilicate cluster. Coloring scheme is Si (yellow), O (red), and Li (pink) [490].

A more recent study by Lodesani et al. [487] estimated the Helmholtz free energy from MD simulations with a glass and variable crystalline phase. By estimating the Helmholtz free energy with a seeding approach, they were able to find the effective work function for nucleation without resorting to Monte-Carlo or more extreme computational methods. The method proposed by Lodesani et al. [487] was tested on lithium disilicate glass-ceramics and the work function calculated are both in good agreement with experiments.

The computational studies of glass-ceramics reviewed here can be split into two categories studies testing CNT and studies trying to calculate the work to form a nucleus without any such

assumptions on the form. These methods are *not* mutually exclusive. While we are without an agreed upon model that accurately calculates the work function directly, we are forced to rely on techniques that directly calculate the work. The unfortunate downside of directly calculating the work function is that it is computationally costly for one value *and* it then must be used at every temperature of interest. This computational cost is the main motivator for trying to find a form for nucleation with the clearest option still being CNT.

7.3. Mechanical properties

Mechanical properties are of crucial importance to almost every commercial glass-cearmic with many glass-ceramics being used due to their improved strength [84]. However, a quantifiable relationship between the crystalline phases present and the mechanical strengthening remains elusive. This leaves two options to quantify the mechanical changes: experiments and numerical simulations. We will focus on numerical simulations in this section. Though PEL or MC could offer insights into glass-ceramic mechanical properties, there is no current research on this and as such, most work uses MD. This work recently has been largely driven by industry wanting to understand how to globally optimize their ceramming processes as well as any new techniques to give a competitive edge. In particular, there is excellent work done by Deng and Harris et al. [520–523]. Their work stands as a recent standard for simulating mechanical properties of glass-ceramics. In order to simulate an effective mechanical response of a glass-ceramic, there are generally three steps analogous to any experimental procedure: synthesis, experiment, and analysis. The experiment and analysis of the mechanical testing in MD is largely the same across all materials and as such, will not be emphasized here. The reader is recommended to study this article for further information [501].

In order to simulate an effective mechanical response of a glass-ceramic, there are generally three steps analogous to any experimental procedure: synthesis, experiment, and analysis. Synthesis has mainly been the most complicated of these three steps as generally it is not possible for crystals to form spontaneously in MD simulations. Thus, to generate the initial structure, a set of atoms corresponding to the desired chemical compositions are placed in a box, heated, and then cooled resulting in a glass structure. Deng and Harris [515] proposed a method that then took these glass materials and inserted crystalline components followed by a relaxation to try to create a realistic interface. Molecular dynamics simulations seem to be the current preferred approach to understanding the mechanical properties due to the accessibility and the atomistic view offered. However, there is an innate simulation cost with most MD simulations being far shorter than a millisecond. In the future, other simulation techniques could provide deeper insights, such as peri dynamics in which the atomistic view is sacrificed to look at a larger material with a longer time span. Another technique that has been emphasized in recent years is machine learning (ML); ML offers a unique approach that can generally map an input to an output. This is a very powerful tool if the transform can be properly parameterized and modeled. Examples from Bauchy's group [524–526] and more recently by DeCeanne et al. [527, 528] can be found for glasses and glass-ceramics, respectively.

7.4. Application to DGCs

The vast majority of glass-ceramics and glass-like materials as a whole have been designed through experimental approaches, but we have presented methods to begin to understand modeling approaches. Experimentally, there is no guaranteed way to truly reach the optimize composition; however, these methods can allow for a true optimization of the DGCs. The

nucleation can be calculated using these computational methods, the growth calculated using methods discussed in Chapter 3, and then the mechanical properties and dissolution can be calculated through molecular dynamics. Unfortunately, these methods are not currently computationally fast enough to perform an efficient optimization. There are some ways to speed these methods such as machine learning or approximations. Machine learning could be used in applications like growth and nucleation where the properties are highly dependent on viscosity. There are viscosity machine learning models widely available for the public, thus reducing the need for experimental viscometry and enabling prediction of crystallization [529]. General approximations such as the crystal density and size could be optimized in one system and then applied to other systems, ignoring chemical changes. A thorough review of applications of these modeling techniques to bioactive glasses can be found elsewhere [58].

For the application of DGCs, there is a list of properties that will have to be controlled for commercially favorable materials:

- Strength: Optimized.
- Fracture Toughness: Optimized.
- Color: Matched to other teeth samples.
- Chemical Resistance: Optimized.
- Nucleation and Growth Curves: Controlled. The particular values of these are irrelevant as long as the curves are sufficiently separated and understood for the purpose of controlling the crystalline phase.
- Cost Minimized. This includes both cost of raw batch material and the processing.

Preliminary work in this area is underway, but it is far from predictive to the degree where we are able to control the properties to produce the ideal DGCs. However, as we understand each

of these properties more fully, the financial incentive to produce, research, and manufacture DGCs increases.

8. Summary, open issues and directions for future studies

The current state of the art in dental glass-ceramics demonstrates their exceptional versatility for aesthetic restoration of the crown, sophisticated regeneration of alveolar bone, dental root surgery, periodontal healing, bone attachment, and dentinal hypersensitivity treatment. However, we have not yet achieved the full potential of glass-ceramics in dentistry.

All-ceramic restorations are now widely researched to replace metal alloy-containing restorations. This review demonstrates that glass-ceramics are excellent candidates for all-ceramic tooth reconstruction. Continued R&D efforts are underway to improve the mechanical and aesthetic features of DGCs, enabling them to compete with other contenders such as zirconia, alumina and their polymer-infiltrated derivatives for posterior restorations. Comprehensive knowledge of toughening mechanisms is a primary step for developing tough, strong, and durable materials. The mechanical properties of DGCs are a hot topic of research that can be improved by engineering the morphology of crystals embedded in the residual glass. The crystal morphology can be modulated and tailored at the micro/nano-scale by properly designing composition and thermal treatments. New approaches and technologies can facilitate achieving these objectives. For example, new chemistry-based synthesizing methods like sol-gel could be further employed to expand the range of glass-ceramic composition. Researchers should pursue advanced sintering/crystallization processes, such as microwave heating [530], laser crystallization [531,532], spark-plasma sintering [356], biomimetic assemblage of crystals, textured crystallization, and electron beam crystallization. Chemical strengthening of restorative

DGCs by ion exchange is a promising route that should be further explored [533-537]. It may be ideal for developing restorative DGCs which in contact with bone and surrounding tissues show a cement-like behavior and facilitate biological surface responses for marginal attachment. Glass-ceramic matrix composites reinforced with tough ceramics or ductile biocompatible metals have been rarely investigated for restorative dentistry and demand additional attention.

The role of DGCs in imparting bone attachment and regenerative properties (root surgery and alveolar bone reconstruction) to otherwise inert materials is another important line of research. Glass-ionomer composites are widely used in restorative dentistry. We believe that glass-ceramic powders, including gel-derived bioactive formulations, could also be used as inorganic fillers in these important composite materials [538,539]. DGCs could be included in polymer-based injectable resins or coated on metallic implants. Bioactive DGCs as injectable pastes or ionomer cements can better fill the bone defect, even with complex shapes, and also have superior mechanical properties. Coating implants with DGCs still demand further attention. There is an undeniable need for designing suitable DGC compositions, using cost-effective deposition technologies, adjusting thermal expansion coefficient to obtain good interfacial adhesion between coating and implant, enhancing bone-bonding ability, regulating dissolution to avoid coating detachment prior to bone regeneration, and implant osteointegration.

Dental tissue engineering for the construction of tooth organs is a brand new and highly interesting research direction. A distinct shift is occurring in regenerative medicine from synthetic materials or tissue grafts to a more explicit approach that applies scaffolds for hosting cells and/or biological molecules to create functional replacement tissues in diseased or damaged dental sites. Periodontal tissue engineering, which is not limited to alveolar bone reconstruction (ideally, “integral” regeneration of periodontium, including tooth, cementum, periodontal

ligament, and gum) should be further followed. Early evidence shows that ionic dissolution products released from bioactive glasses and DGCs can stimulate the regeneration of other periodontal tissues, like cementum (lithium ions). Tremendous potential exists for functionally graded and multilayer scaffolds, which could simultaneously regenerate more than one dental tissue. DGC scaffolds are typically rigid, brittle, and challenging to be implanted/shaped. The goal of many dental scientists is to have pliable scaffolds that can be easily introduced into the defect site at the time of surgery with minimal or no previous pre-treatment by surgeons. We believe there are clear signs that DGCs, either alone or in combination with other materials like polymers, will find a wide range of applications for bone/tissue therapy in the world's aging population. However, (expensive and time-consuming) clinical tests should be encouraged to evaluate DGCs in real application cases. These ideas and several others are achieved by increasing interactions among materials engineers and scientists, chemists, dentists and biologists.

From the perspective of fundamental science, the crystallite concentration, size, and chemistry can be controlled through careful design of the base glass chemistry and the heat-treatment cycle used for nucleation and crystal growth. These composition and process parameters give new dimensions for optimizing the properties of DGCs. The success of DGCs is based on achieving unique combinations of attributes, including appropriate optical, thermal, mechanical, and biological properties, often which cannot be achieved by an "ordinary" non-crystalline glass. For many glass-ceramics, such as DGCs, formable and machinable materials are also critical concerns. The successful design of next-generation industrial glass-ceramic products should be aided by a renewed focus on the fundamental physics and chemistry governing these high-tech materials. Although the thermodynamic and kinetic aspects of

crystallization are of the utmost importance for designing industrial materials, there remains an insufficient theoretical understanding of these basic processes in glass-ceramics. Future development of new theoretically rigorous simulation and machine learning-based modeling will hopefully enable quantitatively accurate predictions of glass-ceramic microstructures and properties.

A detailed understanding of glass-ceramic materials is an exceptionally challenging problem, especially for many-component oxide systems like DGCs. However, this presents a unique opportunity to build a solid foundation for realizing the many exciting future applications of DGCs described in this article and to train the next generation of dental glass-ceramic scientists.

References

[1] Research and Market Ltd. Dental Implants Market: Global Industry Trends, Share, Size, Growth, Opportunity and Forecast 2021-2026. 2021.

[2] Sakaguchi RL, Powers JM. Craig's restorative dental materials-e-book. Elsevier Health Sciences; 2012.

[3] Research and Market Ltd. Bio-Implants Market: Global Industry Trends, Share, Size, Growth, Opportunity and Forecast 2021-2026. 2021.

[4] Montazerian M, Zanotto ED. Bioactive and inert dental glass-ceramics. J Biomed Mater Res Part A 2017;105:619–39.

[5] Powers J, Wataha J. Dental materials: foundations and applications. 11. painos. St Louis Missouri Elsevier 2017.

[6] Zhang Y-R, Du W, Zhou X-D, Yu H-Y. Review of research on the mechanical properties of the human tooth. Int J Oral Sci 2014;6:61–9.

[7] Arena A, Prete F, Rambaldi E, Bignozzi MC, Monaco C, Di Fiore A, et al. Nanostructured zirconia-based ceramics and composites in dentistry: A state-of-the-art review. Nanomaterials 2019;9:1393.

[8] Montazerian M, Singh SP, Zanotto ED. An analysis of glass-ceramic research and commercialization. Am Ceram Soc Bull 2015;94:30–5.

[9] Höland W. Biocompatible and bioactive glass-ceramics—state of the art and new directions. J Non Cryst Solids 1997;219:192–7.

[10] Höland W, Rheinberger V, Apel E, van't Hoen C, Höland M, Dommann A, et al. Clinical applications of glass-ceramics in dentistry. J Mater Sci Mater Med 2006;17:1037–42.

[11] Höland W, Rheinberger V. Bioengineering of glass-ceramics and ceramics for dental restoration. Bioeng Princ Methodol Appl USA Nov Sci Publ Inc 2010:169–78.

[12] Montazerian M, Zanotto ED. Bioactive glass-ceramics: processing, properties and applications. Bioact. Glas., 2016, p. 27–60.

[13] Montazerian M, Dutra Zanotto E. History and trends of bioactive glass-ceramics. J Biomed Mater Res Part A 2016;104:1231–49.

[14] Hench LL. The future of bioactive ceramics. J Mater Sci Mater Med 2015;26:1–4.

[15] Pollington S. Novel glass-ceramics for dental restorations. J Contemp Dent Pr 2011;12:60–7.

[16] Holand W, Beall GH. Glass-ceramic technology. John Wiley & Sons; 2019.

[17] El-Meliegy E, Van Noort R. Glasses and glass ceramics for medical applications. Springer science & business media; 2011.

[18] Saint-Jean SJ. Dental glasses and glass-ceramics. Adv. Ceram. Dent., Elsevier; 2014, p. 255–77.

[19] Johnson A, Sinthuprasirt P, Fathi H, Pollington S. Current glassceramic systems used in dentistry. Curr Trends Glas Ceram Mater UK Bentham Sci Publ Ltd 2013:49–72.

[20] Hupa L, Yli-Urpo A. Dental applications of glasses. Bio-Glasses An Introd 1st Ed, UK John Wiley Sons Ltd 2012:159–75.

[21] Fu L, Engqvist H, Xia W. Glass–ceramics in dentistry: a review. Materials (Basel) 2020;13:1049.

[22] Mauro JC, Zanotto ED. Two centuries of glass research: historical trends, current status, and grand challenges for the future. Int J Appl Glas Sci 2014;5:313–27.

[23] Kelly JR, Nishimura I, Campbell SD. Ceramics in dentistry: historical roots and current perspectives. J Prosthet Dent 1996;75:18–32.

[24] Kelly JR, Benetti P. Ceramic materials in dentistry: historical evolution and current practice. Aust Dent J 2011;56:84–96.

[25] Zhang Y, Kelly JR. Dental ceramics for restoration and metal veneering. Dent Clin 2017;61:797–819.

[26] Hench LL, Best SM. Ceramics, glasses, and glass-ceramics: basic principles. Biomater. Sci., Elsevier; 2013, p. 128–51.

[27] Silva LH da, Lima E de, Miranda RB de P, Favero SS, Lohbauer U, Cesar PF. Dental ceramics: a review of new materials and processing methods. Braz Oral Res 2017;31.

[28] Malament KA, Grossman DG. The cast glass-ceramic restoration. J Prosthet Dent 1987;57:674–83.

[29] Wildgoose DG, Johnson A, Winstanley RB. Glass/ceramic/refractory techniques, their development and introduction into dentistry: A historical literature review. J Prosthet Dent 2004;91:136–43.

[30] Ironside JG, Swain M V. Ceramics in dental restorations—a review and critical issues. J Aust Ceram Soc 1998;34:78–91.

[31] Rosenblum MA, Schulman A. A review of all-ceramic restorations. J Am Dent Assoc 1997;128:297–307.

[32] Lang SA, Starr CB. Castable glass ceramics for veneer restorations. J Prosthet Dent 1992;67:590–4.

[33] Rekow ED, Silva N, Coelho PG, Zhang Y, Guess P, Thompson VP. Performance of dental ceramics: challenges for improvements. J Dent Res 2011;90:937–52.

[34] Denry IL, Holloway JA. Effect of magnesium content on the microstructure and crystalline phases of fluoramphibole glass-ceramics. J Biomed Mater Res An Off J Soc Biomater Japanese Soc Biomater Aust Soc Biomater Korean Soc Biomater 2000;53:289–96.

[35] Kokubo T. Bioceramics and their clinical applications. Elsevier; 2008.

[36] Salinas AJ, Vallet-Regí M. Bioactive ceramics: from bone grafts to tissue engineering. RSC Adv 2013;3:11116–31.

[37] Baino F, Novajra G, Miguez-Pacheco V, Boccaccini AR, Vitale-Brovarone C. Bioactive glasses: special applications outside the skeletal system. J Non Cryst Solids 2016;432:15–30.

[38] Miguez-Pacheco V, Hench LL, Boccaccini AR. Bioactive glasses beyond bone and teeth:

Emerging applications in contact with soft tissues. Acta Biomater 2015;13:1–15.

[39] Hench LL. An introduction to bioceramics. vol. 1. World scientific; 1993.

[40] Kokubo T. Bioactive glass ceramics: properties and applications. Biomaterials 1991;12:155–63.

[41] Höland W, Vogel W, Naumann K, Gummel J. Interface reactions between machinable bioactive glass-ceramics and bone. J Biomed Mater Res 1985;19:303–12.

[42] Peitl O, La Torre GP, Hench LL. Effect of crystallization on apatite-layer formation of bioactive glass 45S5. J Biomed Mater Res An Off J Soc Biomater Japanese Soc Biomater 1996;30:509–14.

[43] Peitl O, Zanotto ED, Hench LL. Highly bioactive P_2O_5–Na_2O–CaO–SiO_2 glass-ceramics. J Non Cryst Solids 2001;292:115–26.

[44] Zanotto ED, Mauro JC. The glassy state of matter: Its definition and ultimate fate. J Non Cryst Solids 2017;471:490–5.

[45] Varshneya AK. Fundamentals of inorganic glasses. Elsevier; 2013.

[46] Zanotto ED. Bright future for glass-ceramics. Am Ceram Soc Bull 2010;89:19–27.

[47] Navarro JMF. El vidrio: constitución, fabricación, propiedades. Consejo Seuperior de Investigaciones Científicas, Instituto de Cerámica y Vidrio; 1985.

[48] David Pye L. Arrival of the Glass Age Affirmed 2016.

[49] Morse DL, Evenson JW. Welcome to the glass age. Int J Appl Glas Sci 2016;7:409–12.

[50] Bolt M. Glass: The eye of science. Int J Appl Glas Sci 2017;8:4–22.

[51] Hench LL. Glass and glass-ceramic technologies to transform the world. Int J Appl Glas Sci 2011;2:162–76.

[52] Ballato J, Ebendorff-Heidepriem H, Zhao J, Petit L, Troles J. Glass and process development for the next generation of optical fibers: A review. Fibers 2017;5:11.

[53] Varshneya AK, Bihuniak PP. Cover screens for personal electronic devices: Strengthened glass or sapphire. Am Ceram Soc Bull 2018;96:21–5.

[54] Li HX, Lu ZC, Wang SL, Wu Y, Lu ZP. Fe-based bulk metallic glasses: Glass formation, fabrication, properties and applications. Prog Mater Sci 2019;103:235–318.

[55] Shi Y. Size-dependent mechanical responses of metallic glasses. Int Mater Rev 2019;64:163–80.

[56] Lin C, Rüssel C, Dai S. Chalcogenide glass-ceramics: functional design and crystallization mechanism. Prog Mater Sci 2018;93:1–44.

[57] Montazerian M, Zanotto ED. A guided walk through Larry Hench's monumental discoveries. J Mater Sci 2017;52:8695–732.

[58] Montazerian M, Zanotto ED, Mauro JC. Model-driven design of bioactive glasses: from molecular dynamics through machine learning. Int Mater Rev 2020;65:297–321.

[59] Chiriac H, Óvári TA. Amorphous glass-covered magnetic wires: preparation, properties, applications. Prog Mater Sci 1996;40:333–407.

[60] Mauro JC. Materials Kinetics: Transport and Rate Phenomena. Elsevier; 2020.

[61] Taqieddin A, Allshouse MR, Alshawabkeh AN. Critical Review—Mathematical formulations of electrochemically gas-evolving systems. J Electrochem Soc 2018;165:E694.

[62] Montazerian M, Zanotto ED. Restorative dental glass-ceramics: current status and trends. Clin. Appl. Biomater., Springer; 2017, p. 313–36.

[63] Tammann G. Über die Abhängigkeit der Zahl der Kerne, welche sich in verschiedenen unterkühlten Flüssigkeiten bilden, von der Temperatur. Zeitschrift Für Phys Chemie 1898;25:441–79.

[64] Gránásy L. Diffuse interface theory of nucleation. J Non Cryst Solids 1993;162:301–3.

[65] Spaepen F. Homogeneous nucleation and the temperature dependence of the crystal-melt interfacial tension. Solid State Phys 1994;47:1–32.

[66] Gránásy L. Diffuse interface model of crystal nucleation. J Non Cryst Solids 1997;219:49–56.

[67] Granasy L, Tóth GI, Warren JA, Podmaniczky F, Tegze G, Ratkai L, et al. Phase-field modeling of crystal nucleation in undercooled liquids–A review. Prog Mater Sci 2019;106:100569.

[68] Kelton KF. Solid State Physics: Advances in Research and Applications 1991.

[69] Gránásy L, Iglói F. Comparison of experiments and modern theories of crystal nucleation. J Chem Phys 1997;107:3634–44.

[70] Hillig WB, Turnbull D. Theory of crystal growth in undercooled pure liquids. J Chem Phys 1956;24:914.

[71] Deubener J, Brückner R, Sternitzke M. Induction time analysis of nucleation and crystal growth in di-and metasilicate glasses. J Non Cryst Solids 1993;163:1–12.

[72] Johnson WA. Reaction kinetics in processes of nucleation and growth. Am Inst Min Met Petro Eng 1939;135:416–58.

[73] Avrami M. Kinetics of phase change. I General theory. J Chem Phys 1939;7:1103–12.

[74] Avrami M. Kinetics of phase change. II transformation-time relations for random distribution of nuclei. J Chem Phys 1940;8:212–24.

[75] Avrami M. Kinetics of phase change. III: Granulation, phase change and microstructure. J Chem Phys 1941;9:177–84.

[76] Christian JW. The theory of transformations in metals and alloys. Newnes; 2002.

[77] Montazerian M, Zanotto ED. The Glassy State. In: Pomeroy M, editor. Encycl. Mater. Tech. Ceram. Glas., Oxford: Elsevier; 2021, p. 448–61. https://doi.org/https://doi.org/10.1016/B978-0-12-803581-8.11728-X.

[78] Gutzow I, Schmelzer J. The vitreous state. Springer; 1995.

[79] Henderson DW. Thermal analysis of nonisothermal transformations involving nucleation and growth. J Non-Cryst Solids 1979;30:301.

[80] Matusita K, Komatsu T, Yokota R. Kinetics of non-isothermal crystallization process and

activation energy for crystal growth in amorphous materials. J Mater Sci 1984;19:291–6.

[81] Farjas Silva J, Roura Grabulosa P. Modification of the Kolmogorov-Johnson-Mehl-Avrami rate equation for non-isothermal experiments and its analytical solution. © Acta Mater 2006, Vol 54, Núm 20, p 5573-5579 2006.

[82] Illeková E, Šesták J. Crystallization of metallic micro-, nano-, and non-crystalline alloys. Therm. Anal. Micro, Nano-and Non-Crystalline Mater., Springer; 2012, p. 257–89.

[83] Zanotto ED. Glass Crystallization Research—A 36-Year Retrospective. Part I, Fundamental Studies. Int J Appl Glas Sci 2013;4:105–16.

[84] Beall GH. Dr. S. Donald (Don) Stookey (1915–2014): Pioneering Researcher and Adventurer. Front Mater 2016;3:37.

[85] Beall GH. Design and properties of glass-ceramics. Annu Rev Mater Sci 1992;22:91–119.

[86] Kaur G, Pickrell G, Sriranganathan N, Kumar V, Homa D. Review and the state of the art: sol–gel and melt quenched bioactive glasses for tissue engineering. J Biomed Mater Res Part B Appl Biomater 2016;104:1248–75.

[87] Hench LL, West JK. The sol-gel process. Chem Rev 1990;90:33–72.

[88] Hench LL. Sol-gel silica: properties, processing and technology transfer. William Andrew; 1998.

[89] Fiume E, Barberi J, Verné E, Baino F. Bioactive glasses: from parent 45S5 composition to scaffold-assisted tissue-healing therapies. J Funct Biomater 2018;9:24.

[90] Baino F, Fiume E, Miola M, Verné E. Bioactive sol-gel glasses: processing, properties, and applications. Int J Appl Ceram Technol 2018;15:841–60.

[91] Rathee M, Bhoria M, Malik P. Shade Matching in Aesthetic Dentistry: An Overview. Med Sci 2014;3.

[92] Sarna-Boś K, Batyra A, Oleszek-Listopad J, Piórkowska-Skrabucha B, Borowicz J, Szymańska J. A comparison of the traditional casting method and the galvanoforming technique in gold alloy prosthetic restorations. Curr Issues Pharm Med Sci 2015;28:196–9.

[93] Zhao Y, Chen J, Fang M, Li N, Sun X, Xiao Y, et al. Effect of dental heat pressing on the microstructure of SiO_2–K_2O–B_2O_3–MgO–F glass–ceramic. Int J Appl Ceram Technol 2008;5:649–56.

[94] Albakry M, Guazzato M, Swain MV. Influence of hot pressing on the microstructure and fracture toughness of two pressable dental glass–ceramics. J Biomed Mater Res Part B Appl Biomater An Off J Soc Biomater Japanese Soc Biomater Aust Soc Biomater Korean Soc Biomater 2004;71:99–107.

[95] Gorman CM, McDevitt WE, Hill RG. Comparison of two heat-pressed all-ceramic dental materials. Dent Mater 2000;16:389–95.

[96] Azar B, Eckert S, Kunkela J, Ingr T, Mounajjed R. The marginal fit of lithium disilicate crowns: Press vs. CAD/CAM. Braz Oral Res 2018;32.

[97] Li RWK, Chow TW, Matinlinna JP. Ceramic dental biomaterials and CAD/CAM technology: state of the art. J Prosthodont Res 2014;58:208–16.

[98] Assembly FG. CAD/CAM Dentistry. Int Dent J 2018;68:18–9.

[99] Banks RG. Conservative posterior ceramic restorations: a literature review. J Prosthet Dent 1990;63:619–26.

[100] Tidehag P, Shen Z. Digital dentistry calls the change of ceramics and ceramic processes. Adv Appl Ceram 2019;118:83–90.

[101] Hench LL. The story of Bioglass®. J Mater Sci Mater Med 2006;17:967–78.

[102] Hench LL. Genetic design of bioactive glass. J Eur Ceram Soc 2009;29:1257–65.

[103] Greenspan DC. Bioactive glass: Mechanisms of bone bonding. Tandläkartidningen Årk 1999;91:1–32.

[104] Sedighi O, Alaghmandfard A, Montazerian M, Baino F. A Critical Review of Bioceramics for Magnetic Hyperthermia. J Am Ceram Soc n.d.;n/a. https://doi.org/https://doi.org/10.1111/jace.17861.

[105] Rahaman MN, Day DE, Bal BS, Fu Q, Jung SB, Bonewald LF, et al. Bioactive glass in tissue engineering. Acta Biomater 2011;7:2355–73.

[106] Hum J, Boccaccini AR. Bioactive glasses as carriers for bioactive molecules and therapeutic drugs: a review. J Mater Sci Mater Med 2012;23:2317–33.

[107] Miguez-Pacheco V, Greenspan D, Hench LL, Boccaccini AR. Bioactive glasses in soft tissue repair. Am Ceram Soc Bull 2015;94:27–31.

[108] Kargozar S, Mozafari M, Hamzehlou S, Kim H-W, Baino F. Mesoporous bioactive glasses (MBGs) in cancer therapy: Full of hope and promise. Mater Lett 2019;251:241–6.

[109] Kargozar S, Mozafari M, Hamzehlou S, Baino F. Using bioactive glasses in the management of burns. Front Bioeng Biotechnol 2019;7:62.

[110] Hench LL, Roki N, Fenn MB. Bioactive glasses: Importance of structure and properties in bone regeneration. J Mol Struct 2014;1073:24–30.

[111] Abbasi Z, Bahrololoom ME, Shariat MH, Bagheri R. Bioactive glasses in dentistry: a review. J Dent Biomater 2015;2:1–9.

[112] Fu Q, Saiz E, Rahaman MN, Tomsia AP. Bioactive glass scaffolds for bone tissue engineering: state of the art and future perspectives. Mater Sci Eng C 2011;31:1245–56.

[113] Thompson ID, Hench LL. Mechanical properties of bioactive glasses, glass-ceramics and composites. Proc Inst Mech Eng Part H J Eng Med 1998;212:127–36.

[114] W. Holand. Glass-Ceramics. Bio-Glasses An Introd John Wiley Sons, Inc 2012:97–105.

[115] Owens GJ, Singh RK, Foroutan F, Alqaysi M, Han C-M, Mahapatra C, et al. Sol–gel based materials for biomedical applications. Prog Mater Sci 2016;77:1–79.

[116] Jones JR. Review of bioactive glass: from Hench to hybrids. Acta Biomater 2013;9:4457–86.

[117] Fiume E, Migneco C, Verné E, Baino F. Comparison between Bioactive Sol-Gel and Melt-Derived Glasses/Glass-Ceramics Based on the Multicomponent SiO_2–P_2O_5–CaO–MgO–Na_2O–K_2O System. Materials (Basel) 2020;13:540.

[118] Jones JR, Ehrenfried LM, Hench LL. Optimising bioactive glass scaffolds for bone tissue

engineering. Biomaterials 2006;27:964–73.

[119] Brien FJO. Biomaterials & scaffolds Every day thousands of surgical procedures are performed to replace. Mater Today 2011;14:88–95.

[120] Baino F, Fiume E, Barberi J, Kargozar S, Marchi J, Massera J, et al. Processing methods for making porous bioactive glass-based scaffolds—A state-of-the-art review. Int J Appl Ceram Technol 2019;16:1762–96.

[121] Baino F, Barberi J, Fiume E, Orlygsson G, Massera J, Verné E. Robocasting of Bioactive SiO_2-P_2O_5-CaO-MgO-Na_2O-K_2O Glass Scaffolds. J Healthc Eng 2019;2019.

[122] Gibon E, Córdova LA, Lu L, Lin T, Yao Z, Hamadouche M, et al. The biological response to orthopedic implants for joint replacement. II: Polyethylene, ceramics, PMMA, and the foreign body reaction. J Biomed Mater Res Part B Appl Biomater 2017;105:1685–91.

[123] Gerhardt L-C, Boccaccini AR. Bioactive glass and glass-ceramic scaffolds for bone tissue engineering. Materials (Basel) 2010;3:3867–910.

[124] Baino F, Novajra G, Vitale-Brovarone C. Bioceramics and scaffolds: a winning combination for tissue engineering. Front Bioeng Biotechnol 2015;3:202.

[125] Baino F, Caddeo S, Novajra G, Vitale-Brovarone C. Using porous bioceramic scaffolds to model healthy and osteoporotic bone. J Eur Ceram Soc 2016;36:2175–82.

[126] Chen QZ, Thompson ID, Boccaccini AR. 45S5 Bioglass®-derived glass–ceramic scaffolds for bone tissue engineering. Biomaterials 2006;27:2414–25.

[127] Bretcanu O, Samaille C, Boccaccini AR. Simple methods to fabricate Bioglass®-derived glass–ceramic scaffolds exhibiting porosity gradient. J Mater Sci 2008;43:4127–34.

[128] Gmeiner R, Deisinger U, Schönherr J, Lechner B, Detsch R, Boccaccini AR, et al. Additive manufacturing of bioactive glasses and silicate bioceramics. J Ceram Sci Technol 2015;6:75–86.

[129] Nommeots-Nomm A, Labbaf S, Devlin A, Todd N, Geng H, Solanki AK, et al. Highly degradable porous melt-derived bioactive glass foam scaffolds for bone regeneration. Acta Biomater 2017;57:449–61.

[130] Fiume E, Tulyaganov D, Ubertalli G, Verné E, Baino F. Dolomite-Foamed Bioactive Silicate Scaffolds for Bone Tissue Repair. Materials (Basel) 2020;13:628.

[131] Poologasundarampillai G, Lee PD, Lam C, Kourkouta A, Jones JR. Compressive strength of bioactive sol–gel glass foam scaffolds. Int J Appl Glas Sci 2016;7:229–37.

[132] Baino F, Fiume E, Miola M, Leone F, Onida B, Verné E. Fe-doped bioactive glass-derived scaffolds produced by sol-gel foaming. Mater Lett 2019;235:207–11.

[133] Fukasawa T, Deng Z-Y, Ando M, Ohji T, Goto Y. Pore structure of porous ceramics synthesized from water-based slurry by freeze-dry process. J Mater Sci 2001;36:2523–7.

[134] Deville S, Saiz E, Tomsia AP. Freeze casting of hydroxyapatite scaffolds for bone tissue engineering. Biomaterials 2006;27:5480–9.

[135] Fu Q, Rahaman MN, Bal BS, Brown RF. Preparation and in vitro evaluation of bioactive glass (13–93) scaffolds with oriented microstructures for repair and regeneration of load-bearing bones. J Biomed Mater Res Part A An Off J Soc Biomater Japanese Soc

Biomater Aust Soc Biomater Korean Soc Biomater 2010;93:1380–90.

[136] Lee JW, Kim JY, Cho D-W. Solid free-form fabrication technology and its application to bone tissue engineering. Int J Stem Cells 2010;3:85.

[137] Melchels FPW, Feijen J, Grijpma DW. A review on stereolithography and its applications in biomedical engineering. Biomaterials 2010;31:6121–30.

[138] Chua CK, Wong CH, Yeong WY, Chua CK, Wong CH, Yeong WY. Chapter One– Introduction to 3D Printing or Additive Manufacturing. Stand Qual Control Meas Sci 3D Print Addit Manuf 2017:1–29.

[139] Lorrison JC, Goodridge RD, Daigarno KW, Wood DJ. Selective laser sintering of bioactive glass-ceramics. 2002 Int. Solid Free. Fabr. Symp., 2002.

[140] Shirazi SFS, Gharehkhani S, Mehrali M, Yarmand H, Metselaar HSC, Kadri NA, et al. A review on powder-based additive manufacturing for tissue engineering: selective laser sintering and inkjet 3D printing. Sci Technol Adv Mater 2015.

[141] Liu J, Hu H, Li P, Shuai C, Peng S. Fabrication and characterization of porous 45S5 glass scaffolds via direct selective laser sintering. Mater Manuf Process 2013;28:610–5.

[142] Gao C, Liu T, Shuai C, Peng S. Enhancement mechanisms of graphene in nano-58S bioactive glass scaffold: mechanical and biological performance. Sci Rep 2014;4:1–10.

[143] Kolan KCR, Leu MC, Hilmas GE, Brown RF, Velez M. Fabrication of 13-93 bioactive glass scaffolds for bone tissue engineering using indirect selective laser sintering. Biofabrication 2011;3:25004.

[144] Tesavibul P, Felzmann R, Gruber S, Liska R, Thompson I, Boccaccini AR, et al. Processing of 45S5 Bioglass® by lithography-based additive manufacturing. Mater Lett 2012;74:81–4.

[145] Felzmann R, Gruber S, Mitteramskogler G, Tesavibul P, Boccaccini AR, Liska R, et al. Lithography-based additive manufacturing of cellular ceramic structures. Adv Eng Mater 2012;14:1052–8.

[146] Thavornyutikarn B, Chantarapanich N, Sitthiseripratip K, Thouas GA, Chen Q. Bone tissue engineering scaffolding: computer-aided scaffolding techniques. Prog Biomater 2014;3:61–102.

[147] Li Z, Chen X, Zhao N, Dong H, Li Y, Lin C. Stiff macro-porous bioactive glass–ceramic scaffold: Fabrication by rapid prototyping template, characterization and in vitro bioactivity. Mater Chem Phys 2013;141:76–80.

[148] Baino F, Fiume E. 3D printing of hierarchical scaffolds based on mesoporous bioactive glasses (MBGs)—Fundamentals and applications. Materials (Basel) 2020;13:1688.

[149] CESARANO III J. Robocasting of ceramics and composites using fine particle suspensions. Sandia National Labs., Albuquerque, NM (US); Sandia National Labs …; 1999.

[150] Wu C, Luo Y, Cuniberti G, Xiao Y, Gelinsky M. Three-dimensional printing of hierarchical and tough mesoporous bioactive glass scaffolds with a controllable pore architecture, excellent mechanical strength and mineralization ability. Acta Biomater 2011;7:2644–50.

[151] Zhang J, Zhao S, Zhu Y, Huang Y, Zhu M, Tao C, et al. Three-dimensional printing of strontium-containing mesoporous bioactive glass scaffolds for bone regeneration. Acta Biomater 2014;10:2269–81.

[152] Albrektsson T, Johansson C. Osteoinduction, osteoconduction and osseointegration. Eur Spine J 2001;10:S96–101.

[153] Osman RB, Swain M V. A critical review of dental implant materials with an emphasis on titanium versus zirconia. Materials (Basel) 2015;8:932–58.

[154] Al Mugeiren OM, Baseer MA. Dental implant bioactive surface modifiers: An update. J Int Soc Prev Community Dent 2019;9:1.

[155] Sola A, Bellucci D, Cannillo V, Cattini A. Bioactive glass coatings: a review. Surf Eng 2011;27:560–72.

[156] Joy-anne NO, Su Y, Lu X, Kuo P-H, Du J, Zhu D. Bioactive glass coatings on metallic implants for biomedical applications. Bioact Mater 2019;4:261–70.

[157] Baino F, Verné E. Glass-based coatings on biomedical implants: A state-of-the-art review. Biomed Glas 2017;3:1–17.

[158] Verné E. Bioactive glass and glass-ceramic coatings. Bio-Glasses–An Introd 2012:107–19.

[159] Zhao L, Chu K. P.; Zhang, Y.; Wu, Z. Antibacterial Coatings on Titanium Implants. J Biomed Mater Res, Part B 2009;91:470–80.

[160] Brunello G, Elsayed H, Biasetto L. Bioactive Glass and Silicate-Based Ceramic Coatings on Metallic Implants: Open Challenge or Outdated Topic? Materials (Basel) 2019;12:2929.

[161] Majumdar A, Jana S. Glass and glass-ceramic coatings, versatile materials for industrial and engineering applications. Bull Mater Sci 2001;24:69–77.

[162] Sergi R, Bellucci D, Cannillo V. A comprehensive review of bioactive glass coatings: State of the art, challenges and future perspectives. Coatings 2020;10:757.

[163] Al-Noaman A, Rawlinson SCF, Hill RG. The role of MgO on thermal properties, structure and bioactivity of bioactive glass coating for dental implants. J Non Cryst Solids 2012;358:3019–27.

[164] Pierlot C, Pawlowski L, Bigan M, Chagnon P. Design of experiments in thermal spraying: A review. Surf Coatings Technol 2008;202:4483–90.

[165] ASTM. ASTM F1854-15: Standard Test Method for Stereological Evaluation of Porous Coatings on Medical. 2015.

[166] Zhang Y, Zuo TT, Tang Z, Gao MC, Dahmen KA, Liaw PK, et al. Microstructures and properties of high-entropy alloys. Prog Mater Sci 2014;61:1–93.

[167] Garcia E, Miranzo P, Sainz MA. Thermally sprayed wollastonite and wollastonite-diopside compositions as new modulated bioactive coatings for metal implants. Ceram Int 2018;44:12896–904.

[168] Surmenev R, Vladescu A, Surmeneva M, Ivanova A, Braic M, Grubova I, et al. Radio frequency magnetron sputter deposition as a tool for surface modification of medical

implants. Mod. Technol. Creat. thin-film Syst. coatings, InTech; 2017, p. 213–48.

[169] Bosco R, Van Den Beucken J, Leeuwenburgh S, Jansen J. Surface engineering for bone implants: a trend from passive to active surfaces. Coatings 2012;2:95–119.

[170] Mittra J, Abraham GJ, Kesaria M, Bahl S, Gupta A, Shivaprasad SM, et al. Role of substrate temperature in the pulsed laser deposition of zirconium oxide thin film. Mater. Sci. Forum, vol. 710, Trans Tech Publ; 2012, p. 757–61.

[171] Figueira RB, Fontinha IR, Silva CJR, Pereira E V. Hybrid sol-gel coatings: smart and green materials for corrosion mitigation. Coatings 2016;6:12.

[172] Singh BP, Jena BK, Bhattacharjee S, Besra L. Development of oxidation and corrosion resistance hydrophobic graphene oxide-polymer composite coating on copper. Surf Coatings Technol 2013;232:475–81.

[173] Boccaccini AR, Keim S, Ma R, Li Y, Zhitomirsky I. JR Soc. Interface 7. S581 2010.

[174] Lakes RS, Park J. Biomaterials: an introduction. Springer Science & Business Media; 1992.

[175] Wang M. Developing bioactive composite materials for tissue replacement. Biomaterials 2003;24:2133–51.

[176] Hull D. An Introduction to Composite Materials 1998.

[177] Geesink R. Hydroxyl-apatite coated hip implants: experimental and clinical studies. Bone-Bonding Biomater 1992.

[178] Elliott JC. Handbook of Structure and Chemistry of the Apatite and Other Calcium Orthophosphates. Vol. 18 1994.

[179] Kokubo T. Bioactivity of glasses and glass-ceramics. Bone-Bonding Biomater 1992:31–46.

[180] Wang M. Bioactive ceramic–polymer composites for bone replacement. Proc. 13th Int. Conf. Compos. Mater. (ICCM-13), Beijing, China. Pap., vol. 1541, 2001.

[181] Bonfield W. Materials for the replacement of osteoarthritic hip joints. Met Mater 1987;3:712–6.

[182] Fung Y. Biomechanics: mechanical properties of living tissues. Springer Science & Business Media; 2013.

[183] Aoki H. Medical applications of hydroxyapatite. Tokyo, St Louis: Ishiyaku EuroAmerica 1994.

[184] Bonfield W. Hydroxyapatite-Reinforced Polyethylene as an Analogous Material for Bone Replacement a. Ann N Y Acad Sci 1988;523:173–7.

[185] Wang M, Bonfield W, Li M, Guiu F. Interphase in composite materials. Key Eng. Mater., vol. 127, Trans Tech Publ; 1997, p. 583–90.

[186] Guild FJ, Bonfield W. Predictive modelling of hydroxyapatite-polyethylene composite. Biomaterials 1993;14:985–93.

[187] M. Wang WB. HAPEX for otologic implants— manufacture, structure and properties. IRC Rep to Smith Nephew Richards Inc, IRC Biomed Mater 1995.

[188] Clarke KI, Graves SE, Wong ATC, Triffitt JT, Francis MJO, Czernuszka JT. Investigation into the formation and mechanical properties of a bioactive material based on collagen and calcium phosphate. J Mater Sci Mater Med 1993;4:107–10.

[189] Wang M, Weng J, Poret K. Manufacture and characterisation of biodegradable composites consisting of bioceramics and chitin. Proc. 13th Int. Conf. Compos. Mater. (ICCM-13), Beijing, China, 2001.

[190] Kikuchi M, Itoh S, Ichinose S, Shinomiya K, Tanaka J. Self-organization mechanism in a bone-like hydroxyapatite/collagen nanocomposite synthesized in vitro and its biological reaction in vivo. Biomaterials 2001;22:1705–11.

[191] Taurio R, Törmälä P. Coral based and sintered hydroxylapatite blocks reinforced with fibrous cage-like polylactide composite: a comparative study. Bioceramics, Elsevier; 1991, p. 287–94.

[192] Wang M, Bonfield W, Hench LL. Bioglass®/high density polyethylene composite as a new soft tissue bonding material. Bioceramics 1995;8:383–8.

[193] Wang M, Kokubo T, Bonfield W, Nakamura T, Miyaji F. A-W Glass-ceramic Reinforced Polyethylene for Medical Applications, International symposium; 9th, Ceramics in medicine: Bioceramics. Ceram. Med. Bioceram. Bioceram. -CONFERENCE-, Int. Symp. 9th, Ceram. Med. Bioceram., vol. 9, Pergamon; 1996, p. 387–90.

[194] Reis RL. Bioinert and biodegradable polymeric matrix composites filled with bioactive SiO_2-3CaO P_2O_5-MgO glasses and glass-ceramics. Bioceramics 1997;10:415–8.

[195] Bakar MSA, Cheang P, Khor KA. Thermal processing of hydroxyapatite reinforced polyetheretherketone composites. J Mater Process Technol 1999;89:462–6.

[196] Wang M, Weng J, Ni J, Goh CH, Wang CX. Developing tricalcium phosphate/polyhydroxybutyrate composite as a new biodegradable material for clinical applications. Key Eng Mater 2001;192.

[197] Sousa RA, Reis RL, Cunha AM, Bevis MJ. Structure and properties of hydroxylapatite reinforced starch bone-analogue composites. Key Eng Mater 2001;192.

[198] Wang M, Wang CX, Weng J, Ni J, Quek PY. Production and evaluation of biodegradable hydroxyapatite/polyhydroxybutyrate composite. Proc. 10th Int. Conf. Biomed. Eng. Singapore, 2000, p. 545–6.

[199] Wang M, Bonfield W. Processing of highly filled polyethylene for medical applications. Polym Process Towar AD2000, Singapore Singapore Univ Press 1996:203–4.

[200] Baino F, Fiorilli S, Vitale-Brovarone C. Composite biomaterials based on sol-gel mesoporous silicate glasses: A review. Bioengineering 2017;4:15.

[201] El-Fiqi A, Lee JH, Lee E-J, Kim H-W. Collagen hydrogels incorporated with surface-aminated mesoporous nanobioactive glass: improvement of physicochemical stability and mechanical properties is effective for hard tissue engineering. Acta Biomater 2013;9:9508–21.

[202] El-Kady AM, Ali AF, Farag MM. Development, characterization, and in vitro bioactivity studies of sol–gel bioactive glass/poly (L-lactide) nanocomposite scaffolds. Mater Sci Eng C 2010;30:120–31.

[203] Li X, Wang X, Zhang L, Chen H, Shi J. MBG/PLGA composite microspheres with prolonged drug release. J Biomed Mater Res Part B Appl Biomater An Off J Soc Biomater Japanese Soc Biomater Aust Soc Biomater Korean Soc Biomater 2009;89:148–54.

[204] Wu C, Ramaswamy Y, Zhu Y, Zheng R, Appleyard R, Howard A, et al. The effect of mesoporous bioactive glass on the physiochemical, biological and drug-release properties of poly (DL-lactide-co-glycolide) films. Biomaterials 2009;30:2199–208.

[205] Su J, Cao L, Yu B, Song S, Liu X, Wang Z, et al. Composite scaffolds of mesoporous bioactive glass and polyamide for bone repair. Int J Nanomedicine 2012;7:2547.

[206] Li X, Shi J, Dong X, Zhang L, Zeng H. A mesoporous bioactive glass/polycaprolactone composite scaffold and its bioactivity behavior. J Biomed Mater Res Part A An Off J Soc Biomater Japanese Soc Biomater Aust Soc Biomater Korean Soc Biomater 2008;84:84–91.

[207] Yun H, Kim S, Park EK. Bioactive glass–poly (ε-caprolactone) composite scaffolds with 3 dimensionally hierarchical pore networks. Mater Sci Eng C 2011;31:198–205.

[208] Wu C, Zhu Y, Chang J, Zhang Y, Xiao Y. Bioactive inorganic-materials/alginate composite microspheres with controllable drug-delivery ability. J Biomed Mater Res Part B Appl Biomater 2010;94:32–43.

[209] Luo Y, Wu C, Lode A, Gelinsky M. Hierarchical mesoporous bioactive glass/alginate composite scaffolds fabricated by three-dimensional plotting for bone tissue engineering. Biofabrication 2012;5:15005.

[210] Chandrasekaran A, Novajra G, Carmagnola I, Gentile P, Fiorilli S, Miola M, et al. Physico-chemical and biological studies on three-dimensional porous silk/spray-dried mesoporous bioactive glass scaffolds. Ceram Int 2016;42:13761–72.

[211] Wu C, Zhang Y, Zhou Y, Fan W, Xiao Y. A comparative study of mesoporous glass/silk and non-mesoporous glass/silk scaffolds: physiochemistry and in vivo osteogenesis. Acta Biomater 2011;7:2229–36.

[212] Li N, Jiang C, Zhang X, Gu X, Zhang J, Yuan Y, et al. Preparation of an rhBMP-2 loaded mesoporous bioactive glass/calcium phosphate cement porous composite scaffold for rapid bone tissue regeneration. J Mater Chem B 2015;3:8558–66.

[213] Jia T, Chen J, Feng X, Chang J. Symbolfabrication and characterization of chitosan/mesoporous bioactive glasses porous films. J Clin Rehabil Tissue Eng Res 2011;15:7877–80.

[214] Zhang Y, Griggs JA, Benham AW. Influence of powder/liquid mixing ratio on porosity and translucency of dental porcelains. J Prosthet Dent 2004;91:128–35.

[215] Bagis B, Turgut S. Optical properties of current ceramics systems for laminate veneers. J Dent 2013;41:e24–30.

[216] Vichi A, Louca C, Corciolani G, Ferrari M. Color related to ceramic and zirconia restorations: a review. Dent Mater 2011;27:97–108.

[217] Kurt M, Güngör MB, Nemli SK, Bal BT. Effects of glazing methods on the optical and surface properties of silicate ceramics. J Prosthodont Res 2020;64:202–9.

[218] Chang J, Da Silva JD, Sakai M, Kristiansen J, Ishikawa-Nagai S. The optical effect of

composite luting cement on all ceramic crowns. J Dent 2009;37:937–43.

[219] Sravanthi Y, Ramani Y V, Rathod AM, Ram SM, Turakhia H. The comparative evaluation of the translucency of crowns fabricated with three different all-ceramic materials: an in vitro study. J Clin Diagnostic Res JCDR 2015;9:ZC30.

[220] Hermanson AS, Bush MA, Miller RG, Bush PJ. Ultraviolet illumination as an adjunctive aid in dental inspection. J Forensic Sci 2008;53:408–11.

[221] Lee Y-K. Fluorescence properties of human teeth and dental calculus for clinical applications. J Biomed Opt 2015;20:40901.

[222] Tabatabaei MH, Nahavandi AM, Khorshidi S, Hashemikamangar SS. Fluorescence and opalescence of two dental composite resins. Eur J Dent 2019;13:527.

[223] Kim H-K, Kim S-H. Effect of the number of coloring liquid applications on the optical properties of monolithic zirconia. Dent Mater 2014;30:e229–37.

[224] Turgut S. Optical properties of currently used zirconia-based esthetic restorations fabricated with different techniques. J Esthet Restor Dent 2020;32:26–33.

[225] Shahmiri R, Standard OC, Hart JN, Sorrell CC. Optical properties of zirconia ceramics for esthetic dental restorations: A systematic review. J Prosthet Dent 2018;119:36–46.

[226] Yang C-C, Ding S-J, Lin T-H, Yan M. Mechanical and optical properties evaluation of rapid sintered dental zirconia. Ceram Int 2020;46:26668–74.

[227] Lee J-H, Kim S-H, Han J-S, Yeo I-SL, Yoon H-I, Lee J. Effects of ultrasonic scaling on the optical properties and surface characteristics of highly translucent CAD/CAM ceramic restorative materials: An in vitro study. Ceram Int 2019;45:14594–601.

[228] Bitencourt SB, Bastos NA, Mazza LC, Rangel EC, De Souza GM, da Silva Pereira F, et al. Effect of handling material on mechanical and optical properties of feldspathic porcelain. J Esthet Restor Dent 2020.

[229] dos Reis MC, Silva VRM, Sgura R, da Cruz NC, Rangel EC, Medeiros IS. Surface characteristics and optical properties of plasma deposited films on indirect aesthetic restorative dental materials. Surf Coatings Technol 2018;348:55–63.

[230] Vasiliu R-D, Porojan SD, Bîrdeanu MI, Porojan L. Effect of thermocycling, surface treatments and microstructure on the optical properties and roughness of CAD-CAM and heat-pressed glass ceramics. Materials (Basel) 2020;13:381.

[231] Porojan L, Vasiliu R-D, Bîrdeanu M-I, Porojan S-D. Surface Characterization and Optical Properties of Reinforced Dental Glass-Ceramics Related to Artificial Aging. Molecules 2020;25:3407.

[232] Miranda JS, Barcellos ASP, MartinelliLobo CM, Caneppele TMF, Amaral M, Kimpara ET. Effect of staining and repeated firing on the surface and optical properties of lithium disilicate. J Esthet Restor Dent 2020;32:113–8.

[233] Kleebusch E, Patzig C, Höche T, Rüssel C. Phase formation during crystallization of a Li_2O-Al_2O_3-SiO_2 glass with ZrO_2 as nucleating agent–An X-ray diffraction and (S) TEM-study. Ceram Int 2017;43:9769–77.

[234] Marghussian VK, Mesgar AS-M. Effects of composition on crystallization behaviour and mechanical properties of bioactive glass-ceramics in the $MgO–CaO–SiO_2–P_2O_5$ system.

Ceram Int 2000;26:415–20.

[235] Lu AX, Ke ZB, Xiao ZH, Zhang XF, Li XY. Effect of heat-treatment condition on crystallization behavior and thermal expansion coefficient of Li_2O–ZnO–Al_2O_3–SiO_2–P_2O_5 glass–ceramics. J Non Cryst Solids 2007;353:2692–7.

[236] Alizadeh P, Marghussian VK. Effect of nucleating agents on the crystallization behaviour and microstructure of SiO_2–CaO–MgO (Na_2O) glass-ceramics. J Eur Ceram Soc 2000;20:775–82.

[237] Baldi G, Generali E, Leonelli C, Manfredini T, Pellacani GC, Siligardi C. Effects of nucleating agents on diopside crystallization in new glass-ceramics for tile-glaze application. J Mater Sci 1995;30:3251–5.

[238] Romero M, Rincón JM, Acosta A. Effect of iron oxide content on the crystallisation of a diopside glass–ceramic glaze. J Eur Ceram Soc 2002;22:883–90.

[239] Thakur OP, Kumar D, Parkash O, Pandey L. Effect of K2O addition on crystallization and microstructural behaviour of the strontium titanate-borosilicate glass-ceramic system. Mater Lett 1995;23:253–60.

[240] Chavoutier M, Caurant D, Majérus O, Boulesteix R, Loiseau P, Jousseaume C, et al. Effect of TiO_2 content on the crystallization and the color of (ZrO_2, TiO_2)-doped Li_2O–Al_2O_3–SiO_2 glasses. J Non Cryst Solids 2014;384:15–24.

[241] Denry IL, Holloway JA. Effect of sodium content on the crystallization behavior of fluoramphibole glass–ceramics. J Biomed Mater Res An Off J Soc Biomater Japanese Soc Biomater Aust Soc Biomater Korean Soc Biomater 2002;63:48–52.

[242] Denry IL, Holloway JA, Nakkula RJ, Walters JD. Effect of niobium content on the microstructure and thermal properties of fluorapatite glass-ceramics. J Biomed Mater Res Part B Appl Biomater An Off J Soc Biomater Japanese Soc Biomater Aust Soc Biomater Korean Soc Biomater 2005;75:18–24.

[243] Yu Q, Yan C, Yong D, Feng Y, Liu D, Bin Y. Effect of Fe_2O_3 on non-isothermal crystallization of CaO–MgO–Al_2O_3–SiO_2 glass. Trans Nonferrous Met Soc China 2015;25:2279–84.

[244] Demirkesen E, Maytalman E. Effect of Al_2O_3 additions on the crystallization behaviour and bending strength of a Li_2O–ZnO–SiO_2 glass-ceramic. Ceram Int 2001;27:99–104.

[245] Rezvani M, Eftekhari-Yekta B, Solati-Hashjin M, Marghussian VK. Effect of Cr_2O_3, Fe_2O_3 and TiO_2 nucleants on the crystallization behaviour of SiO_2–Al_2O_3–CaO–MgO (R2O) glass-ceramics. Ceram Int 2005;31:75–80.

[246] Chen J, Zhang Y, Deng C, Dai X, Li L. Effect of the Ba/Ti ratio on the microstructures and dielectric properties of barium titanate-based glass–ceramics. J Am Ceram Soc 2009;92:1350–3.

[247] Torres FJ, Alarcón J. Effect of additives on the crystallization of cordierite-based glass-ceramics as glazes for floor tiles. J Eur Ceram Soc 2003;23:817–26.

[248] Zheng Q, Zhang Y, Montazerian M, Gulbiten O, Mauro JC, Zanotto ED, et al. Understanding glass through differential scanning calorimetry. Chem Rev 2019;119:7848–939.

[249] Theodorou GS, Patsiaoura D, Kontonasaki E, Chrissafis K. Thermal Analysis of Glass-Ceramics and Composites in Biomedical and Dental Sciences. Thermodyn. Biophys. Biomed. Nanosyst., Springer; 2019, p. 245–95.

[250] Watson ES, O'neill MJ. Differential microcalorimeter 1966.

[251] Karpukhina N, Hill RG, Law R V. Crystallisation in oxide glasses–a tutorial review. Chem Soc Rev 2014;43:2174–86.

[252] Komatsu T. Design and control of crystallization in oxide glasses. J Non Cryst Solids 2015;428:156–75.

[253] Rodrigues AM, Cassar DR, Fokin VM, Zanotto ED. Crystal growth and viscous flow in barium disilicate glass. J Non Cryst Solids 2018;479:55–61.

[254] Zanotto ED. Glass Crystallization Research–A 36-Year Retrospective. Part II, Methods of Study and Glass-Ceramics. Int J Appl Glas Sci 2013;4:117–24.

[255] Davis MJ, Zanotto ED. Glass-ceramics and realization of the unobtainable: Property combinations that push the envelope. MRS Bull 2017;42:195–9.

[256] Montazerian M, Yekta BE, Marghussian VK, Bellani CF, Siqueira RL, Zanotto ED. Bioactivity and Cell proliferation in radiopaque gel-derived $CaO–P_2O_5–SiO_2–ZrO_2$ glass and glass–ceramic powders. Mater Sci Eng C 2015;55:436–47.

[257] Goldstein JI, Newbury DE, Michael JR, Ritchie NWM, Scott JHJ, Joy DC. Scanning electron microscopy and X-ray microanalysis. Springer; 2017.

[258] Mohammed A, Abdullah A. Scanning electron microscopy (SEM): A review. Proc. 2018 Int. Conf. Hydraul. Pneum. Băile Govor. Rom., 2018, p. 7–9.

[259] Pinckney LR, Beall GH. Microstructural evolution in some silicate glass–ceramics: a review. J Am Ceram Soc 2008;91:773–9.

[260] Abo-Mosallam HA, Mahdy EA. Crystallization behavior and properties of fluorcanasite–lithium disilicate glasses for potential use in dental application. Ceram Int 2019;45:21144–9.

[261] Milleding P, Wennerberg A, Alaeddin S, Karlsson S, Simon E. Surface corrosion of dental ceramics in vitro. Biomaterials 1999;20:733–46.

[262] Ma Z, Dong G, Lv C, Qiu J. Core–shell glass fibers with high bioactivity and good flexibility. Mater Lett 2012;88:136–9.

[263] Alaghmandfard A, Madaah Hosseini HR. A facile, two-step synthesis and characterization of Fe3O4–LCysteine–graphene quantum dots as a multifunctional nanocomposite. Appl Nanosci 2021. https://doi.org/10.1007/s13204-020-01642-1.

[264] Kleebusch E, Patzig C, Höche T, Rüssel C. A modified B_2O_3 containing Li_2O-Al_2O_3-SiO_2 glass with ZrO_2 as nucleating agent-Crystallization and microstructure studied by XRD and (S) TEM-EDX. Ceram Int 2018;44:19818–24.

[265] Jaimes ATC, de Pablos-Martín A, Hurle K, e Silva JM de S, Berthold L, Kittel T, et al. Deepening our understanding of bioactive glass crystallization using TEM and 3D nano-CT. J Eur Ceram Soc 2021;41:4958–69.

[266] Montazerian M, Zanotto ED. Tough, strong, hard, and chemically durable

enstatite-zirconia glass-ceramic. J Am Ceram Soc 2020;103:5036–49.

[267] Khan AS, Khalid H, Sarfraz Z, Khan M, Iqbal J, Muhammad N, et al. Vibrational spectroscopy of selective dental restorative materials. Appl Spectrosc Rev 2017;52:507–40.

[268] Movasaghi Z, Rehman S, ur Rehman DI. Fourier transform infrared (FTIR) spectroscopy of biological tissues. Appl Spectrosc Rev 2008;43:134–79.

[269] Ramakrishnaiah R, Rehman GU, Basavarajappa S, Al Khuraif AA, Durgesh BH, Khan AS, et al. Applications of Raman spectroscopy in dentistry: analysis of tooth structure. Appl Spectrosc Rev 2015;50:332–50.

[270] Par M, Gamulin O, Marovic D, Klaric E, Tarle Z. Raman spectroscopic assessment of degree of conversion of bulk-fill resin composites–changes at 24 hours post cure. Oper Dent 2015;40:E92–101.

[271] Navarra CO, Cadenaro M, Frassetto A, Fontanive L, Di Lenarda R, Breschi L. Degree of conversion of self-etch adhesives: in situ micro-Raman analysis. Oper Dent 2016;41:501–10.

[272] Dickey B, Price R, Boyd D. Evidence of a complex species controlling the setting reaction of glass ionomer cements. Dent Mater 2016;32:596–605.

[273] Esmati N, Khodaei T, Salahinejad E, Sharifi E. Fluoride doping into SiO_2-MgO-CaO bioactive glass nanoparticles: bioactivity, biodegradation and biocompatibility assessments. Ceram Int 2018;44:17506–13.

[274] Ghahsareh ZS, Banijamali S, Aghaei A. Cerium oxide containing canasite based glass-ceramics for dental applications: Crystallization behavior, mechanical and chemical properties. Ceram Int 2022;48:8489–501.

[275] Deshpande AV, Satyanarayana P. Study of Lithium Disilicate Based Nano Glass Ceramics Containing P2O5. 2021.

[276] Fenn MB, Xanthopoulos P, Pyrgiotakis G, Grobmyer SR, Pardalos PM, Hench LL. Raman spectroscopy for clinical oncology. Adv Opt Technol 2011;2011.

[277] Mai C, Satha H, Thollet G, Vigier G, Andrieu G. Saxs, waxd and tem of the early stages of crystallization in TiO_2-ZrO_2-MgO-Li_2O-Al_2O_3-SiO_2 glass. J Non Cryst Solids 1989;108:201–6.

[278] Oversluizen M, Bras W, Greaves GN, Clark SM, Thomas JM, Sankar G, et al. SAXS/WAXS studies of the devitrification of Cr-doped cordierite glass using synchrotron radiation. Nucl Instruments Methods Phys Res Sect B Beam Interact with Mater Atoms 1995;97:184–9.

[279] Kellermann G, Craievich AF. Isothermal aggregation of Ag atoms in sodium borate glass. Phys Rev B 2004;70:54106.

[280] Autefage H, Allen F, Tang HM, Kallepitis C, Gentleman E, Reznikov N, et al. Multiscale analyses reveal native-like lamellar bone repair and near perfect bone-contact with porous strontium-loaded bioactive glass. Biomaterials 2019;209:152–62.

[281] Haas S, Hoell A, Wurth R, Rüssel C, Boesecke P, Vainio U. Analysis of nanostructure and nanochemistry by ASAXS: Accessing phase composition of oxyfluoride glass

ceramics doped with Er 3+/Yb 3+. Phys Rev B 2010;81:184207.

[282] Raghuwanshi VS, Rüssel C, Hoell A. Crystallization of ZrTiO4 nanocrystals in lithium-alumino-silicate glass ceramics: anomalous small-angle X-ray scattering investigation. Cryst Growth Des 2014;14:2838–45.

[283] Hoell A, Raghuwanshi VS, Bocker C, Herrmann A, Rüssel C, Höche T. Crystallization of BaF 2 from droplets of phase separated glass–evidence of a core–shell structure by ASAXS. CrystEngComm 2020;22:5031–9.

[284] Raghuwanshi VS, Hoell A, Bocker C, Rüssel C. Experimental evidence of a diffusion barrier around BaF 2 nanocrystals in a silicate glass system by ASAXS. CrystEngComm 2012;14:5215–23.

[285] Kleebusch E, Patzig C, Höche T, Rüssel C. Effect of the concentrations of nucleating agents ZrO 2 and TiO 2 on the crystallization of Li 2 O–Al 2 O 3–SiO 2 glass: an X-ray diffraction and TEM investigation. J Mater Sci 2016;51:10127–38.

[286] Hollamby MJ. Practical applications of small-angle neutron scattering. Phys Chem Chem Phys 2013;15:10566–79.

[287] Wright AF, Talbot J, Fender BEF. Nucleation and growth studies by small angle neutron scattering and results for a glass ceramic. Nature 1979;277:366–8.

[288] Bandyopadhyay AK, Wright AF. A Redissolution Process during Particle Growth of a Glass-Ceramic studied by Small Angle Neutron Scattering. Trans Indian Ceram Soc 1987;46:102–7.

[289] Bandyopadhyay AK, Labarbe P, Zarzycki J, Wright AF. Nucleation and crystallization studies of a basalt glass-ceramic by small-angle neutron scattering. J Mater Sci 1983;18:709–16.

[290] Kichanov SE, Gorshkova YE, Rachkovskaya GE, Kozlenko DP, Zakharevich GB, Savenko BN. Structural evolution of luminescence nanoparticles with rare-earth ions in the oxyfluoride glass ceramics. Mater Chem Phys 2019;237:121830.

[291] Kichanov SE, Kozlenko DP, Gorshkova YE, Rachkovskaya GE, Zakharevich GB, Savenko BN. Structural studies of nanoparticles doped with rare-earth ions in oxyfluoride lead-silicate glasses. J Nanoparticle Res 2018;20:1–7.

[292] Kilcoyne SH, Bentley PM, Al-Jawad M, Bubb NL, Al-Shammary HAO, Wood DJ. A small angle neutron scattering study of mica based glass-ceramics with applications in dentistry. Phys B Condens Matter 2004;350:E529–31.

[293] Fernandez-Martin C, Bruno G, Crochet A, Ovono Ovono D, Comte M, Hennet L. Nucleation and growth of nanocrystals in glass-ceramics: an in situ SANS perspective. J Am Ceram Soc 2012;95:1304–12.

[294] Yano J, Yachandra VK. X-ray absorption spectroscopy. Photosynth Res 2009;102:241–54.

[295] Cormier L, Dargaud O, Calas G, Jousseaume C, Papin S, Trcera N, et al. Zr environment and nucleation role in aluminosilicate glasses. Mater Chem Phys 2015;152:41–7.

[296] Dargaud O, Cormier L, Menguy N, Galoisy L, Calas G, Papin S, et al. Structural role of Zr4+ as a nucleating agent in a MgO–$Al2O_3$–SiO_2 glass-ceramics: A combined XAS and

HRTEM approach. J Non Cryst Solids 2010;356:2928–34.

[297] Cormier L, Dargaud O, Menguy N, Henderson GS, Guignard M, Trcera N, et al. Investigation of the Role of Nucleating Agents in $MgO-SiO_2-Al_2O_3-SiO_2-TiO_2$ Glasses and Glass-Ceramics: A XANES Study at the Ti K-and L2, 3-Edges. Cryst Growth Des 2011;11:311–9.

[298] Cochain B, Cormier L, Novikova A, Lelong G, Belin S, Zhang XH. In situ local environment and partitioning of Ni2+ ions during crystallization of an oxyfluoride glass. J Non Cryst Solids 2015;408:7–12.

[299] Cormier L, Cochain B, Dugue A, Dargaud O. Transition Elements and Nucleation in Glasses Using X-ray Absorption Spectroscopy. Int J Appl Glas Sci 2014;5:126–35.

[300] Patzig C, Höche T, Hu Y, Ikeno H, Krause M, Dittmer M, et al. Zr coordination change during crystallization of $MgO–Al_2O_3–SiO_2–ZrO_2$ glass ceramics. J Non Cryst Solids 2014;384:47–54.

[301] Mastelaro VR, Zanotto ED, Lequeux N, Cortes R. Relationship between short-range order and ease of nucleation in Na2Ca2Si3O9, CaSiO3 and PbSiO3 glasses. J Non Cryst Solids 2000;262:191–9.

[302] Cicconi MR, de Ligny D, Gallo TM, Neuville DR. Ca neighbors from XANES spectroscopy: A tool to investigate structure, redox, and nucleation processes in silicate glasses, melts, and crystals. Am Mineral 2016;101:1232–5.

[303] Neuville DR, Cormier L, De Ligny D, Roux J, Flank AM, Lagarde P. Environments around Al, Si, and Ca in aluminate and aluminosilicate melts by X-ray absorption spectroscopy at high temperature. Am Mineral 2008;93:228–34.

[304] Neuville DR, de Ligny D, Henderson GS. Advances in Raman spectroscopy applied to earth and material sciences. Rev Mineral Geochemistry 2014;78:509–41.

[305] Neuville DR, Cormier L, Caurant D, Montagne L, Charpentier T, Chevalier J, et al. From glass to crystal-Nucleation, growth and de-mixing, from research to applications; Du verre au cristal-Nucleation, croissance et demixtion, de la recherche aux applications 2013.

[306] Zanotto ED, Tsuchida JE, Schneider JF, Eckert H. Thirty-year quest for structure–nucleation relationships in oxide glasses. Int Mater Rev 2015;60:376–91.

[307] Hill R, Calver A, Stamboulis A, Bubb N. Real-Time nucleation and crystallization studies of a fluorapatite glass–ceramics using small-Angle neutron scattering and neutron diffraction. J Am Ceram Soc 2007;90:763–8.

[308] Hill RG, O'Donnell MD, Law R V, Karpukhina N, Cochrane B, Tulyaganov DU. The early stages of nucleation and crystallisation of an apatite glass-ceramic: Evidence for nano-scale crystallisation. J Non Cryst Solids 2010;356:2935–41.

[309] Montazerian M, Schneider JF, Yekta BE, Marghussian VK, Rodrigues AM, Zanotto ED. Sol–gel synthesis, structure, sintering and properties of bioactive and inert nano-apatite–zirconia glass–ceramics. Ceram Int 2015;41:11024–45.

[310] Eckert H. Structural characterization of bioactive glasses by solid state NMR. J Sol-Gel Sci Technol 2018;88:263–95.

[311] Morimoto S, Albanesi RB, Sesma N, Agra CM, Braga MM. Main Clinical Outcomes of

Feldspathic Porcelain and Glass-Ceramic Laminate Veneers: A Systematic Review and Meta-Analysis of Survival and Complication Rates. Int J Prosthodont 2016;29.

[312] Denry IL, Holloway JA. Elastic constants, Vickers hardness, and fracture toughness of fluorrichterite-based glass–ceramics. Dent Mater 2004;20:213–9.

[313] Denry IL, Lejus AM, Thery J, Masse M. Preparation and characterization of a new lithium-containing glass-ceramic. Mater Res Bull 1999;34:1615–27.

[314] Uno T, Kasuga T, Nakajima K. High-strength mica-containing glass-ceramics. J Am Ceram Soc 1991;74:3139–41.

[315] Qin F, Zheng S, Luo Z, Li Y, Guo L, Zhao Y, et al. Evaluation of machinability and flexural strength of a novel dental machinable glass-ceramic. J Dent 2009;37:776–80.

[316] Cheng K, Wan J, Liang K. Hot-Pressed Mica Glass-Ceramics with High Strength and Toughness. J Am Ceram Soc 1999;82:1633–4.

[317] Cheng K, Wan J, Liang K. Enhanced mechanical properties of oriented mica glass-ceramics. Mater Lett 1999;39:350–3.

[318] Habelitz S, Carl G, Rüssel C. Processing, microstructure and mechanical properties of extruded mica glass-ceramics. Mater Sci Eng A 2001;307:1–14.

[319] Denry IL, Baranta G, Holloway JA, Gupta PK. Effect of processing variables on texture development in a mica-based glass–ceramic. J Biomed Mater Res Part B Appl Biomater An Off J Soc Biomater Japanese Soc Biomater Aust Soc Biomater Korean Soc Biomater 2003;64:70–7.

[320] Denry IL, Holloway JA. Effect of heat pressing on the mechanical properties of a mica-based glass-ceramic. J Biomed Mater Res Part B Appl Biomater An Off J Soc Biomater Japanese Soc Biomater Aust Soc Biomater Korean Soc Biomater 2004;70:37–42.

[321] Uno T, Kasuga T, Nakayama S, Ikushima AJ. Microstructure of Mica-Based Nanocomposite Glass-Ceramics. J Am Ceram Soc 1993;76:539–41.

[322] Li H, You D-Q, Zhou C-R, Ran J-G. Study on machinable glass-ceramic containing fluorophlogopite for dental CAD/CAM system. J Mater Sci Mater Med 2006;17:1133–7.

[323] Montazerian M, Alizadeh P, Yekta BE. Pressureless sintering and mechanical properties of mica glass–ceramic/Y-PSZ composite. J Eur Ceram Soc 2008;28:2687–92.

[324] Montazerian M, Alizadeh P, Yekta BE. Processing and properties of a mica–apatite glass–ceramic reinforced with Y-PSZ particles. J Eur Ceram Soc 2008;28:2693–9.

[325] Srichumpong T, Phokhinchatchanan P, Thongpun N, Chaysuwan D, Suputtamongkol K. Fracture toughness of experimental mica-based glass-ceramics and four commercial glass-ceramics restorative dental materials. Dent Mater J 2019:2018–77.

[326] Serbena FC, Mathias I, Foerster CE, Zanotto ED. Crystallization toughening of a model glass-ceramic. Acta Mater 2015;86:216–28.

[327] Brochu J-F, El-Mowafy O. Longevity and clinical performance of IPS-Empress ceramic restorations-a literature review. Journal-Canadian Dent Assoc 2002;68:233–8.

[328] Guazzato M, Albakry M, Swain MV, Ironside J. Mechanical properties of In-Ceram

Alumina and In-Ceram Zirconia. Int J Prosthodont 2002;15.

[329] Ho W, Rheinberger V, Wegner S, Frank M. Needle-like apatite-leucite glass-ceramic as a base material for the veneering of metal restorations in dentistry. J Mater Sci Mater Med 2000;11:11–7.

[330] Szabo I, Nagy B, Völksch G, Höland W. Structure, chemical durability and microhardness of glass-ceramics containing apatite and leucite crystals. J Non Cryst Solids 2000;272:191–9.

[331] Michel K, Pantano CG, Ritzberger C, Rheinberger V, Höland W. Coatings on Glass–Ceramic Granules for Dental Restorative Biomaterials. Int J Appl Glas Sci 2011;2:30–8.

[332] Theocharopoulos A, Chen X, Wilson RM, Hill R, Cattell MJ. Crystallization of high-strength nano-scale leucite glass-ceramics. Dent Mater 2013;29:1149–57.

[333] Aurélio IL, Fraga S, Dorneles LS, Bottino MA, May LG. Extended glaze firing improves flexural strength of a glass ceramic. Dent Mater 2015;31:e316–24.

[334] Ritzberger C, Apel E, Höland W, Peschke A, Rheinberger VM. Properties and clinical application of three types of dental glass-ceramics and ceramics for CAD-CAM technologies. Materials (Basel) 2010;3:3700–13.

[335] Cattell MJ, Chadwick TC, Knowles JC, Clarke RL, Lynch E. Flexural strength optimisation of a leucite reinforced glass ceramic. Dent Mater 2001;17:21–33.

[336] Cattell MJ, Chadwick TC, Knowles JC, Clarke RL, Samarawickrama DYD. The nucleation and crystallization of fine grained leucite glass-ceramics for dental applications. Dent Mater 2006;22:925–33.

[337] Chen X, Chadwick TC, Wilson RM, Hill R, Cattell MJ. Crystallization of high-strength fine-sized leucite glass-ceramics. J Dent Res 2010;89:1510–6.

[338] Chen X, Chadwick TC, Wilson RM, Hill RG, Cattell MJ. Crystallization and flexural strength optimization of fine-grained leucite glass-ceramics for dentistry. Dent Mater 2011;27:1153–61.

[339] Theocharopoulos A, Chen X, Hill R, Cattell MJ. Reduced wear of enamel with novel fine and nano-scale leucite glass-ceramics. J Dent 2013;41:561–8.

[340] Zhang Z, Yi Y, Wang X, Guo J, Li D, He L, et al. A comparative study of progressive wear of four dental monolithic, veneered glass-ceramics. J Mech Behav Biomed Mater 2017;74:111–7.

[341] Strbac GD, Unger E, Donner R, Bijak M, Watzek G, Zechner W. Thermal effects of a combined irrigation method during implant site drilling. A standardized in vitro study using a bovine rib model. Clin Oral Implants Res 2014;25:665–74.

[342] Tsitrou EA, Northeast SE, van Noort R. Brittleness index of machinable dental materials and its relation to the marginal chipping factor. J Dent 2007;35:897–902.

[343] Ritzberger C, Schweiger M, Höland W. Principles of crystal phase formation in Ivoclar Vivadent glass-ceramics for dental restorations. J Non Cryst Solids 2016;432:137–42.

[344] Lien W, Roberts HW, Platt JA, Vandewalle KS, Hill TJ, Chu T-MG. Microstructural evolution and physical behavior of a lithium disilicate glass–ceramic. Dent Mater 2015;31:928–40.

[345] Ortiz AL, Borrero-López O, Guiberteau F, Zhang Y. Microstructural development during heat treatment of a commercially available dental-grade lithium disilicate glass-ceramic. Dent Mater 2019;35:697–708.

[346] Simba BG, Ribeiro MV, Alves MFRP, Amarante JEV, Strecker K, dos Santos C. Effect of the temperature on the mechanical properties and translucency of lithium silicate dental glass-ceramic. Ceram Int 2021;47:9933–40.

[347] Chung K, Liao J, Duh J, CHAN DC. The effects of repeated heat-pressing on properties of pressable glass-ceramics. J Oral Rehabil 2009;36:132–41.

[348] Bischoff C, Eckert H, Apel E, Rheinberger VM, Höland W. Phase evolution in lithium disilicate glass–ceramics based on non-stoichiometric compositions of a multi-component system: structural studies by 29 Si single and double resonance solid state NMR. Phys Chem Chem Phys 2011;13:4540–51.

[349] Anusavice KJ, Zhang N. Effect of crystallinity on strength and fracture toughness of Li_2O-Al_2O_3-CaO-SiO_2 glass-ceramics. J Am Ceram Soc 1997;80:1353–8.

[350] ElBatal HA, Khalil EMA, Hamdy YM. In vitro behavior of bioactive phosphate glass–ceramics from the system P2O5–Na2O–CaO containing titania. Ceram Int 2009;35:1195–204.

[351] Kim J-W, Covel NS, Guess PC, Rekow ED, Zhang Y. Concerns of hydrothermal degradation in CAD/CAM zirconia. J Dent Res 2010;89:91–5.

[352] Guess PC, Zhang Y, Kim J-W, Rekow ED, Thompson VP. Damage and reliability of Y-TZP after cementation surface treatment. J Dent Res 2010;89:592–6.

[353] Apel E, van't Hoen C, Rheinberger V, Höland W. Influence of ZrO2 on the crystallization and properties of lithium disilicate glass-ceramics derived from a multi-component system. J Eur Ceram Soc 2007;27:1571–7.

[354] Höland W, Rheinberger V, Schweiger M. Control of nucleation in glass ceramics. Philos Trans R Soc London Ser A Math Phys Eng Sci 2003;361:575–89.

[355] Tulyaganov DU, Agathopoulos S, Kansal I, Valerio P, Ribeiro MJ, Ferreira JMF. Synthesis and properties of lithium disilicate glass-ceramics in the system SiO_2–Al_2O_3–K_2O–Li_2O. Ceram Int 2009;35:3013–9.

[356] Al Mansour F, Karpukhina N, Grasso S, Wilson RM, Reece MJ, Cattell MJ. The effect of spark plasma sintering on lithium disilicate glass-ceramics. Dent Mater 2015;31:e226–35.

[357] Wang F, Yu T, Chen J. Biaxial flexural strength and translucent characteristics of dental lithium disilicate glass ceramics with different translucencies. J Prosthodont Res 2019;64:71–7.

[358] Baumgartner S, Gmeiner R, Schönherr JA, Stampfl J. Stereolithography-based additive manufacturing of lithium disilicate glass ceramic for dental applications. Mater Sci Eng C 2020;116:111180.

[359] Khalkhali Z, Eftekhari yekta B, Marghussian VK. Mechanical and Chemical Properties of Zr and P-Doped Lithium Disilicate Glass Ceramics in Dental Restorations. Int J Appl Ceram Technol 2012;9:497–506.

[360] Belli R, Wendler M, Zorzin JI, da Silva LH, Petschelt A, Lohbauer U. Fracture toughness

mode mixity at the connectors of monolithic 3Y-TZP and LS2 dental bridge constructs. J Eur Ceram Soc 2015;35:3701–11.

[361] Wang G, Wang S, Bian C, Li Y, Shao J. Tribological behavior evaluation of dental fluorapatite glass ceramic. J Aust Ceram Soc 2019;55:363–70.

[362] Wang G, Fu K, Wang S, Yang B. Optimization of mechanical and tribological properties of a dental SiO_2–Al_2O_3–K_2O–CaO–P_2O_5 glass-ceramic. J Mech Behav Biomed Mater 2020;102:103523.

[363] Hsu SM, Ren F, Batich C, Clark AE, Craciun V, Esquivel-Upshaw JF. Dissolution activation energy of a fluorapatite glass-ceramic veneer for dental applications. Mater Sci Eng C 2020;111:110802.

[364] Hsu S-M, Ren F, Chen Z, Kim M, Fares C, Clark AE, et al. Novel coating to minimize corrosion of glass-ceramics for dental applications. Materials (Basel) 2020;13:1215.

[365] Schweiger M, Frank M, Von Clausbruch SC, Höland W, Rheinberger V. Microstructure and properties of a composite system for dental applications composed of glass-ceramics in the SiO_2–Li_2O–ZrO_2–P_2O_5 system and ZrO_2-ceramic (TZP). J Mater Sci 1999;34:4563–72.

[366] Souza MT, Peñarrieta-Juanito GM, Henriques B, Silva FS, de Oliveira APN, Souza JCM. Lithium-zirconium silicate glass-ceramics for restorative dentistry: physicochemical analysis and biological response in contact with human osteoblast. Materialia 2018;2:37–45.

[367] Casasola R, Pérez JM, Romero M. Surface and volume crystallization in fluorrichterite based glasses. J Asian Ceram Soc 2020;8:642–52.

[368] Tulyaganov DU, Agathopoulos S, Fernandes HR, Ventura JM, Ferreira JMF. Preparation and crystallization of glasses in the system tetrasilicic mica-fluorapatite-diopside. J Eur Ceram Soc 2004;24:3521–8.

[369] Alizadeh P, Yekta BE, Javadi T. Sintering behavior and mechanical properties of the mica–diopside machinable glass-ceramics. J Eur Ceram Soc 2008;28:1569–73.

[370] Faeghi-Nia A, Marghussian VK, Taheri-Nassaj E, Pascual MJ, Durán A. Pressureless Sintering of Apatite/Wollastonite–Phlogopite Glass–Ceramics. J Am Ceram Soc 2009;92:1514–8.

[371] Almuhamadi J, Karpukhina N, Cattell M. Diopside glass-ceramics for dental and biomedical applications. Adv. Sci. Technol., vol. 96, Trans Tech Publ; 2014, p. 15–20.

[372] Sinthuprasirt P, van Noort R, Moorehead R, Pollington S. Evaluation of a novel multiple phase veneering ceramic. Dent Mater 2015;31:443–52.

[373] VanNoort R, Shareef MY, Johnson A, James PF. Properties of a canasite-based castable glass-ceramic. J. Dent. Res., vol. 76, AMER ASSOC DENTAL RESEARCH 1619 DUKE ST, ALEXANDRIA, VA 22314; 1997, p. 61.

[374] Johnson A, Van Noort R, Hatton P V, Walsh JM. The effect of investment material and ceramming regime on the surface roughness of two castable glass–ceramic materials. Dent Mater 2003;19:218–25.

[375] Zhang N, Anusavice KJ. Effect of alumina on the strength, fracture toughness, and crystal

structure of fluorcanasite glass-ceramics. J Am Ceram Soc 1999;82:2509–13.

[376] Bubb NL, Wood DJ, Streit P. Reduction of the solubility of fluorcanasite based glass ceramics by additions of SiO_2 and $AlPO_4$. Glas Technol 2004;45:91–3.

[377] Stokes CW, Van Noort R, Hand RJ. Investigation of the chemical solubility of mixed-alkali fluorcanasite forming glasses. J Non Cryst Solids 2006;352:142–9.

[378] Hawsawi RA, Miller CA, Moorehead RD, Stokes CW. Evaluation of reproducibility of the chemical solubility of dental ceramics using ISO 6872: 2015. J Prosthet Dent 2020;124:230–6.

[379] Pollington S, van Noort R. Manufacture, characterisation and properties of novel fluorcanasite glass–ceramics. J Dent 2012;40:1006–17.

[380] Pollington S, Fabianelli A, van Noort R. Microtensile bond strength of a resin cement to a novel fluorcanasite glass-ceramic following different surface treatments. Dent Mater 2010;26:864–72.

[381] Eilaghi M, Montazerian M, Yekta BE. Effect of partial substitution of K_2O for Na_2O on sintering, crystallization and mechanical properties of SiO_2-CaO-K_2O-Na_2O-CaF_2 glass-ceramics. Trans Indian Ceram Soc 2016;75:1–6.

[382] Takav P, Banijamali S, Zadeh ASAH, Mobasherpour I. Influence of TiO2 content on phase evolution, microstructure and properties of fluorcanasite glass-ceramics prepared through sintering procedure for dental restoration applications. Ceram Int 2018;44:7057–66.

[383] Hill R, Wood D. Apatite-mullite glass-ceramics. J Mater Sci Mater Med 1995;6:311–8.

[384] Clifford A, Hill R. Apatite-mullite glass-ceramics. J Non Cryst Solids 1996;196:346–51.

[385] Gorman CM, Hill RG. Heat-pressed ionomer glass–ceramics. Part II. Mechanical property evaluation. Dent Mater 2004;20:252–61.

[386] Gorman CM, Hill RG. Heat-pressed ionomer glass-ceramics. Part I: an investigation of flow and microstructure. Dent Mater 2003;19:320–6.

[387] Jusoh WNW, Matori KA, Zaid MHM, Zainuddin N, Khiri MZA, Rahman NAA, et al. INFLUENCE OF DIFFERENT CaF2 CONTENTS AND HEAT TREATMENT TEMPERATURES ON APATITE-MULLITE GLASS CERAMICS DERIVED FROM WASTE MATERIALS. Ceramics–Silikáty 2020;64:447–59.

[388] Fathi H, Johnson A, van Noort R, Ward JM, Brook IM. The effect of calcium fluoride (CaF2) on the chemical solubility of an apatite–mullite glass–ceramic material. Dent Mater 2005;21:551–6.

[389] Fathi H, Johnson A, van Noort R, Ward JM. The influence of calcium fluoride (CaF_2) on biaxial flexural strength of apatite–mullite glass–ceramic materials. Dent Mater 2005;21:846–51.

[390] Fathi HM, Miller C, Stokes C, Johnson A. The effect of ZrO_2 and TiO_2 on solubility and strength of apatite–mullite glass–ceramics for dental applications. J Mater Sci Mater Med 2014;25:583–94.

[391] Fathi HM, Johnson A. The effect of TiO_2 concentration on properties of apatite-mullite glass-ceramics for dental use. Dent Mater 2016;32:311–22.

[392] Mollazadeh S, Yekta BE, Javadpour J, Yusefi A, Jafarzadeh TS. The role of TiO_2, ZrO_2, BaO and SiO_2 on the mechanical properties and crystallization behavior of fluorapatite–mullite glass–ceramics. J Non Cryst Solids 2013;361:70–7.

[393] Mollazadeh S, Ajalli S, Kashi TSJ, Yekta BE, Javadpour J, Jafari S, et al. The effect of aqueous media on the mechanical properties of fluorapatite–mullite glass–ceramics. Dent Mater 2015;31:1370–6.

[394] Morimoto S, Rebello de Sampaio FBW, Braga MM, Sesma N, Özcan M. Survival rate of resin and ceramic inlays, onlays, and overlays: a systematic review and meta-analysis. J Dent Res 2016;95:985–94.

[395] Fradeani M, Redemagni M. An 11-year clinical evaluation of leucite-reinforced glass-ceramic crowns: a retrospective study. QUINTESSENCE Int Ed 2002;33:503–10.

[396] Gehrt M, Wolfart S, Rafai N, Reich S, Edelhoff D. Clinical results of lithium-disilicate crowns after up to 9 years of service. Clin Oral Investig 2013;17:275–84.

[397] Solá-Ruiz MF, Lagos-Flores E, Román-Rodriguez JL, Del Rio Highsmith J, Fons-Font A, Granell-Ruiz M. Survival rates of a lithium disilicate-based core ceramic for three-unit esthetic fixed partial dentures: a 10-year prospective study. Int J Prosthodont 2013;26.

[398] Makarouna M, Ullmann K, Lazarek K, Boening KW. Six-year clinical performance of lithium disilicate fixed partial dentures. Int J Prosthodont 2011;24.

[399] Belli R, Petschelt A, Hofner B, Hajtó J, Scherrer SS, Lohbauer U. Fracture rates and lifetime estimations of CAD/CAM all-ceramic restorations. J Dent Res 2016;95:67–73.

[400] Splieth CH, Tachou A. Epidemiology of dentin hypersensitivity. Clin Oral Investig 2013;17:3–8.

[401] Porto ICCM, Andrade AKM, Montes MAJR. Diagnosis and treatment of dentinal hypersensitivity. J Oral Sci 2009;51:323–32.

[402] Orchardson R. Clinical features of hypersensitive teeth. Br Dent J 1987;162:253–6.

[403] Gillam DG, Orchardson R. Advances in the treatment of root dentine sensitivity: mechanisms and treatment principles. Endod Top 2006;13:13–33.

[404] Holland G, Narhi MN, Addy M, Gangarosa L, Orchardson R. Guidelines for the design and conduct of clinical trials on dentine hypersensitivity. J Clin Periodontol 1997;24:808–13.

[405] Davari AR, Ataei E, Assarzadeh H. Dentin hypersensitivity: etiology, diagnosis and treatment; a literature review. J Dent 2013;14:136.

[406] Bartold PM. Dentinal hypersensitivity: a review. Aust Dent J 2006;51:212–8.

[407] Frank RM. Attachment sites between the odontoblast process and the intradentinal nerve fibre. Arch Oral Biol 1968;13:833-IN39.

[408] Bernick S. Innervation of the human tooth. Anat Rec 1948;101:81–107.

[409] Brännström M. THE HYDRODYNAMICS OF THE DENTINE; ITS POSSIBLE RELATIONSHIP TO DENTINAL-PAIN 1972.

[410] Brannstrom M, Johnson G, Nordenvall K-J. Transmission and control of dentinal pain: resin impregnation for the desensitization of dentin. J Am Dent Assoc 1979;99:612–8.

[411] Tai BJ, Bian Z, Jiang H, Greenspan DC, Zhong J, Clark AE, et al. Anti-gingivitis effect of a dentifrice containing bioactive glass (NovaMin®) particulate. J Clin Periodontol 2006;33:86–91.

[412] Crovace MC, Souza MT, Chinaglia CR, Peitl O, Zanotto ED. Biosilicate®—A multipurpose, highly bioactive glass-ceramic. In vitro, in vivo and clinical trials. J Non Cryst Solids 2016;432:90–110.

[413] Zanotto ED, Ravagnani C, Peitl Filho O, Panzeri H, Lara EG. Process and compositions for preparing particulate, bioactive or resorbable biosilicates for use in the treatment of oral ailments 2006.

[414] Tirapelli C, Panzeri H, Soares RG, Peitl O, Zanotto ED. A novel bioactive glass-ceramic for treating dentin hypersensitivity. Braz Oral Res 2010;24:381–7.

[415] Tirapelli C, Panzeri H, Lara EHG, Soares RG, Peitl O, Zanotto ED. The effect of a novel crystallised bioactive glass-ceramic powder on dentine hypersensitivity: a long-term clinical study. J Oral Rehabil 2011;38:253–62.

[416] Pintado-Palomino K, Peitl Filho O, Zanotto ED, Tirapelli C. A clinical, randomized, controlled study on the use of desensitizing agents during tooth bleaching. J Dent 2015;43:1099–105.

[417] Zhong Y, Liu J, Li X, Yin W, He T, Hu D, et al. Effect of a novel bioactive glass-ceramic on dentinal tubule occlusion: an in vitro study. Aust Dent J 2015;60:96–103.

[418] Juraski A, Ana PA, Daghastanli N, Santos C, Fernandes MH V, Daguano J. In vitro study of dentin hypersensitivity treated by whitlockite glass-ceramics. BioRxiv 2017:226068.

[419] Gillam DG, Tang JY, Mordan NJ, Newman HN. The effects of a novel Bioglass® dentifrice on dentine sensitivity: a scanning electron microscopy investigation. J Oral Rehabil 2002;29:305–13.

[420] Pradeep AR, Sharma A. Comparison of clinical efficacy of a dentifrice containing calcium sodium phosphosilicate to a dentifrice containing potassium nitrate and to a placebo on dentinal hypersensitivity: a randomized clinical trial. J Periodontol 2010;81:1167–73.

[421] Earl JS, Leary RK, Muller KH, Langford RM, Greenspan DC. Physical and chemical characterization of dentin surface following treatment with NovaMin technology. J Clin Dent 2011;22:62–7.

[422] Galler KM, Cavender A, Yuwono V, Dong H, Shi S, Schmalz G, et al. Self-assembling peptide amphiphile nanofibers as a scaffold for dental stem cells. Tissue Eng Part A 2008;14:2051–8.

[423] Santos FA, Pochapski MT, Martins MC, Zenóbio EG, Spolidoro LC, Marcantonio Jr E. Comparison of biomaterial implants in the dental socket: histological analysis in dogs. Clin Implant Dent Relat Res 2010;12:18–25.

[424] Hu B, Nadiri A, Bopp-Kuchler S, Perrin-Schmitt F, Wang S, Lesot H. Dental epithelial histo-morphogenesis in the mouse: positional information versus cell history. Arch Oral Biol 2005;50:131–6.

[425] Honda MJ, Sumita Y, Kagami H, Ueda M. Histological and immunohistochemical studies of tissue engineered odontogenesis. Arch Histol Cytol 2005;68:89–101.

[426] Sumita Y, Honda MJ, Ohara T, Tsuchiya S, Sagara H, Kagami H, et al. Performance of collagen sponge as a 3-D scaffold for tooth-tissue engineering. Biomaterials 2006;27:3238–48.

[427] Edwards PC, Mason JM. Gene-enhanced tissue engineering for dental hard tissue regeneration:(2) dentin-pulp and periodontal regeneration. Head Face Med 2006;2:1–9.

[428] Young CS, Abukawa H, Asrican R, Ravens M, Troulis MJ, Kaban LB, et al. Tissue-engineered hybrid tooth and bone. Tissue Eng 2005;11:1599–610.

[429] Ohgushi H, Miyake J, Tateishi T. Mesenchymal stem cells and bioceramics: strategies to regenerate the skeleton. Novartis Found. Symp., Wiley Online Library; 2003, p. 118–26.

[430] Iviglia G, Kargozar S, Baino F. Biomaterials, current strategies, and novel nano-technological approaches for periodontal regeneration. J Funct Biomater 2019;10:3.

[431] Han P, Wu C, Chang J, Xiao Y. The cementogenic differentiation of periodontal ligament cells via the activation of Wnt/β-catenin signalling pathway by Li+ ions released from bioactive scaffolds. Biomaterials 2012;33:6370–9.

[432] Zhang Y, Wei L, Wu C, Miron RJ. Periodontal regeneration using strontium-loaded mesoporous bioactive glass scaffolds in osteoporotic rats. PLoS One 2014;9:e104527.

[433] Poologasundarampillai G, Wang D, Li S, Nakamura J, Bradley R, Lee PD, et al. Cotton-wool-like bioactive glasses for bone regeneration. Acta Biomater 2014;10:3733–46.

[434] Baino F, Verné E. Production and characterization of glass-ceramic materials for potential use in dental applications: Thermal and mechanical properties, microstructure, and in vitro bioactivity. Appl Sci 2017;7:1330.

[435] Saadaldin SA, Dixon SJ, Costa DO, Rizkalla AS. Synthesis of bioactive and machinable miserite glass-ceramics for dental implant applications. Dent Mater 2013;29:645–55.

[436] Orita K, Goto K, Kuroda Y, Kawai T, Okuzu Y, Takaoka Y, et al. Long-term outcome of primary total hip arthroplasty with cementless bioactive glass ceramic bottom-coated implants and highly cross-linked polyethylene: A minimum 10-year analysis. J Orthop Sci 2022.

[437] Montazerian M, Hosseinzadeh F, Migneco C, Fook MVL, Baino F. Bioceramic coatings on metallic implants: An overview. Ceram Int 2022.

[438] Zhao Y, Song M, Chen C, Liu J. Effects of the substrate temperature on the bioglass films deposited by pulsed laser. Appl Surf Sci 2008;254:6897–901.

[439] Zhao Y, Song M, Liu J. Characteristics of bioactive glass coatings obtained by pulsed laser deposition. Surf Interface Anal An Int J Devoted to Dev Appl Tech Anal Surfaces, Interfaces Thin Film 2008;40:1463–8.

[440] Floroian L, Savu B, Stanciu G, Popescu AC, Sima F, Mihailescu IN, et al. Nanostructured bioglass thin films synthesized by pulsed laser deposition: CSLM, FTIR investigations and in vitro biotests. Appl Surf Sci 2008;255:3056–62.

[441] Rau J V, Teghil R, Fosca M, De Bonis A, Cacciotti I, Bianco A, et al. Bioactive glass–ceramic coatings prepared by pulsed laser deposition from RKKP targets (sol–gel vs melt-processing route). Mater Res Bull 2012;47:1130–7.

[442] Chen X, Zhang M, Pu X, Yin G, Liao X, Huang Z, et al. Characteristics of heat-treated

plasma-sprayed CaO–MgO–SiO_2-based bioactive glass–ceramic coatings on Ti–6Al–4V alloy. Surf Coatings Technol 2014;249:97–103.

[443] Zhang M, Pu X, Chen X, Yin G. In-vivo performance of plasma-sprayed CaO–MgO–SiO_2-based bioactive glass-ceramic coating on Ti–6Al–4V alloy for bone regeneration. Heliyon 2019;5:e02824.

[444] Padture NP, Schlichting KW, Bhatia T, Ozturk A, Cetegen B, Jordan EH, et al. Towards durable thermal barrier coatings with novel microstructures deposited by solution-precursor plasma spray. Acta Mater 2001;49:2251–7.

[445] Karthikeyan J, Berndt CC, Tikkanen J, Wang JY, King AH, Herman H. Preparation of nanophase materials by thermal spray processing of liquid precursors. Nanostructured Mater 1997;9:137–40.

[446] Xiao Y, Song L, Liu X, Huang Y, Huang T, Wu Y, et al. Applied Surface Science Nanostructured bioactive glass – ceramic coatings deposited by the liquid precursor plasma spraying process. Appl Surf Sci 2011;257:1898–905. https://doi.org/10.1016/j.apsusc.2010.09.023.

[447] Xiao Y, Song L, Liu X, Huang Y, Huang T, Chen J, et al. Bioactive glass-ceramic coatings synthesized by the liquid precursor plasma spraying process. J Therm Spray Technol 2011;20:560–8.

[448] Araújo M, Miola M, Venturello A, Baldi G, Pérez J, Verné E. Glass coatings on zirconia with enhanced bioactivity. J Eur Ceram Soc 2016;36:3201–10.

[449] Braem A, Mattheys T, Neirinck B, Miran Č, Schrooten J, Biest O Van Der, et al. Bioactive glass – ceramic coated titanium implants prepared by electrophoretic deposition 2012;32:2267–73. https://doi.org/10.1016/j.msec.2012.06.013.

[450] Díaz LA, Cabal B, Prado C, Moya JS, Torrecillas R, Fernández A, et al. High-velocity suspension flame sprayed (HVSFS) soda-lime glass coating on titanium substrate: Its bactericidal behaviour. J Eur Ceram Soc 2016;36:2653–8.

[451] Llama-Palacios A, Sánchez MC, Díaz LA, Cabal B, Suárez M, Moya JS, et al. In vitro biofilm formation on different ceramic biomaterial surfaces: Coating with two bactericidal glasses. Dent Mater 2019;35:883–92.

[452] Chatzistavrou X, Tsigkou O, Amin HD, Paraskevopoulos KM, Salih V, Boccaccini AR. Sol–gel based fabrication and characterization of new bioactive glass–ceramic composites for dental applications. J Eur Ceram Soc 2012;32:3051–61.

[453] Friedrich D. Treatment of extended periodontal defects using a b-TCP composite material. Dent Implant 2009.

[454] Buser D, Brägger U, Lang NP, Nyman S. Regeneration and enlargement of jaw bone using guided tissue regeneration. Clin Oral Implants Res 1990;1:22–32.

[455] Kay SA, Wisner-Lynch L, Marxer M, Lynch SE. Guided bone regeneration: integration of a resorbable membrane and a bone graft material. Pract Periodontics Aesthetic Dent PPAD 1997;9:185–94.

[456] Zitzmann N, Naef R, Schärer P, Schüpbach P. Guided bone regeneration and augmentation in implant surgery, using Bio-Oss together with the membrane technique.

Dtsch Zahnarztl Z 1996;6:51.

[457] Alves NM, Mano JF. Chitosan derivatives obtained by chemical modifications for biomedical and environmental applications. Int J Biol Macromol 2008;43:401–14.

[458] Chatelet C, Damour O, Domard A. Influence of the degree of acetylation on some biological properties of chitosan films. Biomaterials 2001;22:261–8.

[459] Lahiji A, Sohrabi A, Hungerford DS, Frondoza CG. Chitosan supports the expression of extracellular matrix proteins in human osteoblasts and chondrocytes. J Biomed Mater Res 2000;51:586–95.

[460] Li Z, Ramay HR, Hauch KD, Xiao D, Zhang M. Chitosan–alginate hybrid scaffolds for bone tissue engineering. Biomaterials 2005;26:3919–28.

[461] Lu HH, El-Amin SF, Scott KD, Laurencin CT. Three-dimensional, bioactive, biodegradable, polymer–bioactive glass composite scaffolds with improved mechanical properties support collagen synthesis and mineralization of human osteoblast-like cells in vitro. J Biomed Mater Res Part A An Off J Soc Biomater Japanese Soc Biomater Aust Soc Biomater Korean Soc Biomater 2003;64:465–74.

[462] Mi F-L, Shyu S-S, Wu Y-B, Lee S-T, Shyong J-Y, Huang R-N. Fabrication and characterization of a sponge-like asymmetric chitosan membrane as a wound dressing. Biomaterials 2001;22:165–73.

[463] Zhang Y, Zhang M. Synthesis and characterization of macroporous chitosan/calcium phosphate composite scaffolds for tissue engineering. J Biomed Mater Res An Off J Soc Biomater Japanese Soc Biomater Aust Soc Biomater Korean Soc Biomater 2001;55:304–12.

[464] Mota J, Yu N, Caridade SG, Luz GM, Gomes ME, Reis RL, et al. Chitosan/bioactive glass nanoparticle composite membranes for periodontal regeneration. Acta Biomater 2012;8:4173–80.

[465] Kong L, Gao Y, Lu G, Gong Y, Zhao N, Zhang X. A study on the bioactivity of chitosan/nano-hydroxyapatite composite scaffolds for bone tissue engineering. Eur Polym J 2006;42:3171–9.

[466] Kopperud SE, Tveit AB, Gaarden T, Sandvik L, Espelid I. Longevity of posterior dental restorations and reasons for failure. Eur J Oral Sci 2012;120:539–48.

[467] Suljak JP, Hatibovic-Kofman S. A fluoride release-adsorption-release system applied to fluoride-releasing restorative materials. Quintessence Int (Berl) 1996;27.

[468] Imazato S, Imai T, Russell RRB, Torii M, Ebisu S. Antibacterial activity of cured dental resin incorporating the antibacterial monomer MDPB and an adhesion-promoting monomer. J Biomed Mater Res An Off J Soc Biomater Japanese Soc Biomater Aust Soc Biomater 1998;39:511–5.

[469] Balazs DJ, Triandafillu K, Wood P, Chevolot Y, Van Delden C, Harms H, et al. Inhibition of bacterial adhesion on PVC endotracheal tubes by RF-oxygen glow discharge, sodium hydroxide and silver nitrate treatments. Biomaterials 2004;25:2139–51.

[470] Chatzistavrou X, Fenno JC, Faulk D, Badylak S, Kasuga T, Boccaccini AR, et al. Fabrication and characterization of bioactive and antibacterial composites for dental

applications. Acta Biomater 2014;10:3723–32.

[471] Freytes DO, Martin J, Velankar SS, Lee AS, Badylak SF. Preparation and rheological characterization of a gel form of the porcine urinary bladder matrix. Biomaterials 2008;29:1630–7.

[472] Chatzistavrou X, Esteve D, Hatzistavrou E, Kontonasaki E, Paraskevopoulos KM, Boccaccini AR. Sol–gel based fabrication of novel glass-ceramics and composites for dental applications. Mater Sci Eng C 2010;30:730–9.

[473] Mount GJ. Clinical performance of glass-ionomers. Biomaterials 1998;19:573–9.

[474] Liu Y, Tan Y, Lei T, Xiang Q, Han Y, Huang B. Effect of porous glass–ceramic fillers on mechanical properties of light-cured dental resin composites. Dent Mater 2009;25:709–15.

[475] Mollazadeh S, Javadpour J, Eftekhari Yekta B, Jafarzadeh TS, Youssefi A. Synthesis and characterisation of dental composite materials reinforced with fluoroapatite–mullite glass–ceramic particles. Adv Appl Ceram 2013;112:294–300.

[476] Mauro JC, Loucks RJ, Gupta PK. Fictive temperature and the glassy state. J Am Ceram Soc 2009;92:75–86.

[477] Wilkinson CJ, Mauro YZ, Mauro JC. RelaxPy: Python code for modeling of glass relaxation behavior. SoftwareX 2018;7:255–8.

[478] Wilkinson C, Mauro JC. Explorer.py: Mapping the energy landscapes of complex materials. SoftwareX 2020;Submitted.

[479] Smedskjaer MM, Mauro JC, Sen S, Yue Y. Quantitative design of glassy materials using temperature-dependent constraint theory. Chem Mater 2010;22:5358–65.

[480] Mauro JC, Allan DC, Potuzak M. Nonequilibrium viscosity of glass. Phys Rev B 2009;80:94204.

[481] Heuer A. Exploring the potential energy landscape of glass-forming systems: from inherent structures via metabasins to macroscopic transport. J Phys Condens Matter 2008;20:373101.

[482] Mauro JC, Smedskjaer MM. Statistical mechanics of glass. J Non Cryst Solids 2014;396:41–53.

[483] Micoulaut M. Relaxation and physical aging in network glasses: a review. Reports Prog Phys 2016;79:66504.

[484] Mauro JC. Decoding the glass genome. Curr Opin Solid State Mater Sci 2018;22:58–64.

[485] Prado SCC, Rino JP, Zanotto ED. Successful test of the classical nucleation theory by molecular dynamic simulations of BaS. Comput Mater Sci 2019;161:99–106.

[486] Tipeev AO, Zanotto ED. Nucleation kinetics in supercooled Ni50Ti50: Computer simulation data corroborate the validity of the Classical Nucleation Theory. Chem Phys Lett 2019;735:136749.

[487] Lodesani F, Menziani MC, Maeda K, Takato Y, Urata S, Pedone A. Disclosing crystal nucleation mechanism in lithium disilicate glass through molecular dynamics simulations and free-energy calculations. Sci Rep 2020;10:1–14. https://doi.org/10.1038/s41598-020-74764-9.

[488] McKenzie ME, Goyal S, Loeffler T, Cai L, Dutta I, Baker DE, et al. Implicit glass model for simulation of crystal nucleation for glass-ceramics. Npj Comput Mater 2018;4:1–7. https://doi.org/10.1038/s41524-018-0116-5.

[489] McKenzie ME, Mauro JC. Hybrid Monte Carlo technique for modeling of crystal nucleation and application to lithium disilicate glass-ceramics. Comput Mater Sci 2018;149:202–7.

[490] Wilkinson CJ, Cassar DR, DeCeanne A V., Kirchner KA, McKenzie ME, Zanotto ED, et al. Energy landscape modeling of crystal nucleation. Acta Mater 2021;2017: 117163. https://doi.org/10.1016/j.actamat.2021.117163.

[491] Cassar DR. ViscNet: Neural Network for predicting the fragility index and the temperature-dependency of viscosity 2020:1–33.

[492] Musgraves JD, Hu J, Calvez L. Springer Handbook of Glass. Springer US; 2021.

[493] Reichelt K. Nucleation and growth of thin films. Vacuum 1988;38:1083–99. https://doi.org/10.1016/0042-207X(88)90004-8.

[494] Pedone A, Malavasi G, Menziani MC, Cormack AN, Segre U. A new self-consistent empirical interatomic potential model for oxides, silicates, and silica-based glasses. J Phys Chem B 2006;110:11780–95.

[495] Mauro JC, Varshneya A. Model interaction potentials for selenium from ab initio molecular simulations. Phys Rev B 2005;71:214105. https://doi.org/10.1103/PhysRevB.71.214105.

[496] Cygan RT, Liang J-J, Kalinichev AG. Molecular models of hydroxide, oxyhydroxide, and clay phases and the development of a general force field. J Phys Chem B 2004;108:1255–66.

[497] Van Duin ACT, Strachan A, Stewman S, Zhang Q, Xu X, Goddard WA. ReaxFFSiO reactive force field for silicon and silicon oxide systems. J Phys Chem A 2003;107:3803–11.

[498] Hahn SH, Rimsza J, Criscenti L, Sun W, Deng L, Du J, et al. Development of a ReaxFF reactive force field for NaSiO x/water systems and its application to sodium and proton self-diffusion. J Phys Chem C 2018;122:19613–24.

[499] Allen MP, Tildesley DJ. Computer simulation of liquids. Oxford university press; 2017.

[500] Plimpton S. Fast parallel algorithms for short-range molecular dynamics. J Comput Phys 1995;117:1–19.

[501] Allen M, Tildesley D. Computer Simulations of Liquids. 2nd ed. Oxford University Press; 2017.

[502] Li X, Song W, Yang K, Krishnan NMA, Wang B, Smedskjaer MM, et al. Cooling rate effects in sodium silicate glasses: Bridging the gap between molecular dynamics simulations and experiments. J Chem Phys 2017;147:74501.

[503] Deng L, Du J. Development of boron oxide potentials for computer simulations of multicomponent oxide glasses. J Am Ceram Soc 2018;DOI:10.111:1–24. https://doi.org/10.1111/jace.16082.

[504] Bauchy M, Micoulaut M. Atomic scale foundation of temperature-dependent bonding

constraints in network glasses and liquids. J Non Cryst Solids 2011;357:2530–7.

[505] Wilkinson CJ, Potter AR, Welch RS, Bragatto C, Zheng Q, Bauchy M, et al. Topological origins of the mixed alkali effect in glass. J Phys Chem B 2019;123:7482–9.

[506] Yu Y, Krishnan NMA, Smedskjaer MM, Sant G, Bauchy M. The hydrophilic-to-hydrophobic transition in glassy silica is driven by the atomic topology of its surface. J Chem Phys 2018;148:74503.

[507] Aga RS, Morris JR, Hoyt JJ, Mendelev M. Quantitative parameter-free prediction of simulated crystal-nucleation times. Phys Rev Lett 2006;96:245701.

[508] Mahata A, Zaeem MA, Baskes MI. Understanding homogeneous nucleation in solidification of aluminum by molecular dynamics simulations. Model Simul Mater Sci Eng 2018;26:25007.

[509] Cassar DR. Crystallization driving force of supercooled oxide liquids. Int J Appl Glas Sci 2016;7:262–9.

[510] Tipeev AO, Zanotto ED, Rino JP. Crystal Nucleation Kinetics in Supercooled Germanium: MD Simulations versus Experimental Data. J Phys Chem B 2020;124:7979–88.

[511] Stillinger FH. Supercooled liquids, glass transitions, and the Kauzmann paradox. J Chem Phys 1988;88:7818–25.

[512] Stillinger FH, Weber TA. Hidden structure in liquids. Phys Rev A 1982;25:978.

[513] Mousseau N, Barkema GT. Traveling through potential energy landscapes of disordered materials: The activation-relaxation technique. Phys Rev E 1998;57:2419.

[514] Pedone A, Malavasi G, Menziani MC, Cormack AN, V AU, York N. A New Self-Consistent Empirical Interatomic Potential Model for Oxides, Silicates, and Silica-Based Glasses. J Phys Chem B 2006;110:11780–95.

[515] Li P, Henkelman G, Keith JA, Johnson JK. Elucidation of aqueous solvent-mediated hydrogen-transfer reactions by ab initio molecular dynamics and nudged elastic-band studies of NaBH4 hydrolysis. J Phys Chem C 2014;118:21385–99.

[516] Henkelman G, Uberuaga BP, Jónsson H. A climbing image nudged elastic band method for finding saddle points and minimum energy paths. J Chem Phys 2000;113:9901–4.

[517] Henkelman G, Jónsson H. Improved tangent estimate in the nudged elastic band method for finding minimum energy paths and saddle points. J Chem Phys 2000;113:9978–85.

[518] Prada-Gracia D, Gómez-Gardeñes J, Echenique P, Falo F. Exploring the free energy landscape: From dynamics to networks and back. PLoS Comput Biol 2009;5:e1000415. https://doi.org/10.1371/journal.pcbi.1000415.

[519] Bording JK, Taftø J. Molecular-dynamics simulation of growth of nanocrystals in an amorphous matrix. Phys Rev B - Condens Matter Mater Phys 2000;62:8098–103. https://doi.org/10.1103/PhysRevB.62.8098.

[520] Deng B, Luo J, Harris JT, Smith CM, McKenzie ME. Toughening of Li_2O-$2SiO_2$ glass-ceramics induced by intriguing deformation behavior of lithium disilicate nanocrystal. J Am Ceram Soc 2020;103:965–72.

[521] Deng B, Harris JT, Luo J. Atomic picture of crack propagation in Li_2O-$2SiO_2$ glass-ceramics revealed by molecular dynamics simulations. J Am Ceram Soc 2020;103:4304–12.

[522] Deng B, Harris JT. A novel approach to generate glass-ceramics samples for molecular dynamics simulations. Comput Mater Sci 2021;186:110008.

[523] Deng B, Luo J, Harris JT, Smith CM, Wilkinson TM. Toward revealing full atomic picture of nanoindentation deformation mechanisms in Li_2O-$2SiO_2$ glass-ceramics. Acta Mater 2021;208:116715.

[524] Bishnoi S, Singh S, Ravinder R, Bauchy M, Gosvami NN, Kodamana H, et al. Predicting Young's modulus of oxide glasses with sparse datasets using machine learning. J Non Cryst Solids 2019;524:119643.

[525] Liu H, Fu Z, Yang K, Xu X, Bauchy M. Machine learning for glass science and engineering: A review. J Non-Crystalline Solids X 2019;4:100036.

[526] Ravinder R, Sridhara KH, Bishnoi S, Grover HS, Bauchy M, Kodamana H, et al. Deep learning aided rational design of oxide glasses. Mater Horizons 2020;7:1819–27.

[527] DeCeanne A V, Fry AL, Wilkinson CJ, Dittmer M, Ritzberger C, Rampf M, et al. Experimental analysis and modeling of the Knoop hardness of lithium disilicate glass-ceramics containing lithium tantalate as a secondary phase. J Non Cryst Solids 2022;585:121540.

[528] DeCeanne AV, Wilkinson CJ, Dittmer M, Ritzberger C, Rampf M, Mauro JC. Experimental analysis and machine learning modeling of optical properties of lithium disilicate glass-ceramics comprising lithium tantalate as a secondary phase. International Journal of Applied Glass Science. 2022 Mar 24.

[529] Mauro JC, Ellison AJ, Allan DC, Smedskjaer MM. Topological model for the viscosity of multicomponent glass-forming liquids. Int J Appl Glas Sci 2013;4(4):408–13.

[530] Mahmoud M, Folz D, Suchicital C, Clark D, Fathi Z. Variable frequency microwave (VFM) processing: A new tool to crystallize lithium disilicate glass. Ceram Eng Sci Proc 2006;27(6):143–153.

[531] Liu J, Zhang B, Yan C, Shi Y. The effect of processing parameters on characteristics of selective laser sintering dental glass-ceramic powder. Rapid Prototyp J 2010;16(2):138–145.

[532] Cam P, Neuenschwander B, Schwaller P, Köhli B, Lüscher B, Senn F, Kounga A, Appert C. A novel laser-based method for controlled crystallization in dental prosthesis materials. Prog Biomed Optics Imag - Proc SPIE 201;9306:930607.

[533] Kawai K, Inoue M, Tsuchitani Y. Effect of ion-exchange treatment on mechanical properties of new dental ceramics. Am J Dent 2003;16(5):347–350.

[534] Fischer F, Marx R. Suppression of subcritical crack growth in a leucite-reinforced dental glass by ion exchange. J Biomed Mater Res Part A 2003;66(4):885–9.

[535] Fischer H, Brehme M, Telle R, Marx R. Effect of ion exchange of glazed dental glass ceramics on strength parameters. J Biomed Mater Res Part A 2005;72(2):175–9.

[536] Fischer H, Souza RAD, Wätjen AM, Richter S, Edelhoff D, Mayer J, Martin M, Telle R.

Chemical strengthening of a dental lithium disilicate glass-ceramic material. J Biomed Mater Res Part A 2008;87(3):582–7.

[537] Alzahrani AS, Pintori G, Sglavo VM. Conventional and electric field-assisted ion exchange on glass-ceramics for dental applications. J Eur Ceram Soc 2021;41(10):5341-5348.

[538] Liu Y, Tan Y, Lei T, Xiang Q, Han Y, Huang B. Effect of porous glass–ceramic fillers on mechanical properties of light-cured dental resin composites. Dent Mater 2009;25(6): 709–15.

[539] Mollazadeh S, Javadpour J, Eftekhari Yekta B, Jafarzadeh TS, Youssefi A. Synthesis and characterisation of dental composite materials reinforced with fluoroapatite-mullite glassceramic particles. Adv Appl Ceram 2013;112(5):294–300.